Winter 12-15-2015

Structural Evolution, Chemical Order, and Crystallization of Metallic Liquids and Glasses

Mark Johnson
Washington University in St. Louis

Recommended Citation

Johnson, Mark, "Structural Evolution, Chemical Order, and Crystallization of Metallic Liquids and Glasses" (2015). *Arts & Sciences Electronic Theses and Dissertations*. 655.
https://openscholarship.wustl.edu/art_sci_etds/655

WASHINGTON UNIVERSITY IN ST. LOUIS

Department of Physics

Dissertation Examination Committee:
Kenneth F. Kelton, Chair
Katharine Flores
Patrick Gibbons
Erik Henriksen
Zohar Nussinov
Li Yang

Structural Evolution, Chemical Order, and Crystallization of Metallic Liquids and Glasses

by
Mark Lyell Johnson

A dissertation presented to the
Graduate School of Arts & Sciences
of Washington University in
partial fulfillment of the
requirements for the degree
of Doctor of Philosophy

December 2015
St. Louis, Missouri

Table of Contents

List of Figures

List of Tables

List of Abbreviations

ANL	Argonne National Laboratory
APS	Advanced Photon Source
APS 2011	A series of high-energy XRD experiments at the APS on amorphous ribbons during October
ARCS	Wide Angular-Range Chopper Spectrometer
BCC	Body-Centered Cubic
BESL	Beamline Electrostatic Levitation (Levitator)
BESL 2010	A series of BESL experiments undertaken at the APS during August 2010
BESL 2013	A series of BESL experiments undertaken at the APS during July 2013
BMG	Bulk Metallic Glass
BN	Boron Nitride
BT	Bhatia-Thornton
CALPHAD	Computer Coupling of Phase Diagrams and Thermochemistry
CBBC	Carbon-Bonded B_4C
CCR	Critical Cooling Rate
CCT	Critical Casting Thickness
CN	Coordination Number
CNT	Classical Nucleation Theory
CNA	Common Neighbor Analysis
CNCS	Cold Neutron Chopper Spectrometer
CRMC	Constrained Reverse Monte Carlo
CSRO	Chemical Short-Range Order
DRPHS	Dense Random Packing of Hard Spheres
DSC	Differential Scanning Calorimetry (Calorimeter)
DTA	Differential Thermal Analysis (Analyzer)
EML	Electromagnetic Levitation
ESL	Electrostatic Levitation
EXAFS	Extended X-ray Absorption Fine Structure
FCC	Face-Centered Cubic
FK	Frank-Kasper
FTP	File Transfer Protocol
FWHM	Full-Width at Half Max
FZ	Faber-Ziman
GFA	Glass-Forming Ability
GSAS	General Structure and Analysis Software
HA	Honeycutt-Andersen
HCP	Hexagonal Close-Packed
HV	High Voltage
HYDRA	The combination of four X-ray detectors used during SAXS 2014
IDL	Interactive Data Language
ISRO	Icosahedral Short-Range Order
ISU	Iowa State University

LRO	Long-Range Order
MD	Molecular Dynamics
MMC	Metropolis Monte Carlo
MRO	Medium-Range Order
NESL	Neutron Electrostatic Levitator
NIST	National Institute of Standards and Technology
NOMAD	Nanoscale-Ordered Materials Diffractometer
NOMAD 2014	A series of NESL experiments undertaken at the SNS during September and October 2014
ORNL	Oak Ridge National Laboratory
PCF	Pair-Correlation Function
PDF	Pair-Distribution Function
PPCF	Partial Pair-Correlation Function
PPDF	Partial Pair-Distribution Function
PSD	Position Sensitive Detector
PSF	Partial Structure Factor
RBBC	Reaction Bonded B_4C
RDF	Radial Distribution Function
RF	Radiofrequency
R_G	Radius of Gyration
RMC	Reverse Monte Carlo
SANS	Small-Angle Neutron Scattering
SAS	Small-Angle Scattering
SAXS	Small-Angle X-ray Scattering
SAXS 2014	A series of SAXS and WAXS experiments using the BESL at the APS during November 2014
SNS	Spallation Neutron Source
SRO	Short-Range Order
TEM	Transmission Electron Microscopy (Microscope)
T_g	Glass Transition Temperature
T_L	Liquidus Temperature
TM	Transition Metal
TOF	Time-of-Flight
T_{RG}	Reduced Glass Transition Temperature
T_S	Solidus Temperature
TTL	Transistor-Transistor Logic
T_X	Crystallization Temperature
UV	Ultraviolet
VI (1)	Voronoi Index classification scheme
VI (2)	Virtual Instrument, a LabVIEW program
VULCAN	Engineering Materials Diffractometer
WAXS	Wide-Angle X-ray Scattering
WU-BESL	Washington University's Beamline Electrostatic Levitator
WUSTL	Washington University in St. Louis
XRD	X-ray Diffraction

Acknowledgments

I would first of all like to thank my advisor, Prof. Ken Kelton. His guidance, support, and patience have made this all possible. His dedication and enthusiasm have always been an encouragement. His willingness to take extra time out of a busy schedule to help focus my progress was invaluable. I also thank Prof. Pat Gibbons and Prof. Zohar Nussinov for their mentoring and support throughout my graduate career as my research became more focused. Prof. Gibbons also provided much needed support in microscopy, and was always willing to help.

Within the Kelton group, I would like to thank Dr. Anup Gangopadhyay for his passion and the many useful discussions we have had. I would also like to thank Dr. Nicholas Mauro for his mentorship and invaluable assistance throughout my career here. His dedication and drive to pursuing science is an inspiration. I would like to thank Dr. Adam Vogt for his continual support and friendship. His knowledge and experience and his willingness to help have been greatly appreciated. I also thank all of the other graduate students that I have been fortunate enough to work with over the last five years: Dr. James Bendert, Dr. Kevin Derendorf, Dr. Matthew Blodgett, Chris Pueblo, Robert Ashcraft, Rongrong Dai, and Jen Gewin. Their companionship, support, and technical expertise have been invaluable. In particular, I wish to thank Adam, Chris, Robert, and Rongrong for their assistance in proof reading this dissertation. I would also like to thank the undergraduate students I have had the fortune to work with: Walter Fu, Sirish Veligati, Corie Miller, and Zackary Markow provided invaluable support in all aspects of the experiments. In particular, I thank Zack for the useful discussions and the use of his Voronoi code.

The Physics Department at Washington University has always provided an open and welcoming atmosphere. In particular, I would like to thank the machine shop team including Todd Hardt, Tony Biondo, and Denny Huelsman. Their support throughout our construction projects, as well as their guidance, has made these experiments possible. I would also like to thank Vy Tran and Ryan Soklaski for the use of their Voronoi code, along with many useful discussions.

I would like to thank our collaborators at Iowa State University and Ames National Laboratory: Alan Goldman, Gustav Rustan, Dante Quirinale, Andreas Kreyssig, Matt Kramer, and Matt Besser. They have provided invaluable support and assistance in both X-ray and neutron scattering experiments. In particular, I would like to thank Dante for his friendship, endurance, and support throughout the weeks we spent debugging and repairing the NESL.

I would like to thank the staff at Advanced Photon Source at Argonne National Laboratory for their support and direction during our many X-ray scattering experiments. In particular, Doug Robinson at Sector 6 has always been willing to help make sure our experiments were a success, even when they were not on his beamline. Without his assistance with coordination, things would not have proceeded as smoothly as they did. I would like to thank the team at Sector 1 as well for all of their support during our small-angle scattering run: Jon Almer, Ali Mashayekhi, and Peter Kenesei.

The staff at the Spallation Neutron Source at Oak Ridge National Laboratory provided incredible support throughout the process of commissioning the NESL. In particular I would like to thank Ken Herwig for his continued mentorship, guidance, and logistic support. His excitement for science is contagious. Joerg Neuefeind was always available for technical discussions and the analysis of the neutron data would not have proceeded nearly as quickly

without his support. Konstantin Lokshin and Takeshi Egami of the Joint Institute for Neutron Science, as well as Cory Fletcher and John Carruth of the SNS, have all been instrumental in the ongoing support of the NESL. Their assistance has been invaluable.

I acknowledge the sources of funding that have supported me throughout my graduate career. The Summer Hughes Fellowship, the University Fellowship, and the GAANN fellowship were received under grants from the U.S. Department of Education. My research was funded through grants from NASA (NNX07AK27G and NNX10AU19G) and the NSF (DMR0856199, DMR1206707, and DMR095946). Use of the Advanced Photon Source was supported by the U.S. Department of Energy, Basic Energy Science, Office of Science, under contract no. DE-AC02-06CH11357. The research at the Spallation Neutron Source was sponsored by the Scientific User Facilities Division, Office of Basic Energy Sciences, U.S. Department of Energy.

I would also like to thank my colleagues from my undergraduate institution, the University of Minnesota. My advisor, Prof. Priscilla Cushman, and the graduate students I worked with, Matt Fritts and Scott Fallows, provided much appreciated mentorship and support leading into my graduate career here. My fellow undergraduate students: Kirby Myers, Brian Mulligan, and Katharine Szutz made my time at UMN worth it. I am deeply indebted to their friendship.

Last but not least, I would like to thank my family. You have always been there for me, despite the distances between us. I would like to thank my parents for their love and support and never giving up on me. I would like to thank the Gladden Clan for giving me a home away from home. I have always been welcomed without question. Your encouragement in the face of struggles has been greatly appreciated. And finally, I thank my amazing wife, Emily, my

smarter half. You have been with me every step of the way, from applying to graduate school in “podunk” Missouri to supporting me through the many lengthy experimental trips I have been called away on. I love you more than words can express.

ABSTRACT OF THE DISSERTATION

Structural Evolution, Chemical Order, and Crystallization of Metallic Liquids and Glasses

by

Mark Lyell Johnson

Doctor of Philosophy in Physics

Washington University in St. Louis, 2015

Professor Kenneth F. Kelton, Chairperson

Over the last 60 years, bulk metallic glasses have emerged as a new class of materials with highly desirable material properties. Their high strength, high elasticity, and corrosion resistance are attractive properties for viable commercial products. At its core, material properties are directly related to the underlying microstructure. By understanding the structural and chemical order in the liquid and undercooled liquid and their relationship to thermophysical properties such as viscosity, a greater understanding of bulk metallic glass formation can be achieved. In this dissertation, electrostatic levitation techniques are used to study the liquid in a containerless environment using a combination of X-ray and neutron scattering techniques. An X-ray diffraction study of liquid and glass Ni-Nb(-Ta) alloys reveals that an acceleration in the rate of structural ordering must take place near the glass transition, providing the framework for a structural description of fragility. X-ray diffraction and thermophysical property measurements of Zr-Ni binary alloys further characterize the structural connection to viscosity, and reveal signatures of chemical ordering in the liquid. By combining X-ray and neutron scattering measurements, the topological and chemical order in $Zr_{80}Pt_{20}$ and $Zr_{77}Rh_{23}$ liquids is characterized. Very different chemical order is found between these alloys, despite their remarkable similarity in topological order. Due to this structural similarity, a new metastable phase is predicted and later identified emerging from a deeply supercooled $Zr_{77}Rh_{23}$ liquid. $Zr_{77}Rh_{23}$ is found to have many metastable crystallization pathways, which are further characterized here. Through simultaneous wide-angle and small-angle X-ray scattering, the devitrification behavior of a bulk metallic glass (Vitreloy 105) is investigated and is found to decompose into two distinct compositions during crystallization. By understanding crystallization pathways in good glass-forming alloys, a better understanding of glass formation and its connections to structural and thermophysical properties can be achieved.

Chapter 1: Introduction

The use of glass in industry and culture has been well documented throughout human history. From cutting tools developed from volcanic rocks (obsidian), to stained glass windows, to the screens used in today's smart phones and electronics (e.g., Gorilla® glass), glasses are and have been integral parts of our culture for thousands of years. Despite their widespread use, a complete understanding of the nature of glass formation remains elusive. Many "rules of thumb" have been developed from extensive experience, but an answer to the fundamental question of "why do some materials form glasses more easily than others?" remains unanswered.

A liquid is distinguished from a crystalline solid by its lack of long-range translational order. However, significant short- and often medium-range order are still present. A glass is formed if the liquid can be cooled sufficiently rapidly below its melting temperature while avoiding crystal formation. The liquid becomes supercooled and will eventually solidify into a glass as the atoms lose mobility, retaining much of the inherent disorder associated with the liquid. Avoiding crystallization is a competitive process involving thermodynamic and kinetic effects that are tied to the atomic-level structure.

Metallic glasses are relatively new materials, with the first discovered as recently as 1960 [1]. They have shown amazing advances in the years since, quickly finding their niche in commercial applications due to their unique combinations of high strength and elasticity, as well as many other desirable properties such as corrosion and fracture resistance [2, 3]. However, their practical implementation has been hindered by the prohibitively high cooling rates often necessary for glass formation. The ease with which a metallic liquid can bypass crystallization is known as its glass-forming ability (GFA). This is greatly affected by the types, number, and relative ratios of the constituent elements.

This dissertation seeks to answer the question of how the thermodynamic and kinetic properties are related to the atomic structure and in particular their relationship to GFA in metallic glasses. It has become clear that chemical order often accompanies topological order, and new equipment was designed, constructed, and commissioned to identify the details of this relationship. By understanding topological and chemical ordering of the liquid and glass and their relationship to the stable and metastable crystalline phases that form, questions of how crystallization is avoided can be answered. This chapter will provide a brief background on the nature of glasses and the glass transition (Sections 1.1 and 1.2). The underlying kinetic and thermodynamic properties relating to glass-forming ability are discussed (Sections 1.2 and 1.3), and connections are made to the general structures observed in liquids and glasses (Section 1.4). This chapter will conclude with a discussion of the levitation technique used to access the supercooled liquid (Section 1.5).

1.1 Crystalline and Non-Crystalline Order

A crystalline solid is characterized by the presence of long-range atomic order (LRO). It consists of structural units that stack together repeatedly, producing a grid-like pattern (Figure 1.1 (a)). Liquids and glasses, on the other hand, are notable for a distinct lack of this long range translational symmetry. However, while their long-range structure is not translationally ordered, their local atomic arrangements are not random. There still exists strong short-range and occasionally medium-range order (SRO and MRO) (Figure 1.1 (b-c)). Even though the structural units are not repeatable, each atom in an amorphous structure will, on average, contain similar local environments. In the case of a network glass, such as the traditional silicate glasses,

(Figure 1.1 (b)), each atom shares a similar number of bonds, but the distribution of bond angles is more diverse than in the corresponding crystal. Due to the non-directional nature of metallic bonds, metallic glasses are instead defined by an average number of neighbors, or coordination number (CN) (Figure 1.1 (c)). However, the fast dynamics inherent in a liquid cause constant changes in the local coordination number as individual atoms continuously move, making and breaking bonds. This results in a broader distribution of the average number of neighbors, but in general it is still well defined.

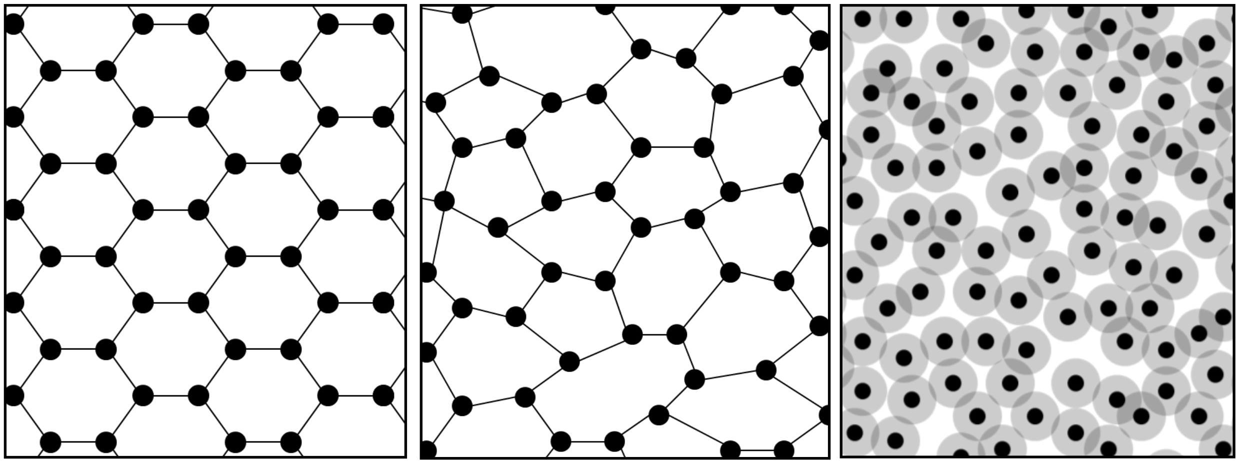

Figure 1.1 Examples of atomic configurations for (a) crystalline, (b) network glass, and (c) metallic glass structures. The overlapping spheres represent bonded atoms in (c).

1.2 Glasses and the Glass Transition

An equilibrium liquid is ergodic, meaning that it can sample all possible configurations due to the high atomic mobility. Ergodicity is broken upon reaching the glass transition, leading to dramatic changes in the thermophysical properties. Volume and entropy (the first derivatives of the Gibb's free energy) both evolve continuously during glass formation, changing the rate of evolution at T_g. This is in contrast to the discontinuous behavior observed during the first-order liquid-crystal phase transition (Figure 1.2 (a)). The second derivatives of the Gibb's free energy for liquids and glasses (e.g., the thermal expansion coefficient, α, and specific heat, C_P) resemble a discontinuity at T_g, but it is spread out over a finite temperature interval rather than a single, well defined transition temperature (Figure 1.2 (b)). This has led to the glass transition being called a "diffuse second order [phase] transition" [4].

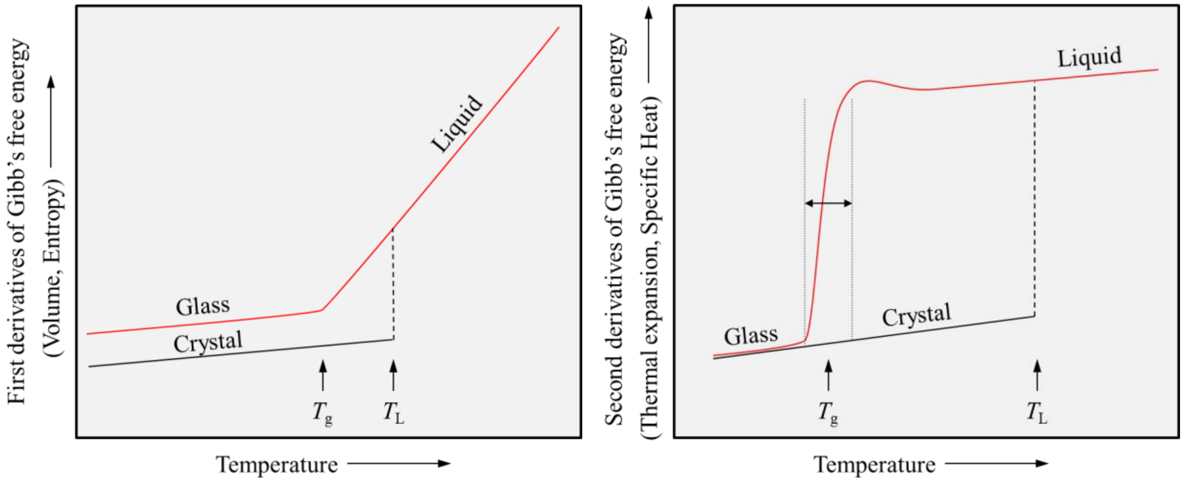

Figure 1.2 (a) First derivatives of the Gibb's free energy and (b) second derivatives of the Gibb's free energy.

If crystallization can be avoided, a glass is formed when the liquid is rapidly cooled below its melting temperature until it reaches T_g, where the structure becomes "frozen in". Empirically, this is the temperature at which the viscosity reaches 10^{12} Pa-s and the relaxation time of atomic rearrangement becomes much larger than the laboratory timescale (e.g., minutes). Avoiding crystallization of the equilibrium phase is, then, the critical step in the formation of undercooled liquids and glasses.

As the temperature decreases, the atomic mobility is reduced and the viscosity, η, rapidly increases by many orders of magnitude as it approaches T_g. For traditional silicate glasses, this is modeled well by an Arrhenius relationship which is characterized by a constant activation energy, E_A, for viscous flow:

$$\eta = \eta_0 \exp\left(E_A / RT\right). \tag{1.1}$$

Here, η_0 is the viscosity at infinite temperature and R is the ideal gas constant. This can be represented in an Angell graph [5] by plotting $\log_{10}\eta$ vs. T_g/T (Figure 1.3). A constant slope on an Angell graph represents a constant E_A, while any curvature implies that E_A is temperature dependent. The diverse behaviors observed in viscosity as liquids are cooled to T_g can be classified by their *fragility* [5], where *strong* systems approach T_g with very little change to their activation energy and *fragile* systems show large positive deviations from Arrhenius behavior (sometimes called super-Arrhenius behavior) upon approaching T_g. Silicates are examples of strong glasses, while *o*-terphenyl (OTP) represents a fragile extreme. Metallic glasses tend to be clustered between these two extremes.

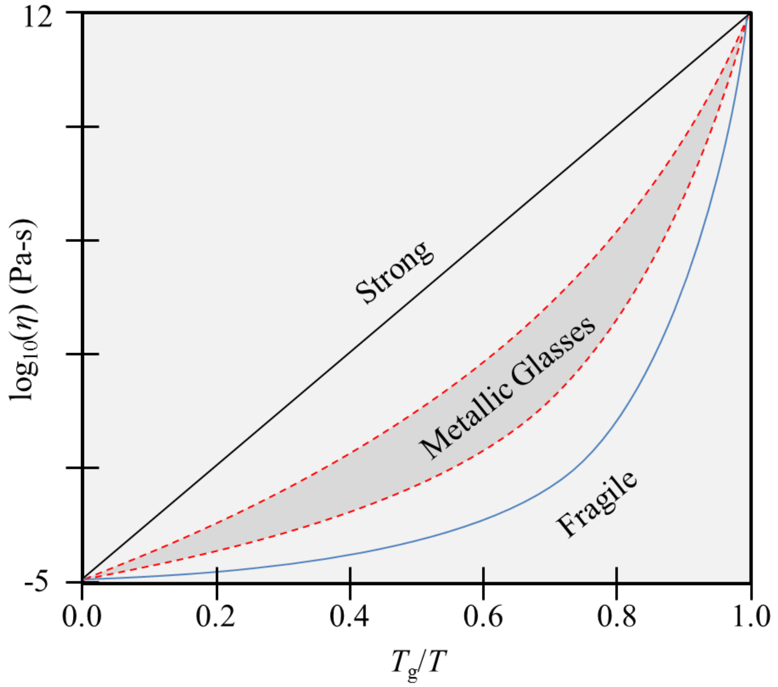

Figure 1.3 Schematic of an Angell plot of viscosity where $\log_{10}(\eta)$ is plotted against inverse temperature and scaled to T_g. All alloys share a common point where the viscosity at T_g is defined to be 10^{12} Pa-s.

The rapid changes in viscosity as the liquid approaches T_g cannot be explained by simple temperature effects and instead imply that some intrinsic property, such as the structure, of the material must also change [6]. The kinetics are directly connected to thermodynamic principles through the Adams-Gibbs relation [7]:

$$\eta = \eta_0 \exp\left(\frac{B}{T\ S_C(T)}\right). \tag{1.2}$$

Here, B is a temperature independent constant and S_C is the temperature-dependent configurational entropy of the system. S_C represents the number of possible configurations the system can sample and directly points to a structural basis for the fragility of a liquid.

A convenient way of understanding the relationship between viscosity and configurational entropy is to examine the *potential energy landscape* [8, 9]. Within this description, a 3N+1 dimensional landscape is constructed which represents all possible configurations that the liquid can sample, where N is the number of atoms (Figure 1.4). The surface represents the potential energy of each configuration, with peaks representing high potential energy and valleys corresponding to low-energy states, such as the stable crystalline configuration or metastable phases such as the glass. Sampling the energy landscape consists of dynamic atomic rearrangements, altering the configuration. High-temperature liquids are very mobile and can sample the entire configuration space, hence they are ergodic. As the temperature is lowered, the configuration can get trapped within *megabasins*, where there is not enough energy to overcome the barrier between adjacent basins. Movement between these megabasins requires large-scale atomic rearrangement and can be characterized by *α-relaxation*. Within each megabasin are many smaller configurational basins which do not require large-scale rearrangement. Sampling between these smaller basins can occur through *β-relaxation* with the rearrangement of small clusters or individual atoms. At high temperatures, the two relaxation times are equal, but as the temperature is lowered, the barriers between megabasins increase and α-relaxation is slowed. The glass transition is reached when the megabasins can no longer be sampled and α-relaxation disappears entirely. This breaks the ergodicity of the liquid and it falls out of equilibrium into the amorphous state.

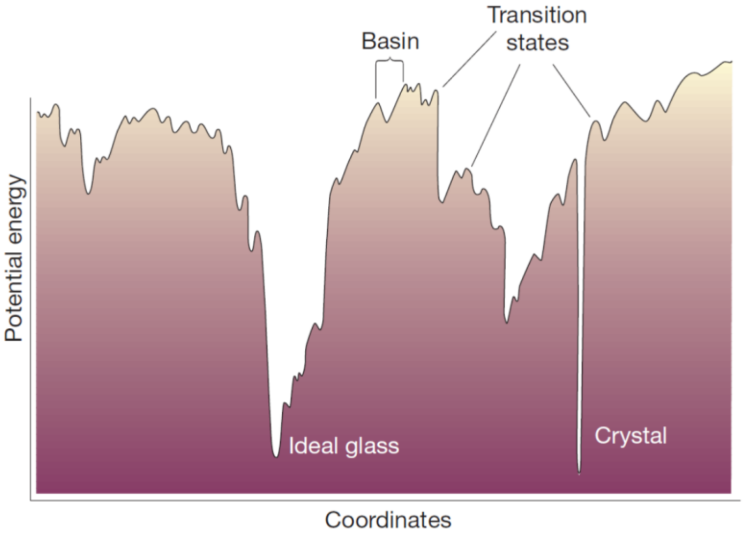

Figure 1.4 A schematic of an energy landscape. The *x*-axis represents every possible configuration. Reprinted by permission from Macmillan Publishers Ltd: Nature [9] Copyright 2001.

This description of the energy landscape helps clarify the previous definition of fragility. If the energy landscape consists of many megabasins, α-relaxation will dominate at high temperatures. As the temperature decreases and α-relaxation begins to slow, β-relaxation will begin to take over and the viscosity will exhibit a rapid change in slope as its relaxation behavior changes. This is representative of very fragile liquids. In contrast if there are only a few megabasins, the relaxation behavior will be dominated by β-relaxation across the entire temperature range, displaying a relatively constant activation energy which is associated with strong liquids.

1.3 Glass-Forming Ability

From window glass to cookware, the role of glass in our everyday lives is undisputed. The reason these glasses have become so widespread is due to the ease with which they can be formed and shaped while retaining their amorphous properties. In other words, their glass-forming ability, or GFA, is very high. The ease with which a material can form a glass is typically defined by two parameters: the critical cooling rate (CCR), defined as the minimum cooling rate that can be used while producing a fully amorphous sample, and the critical casting thickness (CCT), defined as the maximum thickness in the smallest dimension that can be stably formed into a glass. By lowering the CCR, less complex techniques may be used with which to shape the material into a useful application. By increasing the CCT, more robust devices can be designed. These two parameters are related, as rapid cooling techniques require thin materials for optimal heat exchange.

Due to its high CCR (10^6 K/s), the first metallic glass, discovered in 1960 [1], had little practical use. Its shape was restricted to very thin ribbons or foils due to its small CCT (~10 μm). In the mid-1970's, a Pd-Fe-P alloy was successfully formed with a CCT of 1 mm [10]. This was the first bulk metallic glass (BMG), which is defined as having a CCT $\geq$ 1 mm while remaining fully amorphous. Since then, the CCT has increased exponentially as our understanding of the underlying properties governing glass formation has developed (Figure 1.5). The first commercial BMG, Vitreloy 1 ($Zr_{41.2}Ti_{13.8}Cu_{12.5}Ni_{10}Be_{22.5}$) [11] was developed in the early 1990's with a CCR of less than 10 K/s and CCT of up to 14 mm. Many variants have been developed since then, with efforts to remove hazardous alloying elements such as Be.

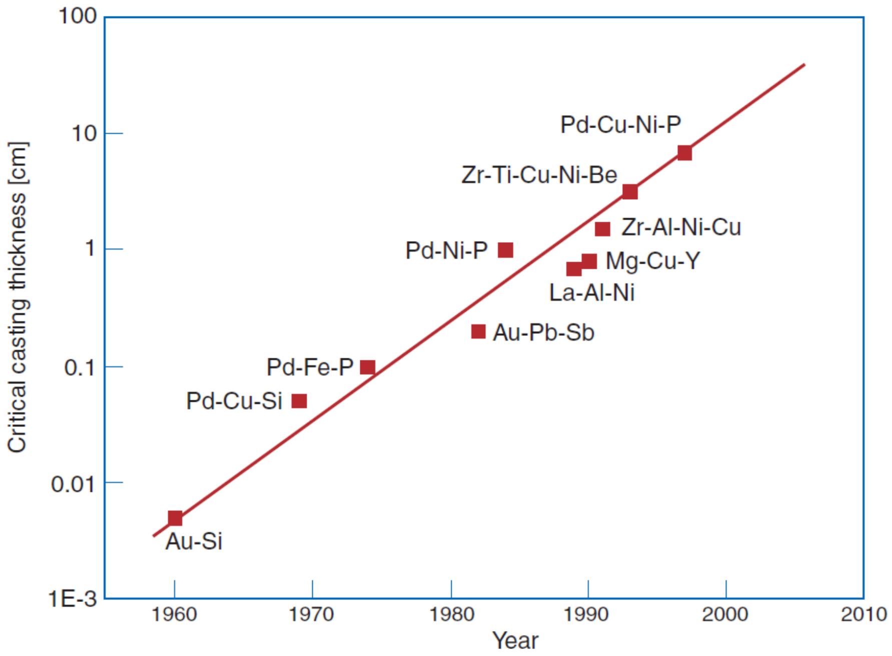

Figure 1.5 Critical Casting Thickness by year. Reprinted by permission from Elsevier: Materials Today [2], Copyright 2004.

In order to make a glass, the liquid phase must persist well below the melting temperature. Whether or not a cluster of a new crystalline phase (daughter) will nucleate within the liquid (parent) depends on the competition between the driving force towards crystallization and the energy barrier that must be overcome. This interaction is represented within classical nucleation theory as the *work of cluster formation* [12]:

$$W(n) = n\Delta\mu + A\sigma\,. \tag{1.3}$$

Within this theory, n is the number of atoms of the daughter phase, $\Delta\mu$ is the difference in chemical potential between the two phases, A is the surface area of the daughter phase, and σ is the interfacial free energy between the two phases. The second term is always positive and represents the energy barrier of forming a new phase. Since forming an interface between the two phases requires atomic rearrangement, it is inherently tied to their structural differences.

Frank's hypothesis of the structures present in liquids and glasses that can significantly increase this term are discussed in Section 1.4. When the daughter phase is thermodynamically preferred, the first term will be negative, representing a driving force towards forming the new phase due to the differences in free energy. As the temperature is reduced, this difference increases. The daughter phase will not grow until clusters larger than a critical size begin to form (i.e., when $dW/dn = 0$). Once clusters containing the critical number of atoms, n^*, have nucleated, they will begin to grow by gaining or losing one atom at a time through atomic collisions. This approach, developed by Volmer and Weber, is the kinetic model of cluster growth assumed within the Classical Theory of Nucleation (CNT) [13]; crystal nucleation within a liquid is directly influenced by the viscosity of the liquid.

The formation of a glass, then, depends on three primary components: (1) the driving free energy for the thermodynamically favored phase, (2) the structural difference represented by the interfacial free energy, and (3) the atomic mobility and viscosity. In this sense, the thermodynamics, structure, and kinetics are all intertwined and understanding their relationship is of direct scientific interest. Optimizing these three factors leads to improved glass formability. In addition to these fundamental relationships, three empirical rules have been developed for optimizing glass formation [14]: (1) an alloy with three or more elements, (2) large atomic size differences (greater than 12%), and (3) containing elements with large negative heats of mixing. In addition to lowering the free energy of the liquid phase and increasing the interfacial free energy term due to preferred clustering, these characteristics reduce atomic mobility and prevent large-scale atomic rearrangements, hindering the nucleation and growth of the crystal.

Many good glass-forming alloys are found at deep eutectics in the phase diagram (Figure 1.6). At a eutectic, the solidus (T_S) and liquidus (T_L) temperatures are equal. This allows the liquid to stably persist at much lower temperatures so the maximum driving free energy at T_g is greatly reduced. According to Turnbull, crystal nucleation is suppressed as the ratio between T_g and T_L increases [15]. This is known as the reduced glass transition temperature, or $T_{rg} = T_g / T_L$.

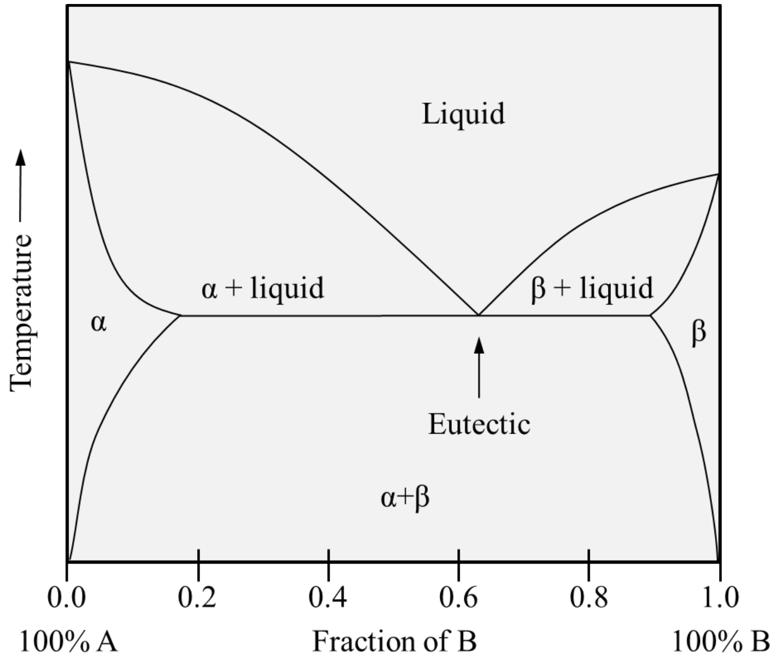

Figure 1.6 Schematic of a phase diagram for a binary A-B alloy with a deep eutectic.

However, as with any attempts at universal descriptions of metallic glasses, there are exceptions to these rules. In particular, a number of binary BMGs have been discovered in recent years with CCTs greater than 2 mm. These include alloys such as Ni-Nb [16], Cu-Zr [17-19], and Cu-Hf [19]. These alloys are excellent models for studying GFA due to their inherent simplicity in comparison with multicomponent systems. The smaller number of components allows the chemical and topological order to be resolved with fewer constraints. These alloys in particular were instrumental in formulating a structural metric of classifying the fragility of a metallic glass [20]. Some of the precursors to that work are discussed in Chapter 3 and Chapter 4.

1.4 Liquid and Amorphous Structure

As discussed in the previous section, one of the primary barriers to crystallization is the energy penalty associated with the formation of an interface between two distinct phases (i.e. the liquid and crystal). If both phases contain significantly different structural arrangements relative to each other, large atomic rearrangements are required in order for the daughter phase to form, increasing the energy penalty. Crystalline structures typically have high packing density due to the structured arrangement of atoms within the lattice. For example, atoms in a face-centered cubic (FCC) and hexagonal close-packed (HCP) lattice each have 12 nearest neighbors. Since the densities of the glass and crystalline phases are typically very close, the glass must also have a tightly packed structure, and yet remain highly disordered in order to break the LRO prevalent in crystals.

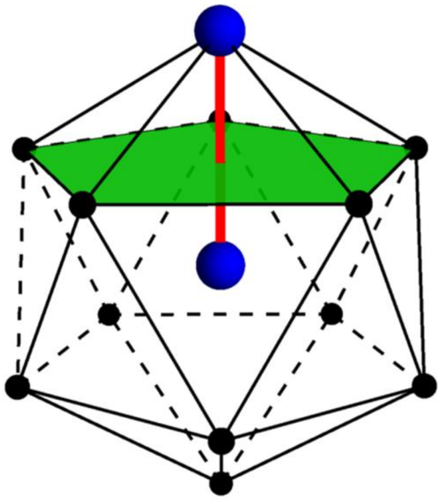

Figure 1.7 Schematic of an icosahedron, consisting of an atom with 12 nearest neighbors. Each vertex atom is equidistant from the central blue atom. Each bonded pair (blue atoms connected by red line) is surrounded by five atoms (green plane) giving five-fold symmetry.

In addition to FCC and HCP lattices, there is another structure that has 12 nearest neighbors. An icosahedron shares the tight packing characteristics, but contains five-fold symmetry which is incompatible with LRO (Figure 1.7). This structural arrangement was first proposed by Frank to explain why a liquid could be supercooled below T_L and has since been demonstrated in both elemental [21-23] and alloy liquids [24, 25]. The icosahedron sacrifices long range periodicity for better rotational symmetry and is actually preferred over FCC and HCP structures for SRO. The five-fold symmetry observed in icosahedral order is similar to the structures first proposed for metallic glasses, based on a dense random packing of hard spheres (DRPHS) [26]. In this model, atoms are treated as hard spheres that stack together to maximize tetrahedral structures [27], which leads to five-edged faces between atoms.

While icosahedral structures cannot fill a flat 3-D space, this packing frustration can be relieved by transforming to a curved 3-D space [28]. In this geometry, equilateral tetrahedral structures can fully fill space. Icosahedral packing then becomes the ideal state for both SRO *and* LRO. Packing frustration in a flat 3-D space is relieved by introducing rotational defects called disclinations. These are represented by six-fold and four-fold bipyramids [28] rather than tetrahedra. This model is appropriate when all atoms are of the same approximate size, but differences in coordination numbers can arise due to atomic size differences. Frank and Kasper developed a classification system for different coordination numbers called Z-clusters, each of which maximizes the tetrahedral structures contained in a cluster [29].

In order to study the atomic structure of metallic liquids and glasses, various scattering techniques are used. The details of the X-ray and neutron scattering techniques used for this dissertation are discussed in detail in Chapter 2. Statistically, an isotropic distribution of atoms can be represented by a *pair-distribution function*, or $g(r)$. It is essentially a 1-D histogram of relative interatomic distances within an atomic configuration and is represented by:

$$g(r) = \frac{1}{4\pi N \rho_0 r^2} \sum_i \sum_j \delta(r - r_{ij}), \text{ where } r_{ij} = \left| r_i - r_j \right| . \qquad 1.4$$

Here, N is the total number of atoms in a configuration with density ρ_0, r_{ij} is the distance between atom i and atom j, and δ is a Dirac delta function. If a common distance is found separating many different atom-pairs, a peak will form at that value of r. Due to the highly periodic arrangement of crystalline atoms, this results in a series of well-defined peaks corresponding to the spacing between atomic planes (Figure 1.8 (a)). In a highly disordered liquid or glass, a very broad distribution of interatomic distances causes a smearing out of the well-defined peaks found in crystals (Figure 1.8 (b-c)). The structural order can also be expressed in inverse-space through a Fourier transform of $g(r)$ to obtain the total static structure factor, $S(q)$:

$$S(q) = 4\pi\rho \int \left(g(r) - 1 \right) \frac{\sin(qr)}{qr} r^2 dr \, . \qquad (1.5)$$

$S(q)$ is related to the signal that is directly measured in a scattering experiment. Similar to $g(r)$, $S(q)$ will have very broad peaks for an amorphous material representing the diverse correlations present in the atomic configuration. As structural order is increased and the average bond lengths become better defined, the peaks sharpen, increasing in amplitude while decreasing their width. Examples of $S(q)$ for crystalline, glassy, and liquid materials are presented in Figure 1.8 (d-f).

The pair-distribution function can be said to describe the *topological order* of the configuration. It is purely a statistical description of the atomic locations, weighted by physical parameters. In addition to topological order, a multi-component system may contain chemically specific atomic arrangements resulting in *chemical order*. Chemically specific distribution functions can be constructed by restricting the sums over *i* and *j* to only count specific types. For instance, in a binary alloy A-B, three separate distributions can be constructed to describe the relative distances between an A and another A, an A and a B, and a B and another B. These are known as the *partial pair-correlation functions* (PPCFs). In an *n*-component alloy, there are $n(n+1)/2$ unique partial functions.

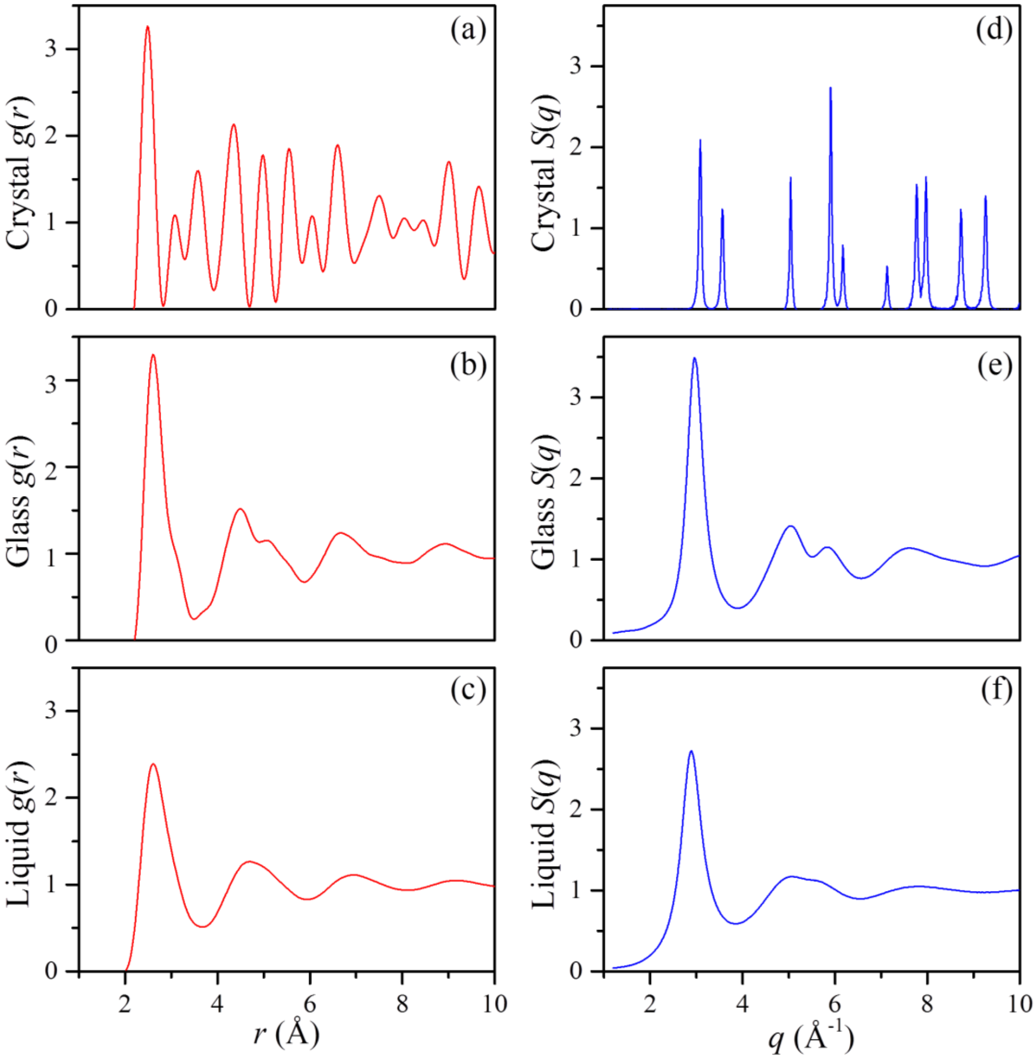

Figure 1.8 Experimental pair-distribution functions for (a) a crystalline material, (b) a glassy material, and (c) a liquid material. (d-f) The corresponding $S(q)$s measured in an experiment.

The total $S(q)$ measured in an experiment is dependent upon the type of scatterer used. X-rays and neutrons scatter through different interactions, so the chemical correlations will have different relative weighting depending on the scattering strength of each element. If sufficient scattering contrast can be obtained, the chemical correlations can be extracted. Understanding the underlying chemical order in addition to the topological order is one of the primary objectives undertaken in this dissertation and is discussed further in Chapter 4 and Chapter 5.

1.5 Electrostatic Levitation

In order to access the liquid in the supercooled regime, heterogeneous nucleation must be avoided. Contact with a container while in the metastable supercooled state can dramatically reduce the interfacial free energy required to form the daughter phase causing crystallization to be very likely once the liquid is cooled below T_L. In order to prevent this, the container must be removed. Crystallization can still occur through homogeneous nucleation due to thermal fluctuations, but this will often allow several hundred degrees of undercooling. Over the years, a number of containerless processing techniques have been developed to this end.

Some of the earliest experiments involving the study of containerless liquids implemented drop tubes. In this technique, a molten sample falls through a tube that is either evacuated or filled with an inert gas. Thermophysical and structural property measurements are very difficult to perform in this configuration, making high-precision measurements very challenging. However, levitation techniques can maintain a stable sample position allowing for optical and other non-contact measurements. Aerodynamic levitation [30] uses jets of inert gas to counter gravity while high-powered lasers melt the sample. Since it involves flowing gas, this can cause difficulties with maintaining a stable temperature and can introduce large temperature gradients across the sample. In addition, processing materials with high vapor pressures becomes problematic. Acoustic levitation [31] counters gravity by producing highly focused sound waves that produce a 3-D potential well. This method adds quite a bit of complexity to the apparatus, and sometimes has difficulty with dense materials.

The primary levitation methods used with metallic alloys are electromagnetic (EML [32]) and electrostatic levitation (ESL [33]). EML levitates samples within an RF coil that induces eddy currents in the sample due to a changing magnetic flux. As a consequence, the sample is simultaneously heated and levitated and temperature control becomes intertwined for these two processes. This method is also limited to metallic materials, so broad applications are limited. Despite its limitations, it does have significant benefits in microgravity, where less current is required to maintain stable levitation. Knowing the precise coupling between the RF coil and the sample, for example, allows precision measurements of the specific heat of the liquid, something much more difficult to do with other levitation methods. The ESL technique applies a high voltage between a negatively charged top electrode and a grounded bottom electrode. The applied voltage induces a positive charge on the surface of a sample which causes it to levitate. This technique does not require the sample to be completely enclosed by a coil, as in EML, which drastically reduces scattering background and increases the available scattering angle for structural scattering experiments. While metallic samples are typically used with ESL, any material that can have an induced surface charge can be studied with this technique, provided that sample evaporation is not a problem. While this process has many benefits, it pays for it with increased complexity. ESLs typically require a very large footprint and can have difficulty levitating large samples (larger than 100 mg) without additional complexity. Samples also lose charge during heating as hydrocarbons and adsorbed gases are evaporated, requiring an ultraviolet (UV) source to recharge the sample through the photoelectric effect. Despite its limitations, ESL provides many advantages in scattering experiments and is the technique used throughout this dissertation.

1.6 Summary

The nature of the topological and chemical atomic structure of metallic glass-forming alloys is one of the key questions that this dissertation seeks to address. The structural order that appears in a glass can be traced back to having origins in the high-temperature liquid. Understanding the thermodynamics, kinetics, and atomic structure of the liquid and supercooled liquid and how they are related to glass formation is crucial to developing improved BMGs. The topics discussed in this chapter provide the background for the research presented in this dissertation. A description of the experimental techniques employed throughout this dissertation is provided in Chapter 2. In Chapter 3, the evolution of structural parameters in Ni-Nb(-Ta) BMGs is used to lay the groundwork for developing a structural view of fragility. This is continued in Chapter 4 with a series of non-bulk-forming Zr-Ni alloys, where structural as well as chemical order is investigated along with their thermophysical properties. Some of the first neutron scattering studies using a newly developed electrostatic levitator (NESL) are presented in Chapter 5, where the chemical and topological order for similar eutectic alloys in the Zr-(noble metal) family are analyzed and compared. From those results, a new metastable phase is predicted and later identified using local structural features of the high-temperature liquid. This new phase, as well as other metastable phases that were found to form, are further investigated in Chapter 6 and discussed in the context of phase selection and crystal growth through metastable processes. Finally, an investigation into the formation of nanoscale heterogeneities prior to crystallization in a Vit105 BMG is presented in Chapter 7. Understanding the crystallization pathways of alloys with a variety of glass-forming abilities is crucial to developing better bulk metallic glasses.

1.7 References

[1] W. Klement, R.H. Willens, P. Duwez, *Nature* **187**, 869 (1960).

[2] M. Telford, *Materials Today* **7**, 36 (2004).

[3] A.L. Greer, *Science* **267**, 1947 (1995).

[4] R. Zallen, *The Physics of Amorphous Solids*, John Wiley & Sons, Inc., 1983.

[5] C.A. Angell, *Journal of Physics and Chemistry of Solids* **49**, 863 (1988).

[6] Y.Q. Cheng, E. Ma, *Progress in Materials Science* **56**, 379 (2011).

[7] G. Adam, J.H. Gibbs, *The Journal of Chemical Physics* **43**, 139 (1965).

[8] M. Goldstein, *The Journal of Chemical Physics* **3728**, (2003).

[9] P.G. Debenedetti, F.H. Stillinger, *Nature* **410**, 259 (2001).

[10] H.S. Chen, *Acta Metallurgica* **22**, 1505 (1974).

[11] A. Peker, W.L. Johnson, *Applied Physics Letters* **63**, 2342 (1993).

[12] K.F. Kelton, A.L. Greer, *Nucleation in Condensed Matter: Applications in Materials and Biology*, Pergamon, 2010.

[13] M. Volmer, A. Weber, *Zeitschrift für Physikalische Chemie* **119**, 277 (1926).

[14] A. Takeuchi, A. Inoue, *Materials Transactions* **46**, 2817 (2005).

[15] D. Turnbull, *Metallurgical Transactions B* **12**, 217 (1981).

[16] L. Xia, W.H. Li, S.S. Fang, B.C. Wei, Y.D. Dong, *Journal of Applied Physics* **99**, 026103 (2006).

[17] D. Wang, Y. Li, B.B. Sun, M.L. Sui, K. Lu, E. Ma, *Applied Physics Letters* **84**, 4029 (2004).

[18] D. Xu, G. Duan, W. Johnson, *Physical Review Letters* **92**, 245504 (2004).

[19] A. Inoue, W. Zhang, *Materials Transactions* **45**, 584 (2004).

[20] N.A. Mauro, M.E. Blodgett, M.L. Johnson, A.J. Vogt, K.F. Kelton, *Nature Communications* **5:4616**, (2014).

[21] D. Holland-Moritz, O. Heinen, R. Bellissent, T. Schenk, *Materials Science and Engineering: A* **449-451**, 42 (2007).

[22] D. Holland-Moritz, T. Schenk, V. Simonet, R. Bellissent, P. Convert, T. Hansen, D.M. Herlach, *Materials Science and Engineering: A* **375-377**, 98 (2004).

[23] T. Schenk, D. Holland-Moritz, V. Simonet, R. Bellissent, D. Herlach, *Physical Review Letters* **89**, 1 (2002).

[24] G.W. Lee, A.K. Gangopadhyay, R.W. Hyers, T.J. Rathz, J.R. Rogers, D.S. Robinson, A.I. Goldman, K.F. Kelton, *Physical Review B* **77**, 184102 (2008).

[25] Y.T. Shen, T.H. Kim, A.K. Gangopadhyay, K.F. Kelton, *Physical Review Letters* **102**, 057801 (2009).

[26] J.D. Bernal, *Nature* **185**, 68 (1960).

[27] A.H. Boerdijk, *Philips Research Reports* **7**, 303 (1952).

[28] R. Nelson, *Physical Review B* **28**, 5515 (1983).

[29] F.C. Frank, J.S. Kasper, *Acta Crystallographica* **12**, 483 (1959).

[30] L. Hennet, S. Krishnan, I. Pozdnyakova, V. Cristiglio, G.J. Cuello, H.E. Fischer, A. Bytchkov, F. Albergamo, D. Zanghi, J.-F. Brun, S. Brassamin, M.L. Saboungi, *Pure and Applied Chemistry* **79**, 1643 (2007).

[31] J.K.R. Weber, D.S. Hampton, D.R. Merkley, C.A. Rey, M.M. Zatarski, P.C. Nordine, *Review of Scientific Instruments* **65**, 456 (1994).

[32] D. Holland-Moritz, T. Schenk, P. Convert, T. Hansen, D.M. Herlach, *Measurement Science and Technology* **16**, 372 (2005).

[33] W.K. Rhim, M. Collender, M.T. Hyson, W.T. Simms, D.D. Elleman, *Review of Scientific Instruments* **56**, 307 (1985).

Chapter 2: Experimental and Analysis Methods

The experiments presented in this dissertation required a wide variety of preparation and analysis techniques. Due to the collaborative nature of these experiments and the number of personnel required for operation, duties such as sample preparation, data acquisition, and data reduction were often shared by all group members. Major experiments were undertaken at both the Advanced Photon Source (APS) at Argonne National Laboratory (ANL) (Section 2.4) and at the Spallation Neutron Source (SNS) at Oak Ridge National Laboratory (ORNL) (Section 2.8). In addition to myself, sample preparation, characterization, and data collection were helped by A. K. Gangopadhyay, V. Wessels, N. A. Mauro, J. C. Bendert, A. J. Vogt, M. E. Blodgett, C. E. Pueblo, J. M. McKnight/Gewin, A. Hope, M. Nadeau, C. Miller, and S. Veligati. The sections that follow describe sample preparation (Section 2.1), sample characterization (Section 2.2), and the experimental details and analysis techniques for both high-energy X-ray diffraction (Sections 2.3-2.6) and time-of-flight (TOF) neutron diffraction (Sections 2.7-2.9). Details of the simulations, structural analysis, and crystal pattern identification presented in this dissertation are discussed in Sections 2.10-2.11.

2.1 Sample Preparation

All samples studied in this dissertation were prepared from material selected for both metallic purity as well as oxygen concentration, both of which greatly affect sample processing. All samples were initially prepared by creating 1 – 2.5 g master ingots via arc-melting in an inert atmosphere. These ingots were subsequently crushed into small pieces, which were used for preparing levitation samples, glass ribbons, or samples for thermal analysis using a Differential Thermal Analyzer (DTA) or Differential Scanning Calorimeter (DSC). All elemental materials were purchased from Alfa Aesar; information on elemental impurities for each material is available from their website (www.alfa.com) by request. Detailed information on all materials used for preparation of samples for this dissertation is listed in Table 2.1.

Table 2.1 Raw material information used in sample preparation.

Element	Stock/Lot #	Purity (%)	Form	Experiments Used
Al	10573/F01R022	99.999	Shot	$Zr_{52.5}Cu_{17.9}Ni_{14.6}Al_{10}Ti_5$
Cu	42958/A06Y011	99.9999	Slug	$Zr_{52.5}Cu_{17.9}Ni_{14.6}Al_{10}Ti_5$
Ni	42333/D18M33 42333/L02X015	99.995 99.995	Slug Slug	$Ni_{59.5}Nb_{40.5}$, $Ni_{62}Nb_{38}$, $Ni_{60}Nb_{20}Ta_{10}$, $Zr_{52.5}Cu_{17.9}Ni_{14.6}Al_{10}Ti_5$
Nb	42846/I28N13	99.95	Slug	$Ni_{59.5}Nb_{40.5}$, $Ni_{62}Nb_{38}$, $Ni_{60}Nb_{20}Ta_{10}$
Pt	43288/J02U012	99.95	Wire	$Zr_{80}Pt_{20}$
Rh	11576/B28Y022	99.8	Wire	$Zr_{77}Rh_{23}$
Ta	42826/E08L09	99.95	Slug	$Ni_{60}Nb_{20}Ta_{10}$
Ti	42394/J31R019	99.995	Slug	$Zr_{52.5}Cu_{17.9}Ni_{14.6}Al_{10}Ti_5$
Zr	42556/A03S011 42556/K30R008 42256/D25Z022	99.95 99.95 99.95	Slug Slug Slug	$Zr_{80}Pt_{20}$, $Zr_{77}Rh_{23}$, $Zr_{52.5}Cu_{17.9}Ni_{14.6}Al_{10}Ti_5$

The master ingots were prepared by weighing pieces of the source material in the correct proportions for the alloys of interest to an accuracy of ±0.1 mg using a Mettler Toledo AB54/FACT mass balance. This precision allowed the alloy composition to be prepared within 0.05 atomic percent (at.%). The mass fraction ($m\%_i$) for the i^{th} element for a given composition was determined by

$$m\%_i = \frac{x_i M_i}{\sum_j x_j M_j}, \tag{2.1}$$

where x_i is the atomic percent, M_i is the molar mass, and the sum is over j encompasses all elements in the alloy. The mass for the i^{th} element, m_i, was determined by

$$m_i = m\%_i I , \tag{2.2}$$

where I is the mass of the master ingot.

Prior to arc-melting, the water-cooled copper hearth was sanded using fine grain (1000 grade) sand paper to remove any copper oxides that might have formed since it was last used. The hearth was then thoroughly cleaned with acetone and methanol to remove any residue and other contamination. The source material was then placed on the hearth. Materials with higher melting temperatures were strategically placed on the top of the pile to minimize evaporation from materials with low melting points and high vapor pressures. The chamber was evacuated using a custom pumping station, designed by M. E. Blodgett, with a GE Motors oil backing pump and Pfeiffer HiCube turbo pump [1]. After evacuating for 20 minutes, the chamber was back-filled with 99.999% pure Ar gas to a pressure of -15 inches of mercury (inHg). This process of pumping and back-filling was repeated a total of three times. After the final evacuation, the chamber was back-filled with Ar gas to just below atmospheric pressure (-5 inHg). A Miller Synchrowave 250 DX arc welding power source, connected to a tungsten tip via a vacuum feed-through, was then used to strike an arc between the tip and the copper hearth.

Prior to melting any sample material, a $Ti_{50}Zr_{50}$ getter was first melted for 30-60 seconds. The getter serves as an O_2 collector and reduces sample contamination. It is good practice to re-melt the getter any time an arc is struck. Once the getter cycle was finished, the sample material was melted for 30-40 seconds, rotating the arc around the sample to maximize mixing. After initial alloy formation, each ingot was flipped over and re-melted 2-3 times. The final ingot mass was measured and the ingots were rejected if the total mass loss resulted in a shift in composition of more than 0.05 at%. This was estimated by assuming that the mass loss was due to the element with the highest vapor pressure. The typical mass loss is less than 0.1%. Additional details of the arc-melting process can be found in other sources [1, 2].

Once the ingot was prepared, individual samples for use in ESL experiments were created by crushing the ingot and arc-melting small pieces of 30-70 mg (for X-ray scattering experiments) or 100-450 mg (for neutron scattering experiments). Each sample was briefly arc-melted a single time in order to minimize evaporation. Since each sample is fully melted during ESL experiments, ensuring mixing at this stage is not necessary as long as the ingots were well mixed.

Glassy ribbons were prepared by induction melting pieces of a crushed ingot under an Ar atmosphere within a graphite crucible and injecting the melt onto a rapidly spinning copper wheel (5,000 – 8,000 rpm). When the molten sample struck the wheel, very thin ribbons (15 – 20 μm thick) were formed and ejected into a collection tube.

2.2 Sample Characterization

In order to properly calibrate the results from the high-energy X-ray and neutron scattering experiments, a number of thermophysical and structural property measurements were required. The solidus (T_S) and liquidus (T_L) temperatures were measured using Differential Thermal Analysis (DTA) techniques (Section 2.2.1). These temperatures are used for calibrating temperature measurements of levitated liquids. Measurements of the glass transition (T_G) and crystallization (T_X) temperatures were measured using Differential Scanning Calorimetry (DSC) techniques (Section 2.2.1). These temperatures are used for calibrating temperature measurements of amorphous ribbon and low-temperature levitated solids. Low-energy X-ray diffraction (Section 2.2.2) was used to determine if as-quenched ribbons were fully amorphous as well as for crystalline phase identification.

2.2.1 Differential Scanning Calorimetry and Differential Thermal Analysis

Differential Scanning calorimetry (DSC) measurements were performed on as-prepared ribbons and crushed ingots to determine phase transition temperatures using a PerkinElmer DSC 7. In the DSC technique, a sample and a reference are placed in adiabatically isolated pans (Al pans for $T_{\max} < 600$ ^{o}C, Cu pans for $T_{\max} > 600$ ^{o}C), which are heated separately. A control algorithm adjusts the power to each pan during a heating or isothermal experiment to maintain the same temperature for each pan. If the sample undergoes a phase transition, either more (endothermic) or less (exothermic) power is required relative to the reference to maintain both pans at the same temperature. The enthalpy of transformation can then be calculated by integrating the differential power. The DSC measurements were made using argon gas to maintain a constant pressure in the sample holder and to help prevent oxidation. As mentioned previously, the results of the DSC measurements were used to determine both the glass transition temperature (T_G) and the crystallization, or devitrification, temperature (T_X) for amorphous samples.

Differential Thermal Analysis (DTA) measurements were made using a Setaram Labsys DTA/DSC on crushed alloy ingot fragments to determine high-temperature phase transformation temperatures, such as the solidus (T_S) or liquidus (T_L) temperatures. Samples were placed in an Al_2O_3 crucible and covered with Al_2O_3 powder, while a reference crucible was loaded with only Al_2O_3 powder. Both crucibles were placed in a common furnace and identical temperature cycles were performed. While similar to the DSC technique, in DTA a single furnace is used to heat both pans and the difference in temperature is measured. In both techniques, the results of the measurements were plotted against temperature rather than time. While both DSC and DTA can be used for similar studies, the DSC has a higher precision for measuring properties such as the specific heat and the enthalpy of transition. While less accurate, the DTA is capable of measurements to much higher temperatures.

2.2.2 Low-Energy X-ray Characterization

In order to ensure that the quenched ribbons were fully amorphous, low-energy X-ray measurements were made using a Rigaku Geigerflex powder diffractometer (Cu K_α, $\lambda = 1.54$ Å). Multiple ribbons were taped to an aluminum frame and studied in a reflection geometry, scanning between 20-120 degrees in 2θ. If sharp diffraction peaks were observed, another quench was performed at higher wheel speeds until only smooth, broad peaks were seen in the diffraction data. Crystal peak positions and phase identifications of Zr-Rh were also determined with this machine by crushing processed samples into a powder, depositing the powder onto pieces of two-sided tape, and mounting it to the aluminum frame. Further details are discussed in Chapter 6.

2.3 Beamline Electrostatic Levitation (BESL)

Much of the data presented in this dissertation are focused on liquid structure and thermophysical property studies. The Washington University Beamline Electrostatic Levitator (WU-BESL) [2-4] was designed using the electrostatic levitation (ESL) technique [3] to provide a containerless environment with which to study the high-temperature and supercooled liquid structure, while simultaneously providing non-contact measurements of thermophysical properties. A multitude of ports on the main chamber body provide line-of-sight to the sample (Figure 2.1). The majority of the wide-angle X-ray scattering (WAXS) data presented in this dissertation were obtained from Station 6-ID-D at the Advanced Photon Source (APS) at Argonne National Laboratory (ANL). Simultaneous wide-angle X-ray scattering and small-angle X-ray scattering (SAXS) data were obtained from Station 1-ID-E at the APS and are presented in Chapter 7. Thermophysical properties (density, viscosity, and temperature data) were obtained during experimental runs as well as at Washington University in St. Louis.

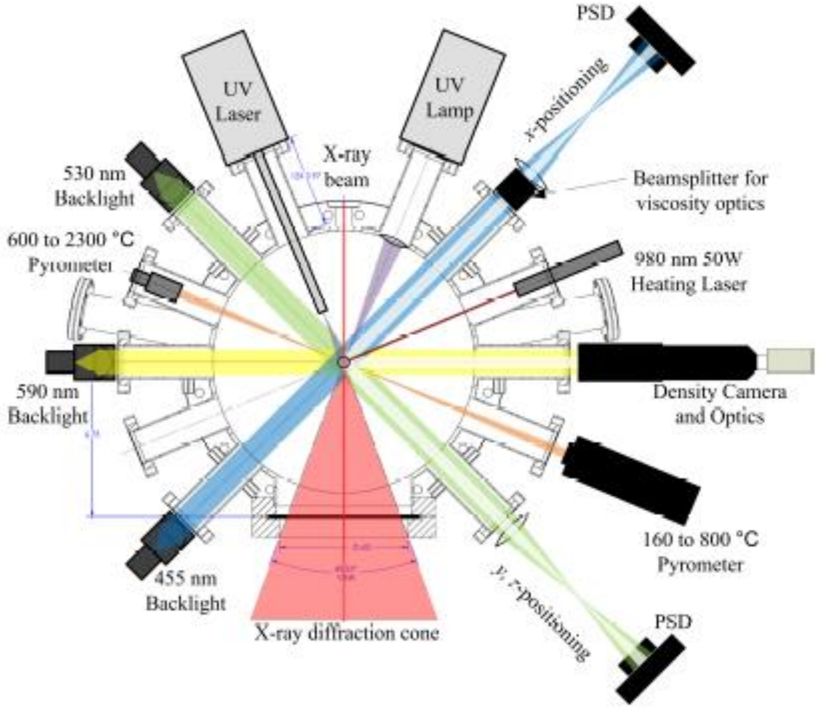

Figure 2.1 A schematic layout of the instruments for non-contact measurements using WU-BESL (Reprinted with permission from [5]).

2.3.1 WU-BESL Setup

WU-BESL consists of a high-vacuum chamber that is typically operated at 10^{-7} Torr. This pressure is achieved using two scroll pumps: one backing a Pfeiffer Vacuum turbo pump for the ultraviolet lamp (UV) and the other backing an Osaka Vacuum turbo pump for the main vacuum system. Within the chamber are a set of charged electrodes producing an electric field of 0 - 2.5 MV/m (Figure 2.2). An amplifier capable of generating a potential difference of 0 to -

20 kV across the vertical components is connected via high-vacuum feedthroughs. The negative potential induces a positive charge on the sample, counteracting the effect of gravity. In order to maintain stable levitation, a pair of orthogonal lateral amplifiers generates electric potential differences of ± 3 kV. Shadows are cast by the levitated samples (m = 10-150 mg, r = 2-4 mm) using a pair of high-powered colored LEDs onto a pair of orthogonal position sensitive detectors (PSDs). The position is tracked by the computer and the voltages are dynamically adjusted to maintain the sample within 10 μm of the desired position [6] (Figure 2.2).

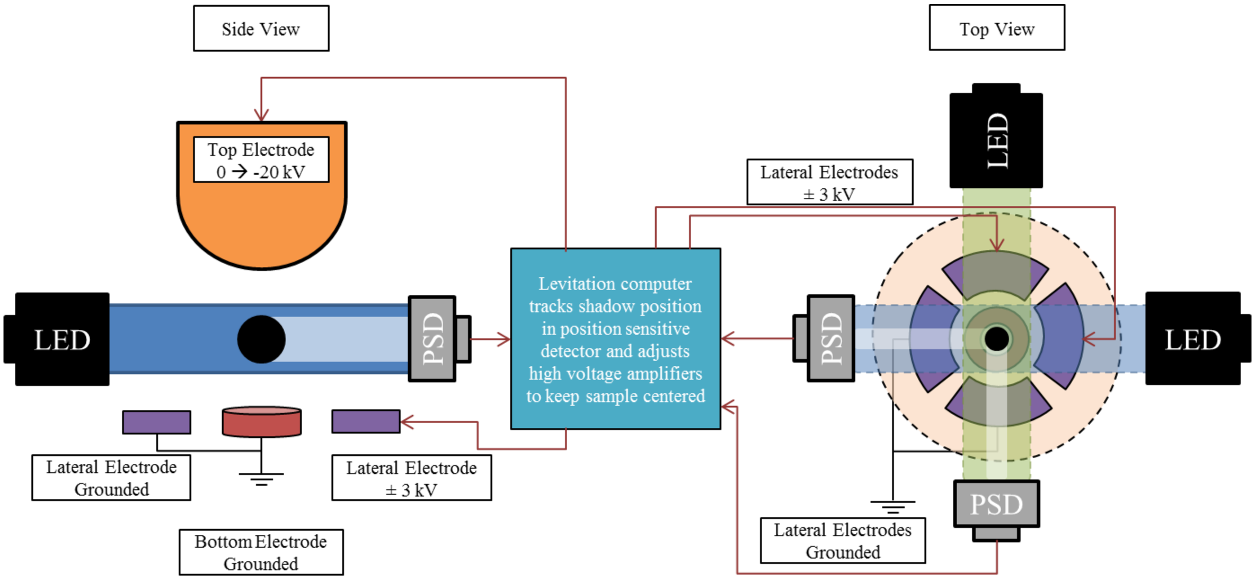

Figure 2.2 The WU-BESL electrode configuration and feedback algorithm. High-powered LEDs placed in orthogonal positions cast a shadow of the sample onto position sensitive detectors, which track the motion of the sample. A feedback algorithm sends signals to the electrodes, modifying the electric potential to adjust sample position.

Samples are heated using a fiber-coupled diode laser (980 nm, 50 W continuous maximum power output). As the sample temperature increases, surface charge is lost. This is replenished via the photoelectric effect using a pair of high-intensity UV sources. Thermionic emission eventually sets in at higher temperature, removing the need for the UV lamps. Once fully melted, the sample maintains a relatively stable charge. At this point, the lines-of-sight from the sample to the UV lamps are blocked by shutters to minimize deposition from evaporation.

2.3.2 Measurements of Thermophysical Properties

Sample temperatures were measured from 160 ^{o}C to 2300 ^{o}C using two infrared pyrometers with overlapping temperature ranges. A single-color Process Sensors Metis MI18 MB8, operating at a 1.89 μm wavelength, was used for low-temperature measurements (160-800 ^{o}C) and a Process Sensors Metis MQ22 two-color ratio pyrometer, operating at 1.40 and 1.65 μm wavelengths, was used for high-temperature measurements (600-2300 ^{o}C). Ratio pyrometers provided more accurate measurements of the temperature because emissivity changes with temperature are normalized out [7]. Relative changes in the emissivity at each of the two close wavelengths are expected to be small. The emissivity ratio was calibrated by matching the melt plateau in the temperature-time curve measured on heating in WU-BESL to the largest endothermic signature measured in a differential thermal analyzer (DTA) (Labsys^{TM} DTA/DSC, Setaram), corresponding to the solidus temperature, T_S. A constant emissivity ratio was assumed for the entire temperature range.

The temperature was correlated with non-contact measurements of the volume. The projected area of the sample was obtained using the shadow method [8, 9] with a Pixelink PL-B74IG CMOS camera and a 455 nm collimated microscope LED, which has a total beam power of 240 mW and a beam diameter of 37 mm. The video data were taken at a frame rate of 20-25 fps. The pixel dimensions were calibrated before and after each sample using 2.38125 ± 0.00076 mm diameter (grade 3) tungsten carbide standards. The volume was determined from the area data, assuming that the sample is symmetric about the vertical axis [10], and the density was calculated by dividing the measured sample mass by the measured volume. A more detailed discussion of the machine vision volume measurement algorithm can be found elsewhere [5, 8].

Liquid viscosity was measured as a function of temperature using the oscillating drop technique [11-13], where a perturbing voltage on the top and bottom electrodes caused sample oscillation. The viscosity is related to the decay time in the surface oscillation when the perturbation is removed. The surface oscillations were measured by a Pixelink PL-B74IG CMOS camera operating at a high frame rate (1500 fps). More detail is given elsewhere [5, 13].

2.3.3 Beamline compatibility

WU-BESL is designed to be a portable unit that can be transported to and installed on various high-energy X-ray beamlines at the APS. Two opposite ports on the main chamber are replaced with 0.015" thick Beryllium windows to allow the X-rays to pass through to the sample, while minimizing the scattering from the chamber. The exit port is large enough to provide a scattering angle 2θ of up to 20^{o}. All instruments connected to the ports around the exterior are designed to be easily removed for transportation.

2.4 High-Energy X-ray Diffraction Measurements

The majority of the X-ray data in this dissertation were not obtained from a single experiment, but collected in several different formats and environments over the space of 4-5 years. Each experiment had slightly different parameters which are laid out in detail in the following sections. Throughout this dissertation, each experimental run is referred to in short-hand to reference the specific environment and settings involved in its acquisition. The short-hand for each experiment is represented by the section titles under Sections 2.4.X. For instance, a reference to “BESL 2010” in this dissertation refers to the data obtained during August 2010 using the experimental details described in Section 2.4.1.

2.4.1 BESL 2010

WU-BESL was installed on Station 6-ID-D at the APS for three weeks during August of 2010 for a study of a broad range of metallic liquids. High-energy X-rays (E = 129.69 keV, λ = 0.095604 Å) were scattered from levitated samples in a transmission geometry using a beam size of 0.7 x 0.7 mm. The scattered X-rays were measured using an amorphous Si flat-panel GE Revolution 41-RT operating at 1 Hz for isothermal measurements and at 2 Hz for free-cooling cycles. The detector was operated using 1024 x 1024 pixels, each of which was 400 x 400 μm in size. The detector was positioned nominally 910 mm from the sample and was regularly calibrated using levitated polycrystalline Si standards and confirmed using a NIST SRM 640c Si standard powder in a capillary located in the approximate position of the levitated samples. The maximum accessible momentum transfer, q_{max}, was 14 Å^{-1}.

A series of standard correction files were obtained both before and after a sample was loaded into the chamber. An *empty chamber* scan was acquired for each frame-rate used during sample acquisition. During this scan, the secondary X-ray shutter was open was but no sample was present. This scan measures secondary scattering from inside the evacuated chamber and the surrounding environment. It also measures the secondary air scattering in the path before and after the Be windows on the chamber. A *dark* scan was acquired with the secondary X-ray shutter closed. The dark scan measures the dark current, or the native counts registered by the detector in the absence of any X-ray beam.

2.4.2 APS 2011

During October 2011, glassy ribbons were studied on Station 6-ID-D at the APS for a focused study of the room-temperature amorphous structure of select glasses. The ribbons were cut into 10-20 mm strips and ~10-15 were mounted to plastic frames. The frames were placed in a special mount on the beamline in transmission geometry. High-energy X-rays (E = 100 keV, λ = 0.1243 Å) with a beam profile of 0.7 x 0.7 mm were used and the scattered signal was collected using the same amorphous Si GE Revolution 41-RT detector used in BESL 2010, but in a higher resolution mode (2048 x 2048 pixels, 200 x 200 μm pixel size) located approximately 200 mm from the sample. The detector was routinely calibrated using NIST SRM 640c Si powder mounted to a metal frame using Kapton tape. For this experiment, $q_{\max}$ was 20 Å^{-1}.

Each sample was scanned for approximately 20 – 60 s. Sample absorption was measured using photodiodes both before and after the sample to gain an estimate of the beam attenuation. During acquisition, the secondary shutter was closed for the first and last 5 s, providing regular dark scans for each sample. Between samples, an empty scan was acquired for approximately 20 s.

2.4.3 BESL 2013

In June 2013, WU-BESL was reinstalled on Station 6-ID-D at the APS for three weeks for a second broad study of metallic liquids and amorphous ribbons. High-energy X-rays (E = 131.9 and 79.7 keV, λ = 0.09403 and 0.1555 Å) were scattered from levitated spheres and mounted ribbons in transmission geometry with a beam size of 0.7 x 0.7 mm. Scattered X-rays were measured using the same amorphous Si flat-panel GE Revolution 41-RT as for the previous experiments at a variety of acquisition rates (1-8 Hz). The detector was operated using 2048 x 2048 pixels, each of which was 200 x 200 μm in size. The detector was positioned nominally

565 mm from the sample and was regularly calibrated using levitated polycrystalline Si standards and confirmed using a NIST SRM 640c Si standard powder in a capillary in the approximate position of levitated samples. For this experiment, q_{max}, was 15 Å^{-1}.

Each liquid sample was scanned for approximately 10 – 20 s during isothermal measurements. During acquisition, the secondary shutter was closed for the first and last 5 s, providing regular dark measurements for each sample. Between samples, an empty scan was performed for approximately 20 s.

Single amorphous ribbons were mounted to a resistive heating apparatus in WU-BESL and held in approximately the same location as the levitated samples. The ribbons were thermally cycled from room temperature to near T_g multiple times, while simultaneously acquiring diffraction images and temperature measurements. The cycling allowed the diffraction patterns to be monitored until they were completely reversible up to T_g, indicating complete structural relaxation prior to crystallization. The relaxed glasses were then held isothermally for 60 s at a series of temperatures that increased towards T_g. They were then heated at a rate of 40 to 100 K/min through T_g until crystallization was observed.

2.4.4 SAXS 2014

In November 2014, WU-BESL was again transported to the APS, but this time it was installed on Station 1-ID-E for simultaneous wide-angle X-ray scattering (WAXS) and small-angle X-ray scattering (SAXS) measurements of potential liquid-liquid phase separation. The SAXS signal was acquired by leaving a gap in the center of the WAXS detectors, allowing the signal to pass through to a second detector located much farther away (Figure 2.3).

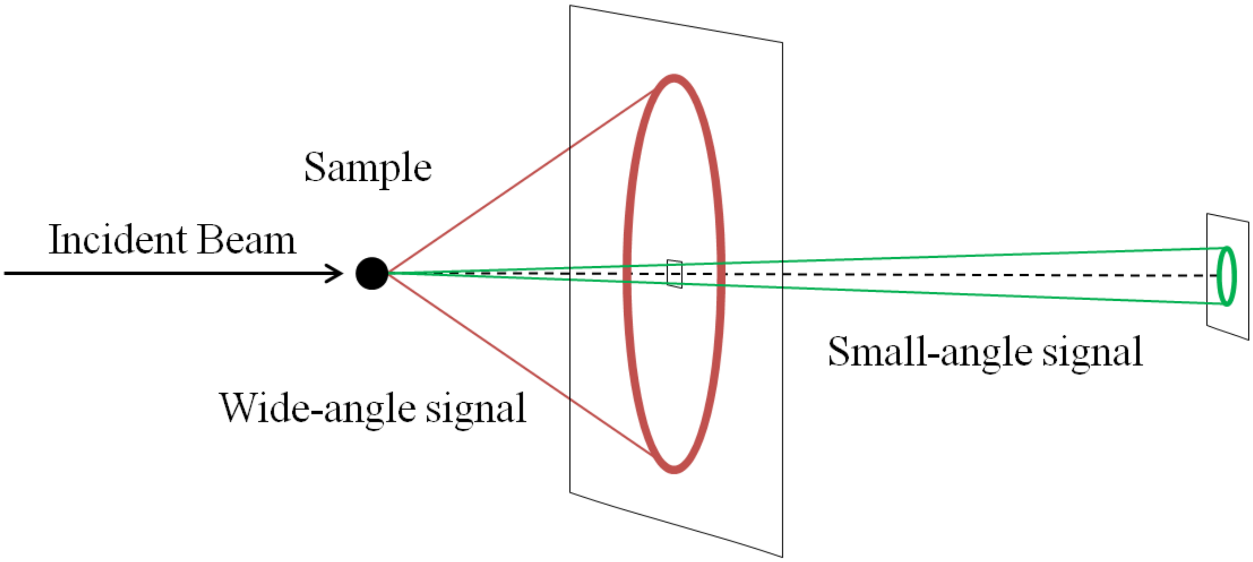

Figure 2.3 Schematic of the setup for simultaneous WAXS and SAXS scattering measurements.

High-energy X-rays (E = 100 keV, λ = 0.12398 Å) were scattered from levitated samples in transmission geometry with a beam size of 0.05 x 0.1 mm (vertical x horizontal). WAXS measurements were performed using four amorphous Si flat-panel GE Revolution 41-RT detectors arranged with a small gap in the center. The configuration of four detectors is referred to as HYDRA (Figure 2.4). The detectors were operated using 2048 x 2048 pixels, each of which was 200 x 200 μm in size. The detectors were positioned nominally 1496 mm from the sample and were regularly calibrated using levitated polycrystalline Si. The maximum usable momentum transfer, q_{max}, was 13 Å^{-1}.

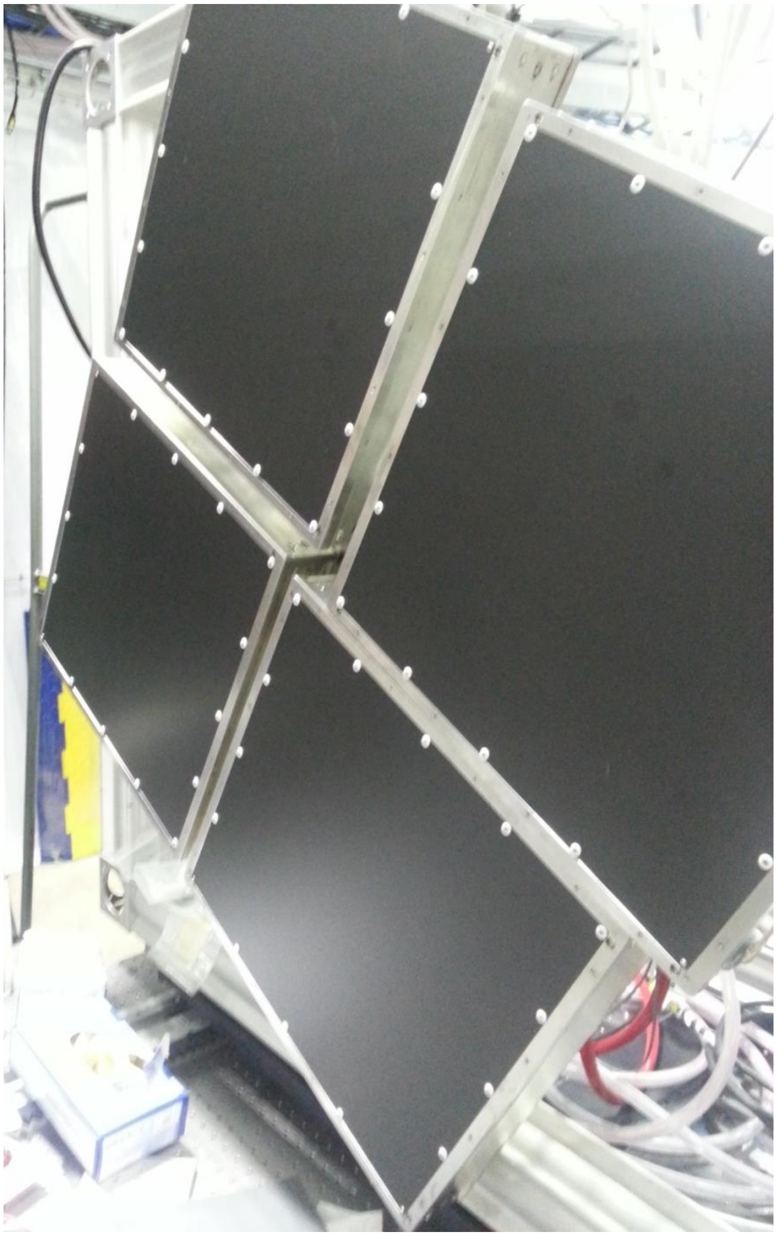

Figure 2.4 Four amorphous Si flat-panel GE Revolution 41-RT detectors in the HYDRA configuration.

In typical WU-BESL experiments, a beamstop is placed just beyond the Be exit window to block crystalline scattering from the window from reaching the detectors. In order to measure a SAXS signal, the small-angle X-rays need a clear path to the SAXS detector. A special jig was devised by mounting a tungsten ring to a wooden shaft and extending it into the beam path. This blocked the scattering from the Be windows from reaching the detector while at the same time allowing transmission of the small-angle signal (Figure 2.5).

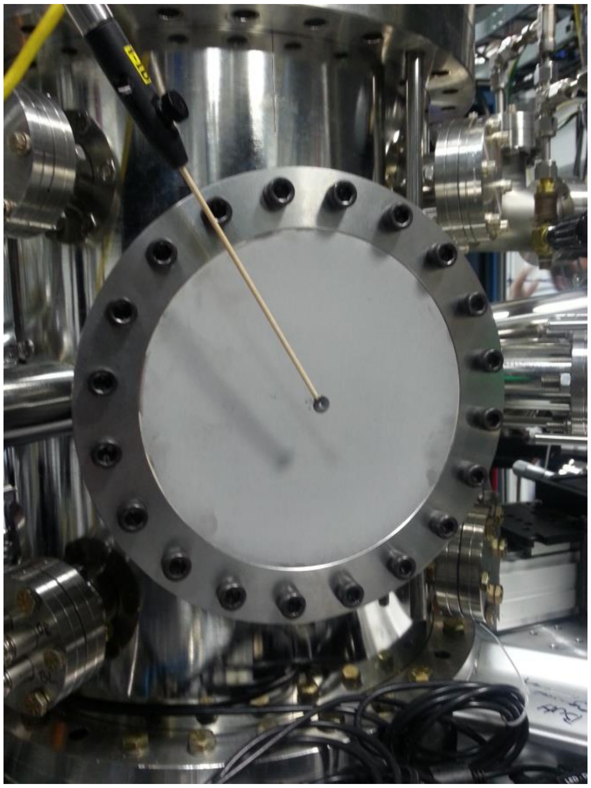

Figure 2.5 Tungsten ring used to block scattering from the Be exit window from reaching the HYDRA detectors while at the same time allowing the SAXS signal to reach the detector.

A PIXIRAD-1 CdTe photon counting pixel detector (Figure 2.6) was used to measure the SAXS signal. The sample-to-detector distance, detector tilt, and detector center were calibrated using a 12.5 x 12.5 mm Lightsmyth reflection grating with 7200 lines/mm (part number SLG-C72-1212A-AI). The detector was located 6,240 mm from the sample and was capable of measuring momentum transfers between 0.01 and 0.25 Å^{-1}, corresponding to correlation lengths of 2.5 – 62.8 nm. A 1 cm thick glassy carbon calibration standard was used for absolute intensity normalization and is discussed in further detail in Section 2.6.2.

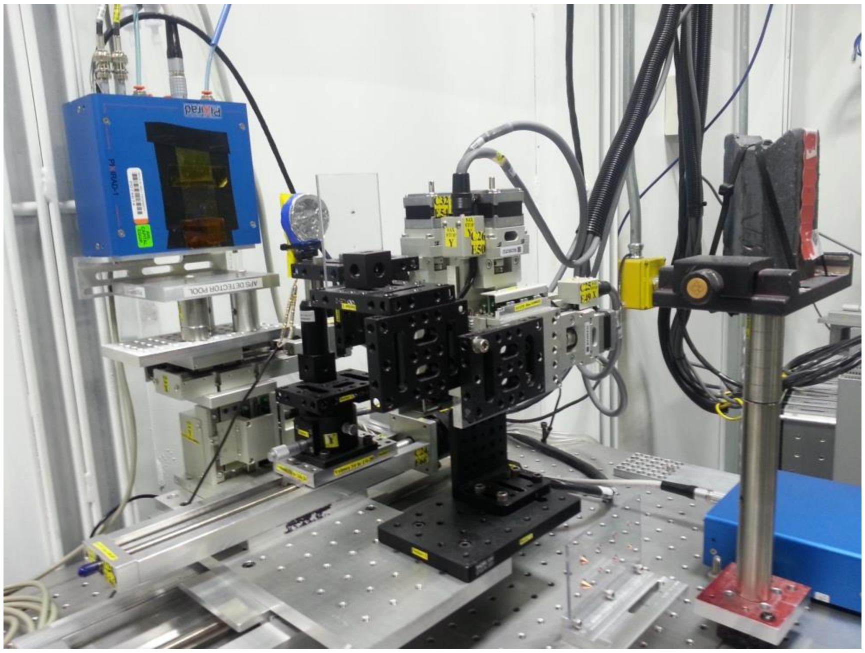

Figure 2.6 PIXIRAD-1 SAXS detector.

2.5 Wide-Angle X-ray Diffraction Analysis

There are many standard corrections that must be applied to properly reduce the measured diffraction to a static structure factor, $S(q)$, or pair-distribution function, $g(r)$. The WAXS data in this dissertation were analyzed using an in-house LabVIEW^{TM} analysis program designed by J. C. Bendert [14]. The software implements all standard X-ray corrections, detailed below. Quantitative corrections for spherical absorption and multiple scattering from a beam striking the sample off-center were also developed by J. C. Bendert [15] and are included in the analysis package. In order to synchronize sample temperature with the X-ray beam, a TTL signal was connected between the two acquisition systems to indicate when the X-ray detector was acquiring. A peak analysis of $S(q)$ was performed using an in-house LabVIEW^{TM} program developed by J. C. Bendert and myself, which can select from a range of fitting functions, including spline fits and Gaussian functions, to properly locate the peak heights and centers and generate an appropriate error based on adjusted scaling parameters (fluorescence and multiplicative scaling from the X-ray analysis program) and statistical adjustment (moving each point in the input curve by its measurement error). The same errors were implemented for the peak analysis of $g(r)$, with the addition of truncation errors (changing the max-q used when Fourier transforming $S(q)$ into $g(r)$) and density errors.

Previous works have discussed the necessary corrections required for proper X-ray scattering experiments in detail [5, 14, 16]. A brief overview of the relevant corrections will be given in this section to provide the reader with some background. This section deals specifically with data acquired at Station 6-ID-D at the APS, but the general form of the corrections are also valid for data acquired at Station 1-ID-E.

Raw intensity data were acquired at the APS in a transmission geometry using a GE Revolution 41-RT amorphous Si flat panel detector. A *dark frame* image was acquired with the X-ray shutter closed to correct for the natural noise within the detector, as well as an *empty chamber* frame with no sample in the beam path to measure the secondary scattering from both the air and the chamber. A background- and dark-corrected scattered intensity was calculated using

$$I_{Corrected} = \Gamma(I_{Raw} - I_{Dark} - (I_{Empty} - I_{EmptyDark})), \tag{2.3}$$

where I_{Raw} is the measured sample intensity and Γ is a detector-specific gain map that corrects for variable efficiency in each pixel and is provided by the instrument scientist.

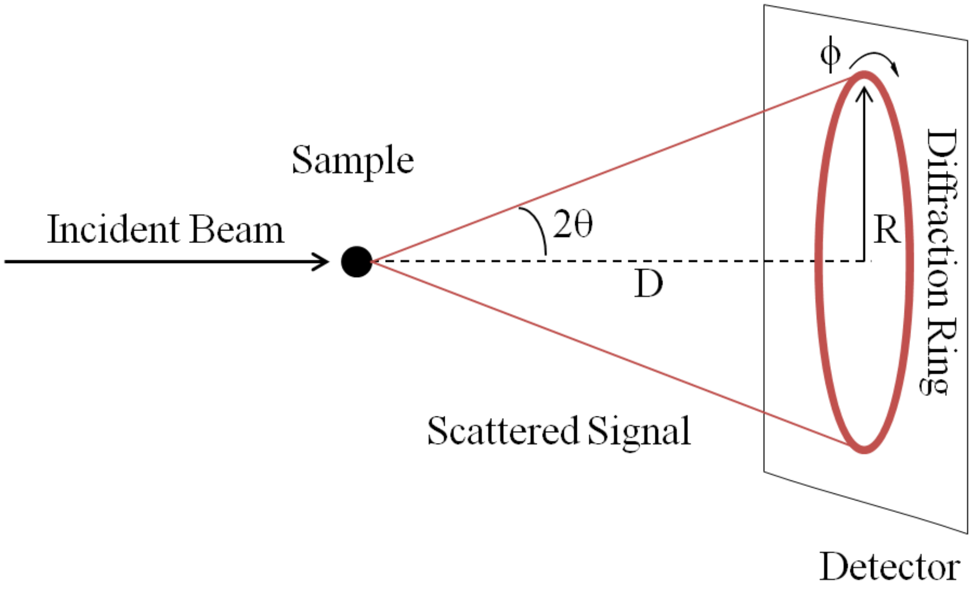

Figure 2.7 Schematic illustration of powder diffraction onto an area detector. Isotropic scattering produces intensity *rings* at a constant 2θ relative to the incident beam where the intensity is constant for all ϕ around the beam axis. The distance to detector, D, and radial distance from the beam center, R, are used to determine 2θ.

Liquid and polycrystalline samples scatter isotropically, producing ring-like patterns on a flat panel detector (Figure 2.7). While, in principle, the detector is positioned perfectly perpendicular to the X-ray beam, this is not always the case in practice. A detector tilted relative to the incident beam will produce an asymmetrical pattern as the scattering distance will not be equal for each pixel in a ring around the center. During each X-ray experiment, the diffraction pattern of multiple levitated Si samples prepared from arc-melting was measured. Using the well-known diffraction pattern of pure Si (diamond lattice, a = 5.43071 Å), the detector image was corrected for angular tilt and rotation by fitting up to 15 diffraction rings. The image was then converted from polar coordinates (R, ϕ) to solid angle coordinates (2θ, ϕ), after adjusting both R and ϕ for the tilt angle. Once expressed in solid angle coordinates, each pixel was corrected for the detector geometry, oblique incidence (accounting for the extra distance a photon must travel within a pixel if it doesn't strike the pixel perpendicularly), and polarization.

Radiation that is polarized in the scattering plane is attenuated, while perpendicular radiation is not. This factor depends on both the scattering angle as well as the angle of the polarization plane.

Self-absorption and multiple scattering were calculated assuming the incident beam was significantly smaller than the radius of the sample. A spherical geometry was used in these calculations, and the detector image was corrected for the asymmetry resulting from the beam striking the sample off-center [15]. The scattered signal is attenuated as it passes through the remainder of the sample after scattering, resulting in a reduction in measured intensity. The absorption correction calculates what the resulting *effective scattering volume* is and adds back in what the true intensity should be. This correction effectively scales the background subtracted intensity by V/V', where V is the actual sample volume and V' is the effective scattering volume. Multiple scattering, or secondary scattering events within the sample after the primary scattering event, also takes this into account but is also dependent upon the new scattering angle from the second scattering event. In principle, a photon could be scattered multiple times within a sample, but in practice, there is very little effect beyond the second scattering event. The multiple scattering factor scales the background subtracted intensity by I_2/I_1, where I_2 is the calculated secondary scattering intensity and I_1 is the primary scattering intensity. For liquid and glass samples measured during BESL 2010 and BESL 2013, the attenuation was calculated from NIST tables using measured sample mass and density. For liquid and glass samples measured during APS 2011 and SAXS 2014, the attenuation was estimated from a photo-diode located in the beamstop.

The liquid and glass samples were all assumed to be isotropic and homogenous and the intensity was integrated around ϕ at a constant 2θ [17]. This produced a one-dimensional pattern as a function of scattering angle with a greatly enhanced signal-to-noise ratio. In order to properly compare measurements made across a variety of energies, the scattering angle 2θ was converted to the appropriate momentum transfer, or q, given by

$$q = \frac{4\pi \sin\left(2\theta/2\right)}{\lambda}, \tag{2.4}$$

which scales with the scattering photon wavelength, λ.

Inelastic scattering of photons results in an energy shift of the scattered photon due to the energy transferred during the recoil. This effect, known as Compton scattering, must be removed from the measured intensity per atom and is denoted by

$$n^{Inc}\left(2\theta\right) = \left(E_{\mathrm{C}} / E\right)^{\alpha} i\left(M\right). \tag{2.5}$$

This intensity contains contributions from radiation pressure ($(E_{\mathrm{C}}/E)^{\alpha}$, also known as the Breit-Dirac recoil factor) as well as a correction to the classical Thompson scattering, made by subtracting the coherent scattering power for a particular atom ($i(M)$) [18, 19]. The exponent, α, is dependent upon whether the detector is a counting detector ($\alpha = 2$) or an intensity detector ($\alpha = 3$) [16]. An intensity detector was used for all data in this dissertation.

Finally, all of these corrections can be combined to produce the coherent scattering cross section, $d\sigma_{\mathrm{C}}/d\Omega$, using

$$\frac{d\sigma_C}{d\Omega} = N \oint d\phi \frac{\Gamma\left(dA/d\Omega\right) I_{Corrected}}{\left(V/V'\right)^{-1} OP\left(1 - I_2/I_1\right)^{-1}} - n^{Inc} - F, \tag{2.6}$$

where N is a normalization factor that converts $d\sigma_{\mathrm{C}}/d\Omega$ from arbitrary units into electron units, F is a correction for fluorescence, O is the correction for oblique incidence, and P is the correction for polarization. The normalization is performed by minimizing the Peterson metric [20] which minimizes the ripples in *G*(*r*) below some minimum cut-off where they become unphysical. This metric is also used in the correction of neutron diffraction measurements and is discussed in more detail in Section A.7. This correction properly normalizes *S*(*q*) to 1 at large-*q*. Fluorescence occurs when atoms absorb a photon and re-emit another at a different wavelength. This results in a background that is flat across all solid angles, typically more intense for samples with larger atomic numbers (*Z*). If a correction of this type is needed to properly normalize small-*Z* samples where the fluorescence is expected to be small, it becomes an adjustable factor to account for experimental unknowns while correcting the data to physically realistic values.

The structure factor, or *S*(*q*), can be calculated from the coherent scattering cross section once all of these corrections have been performed. There are several notable normalization methods, each of which emphasizes slightly different aspects of the structural data. In this dissertation, the primary normalization scheme used is the Faber-Ziman formalism [21]. Within this formalism, the Laue diffuse scattering is subtracted from the coherent scattering cross section and then normalized to the square of the average form factor, as given by

$$S(q) = \frac{\dfrac{d\sigma}{d\Omega} + \left\langle f(q) \right\rangle^2 - \left\langle f(q)^2 \right\rangle}{\left\langle f(q) \right\rangle^2} \quad . \tag{2.7}$$

In this notation, $< f(q) >^2$ represents the square of the average form factor and $< f(q)^2 >$ is the average of the square of the form factor. These are defined by

$$\left\langle f(q) \right\rangle = \sum_i c_i f_i(q) \tag{2.8}$$

and

$$\left\langle f(q)^2 \right\rangle = \sum_i c_i \left(f_i(q) \right)^2 \ , \tag{2.9}$$

where c_i is the fractional atomic composition of the i^th atomic species. The atomic form factor, $f(q)$, is strongly q-dependent and $f(0)$ scales roughly as the atomic number, Z. The form factors used in this dissertation were calculated from tabulated data for all elements up to 75.4 Å^{-1} [22].

Once the total structure factor is calculated, the reduced pair-distribution function, $G(r)$, can be calculated from a Fourier transform using

$$G(r) = 4\pi r \rho_0 \left(g(r) - 1 \right) = \frac{2}{\pi} \int_0^\infty q \left(S(q) - 1 \right) \sin(qr)\, dq \, , \tag{2.10}$$

where $g(r)$ is the pair-distribution function (PDF) and ρ_0 is the atomic number density. In practice, the Fourier transform is over a finite range of q_min to q_max due to limited detector sizes and geometry. If $S(q)$ does not correctly approach unity at large-q, or if q_max is cut off before structural oscillations damp out (which can occur if the experiment cannot access a large enough q-range), large termination error ripples are introduced into the resulting $g(r)$.

2.6 Small-Angle X-ray Scattering Analysis

The principles of small-angle X-ray scattering (SAXS) largely follow from the discussion of wide-angle X-ray scattering (WAXS) (Section 2.5). The primary advantage of SAXS is the ability to examine nanometer-sized compositional fluctuations rather than the atomic level structure (Figure 2.8). Intensity features appearing at a momentum transfer of q correspond to scattering from density inhomogeneities of size $d = 2\pi/q$. Many bulk metallic glasses have been found to decompose on the nanoscale into two phases prior to crystallization [23-28]; small-angle scattering investigations can provide increased understanding of the nucleation and growth of the devitrification products as well as an understanding of the stability observed in good glass-forming systems. The following sections give a brief background on the theory behind small-angle scattering (Section 2.6.1) as well as the corrections implemented in the investigation of liquid-liquid phase separation in a $Zr_{52.5}Cu_{17.9}Ni_{14.6}Al_{10}Ti_5$ (Vit105) bulk metallic glass (Section 2.6.2 and Chapter 7).

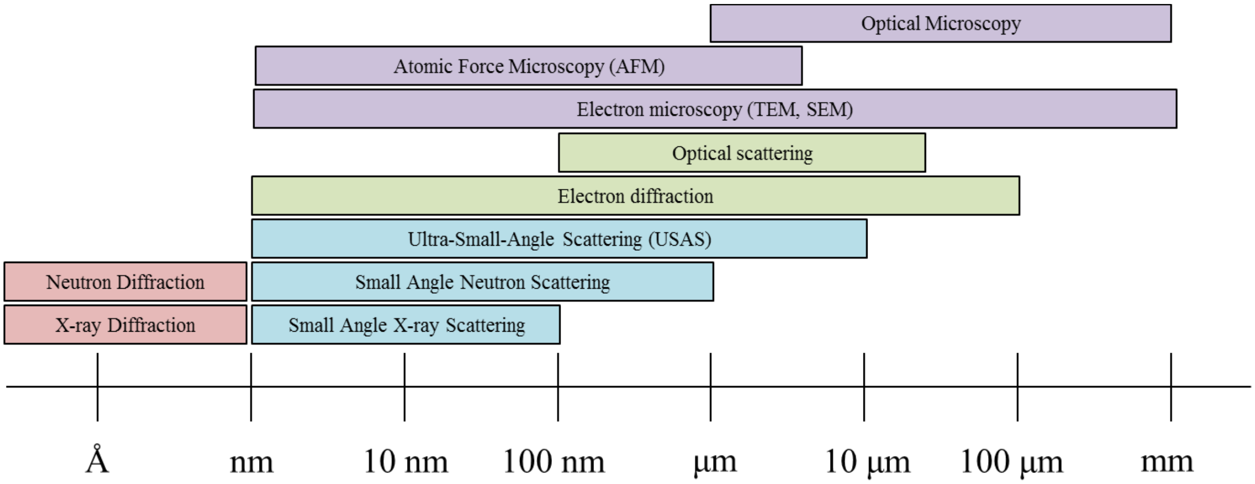

Figure 2.8 Representative sizes accessible with various types of wide-angle scattering techniques (red), small-angle scattering techniques (blue), other scattering methods (green), and direct imaging techniques (purple).

2.6.1 Small-Angle X-ray Scattering Theory

X-ray scattering from a single atom depends on the distribution of electrons around that atom. When scattering from a large cluster of atoms, the probability of scattering then depends on the density of electrons in the given volume, or the *scattering length density*, $\rho(r)$. The scattering amplitude of a particle, $F(q)$, is given by

$$F(q) = \int_V \rho(r) e^{i\mathbf{q}\cdot\mathbf{r}} d\mathbf{r}\,, \tag{2.11}$$

where V is the particle volume.

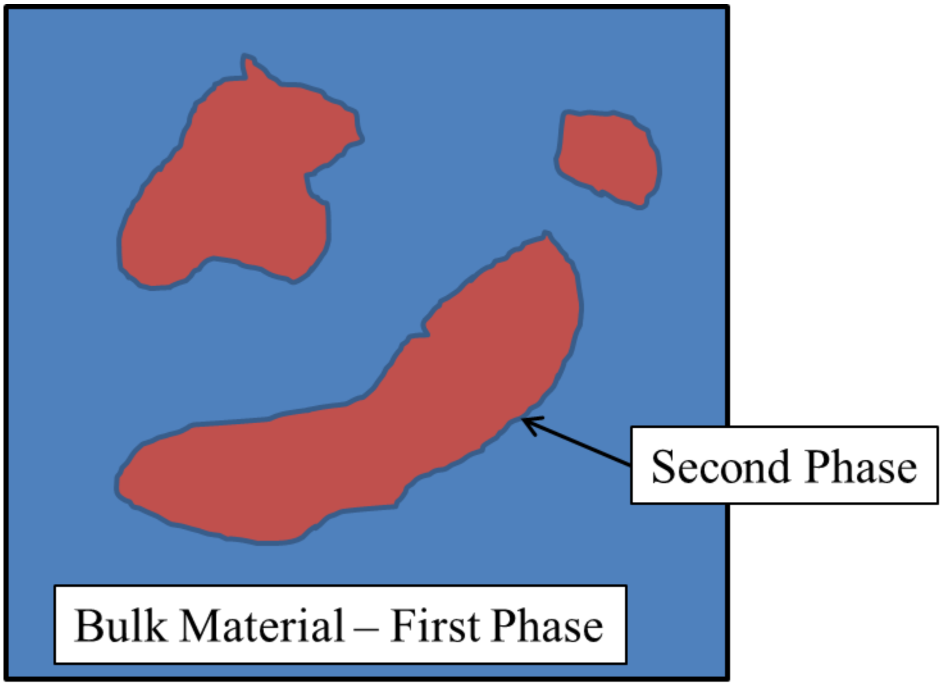

Figure 2.9 Schematic of a second, compositionally distinct, phase formed within the bulk material.

If two compositionally distinct regions form within a sample such as through phase separation or dilute particles suspended within a medium (Figure 2.9), the second component may have a different density of scattering elements, $\rho_2(r)$, than the bulk phase, $\rho_1(r)$. The ability to resolve the difference between the new phase and the bulk depends on the relative difference in scattering length density, $\Delta\rho = |\rho_2 - \rho_1|$, or the *contrast density*. In X-ray scattering, the contrast density is given by

$$\Delta\rho = r_{e^-} \sum_i \Delta c_i f_i(q), \qquad (2.12)$$

where r_{e-} is the Thompson electron radius, Δc_i is the difference in concentration of component i between the scatterer and its average surroundings, and $f_i(q)$ is the atomic form factor. The measured differential cross section is then given by

$$\frac{d\sigma}{d\Omega} = \frac{1}{N}\left| \int_V \Delta\rho \, e^{i\mathbf{q}\cdot\mathbf{r}} d\mathbf{r} \right|^2 , \tag{2.13}$$

and the *macroscopic cross section,* $d\Sigma/d\Omega$, scales as

$$\frac{d\Sigma}{d\Omega} = \frac{N}{V}\frac{d\sigma}{d\Omega} = \frac{1}{V}\left| \int_V \Delta\rho \, e^{i\mathbf{q}\cdot\mathbf{r}} d\mathbf{r} \right|^2 . \tag{2.14}$$

In the limit of $q \rightarrow 0$, the macroscopic cross section reduces to the well-known Guinier relationship [29] given by

$$\lim_{q\rightarrow 0}\frac{d\Sigma}{d\Omega} = N_v \left|\Delta\rho\right|^2 V^2 \exp\left[-\frac{1}{3}(q R_G)^2 \right], \tag{2.15}$$

where N_v is the density of the second region within the bulk phase, V is the region volume, and R_G is the region's radius of gyration, or the mass distribution of the region around a central axis. R_G can thus be used to determine the approximate dimensions of the second region. Since $d\Sigma/d\Omega$ is related to the measured SAXS intensity, $I(q)$, R_G can be calculated from the slope, m, of $\ln(I(q))$ vs. q^2 using

$$R_G = \sqrt{-3\,m} . \tag{2.16}$$

This method is valid only when $q_{\max} R_G \leq 1.2$ where $q_{\max}$ is the largest value in q over which the fit was performed.

2.6.2 Small-Angle X-ray Scattering Corrections

Raw SAXS data were first corrected by subtracting the dark counts obtained when no X-ray beam was present. An empty chamber scan taken with no sample in the beam was also corrected by subtracting the native dark counts. Both empty and dark frames were acquired periodically throughout the experiments for each frame rate. Due to high sample absorption at the energies used (Section 2.4.4), the scattered signal can be greatly attenuated and the empty scan is therefore measured with a higher flux than with the attenuated signal. The difference in signal intensity before and after striking the sample was measured during the SAXS 2014 experiment and the sample transmission factor, T_S, was used to damp the effective empty subtraction using

$$I_S = I_{raw} - I_{dark} - T_S(I_{empty} - I_{dark}) . \tag{2.17}$$

For most samples, T_S was approximately 40%. The macroscopic cross section was calculated using

$$I_S = I_0 A \Delta\Omega \eta T_S d_S \left(\frac{d\Sigma}{d\Omega} \right)_S , \tag{2.18}$$

where I_0 is the incident flux, A is the area of the beam that strikes the sample, $\Delta\Omega$ is the solid angle per detector pixel, η is the detector efficiency, T_S is the sample transmission, and d_S is the sample thickness [30].

In order to extract size information from observed structural features, such as the radius of gyration, R_G (Eqn. 2.16), the intensity must first be normalized to an absolute scale. This allows for direct comparison between other independent experiments [31, 32], as well as accurate calculations of R_G. To do this, the small-angle intensity of a 1 cm thick glassy carbon standard located in the approximate location of a levitated sample was acquired. The measured scattering intensity with appropriate background and dark subtraction for the standard, I_{GC}, follows a similar equation as Eqn. 2.18. By taking a ratio of the measured intensities of the sample and glassy carbon, the majority of the detector corrections will normalize out and the macroscopic sample cross section can be determined by

$$\left(\frac{d\Sigma}{d\Omega}\right)_S = \left(\frac{d\Sigma}{d\Omega}\right)_{GC} \frac{I_S / d_S T_S}{I_{GC} / d_{GC} T_{GC}}, \tag{2.19}$$

where $(d\Sigma/d\Omega)_{GC}$ is the known glassy carbon scattering pattern [30, 31]. A calibration factor, C, can be determined using

$$C = \frac{\left(\frac{d\Sigma}{d\Omega}\right)_{GC}}{I_{GC} / d_{GC} T_{GC}}. \tag{2.20}$$

The absolute intensity can then be quickly calculated for any sample by combining Eqns. 2.17-2.20:

$$\left(\frac{d\Sigma}{d\Omega}\right)_S = C \frac{I_S}{d_S T_S}. \tag{2.21}$$

All analyses were performed using MATLAB scripts created by the beamline scientist at Station 1 at the APS, J. Almer. The entire combination of secondary programs and primary scripts are included in the supplementary DVD attached with this dissertation.

2.7 Neutron Electrostatic Levitation (NESL)

All of the neutron scattering data in this dissertation were acquired using the Neutron Electrostatic Levitator (NESL) which was designed, constructed, and developed at Washington University in St. Louis by K. F. Kelton, N. A. Mauro, K. Derendorf, and A. J. Vogt through collaboration with A. I. Goldman and G. E. Rustan at Ames Laboratory and T. Egami and K. Lokshin at Oak Ridge National Laboratory [33-35]. This device also uses the ESL technique [3] to provide a containerless environment with which to study the high-temperature and supercooled liquid structure of metallic glass-forming liquids. The NESL utilizes an environment similar to WU-BESL, in which non-contact measurements of temperature are acquired simultaneously with scattering data. Due to the highly constrained geometries of the neutron beamlines, however, additional considerations greatly complicated its design and construction.

2.7.1 Design Constraints and Beamline Integration

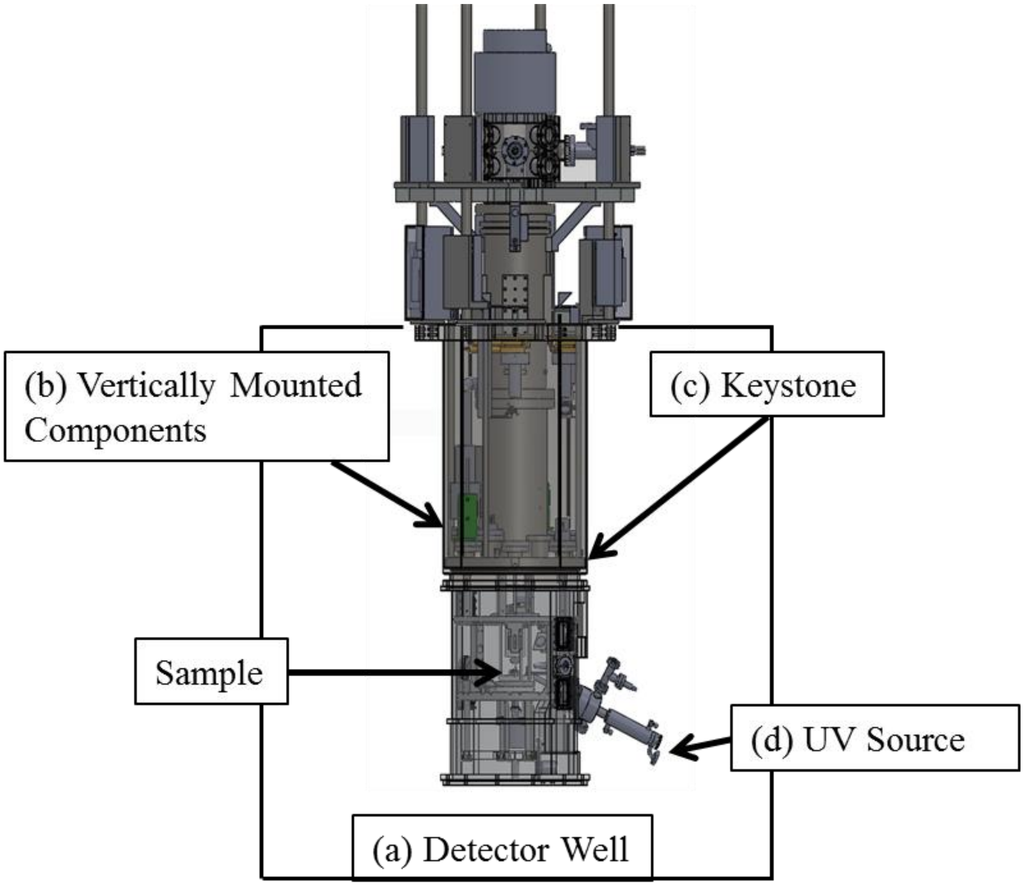

Figure 2.10 A rendering of the Neutron Electrostatic Levitator (NESL) in a vertical orientation for SNS detector wells. Components are mounted vertically to the keystone and reflected off of mirrors. Image adapted from [34] with permission.

The NESL is designed for easy integration into a number of possible instruments at the Spallation Neutron Source (SNS) at Oak Ridge National Laboratory (ORNL). It is intended for elastic scattering studies on the Nanoscale-Ordered Materials Diffractometer (NOMAD) beamline [36], and for inelastic scattering studies on the Wide Angular-Range Chopper Spectrometer (ARCS) and the Cold Neutron Chopper Spectrometer (CNCS). Each of these instruments contains a large detector well into which the sample environment is lowered (Figure 2.10 (a)). The interior walls of the detector well are lined with arrays of detectors covering a wide range of solid angles. Taking advantage of this detector coverage imposes significant design challenges, such as keeping NESL components out of the scattering path to the detectors. In order to accomplish this, each optical component is oriented vertically on the keystone (Figure 2.10 (b-c)) and reflected off of silver-coated mirrors to maintain line-of-sight to the sample (Figure 2.11). To maximize photon flux and effectively maintain sample charge, a UV source is mounted at the base of the NESL (Figure 2.10 (d)) where the capillary extends to within 60 mm of the levitated sample (Figure 2.13). The NESL is mounted to the detector well with a 37” flange to complete the vacuum seal with the neutron detector chamber. Since the UV is mounted external to the NESL chamber, multiple feedthroughs are connected to this flange to provide vacuum, gas, and water lines to the UV source.

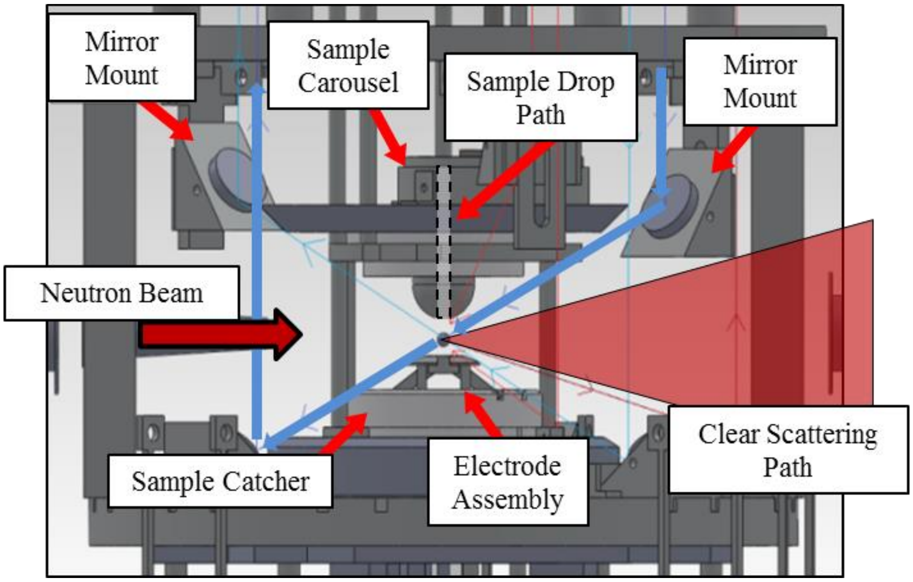

Figure 2.11 Schematic of the electrode assembly, sample catcher, and mirror platforms. The use of mirrors moves components out of the path of the scattered neutrons and reduces secondary scattering. Samples are loaded by dropping a sample from the carousel through the top electrode onto a vertical post (currently lowered below the sample catcher). Image adapted from [34] with permission.

Entrance and exit windows for the direct beam are made from pure vanadium, an element with a relatively small coherent scattering cross section. This ensures that any scattering from these windows contains no coherent scattering signal that would interfere with that from the sample. In addition, interior components surrounding the beam path are covered with reaction bonded B_4C (RBBC) to further reduce internal primary scattering. The entrance window is preceded by rings of carbon-bonded B_4C (CBBC) surrounding a Boron Nitride (BN) pinhole to further collimate the incident beam. External to the exit window is a beamstop consisting of a layer of B_{10} powder held in place by a BN plug (Figure 2.12).

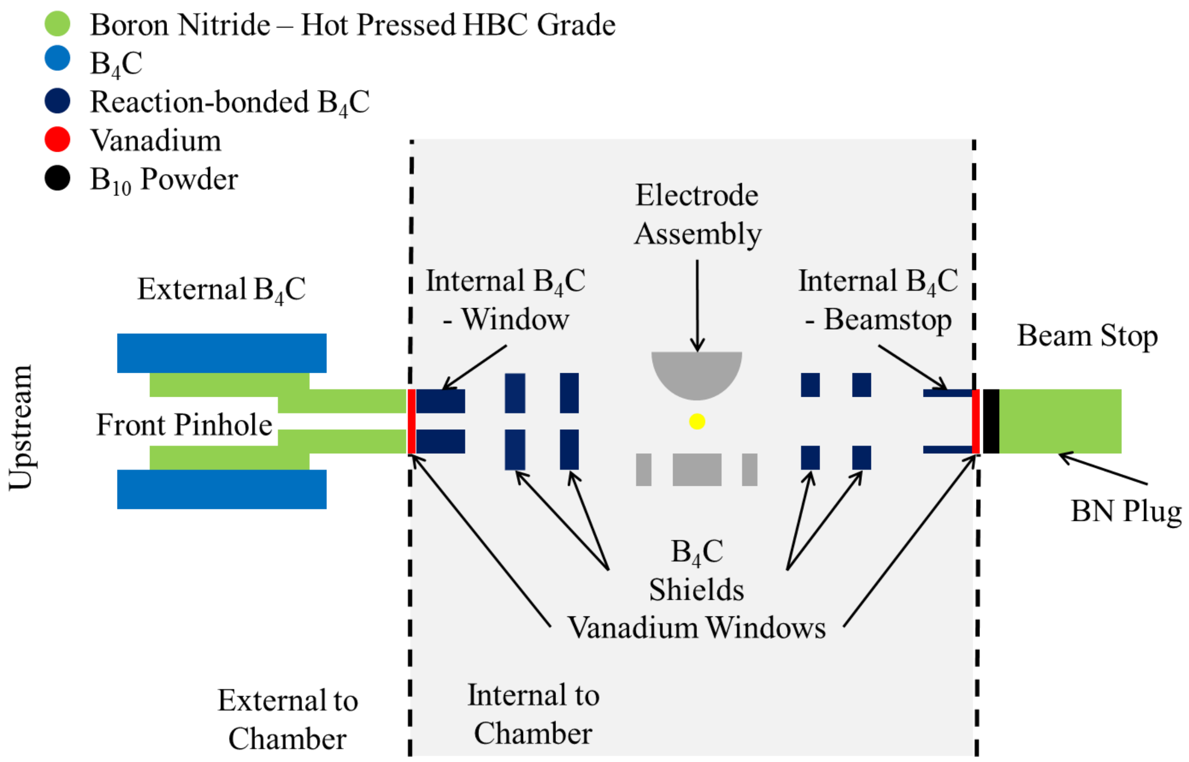

*Sizes to scale (except electrodes), internal distances between parts not to scale

Figure 2.12 Internal collimation optics using neutron-absorbing boron components. Schematic courtesy of A. J. Vogt.

To further reduce background and secondary scattering from the NESL, the majority of components surrounding the sample are constructed out of aluminum, which has a very small neutron scattering cross section. In addition, the vacuum chamber walls consist of thin (1/16”) aluminum windows, further reducing the secondary scatter from the sample environment. Those components, which out of necessity are made from stainless steel (such as the bolts and flanges for the NESL vacuum chamber), are shielded by clamping thick Boraflex^{TM} sheets with approximately 25% boron (a strong absorber of neutrons) over the exit surface. This eliminates most of the secondary scattering from these components.

2.7.2 Optical Components and Levitation

Sample levitation is maintained using a set of charged electrodes in a similar configuration as WU-BESL. A schematic of the electrode assembly and the surrounding environment is shown in Figure 2.11. An amplifier capable of generating a potential difference of 0 to -30 kV across the vertical components is connected via high-vacuum feedthroughs. In order to maintain stable levitation in the center of the electrode assembly, a pair of orthogonal lateral electrodes, similarly connected to high-voltage amplifiers, generates electric potential differences of ± 5 kV. Shadows are cast from the levitated samples (m = 100-450 mg, r = 1.5-3 mm) onto a pair of position sensitive detectors (PSDs) by a pair of orthogonal Helium-Neon positioning lasers (designated *red* and *blue*) (Figure 2.13). The position is measured and vertical and lateral voltages are dynamically adjusted to maintain sample position using a feedback control algorithm [6].

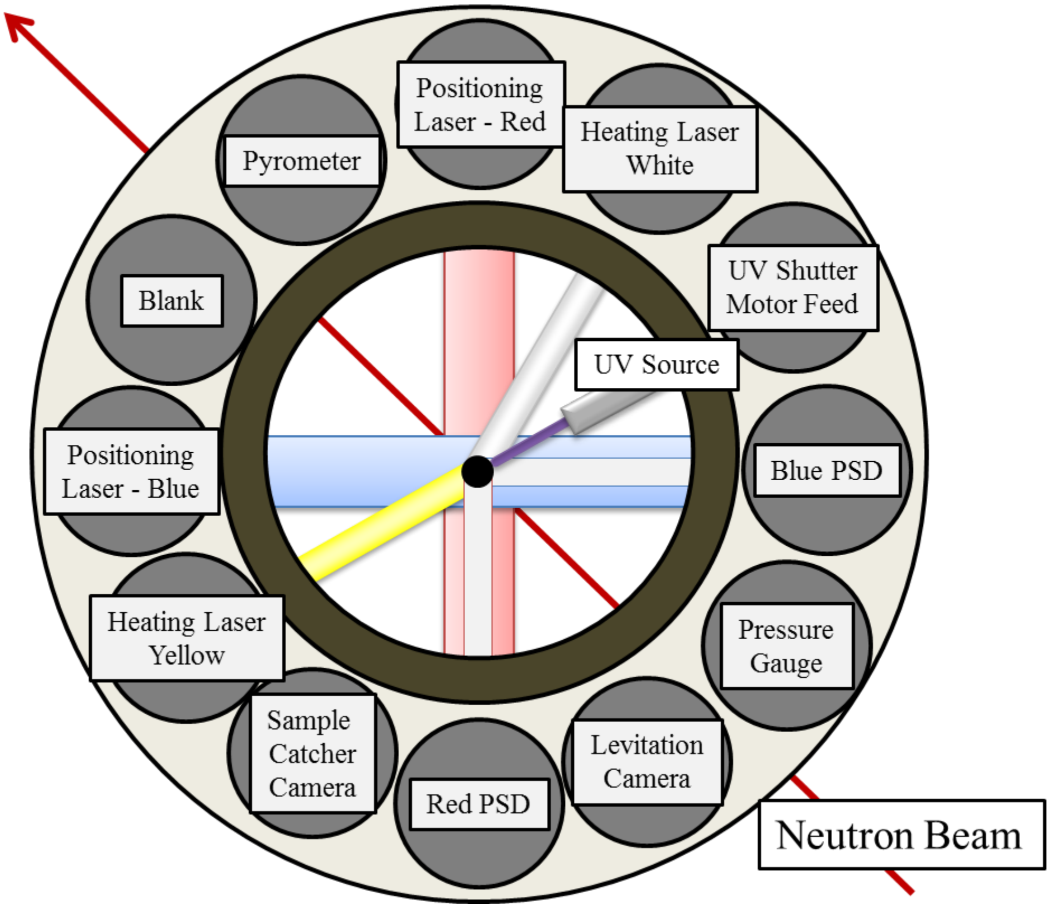

Figure 2.13 Top-view of vertically mounted components on the NESL keystone relative to the incident neutron beam. Example laser paths and shadows are shown with colors appropriate to their labels for clarity. In reality, all lasers are actually red or otherwise outside of the visible spectrum. Schematic constructed with the assistance of A. J. Vogt.

The sample is heated using a pair of diametrically opposed fiber-coupled diode lasers (980 nm, 110 W continuous maximum power output, designated as *yellow* and *white*). Non-contact temperature measurements are performed using a single Process Sensors Metis MQ22 two-color ratio pyrometer with an effective operating range of 500 – 2000 ^{o}C. The emissivity ratio is calibrated by correcting the temperature at the melt plateau to that of the largest heat signature observed in a differential thermal analyzer (DTA) (LabsysTM DTA/DSC, Setaram). A constant emissivity ratio is assumed over the entire temperature range once the sample is molten. Further details of the temperature correction are given in Section A.3.

As the sample increases in temperature, surface charge is lost. As for the ESL discussed in Section 2.3.1, sample charge is maintained via the photoelectric effect by an ultraviolet (UV) source. Thermionic emission eventually removes the need for the UV lamp at higher temperature. Once fully melted, the sample maintains relatively stable charge. Line of sight to the sample from the UV lamp is then blocked by a shutter, minimizing deposition onto the capillary from sample evaporation.

A primary Pfeiffer PKR261 cold cathode vacuum gauge is located on the keystone to measure the chamber pressure near the sample (Figure 2.13), while a second gauge can be mounted higher up on the vacuum chamber, close to the turbo pump. The NESL is operated under high vacuum, typically below 7×10^{-7} Torr. For the experiments presented in this dissertation it was operated around $7\text{-}8 \times 10^{-6}$ Torr due to outgassing issues that have since been diagnosed and repaired.

Samples are loaded in a 30-slot carousel located above the top electrode (Figure 2.11) and are dropped through a hole in the center of the curved top electrode onto the sample post. The post can be lowered to the base of the sample catcher to recover fallen samples. A pair of Pixelink cameras is used to observe the levitated sample as well as the sample catcher to ensure samples are recovered and properly processed (Figure 2.13).

Further details of the integration of the specialized components used in the NESL are extensively discussed elsewhere [2, 33-35].

2.8 Neutron Diffraction Measurements

Time-of-flight (TOF) neutron scattering data were acquired using the NESL during experiments performed at the Spallation Neutron Source (SNS) at Oak Ridge National Laboratory (ORNL). A brief overview of how neutrons are produced at the SNS is presented in Section 2.8.1 and an overview of neutron time-of-flight (TOF) measurements is presented in Section 2.8.2. A description of the Nanoscale-Ordered Materials Diffractometer (NOMAD) instrument [36] and relevant details used during experiments in September and October of 2014, referred to as "NOMAD 2014" throughout this dissertation, are discussed in Section 2.8.3.

2.8.1 Neutron Production

The SNS currently produces the most intense pulsed neutron beams in the world. Neutrons are produced through spallation, where a high-energy proton beam strikes a heavy-metal target and ejects neutrons. In order to accomplish this, a number of steps are required (Figure 2.14).

First, charged hydrogen atoms (H^-) are accelerated to a maximum energy of 1 GeV using a 1000 ft linear accelerator (linac) (Figure 2.14 (a)). The maximum ion beam power that can be produced at the SNS is 1.4 MW, although it is typically operated at a much lower setting (less than 1 MW). The high-energy ions are injected into an accumulator ring that bunches and intensifies the ion beam (Figure 2.14 (b)). The negatively charged ions pass through foils that strip off electrons, producing positively charged hydrogen atoms (H^+; i.e., protons). The protons circulate through the ring for approximately 1200 rotations until they are all released in a short pulse (~10^{-6} s). These pulses are produced at approximately 60 Hz.

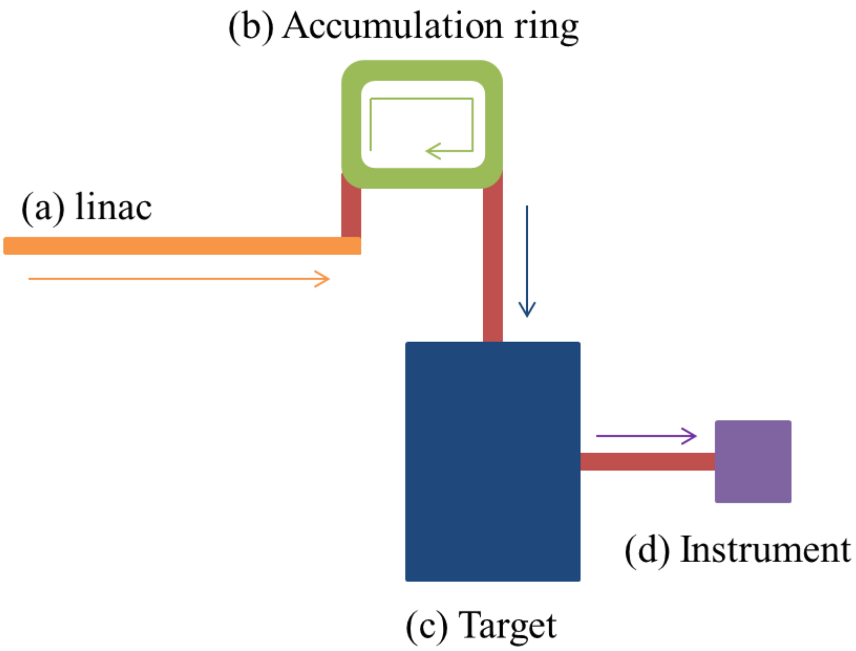

Figure 2.14 Schematic of the steps required for spallation neutron production.

Proton pulses strike a mercury target with each proton capable of *spalling*, or knocking off, approximately 20-30 individual neutrons (Figure 2.14 (c)). The hot neutrons pass through moderators (filled with water or liquid hydrogen), cooling them down until their energies reach the appropriate range specified for each individual instrument. The cooled neutrons are guided to each instrument and further prepared for injection to a sample environment by secondary choppers (Figure 2.14 (d)).

2.8.2 Time-of-Flight (TOF)

At the SNS, pulsed neutrons travel along the primary flight path of length D_1 (19.5 m at NOMAD) until they interact with the sample. Scattered neutrons then travel a distance D_2 (0.5-3 m at NOMAD) from the sample to the detector. The velocity, v, of a neutron arriving at a detector with a time-of-flight (TOF), τ, associated with a specific pulse coming from the up-stream moderator can be described by

$$v = \frac{D_1 + D_2}{\tau}. \tag{2.22}$$

The neutron momentum is given by

$$p = m_n v = \hbar k, \tag{2.23}$$

where m_n is the mass of a neutron, $\hbar$ is Planck's constant, and k is the wave number. By combining Eqns. 2.22 and 2.23, the wavelength of the neutron is given by

$$\lambda = \frac{2\pi}{k} = \frac{2\pi\hbar\tau}{m_n(D_1 + D_2)}. \tag{2.24}$$

The momentum transfer, q, can then be determined from Bragg's law, given earlier in Eqn. 2.4.

While D_1 is well known, D_2 for each individual detector pixel is not as well determined. Diamond powder encased in a vanadium can is placed in the same position as a typical sample to calibrate each pixel in the detector bank to a known powder diffraction pattern. The diamond powder is used to calibrate the detector distances in a similar manner as the Si standards in the X-ray experiments described in Section 2.5.

2.8.3 NOMAD 2014

As a pulsed neutron source, the SNS provides 60 Hz beam pulses to each of the facility's beamlines. At NOMAD, the neutron pulses of the incident beam are controlled by four choppers located upstream of the sample and operated at 30 Hz. By excluding every other pulse from the source, this ensures that slow, long wavelength neutrons in one pulse are not overlapped by fast neutrons of the following pulse. This arrangement provides access to wavelengths between 0.1 - 2.9 Å (10 eV – 10 meV), with a measureable q-range out to 100 Å^{-1}.

TOF data for the scattered neutrons were acquired using ^{3}He linear position sensitive detectors of both 1” and ½” diameter tubes to measure neutron arrival times and positions. The tubes are grouped in packs of 8, with a total of 50 packs providing detector coverage during NOMAD 2014. Each pack is separated into 1024 separate pixels (51200 pixels total) providing 3-175^o coverage in 2θ. The TOF, τ, and pixel for each neutron associated with that pulse are then stored in detector files.

In September 2014, the NESL was installed on the NOMAD beamline at the SNS and neutron scattering data from levitated liquid droplets were acquired using a collimated beam of ~10 mm in diameter near the sample. The first liquid structural data were acquired from $Zr_{64}Ni_{36}$ samples, but after only two days of beam time the experiment was cut short due to target and accelerator failure at the SNS. The NESL remained installed on the NOMAD beamline during facility repairs, and in October 2014, the original experiment was completed. Experimental configurations remained unchanged as the NESL was not moved while facility repairs were performed. TOF data was acquired for four more liquid alloys ($Cu_{46}Zr_{54}$, $Zr_{80}Pt_{20}$, $Zr_{77}Rh_{23}$, and $Ti_{39.5}Zr_{39.5}Ni_{21}$). The results from liquid $Zr_{80}Pt_{20}$ and $Zr_{77}Rh_{23}$ scattering measurements are discussed in Chapter 5.

Because of difficulties in melting large (300 - 450 mg) samples, all successfully melted samples were 90-150 mg in size. Isothermal measurements were performed over 30-60 minutes for sufficient counting statistics. Scattering data for levitated vanadium standards were acquired for 30 minutes each to normalize scattered intensity from the sample to the incident beam spectrum. This will be discussed further in Section 2.9.2. Levitated samples of pure Ni were used to double-check detector position calibrations originally determined from diamond powder standards (Space group $Fd\bar{3}m$, lattice parameter a = 3.5668 Å). A 30 minute scan of the empty chamber was also made to remove background scattering.

2.9 Neutron Diffraction Analysis

While in many ways less complicated than X-ray scattering, there are still a number of corrections required to reduce the measured neutron scattering intensity to a static structure factor, $S(q)$, and pair-distribution function, $g(r)$. Initial reduction of the data acquired during NOMAD 2014 was performed using a sequence of IDL and Python modules developed by the beamline scientist, J. Neuefeind, specifically for the NOMAD beamline [36]. A brief overview of scattering and neutron scattering lengths is presented in Section 2.9.1. A description of the corrections required for neutron diffraction is described in Section 2.9.2, and details on the actual implementation are discussed in Appendix A. Generic IDL scripts useful for future experiments are described in Appendix B and contain more detailed information on each function. Descriptions of custom LabVIEW programs and their relationship to data reduction are described further in Appendix C. The collection of LabVIEW programs used here are included in the supplementary DVD attached with this dissertation.

2.9.1 Neutron Scattering

The structural signal that is extracted from total scattering experiments comes from elastic, coherent scattering, or scattering where the phase relationships in the wave functions of the scattered waves, $\psi(kx - wt)$, are preserved throughout the scattering process. Here, k is the wave number, x is the position, w is the frequency, and t is time. In this process, individual wave functions constructively and destructively interfere with each other resulting in peaks in the measured intensity at specific scattering angles, 2θ. The total coherent scattering wave, Ψ_{coh}, can then be represented as a sum of the amplitudes of the individual scattering waves, or

$$\Psi_{coh} = \sum_i \psi_i \, , \tag{2.25}$$

giving the total measured coherent intensity, I_{coh}, or

$$I_{coh} = \Psi^*_{coh}\Psi_{coh} = \left|\sum_i \psi_i\right|^2 . \tag{2.26}$$

In contrast, incoherent scattering does not maintain the phase relationship between the incident and scattered neutrons. With this change in phase, information regarding the interference of individual wave amplitudes is lost. The incoherent intensity, I_{inc}, is given by

$$I_{inc} = \sum_i I_i = \sum_i \left|\psi_i\right|^2 . \tag{2.27}$$

In the case that all atoms are identical, the incoherent intensity will be identical for each atom and no diffraction information can be extracted.

For the measurements described in this dissertation, all scattering from the sample is assumed to be elastic, where no energy is exchanged between the neutron and the scattering sample. Because neutron energies are comparable to thermal motions in the sample, this assumption is less valid than in the case of high-energy X-ray diffraction measurements [16]. Inelastic neutron scattering results in significant energy transfer, which correspondingly changes the neutron velocities. As a result, inelastically scattered neutrons arrive at the detectors at slightly different times than those scattered elastically, and therefore are assigned an incorrect wavelength. Difficulties in accounting for inelastic scattering are discussed in more detail in Section A.7.

Since neutrons scatter from the nucleus rather than the electron cloud (except in the case of magnetic scattering), there is a dependence on the total nuclear spin in the coherent, σ_c, and incoherent, σ_i, scattering cross sections (typically measured in units of *barns*). Because of this, each element and isotope will have a distinct scattering length, b_c and b_i respectively, for both coherent and incoherent scattering (typically measured in *femtometers*, or *fm*; $1\,barn = 100\,fm^2$). The cross sections are calculated using

$$\sigma_c = 4\pi |b_c|^2 , \quad \sigma_i = 4\pi |b_i|^2 , \tag{2.28}$$

with the total scattering cross section, σ_T, being given by

$$\sigma_T = \sigma_c + \sigma_i . \tag{2.29}$$

The larger the scattering cross section, the higher the probability of interaction. The scattering length, *b*, is a representation of the strength of the scattering and is analogous to the atomic form factor, $f_\mathrm{i}(q)$, in X-ray scattering. However, *b* is a constant for all *q*, because, unlike the distribution of electrons in X-ray scattering, the distribution of nuclear spins is much smaller than the wavelength of typical neutrons used in scattering experiments. These cross sections and scattering lengths vary non-monotonically with nuclear size, and the character of the nuclear interactions can change significantly by simply changing the number of neutrons present in the nucleus [37].

2.9.2 Neutron Corrections

Over time, the power of the proton beam striking the mercury target can vary depending on the ion energy produced by the linear accelerator (Section 2.8.1). Higher power will result in an increased neutron flux, which also results in increased scattering intensity. To account for this, the measured intensities are normalized by the proton charge measured from an upstream monitor. This allows intensity measurements from different scans to be compared on the same scale.

Due to the nature of spallation TOF neutron experiments, the neutron beam consists of a non-uniform distribution of incident neutron energies. The measured scattering intensity from a primarily incoherently scattering sample, such as vanadium, will therefore represent the energy profile of the source spectrum. Since scattering from vanadium is not completely incoherent, any small, residual coherent peaks can be subtracted out and smoothed over, leaving only the profile of the spectrum behind. Once the signal due to scattering from the chamber, I_{Empty}, is removed, the measured intensity from the sample, I_{Sample}, can be normalized to the measured vanadium intensity, I_{V}, at each point in q, correcting for the source spectrum using

$$I_{Normalized} = \frac{I_{Sample} - I_{Empty}}{I_V - I_{Empty}}. \tag{2.30}$$

This normalization has the added benefit of removing the need for detector specific corrections (e.g. pixel efficiency) since both I_{Sample} and I_{V} are measured with the same equipment and the corrections cancel [16].

Self-absorption and multiple scattering, both from the sample and vanadium standard, are significant factors in correcting the measured intensity. The resulting attenuation from self absorption is energy-dependent and is generally tabulated at a constant wavelength. The attenuation coefficients used were measured at a wavelength of $\lambda_{\mathrm{table}} = 1.798$ Å [38], and the energy dependence was assumed to be linear in λ. The absorption cross section at any given λ is then given by

$$\sigma(\lambda) = \sigma \times \frac{\lambda}{\lambda_{table}} . \tag{2.31}$$

Both absorption and multiple scattering corrections also depend on geometry. The geometry is often approximated by simple solutions and is in many cases a fairly accurate assumption. However, the spherical geometry absorption corrections for X-ray scattering using WU-BESL [14, 15] cannot be extended to the geometry of the NESL experiments, since the small size of the X-ray beam relative to the sample greatly simplifies that calculation. Instead, the neutron beam was collimated to span the majority of the 12 mm gap between the top and bottom electrodes during NOMAD 2014, completely covering the entire sample. Geometry- and mass-dependent simulations (designed by J. Neuefeind) were made to generate an estimate of both sample absorption and multiple scattering, which were subsequently applied to correct the data. As with X-ray scattering (Section 2.5), the absorption correction uses the physical dimensions of the sample and estimates the effective scattering volume, *V/V'*. The contribution from multiple scattering, I_2, is then subtracted using

$$I_{Corrected} = \frac{\left(I_{Sample} - I_{Empty}\right)\left(\frac{V}{V'}\right)_{Sample} - I_{2,Sample}}{\left(I_V - I_{Empty}\right)\left(\frac{V}{V'}\right)_V - I_{2,V}} . \tag{2.32}$$

Once the corrected $I(q)$ is obtained, the total static structure factor, $S(q)$, can be calculated in the same manner as in X-ray scattering using

$$S(q) = \frac{I(q) + \langle b \rangle^2 - \langle b^2 \rangle}{\langle b \rangle^2} , \tag{2.33}$$

where $\langle b \rangle^2$ and $\langle b^2 \rangle$ are averaged over each chemical isotope using

$$\langle b \rangle = \sum_i c_i b_i \tag{2.34}$$

and

$$\langle b^2 \rangle = \sum_i c_i b_i^{\,2} \,. \tag{2.35}$$

Here, b_i and c_i are the scattering length and atomic percent of the i^{th} chemical species. This is equivalent to the average atomic form factor used in X-ray scattering, $< f(q) >$ (Eqns. 2.8-2.9).

The initial $S(q)$ generated using the above corrections was frequently found to contain curvature that resulted in small-r ripples occurring at unphysically small distances. These ripples primarily result from inelastic scattering and experimental noise, which corrupt the data. Even when this curvature is correctly accounted for, the data still suffer from poor amplitude normalization. Secondary scattering from the environment can cause issues with proper normalization, resulting in features in $g(r)$ that do not reflect physical behavior. By constraining to physical parameters such as the experimental density, the data can be reduced to an absolute scale and effectively compared with other experimental measurements. In order to correct for these effects, a more technical discussion is necessary. Details of the method used to account for these effects, as well as the practical implementation of all of the above discussed corrections, are presented in detail in Appendix A (in particular, Section A.7).

2.10 Atomic Simulations and Structural Analysis

The experimentally measured $S(q)$ and $g(r)$ are one-dimensional time-averaged representations of a dynamic three-dimensional structure. As such, all phase information is lost during data reduction. While providing a time-averaged picture of the sample's overall structural characteristics, exact atomic locations and dynamics are lost. There are several methods that can be used to extract atomic configurations to study the details of atomic interaction. Molecular Dynamics (MD) simulations employ first principle approaches for atomic interactions with realistic atomic potentials (*ab initio* [39-41]), or classical approaches using embedded atom interactions [42, 43]. Once the configuration has stabilized, the $g(r)$ can be directly calculated from the atomic ensemble. These simulations are very computationally intensive, limiting *ab initio* simulations to small configuration sizes. However, the embedded atom method has shown large improvements in configuration sizes in recent years [44]. The latter simulations require carefully constructed atomic potentials to achieve consistent results, which are of limited availability.

Another simulation method, the Reverse Monte Carlo (RMC) technique [45], uses experimentally determined structures to constrain the simulation. Since this produces results that are consistent with experiment, this method was chosen for the analysis of atomic configurations used in this dissertation. This method is not without disadvantages, however. Details of the RMCs used in this dissertation, as well as the inherent advantages and disadvantages, are discussed in Section 2.10.1. Structural classification schemes based on the resulting atomic configurations are discussed in Sections 2.10.2 and 2.10.3.

2.10.1 Reverse Monte Carlo (RMC)

The Reverse Monte Carlo (RMC) technique [45] randomly adjusts individual atomic positions within a large ensemble of atoms until the calculated scattering pattern agrees with experimentally measured data. In this manner, the technique produces an atomic configuration that is consistent with experimental observations. It is similar to the Metropolis Monte Carlo, but in RMC the difference between experimental and calculated structure factors is minimized rather than the potential energy. Many different types of experimental data can be used to constrain the simulation including X-ray diffraction, neutron diffraction, and Extended X-ray Absorption Fine Structure (EXAFS) measurements. RMC simulations can also be constrained to chemically specific structural data if partial pair-distribution functions (PPDFs) are known, either from experimental determination or MD results. Since the RMCs in this dissertation were constrained with total static structure factors measured from X-ray and neutron scattering, the RMC method will be discussed in this context.

For a typical RMC simulation, a random initial atomic configuration of N atoms is generated with appropriate stoichiometric ratios in a box of a size that is consistent with the atomic density. The initial total structure factor, $S_i(q)$, is calculated from this initial configuration and a χ^2 is calculated with respect to the experimental input, $S_\mathrm{E}(q)$ using

$$\chi_i^2 = \frac{\sum_k \left[S_i(q_k) - S_E(q_k)\right]^2}{\sigma_i^2} . \tag{2.36}$$

Here, σ_i is the uncertainty of the experimental data set. A single atom's position is adjusted within user defined limits, and the final structure factor, $S_\mathrm{f}(q)$, is calculated from this new configuration. If $\chi_f^2 < \chi_i^2$, the move is accepted. If $\chi_f^2 \geq \chi_i^2$, the new position is accepted with a probability of $\exp\left(-\left(\chi_f^2 - \chi_i^2\right)\right)$. Otherwise, the move is rejected.

The RMC technique produces the most disordered configuration that is consistent with the experimental data. As a consequence, the atomic configuration generated by a single RMC is not unique. To account for this, the simulations were repeated multiple times in order to produce multiple independent configurations and gain a measure of the statistical uncertainty in the results.

Additionally, this technique can produce unphysical results if too few constraints are used. An n component alloy requires at least $n(n+1)/2$ inputs to fully constrain all PPDFs. When too few constraints are used, the simulated chemical arrangement of atoms within the ensemble is less reliable. Despite this, the topological distribution of atoms can still be used to study structure independent of chemistry, as is done in Chapter 3.

The RMCs in Chapter 5 were performed using RMC_POT [46]. RMCs from Chapter 3 were performed using RMCA, a more primitive version of the RMC_POT code, and the particular details associated with its analysis are discussed in Section 3.2 and elsewhere [2]. Since our understanding and experience with this technique has improved since using RMCA, the details discussed below are specific to the RMC_POT analysis performed in Chapter 5, though the principles and implementation are very similar in both programs. For more information on input and output file formatting for RMC_POT, see the user guide available on the web at http://www.szfki.hu/~nphys/rmc++/opening.html.

Each simulation was run for approximately 60 hours until the final χ^2 converged to a minimum value. This value was recorded as a function of time and checked for each individual run to ensure that a stable configuration was achieved. The absolute value of the χ^2 depends on the individual σ_i assigned to each input constraint. In this dissertation, the high-energy X-ray $S(q)$s were believed to have the smallest uncertainty and were given a lower σ ($\sigma_X = 0.002$) than the MD partials and neutron structures ($\sigma_{MD} = \sigma_N = 0.005$). This ensured that the final configuration more closely resembled that of the most precise experimental data. When both X-ray and neutron experiments were used to constrain the simulation, the effective density was calculated using the average of the temperatures for each experiment. The liquid density was measured *in situ* using non-contact methods as described in Section 2.3.2.

When constrained by a full set of MD PPDFs, the hard-sphere cutoffs can be determined from the minimum before the first peak in the PPDFs. Since the simulations were constrained with inputs from both X-ray and neutron data rather than all MD partials, the hard-sphere cutoffs were set slightly lower than anticipated from atomic size considerations in order to not bias the final experimental result. In addition to preventing unphysically short atomic distances, the hard-sphere cutoffs serve to speed up the simulation by preferentially moving atoms located below the cutoff distance. In the simulations performed in this dissertation, the maximum distance any atom was allowed to move per step was 0.3 Å on a grid with a spacing of 0.06 Å. This *r*-spacing was chosen since it was the same *r*-spacing as the MD partials used as constraints. A small fraction of the atomic moves (10%) were allowed to swap particles wherein an atom of type A exchanged positions with an atom of type B. This improved mixing and helped reduce the convergence time. Additional details of the RMC_POT program and its implementation are discussed elsewhere [2, 35, 46].

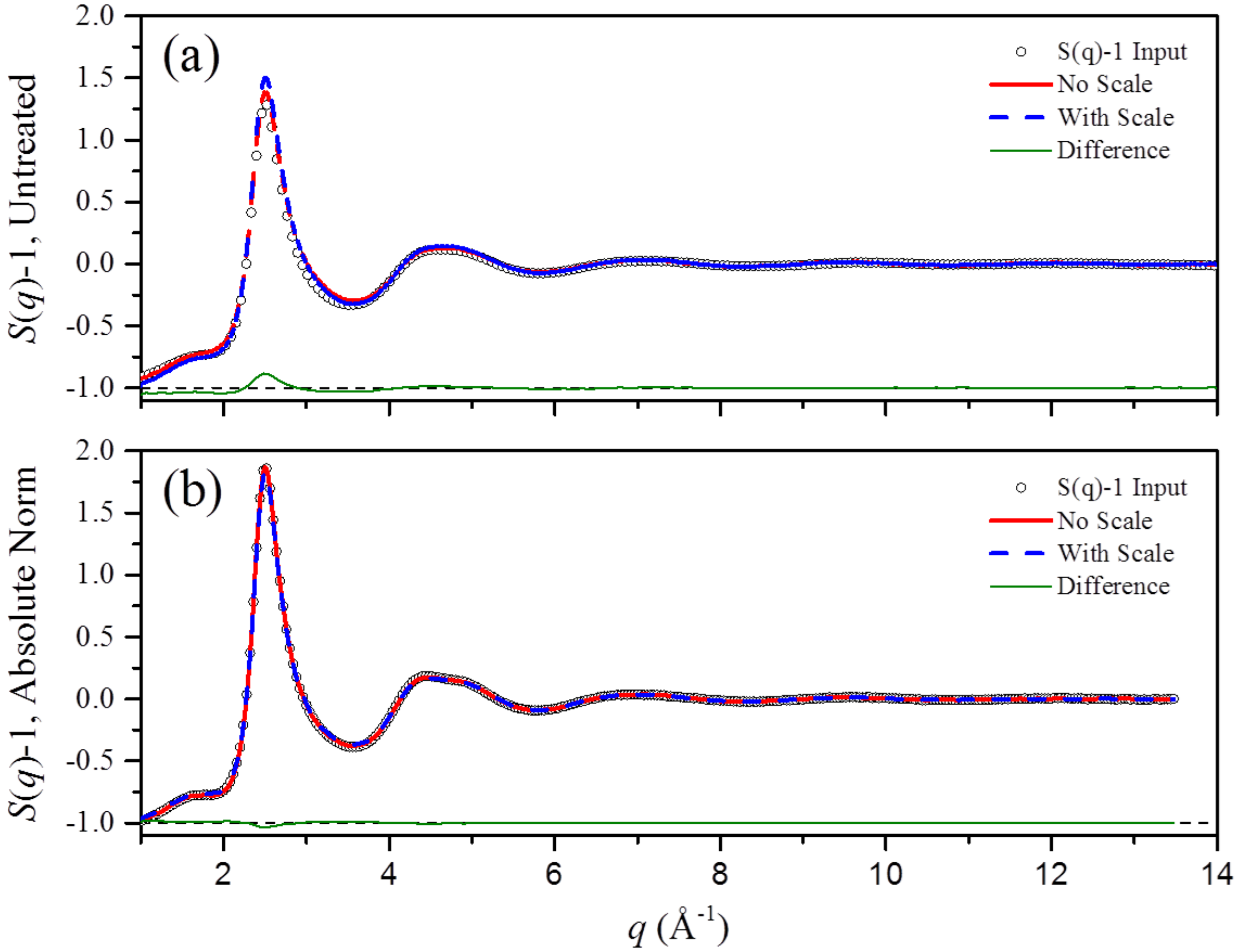

Figure 2.15 (a) RMC simulation results for $Zr_{80}Pt_{20}$ using only experimental X-ray constraints without absolute normalization and (b) RMC simulation results for $Zr_{80}Pt_{20}$ using absolute normalization. The open symbols are the experimental inputs, the red lines are the fits when no multiplicative or additive scaling factors were used, and the dashed blue lines are the fits when both scaling factors were used. Large differences are observed when scaling factors are turned off or on when the experimental $S(q)$s are not corrected for curvature and absolute scaling. Much better agreement is found between converged RMC structures when they have been corrected for curvature and scaling (difference curves in green, offset by -1 for clarity. A dashed black line at -1 guides the eye).

One of the primary differences between the simulations performed in Chapter 3 and Chapter 5 is that the former required implementing multiplicative and additive scaling factors during the simulation in order to produce $S(q)$s that were consistent with experiment. No such adjustments were required for consistent results in Chapter 5. This is primarily because the experimental $S(q)$s used in Chapter 3 were not expressed on the absolute scale, described in Section A.7, since the technique for doing so is fairly new. To test this using RMC_POT, simulations were performed using $Zr_{80}Pt_{20}$ X-ray $S(q)$s that were not corrected for absolute intensity and were compared with simulation results from those that were. In both cases, all three available MD partials were also used as constraints. Additionally, separate simulations were performed with and without a multiplicative scale factor. For simulations without curvature and normalization corrections (Figure 2.15 (a)), the experimental data could not be consistently reproduced. Using a multiplicative scaling factor during the simulation produced results that were significantly different than when no scaling factor was used (difference curve in Figure 2.15 (a)). The fits, when constrained with an $S(q)$ with absolute normalization, showed much better agreement with experiment and the simulated structure factors showed very little difference whether or not a scaling factor was employed (Figure 2.15 (b)). This is additional evidence that the technique described in Section A.7 consistently reduces data to an absolute scale.

2.10.2 Honeycutt-Andersen (HA) Analysis

Honeycutt-Andersen (HA) analysis is a technique used to describe the local environment around a given pair of atoms (called the root pair) in an atomic configuration [47]. It is similar to common neighbor analysis (CNA) [48], but incorporates an additional integer to designate if the root pair are bonded or not and replaces the last integers with an arbitrary number used to eliminate degenerate results. The HA index is comprised of four integers: $ijkl$. For every atom in the ensemble, all potential neighbors are considered. The integer i represents how close the specified root pair is. In other words, $i = 1$ indicates that the root pair of atoms are nearest neighbors, $i = 2$ suggests the second atom is located in the second coordination shell and not bonded to the first (second nearest neighbors), etc. In practice, values of $i > 2$ are rarely considered, and typically only the nearest-neighbor pairs are of interest. The integer j represents the number of common nearest neighbors shared by both atoms in the pair. The integer *k* represents the number of bonds shared between each of the *j* common neighbors. Finally, the integer *l* is used to break degeneracies. It is possible that unique configurations might share the first three numbers, so each unique configuration is assigned a distinct *l* value.

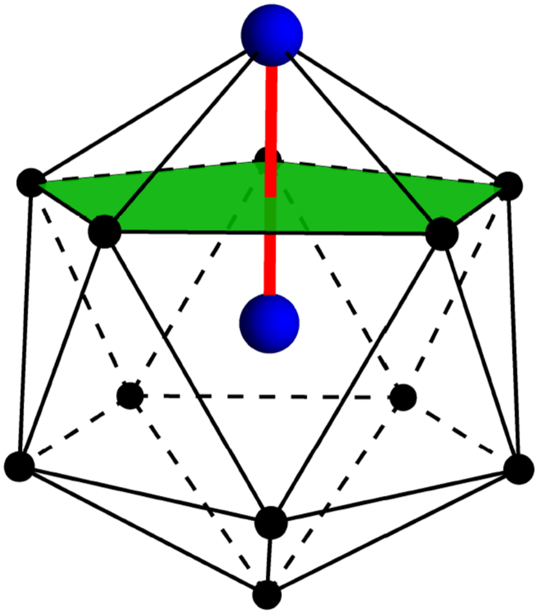

Figure 2.16 Example of the 1551 index in a perfect icosahedron, constituting a pentagonal bipyramid. The root pair of *i=1* is distinguished by the two blue atoms connected by a red line. The *j*=5 shared neighbors are located at the vertices of the green polygon, and the *k*=5 bonds among those atoms are represented by the edges of the green polygon. The central atom is bonded with every other atom, but the bonds are not displayed in order to improve visualization.

These indices can be used to identify the prevalence of particular local atomic environments, such as a fragment of a perfect icosahedron (pentagonal bipyramid) with a central atom. In this case, the bond geometries are represented by the index 1551, indicating the pair of atoms are each bonded to the same 5 atoms which share 5 bonds amongst themselves. Visually, this can be represented by the cap of an icosahedron (Figure 2.16). Distorted icosahedra can be visualized by forcing one of the neighbor atoms to be slightly farther away from the rest, breaking one of the *k*=5 bonds and creating a 1541 geometry *k*=4). If an atom is completely removed such that it is no longer a neighbor to either the root pair or the other surrounding atoms, it becomes 1431. Some common crystalline indices include the body-centered cubic (BCC, 1661), face-centered cubic (FCC, 1421), and hexagonal close packed (HCP, 1422).

It is important to note some of the limitations of this technique. While a 1551 pair represents the cap of an icosahedron, it does not guarantee that the rest of the surrounding structure is consistent with an icosahedral environment. In order to represent a perfect icosahedral structure, the central atom must have a total of twelve 1551 structures associated with it, one formed with each vertex. An MD study of Zr_2M (M=Co, Ni, Cu, and Ag) metallic liquids found that, while the 1551 index was highly prevalent, the majority of atoms only contained 2-3 of these structures on average [49]. When distorted icosahedral structures were also considered (1551 + 1541 + 1431), the average number of these configurations surrounding an individual atom increased to 6-8 with a sizeable fraction (5-10%) of atoms involved in 12. While these indices suggest small pieces of the ensemble contain common configurations, HA analysis alone does not provide a full picture.

2.10.3 Voronoi Tessellation

Voronoi tessellation is a technique used to determine the nearest neighbors of a given central atom [50-52]. Planes are drawn bisecting the lines between a central atom and the atoms surrounding it. The volume nearest to the central atom contained within these bisecting planes is known as the Voronoi cell. It is calculated in the same manner as a Wigner-Seitz primitive cell in reciprocal space. A 2-dimensional example is displayed in Figure 2.17. An atom is considered to be a neighbor if its Voronoi cell shares a face (3D) or edge (2D) with the cell of the central atom. In the case of Figure 2.17, atoms A and B clearly have an edge connecting their cells while the line bisecting atoms A and C disappears as closer atoms cut into it. An example of a 3-dimensional Voronoi cell is displayed in Figure 2.18. When the atomic configuration contains only one species, or when all atomic sizes are approximately the same, this technique, as described above, produces an accurate picture of the local atomic coordination. When there is a large atomic size mismatch, the bisecting planes should instead be calculated relative to the surface of the atom, rather than the center of mass. Failure to account for this can result in planes cutting through the larger atom rather than between the two atoms. Because of this, weighted Voronoi methods have been developed [53].

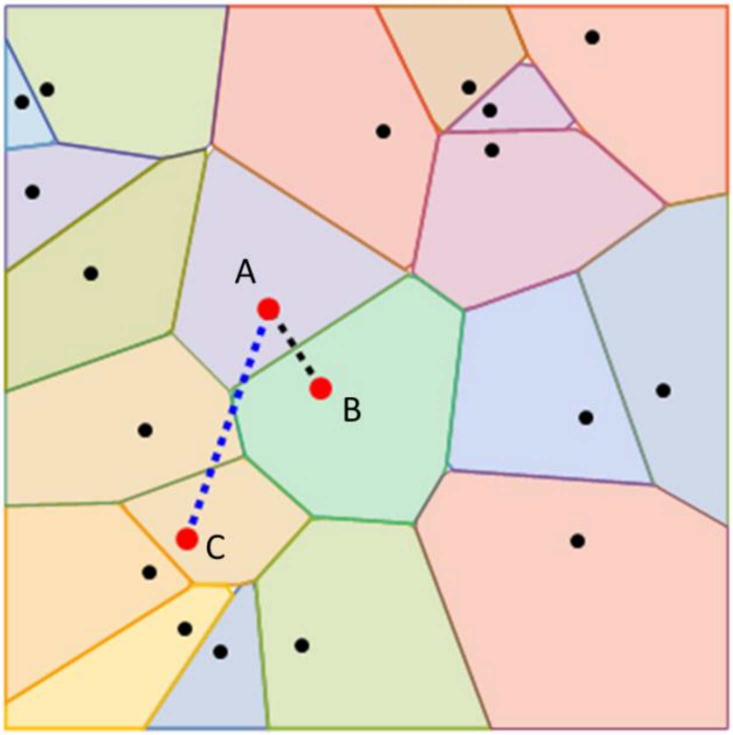

Figure 2.17 A 2D example of constructing a Voronoi cell. A line is drawn bisecting a line connecting each atom (For example, the dashed lines between atoms A and B (black) and A and C (blue)). When all lines are drawn, A and C are clearly not considered neighbors as the enclosed cell around each atom does not share an edge.

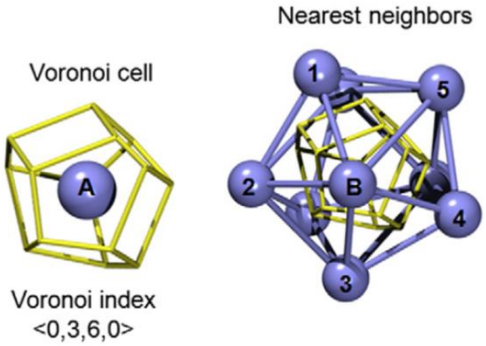

Figure 2.18 Example Voronoi cell for the <0,3,6,0> index (left, yellow bars) for the atomic arrangement on the right. The numbered atoms represent the nearest neighbors shared between the central atom (A) and vertex atom (B) corresponding to an HA index of 1551. Reprinted with permission from [54].

The Voronoi cells are indexed by counting the number of edges of each of the faces on the resulting Voronoi polyhedra. The index is listed in the format $<n_3, n_4, n_5, n_6, \ldots>$ where n_3 is the number of faces with 3 edges, n_4 is the number of faces with 4 edges, etc. The Voronoi cell for a perfect icosahedron, for example, contains twelve faces, each with 5 edges, and can be represented by the index <0 0 12 0>. Since each face corresponds to a neighboring atom, the coordination number (CN) can be uniquely determined from the total number of faces in the Voronoi cell, or by summing up all of the elements in the Voronoi index.

While a large variety of Voronoi indices (VI) typically appear in a disordered liquid, atoms will typically attempt to maximize the polytetrahedral packing according to their atomic size [54]. This ideal packing is characterized by the Frank-Kasper (FK) polyhedra [55] which, for each CN, represents the greatest polytetrahedral packing efficiency. For CN 12, the ideal packing is the icosahedron (<0 0 12 0>). Each FK polyhedron attempts to maximize the 5-sided faces, but disclinations (rotational defects) are necessary to relieve packing frustration resulting in additional 4- and 6-sided faces that must follow the rule $2n_4 + n_5 = 12$. This is typically resolved by removing two n_5 faces and turning them into an n_4 and n_6 pair. The ideal FK polyhedrons for CN 9-16 are listed in Table 2.2. Note that all contain either n_4 or n_6 disclinations, other than CN 12, for idealized local packing.

Table 2.2 Frank-Kasper polyhedra for different CN.

Coordination Number (CN)	**Voronoi Index (VI) for $n_3 – n_7$**	**VI for single disclination**
9	<0 3 6 0 0>	<0 4 4 1 0>
10	<0 2 8 0 0>	<0 3 6 1 0>
11	<0 2 8 1 0>	<0 3 6 2 0>
12	<0 0 12 0 0>	<0 2 8 2 0>
13	<0 1 10 2 0>	<0 2 8 3 0>
14	<0 0 12 2 0>	<0 1 10 3 0>
15	<0 0 12 3 0>	<0 1 10 4 0>
16	<0 0 12 4 0>	<0 1 10 5 0>

While the FK polyhedra represent ideal packing for a given cluster of hard spheres, in the highly disordered liquid and glass structures studied in this dissertation, it is very uncommon to find these VIs in great prevalence. Due to high disorder and rapid dynamics in the liquid, additional disclinations are required to relieve packing stress. These additional disclinations, on top of the ones necessary for the ideal cases, must also follow the $2n_4 + n_5 = 12$ rule. The VIs for the first distortions of CN 9-16 are also listed in Table 2.2. Higher-order distortions are also frequently observed in disordered systems, and additional details can be found elsewhere [35, 54].

In this dissertation, the program Voro++ was used to perform a Voronoi tessellation on the atomic configurations generated from RMC simulations described in Section 2.10.1 [56]. In order to use Voronoi analysis techniques consistent with other recently published results [44], additional custom modifications were performed by V. Tran at Washington University in St. Louis. In some atomic configurations, faces with a very small area can appear. This represents the inclusion of atoms that are slightly farther away than the rest of the coordination shell. In a dynamic liquid, these atoms will be constantly moving around and likely spend very little time bonded to the central atom. Including these small faces artificially inflates the coordination number. In order to account for this, the ability was added to remove faces that were smaller than some specified absolute area. In this dissertation, atoms with a face area smaller than 0.25 $Å^2$ were removed from consideration as a neighbor. The atomic radii that were used for weighted Voronoi tessellation were the Goldschmidt radii. A copy of the program used is included in a DVD of supplementary materials associated with this dissertation.

2.11 Crystal Diffraction Pattern Analysis

Crystalline diffraction patterns are often identified and characterized throughout this dissertation, with emphasis placed on the metastable phase identification of $Zr_{77}Rh_{23}$ (Chapter 6). Some preliminary analysis was performed using the rapid reduction algorithms of the Jade analysis software from MDI before the free trial expired (www.materialsdata.com). The final phase identification and fitting was performed using the python-based General Structure and Analysis Software II (GSAS II) [57], a user friendly redesign of the original software, GSAS [58], developed by the same authors at the APS.

2.11.1 Phase Information

While the primary focus of this dissertation is the study of disordered liquid and glasses, it is often enlightening to identify the crystallization products that form during devitrification and recalescence. However, identification of crystalline phases can be very challenging without prior knowledge of the possible accessible phases. Completely unknown phases can be identified and categorized using transmission electron microscopy (TEM) and other characterization techniques, but the details of these methods are beyond the scope of this dissertation. Instead, knowledge of the equilibrium phase diagram and what phases to expect at a given temperature is the primary tool used to identify crystallization products.

A crystalline lattice can be defined by three unique lattice vectors (a, b, and c) and the angles formed between them (α, β, and γ) (Figure 2.19). The relative lengths of these lattice vectors and the angles formed between them determine the symmetries allowed within the structure. The example in Figure 2.19 is a Primitive lattice (P, Figure 2.20 (a)) with 8 atoms positioned at the vertices of a cube. In this case, $a = b = c$ and $\alpha = \beta = \gamma = 90^o$.

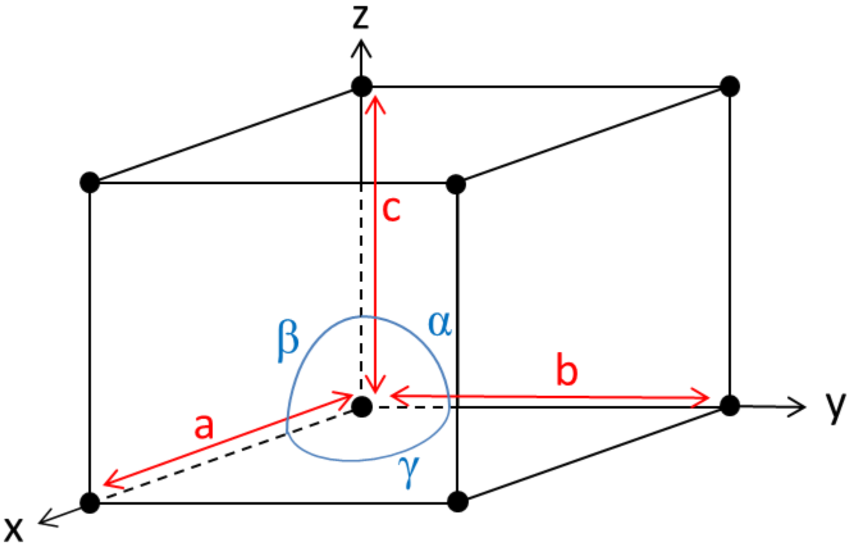

Figure 2.19 Example primitive lattice. Lattice distances are denoted by a, b, and c (red) and the angles between them by α, β, and γ (blue).

Additional atoms can be added to the primitive lattice to generate different symmetries. There are three "centering" methods by which atoms are placed in the center of some part of the Primitive lattice (Figure 2.20). A Face Centered (F) lattice is made by placing 6 additional atoms within the primitive lattice at the center of each face (Figure 2.20 (b)). A Body Centered (I, from the German *Innenzentriert*) lattice is made by adding a single atom at the very center of the primitive lattice such that it is equidistant from each vertex (Figure 2.20 (c)). The Base Centered

(C) lattice adds only two additional atoms to the primitive lattice (Figure 2.20 (d)). It is similar to the FCC lattice in that these atoms are placed in the center of faces, but only a single pair of opposite faces will contain these atoms. An additional "centering" scheme is Rhombohedral (R), but no additional atoms are added to the cell. Instead α, β, and γ are each adjusted such that they are all equal, but not equal to 90^{o}, while keeping $a = b = c$. This is also sometimes called a P lattice, but its use is not consistent.

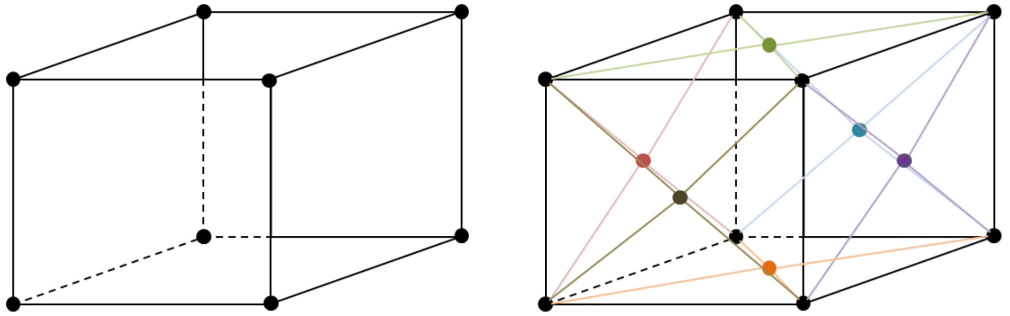

(a) Primitive – P

(b) Face Centered – F

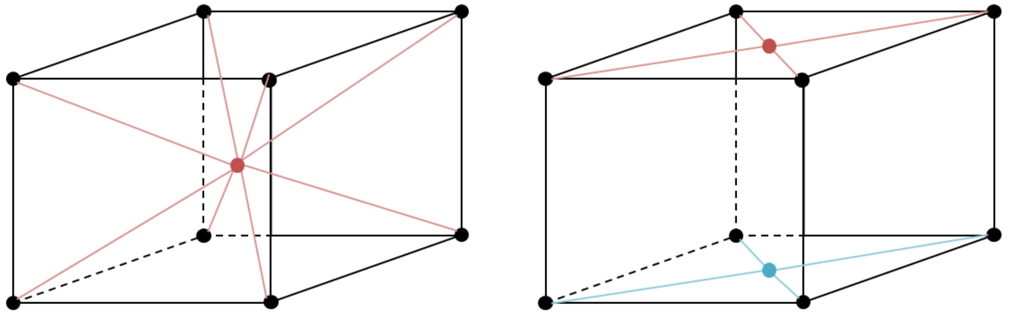

(c) Body Centered – I

(d) Base Centered – C

Figure 2.20 The four lattice "centering" schemes. (a) Primitive (P) is a cube or rectangle. (b) Face Centered (F) has an atom at the center of each face of the P lattice. (c) Body Centered (I) has an interior atom equidistant from each lattice point in the P lattice. (d) Base Centered (C) has an atom in the center of two opposite faces.

Thus far, only cubic symmetries have been discussed. In other words, all lattice parameters are equal and all angles between them are 90^{o}. A total of 14 *Bravais* lattices can be described by using the centering schemes (P, F, I, C, R) and allowing the lattice parameters (a, b, c) and angles (α, β, γ) to vary (Table 2.3). Some centering schemes are redundant when used on multiple different base lattices. The Bravais lattices are the smallest number that can be used to uniquely describe any crystalline symmetry.

Table 2.3 Basic lattices and their allowed centering schemes.

Base Lattice	Centering Schemes	Lattice Parameters	Lattice Angles
Cubic	P, I, F	$a=b=c$	$\alpha = \beta = \gamma = 90^o$
Tetragonal	P, I	$a=b\neq c$	$\alpha = \beta = \gamma = 90^o$
Orthorhombic	P, I, F, C	$a\neq b\neq c$	$\alpha = \beta = \gamma = 90^o$
Hexagonal	P	$a=b\neq c$	$\alpha = \beta = 90^o$, $\gamma = 120^o$
Rhombohedral	R or P	$a=b=c$	$\alpha = \beta = \gamma \neq 90^o$
Monoclinic	R, C	$a\neq b\neq c$	$\alpha = \gamma = 90^o$, $\beta \neq 90^o$
Triclinic	P	$a\neq b\neq c$	$\alpha \neq \beta \neq \gamma \neq 90^o$

Crystalline phases can be identified by their *space group*, which contains information regarding the symmetries within a given atomic arrangement. There are several notable notation schemes such as the Schönflies notation (most commonly used to describe molecular symmetries in spectroscopy), but the primary labeling used in this dissertation is the International (also known as Hermann-Maugin) notation. In the International notation, the label is based on the type of Bravais lattice the structure represents. Depending on the arrangement of atoms within the overall Bravais lattice, 230 individual space groups can be identified. The centering scheme can be determined at a glance: the first character is always a letter corresponding to the centering scheme (Figure 2.20). Additional numbers and letters are used to describe the rotation axes (e.g. *3* for a $360^o/3$ rotation or *-3* (or $\bar{3}$) for an improper rotation of the mirror image), mirror planes (m), glide planes (a, b, c, n, d) and screw axes (numerical subscript after a rotation. e.g. 2_1 is a *2*-fold rotation followed by a translation of ½ the lattice vector). For example, table salt (NaCl) contains a pair of inter-penetrating face centered cubic (FFC) lattices with a space group of

$Fm\bar{3}m$ (Figure 2.21). From its space group it is immediately apparent that this structure contains face centered symmetries with a pair of mirror planes as well as a *3*-fold improper rotation.

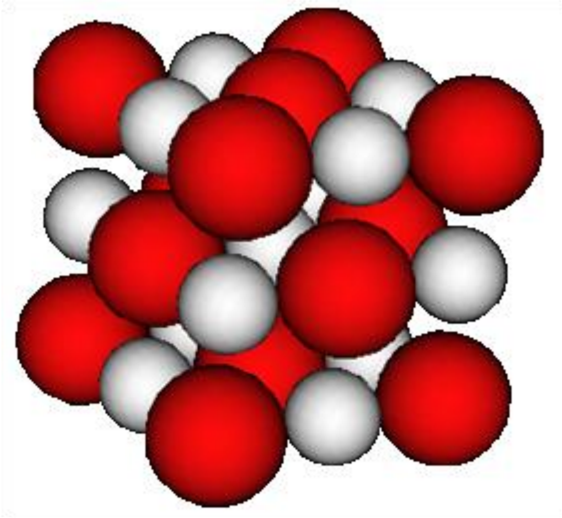

Figure 2.21 Example of table salt, NaCl, with a space group of $Fm\bar{3}m$. Na is represented by the red atoms and Cl by white. It is composed of two inter-penetrating FCC lattices. Plot generated using GSAS II [57].

If the space group is known, the symmetries at any generic point within the unit cell are also known. In other words, if an atom is located at (x, y, z) within a unit cell, the symmetries present in the space group will determine how many more atoms must be present and where they must be located. In the case of a 96 atom unit cell, this greatly reduces the amount of work required to completely reconstruct the entire lattice. Specific lattice sites will have certain allowed symmetries and knowledge of a single one of those points allows the remainder to be filled in. These symmetry sites are known as the *Wyckoff Positions*. They are designated by a number and a letter, where the number represents the multiplicity and the letter specifies the unique symmetries associated with the position (e.g., 4a). These start at *a* and increment up. In the above case of NaCl, there are a total of 27 individual atoms in the unit cell, but only two individual atomic positions are required to populate the full lattice. A Na atom is placed at (0, 0, 0) (the origin, located in the back corner; Wyckoff position 4a) and a Cl atom is placed directly in the center at (½, ½, ½) (Wyckoff position 4b). The individual atomic positions are fractions of the lattice parameter in the *x*, *y*, and *z* directions. The Wyckoff positions for each space group have been tabulated and are available on the web at: http://www.cryst.ehu.es/cgi-bin/cryst/programs/nph-wp-list [59-61].

A compilation of known phases for metallic alloy systems is published in Pearson's Handbook of Crystallographic Data for Intermetallic Phases [62]. Most of the time, the phases of interest are contained therein. However, metastable phases are often not listed, or phases that form under very restrictive conditions.

2.11.2 Phase Identification in GSAS II

All phase identification was performed using the Python-based GSAS II software [57]. The analysis begins with a measured intensity profile, $I(q)$. Since the positions of the diffraction peaks can be used to fingerprint phases, fully correcting the intensities is of less importance as the measured peak positions are typically well defined. In powder diffraction studies (Section 2.2), the raw output from the Rigaku acquisition is already in the form of a 1D intensity curve as a function of scattering angle, 2θ.

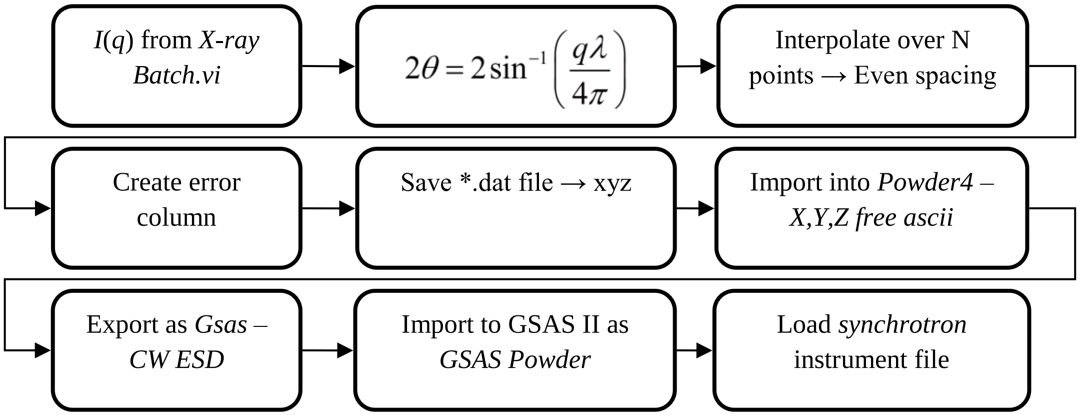

Figure 2.22 Steps required to convert synchrotron *I*(*q*) into a properly formatted *I*(*2θ*) for analysis in GSAS II.

The X-ray batch LabVIEW analysis package [14] can save the intermediate *I*(*q*) during data reduction. Typically crystallographic analysis is done as a function of *2θ* rather than *q*, so the synchrotron *I*(*q*) is converted to I(*2θ*) using the known X-ray energy (Section 2.4) and the inverse of Eqn. 2.4. In order to properly prepare *I*(*q*)s for importing into GSAS, they were first imported into Origin and converted from *q* to 2*θ* (Figure 2.22). The Origin function *Analysis → Mathematics → Interpolate/Extrapolate* was used to re-sample the input *I*(*2θ*) and force an even spacing which is required for importing into GSAS II using the *GSAS-CW ESD* format. An error column was created with relative error of 1%, but this was purely for formatting purposes. The error value is not used in the phase identification. *2θ*, *I*(*2θ*), and 1%Err columns were saved into a *.dat file and then imported into a free program, *Powder4* (http://www.ccp14.ac.uk/tutorial/powder/xyw_to_gsas_esd.html). This program was written by N. Dragoe in order to simplify the process of converting between file formats from various diffraction analysis programs. *I*(*2θ*) was imported using *File → Open → X, Y, Z free ascii* mode. The file was then be exported using *File → Gsas – CW ESD* and saving it as **.gsa* or **.gsas*.

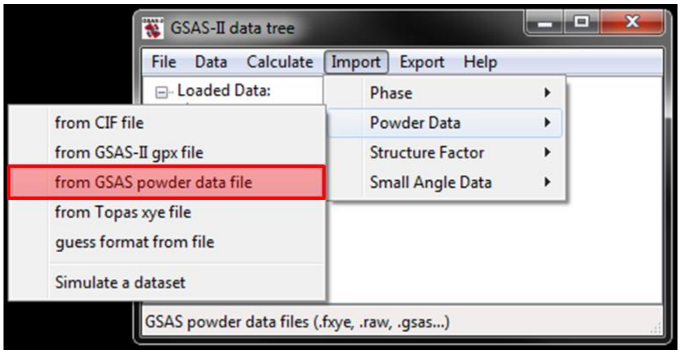

Figure 2.23 Importing into GSAS II.

Once the file was successfully converted to a properly formatted **.gsas* file, it was imported into GSAS II (Figure 2.23) as a *GSAS powder* type file. After loading, GSAS asks to load an instrument parameter file. If *Cancel* is selected, it provides a number of options that relate to various types of instruments such as CuK_α which was used for Rigaku powder files, time-of-flight (TOF), and 0.7 Å synchrotron data. If the latter option is selected, the wavelength can be updated to the value used to acquire the data (Figure 2.24)

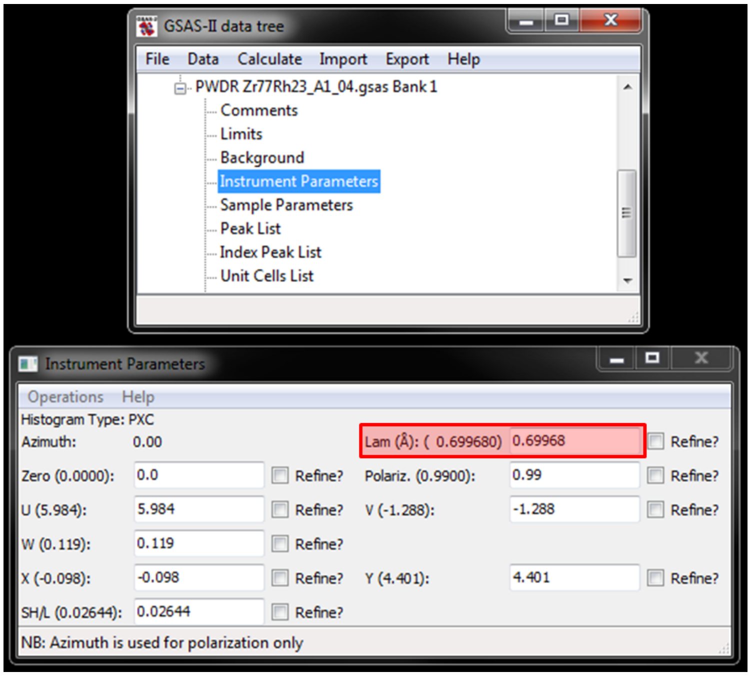

Histogram Type: PXC
Azimuth: 0.00
Lam (Å): (0.699680) 0.69968 ☐ Refine?
Zero (0.0000): 0.0 ☐ Refine?
Polariz. (0.9900): 0.99 ☐ Refine?
U (5.984): 5.984 ☐ Refine?
V (-1.288): -1.288 ☐ Refine?
W (0.119): 0.119 ☐ Refine?
X (-0.098): -0.098 ☐ Refine?
Y (4.401): 4.401 ☐ Refine?
SH/L (0.02644): 0.02644 ☐ Refine?
NB: Azimuth is used for polarization only

Figure 2.24 Adjusting the experimental X-ray wavelength.

In order to identify the phase or phases that formed within the sample, representative diffraction patterns can be calculated within GSAS II based on known space groups, lattice parameters, and atomic lattice sites. Since this is all done with standard procedures within GSAS II, the details will not be covered here. User tutorials and guides can be found at the project home page (https://subversion.xor.aps.anl.gov/trac/pyGSAS).

In order to determine whether or not a chosen phase was consistent with the experimental data, at least one variable must be selected to be free to refine. The first attempts typically use the lattice parameters and relative phase fractions. The refinement is begun using *Calculate → Refine* from the main menu. If a test-phase is going to fit the input data, it will typically be immediately obvious, with the majority of the calculated peaks matching the position of features from the experimental data. If large shifts of lattice parameters are required for the fit to match the data (±0.5 Å), it is likely not a good match unless large atomic size mismatches are observed.

In some situations, a selected phase will very closely match the experimental data with the exception of relative peak amplitudes. During crystallization, as well as when crushing samples into powder, some larger crystallites can form with a preferred orientation, breaking the isotropic assumption. This can be accounted for by allowing *preferred orientation* parameters to be adjusted. Within GSAS II, up to 20 orders of s*pherical harmonics* were refined.

The Rietveld refinement minimizes the difference between the experimentally observed intensity, Y^{obs}, and the calculated curve, Y^{calc}, given by:

$$Y_i^{calc} = I_{b,i} + \sum_{l=1}^{p} k_l \sum_{j=1}^{m} I_j y_j(x_j) \tag{2.37}$$

at each point in 2θ, i. $I_{b,i}$ represents the background at that point, the sum over l covers the number of phases, p, being used to fit the data, k_l is the phase scale factor for the l^{th} phase, and the sum over j covers all m Bragg reflections that contribute to the intensity at point i. I_j is the total intensity from the j^{th} Bragg peak and $y_j(x_j)$ is a function that represents the shape of the peak. The goodness of fit is calculated using a weighted profile residual factor,

$$R_{wp} = \left[\frac{\sum_{i=1}^{n} w_i \left(Y_i^{obs} - Y_i^{calc} \right)^2}{\sum_{i=1}^{n} w_i \left(Y_i^{obs} \right)^2} \right]^{\frac{1}{2}} \times 100\% , \tag{2.38}$$

where $w_i = \left(Y_i^{obs} \right)^{-1}$. A fit is typically considered *good* if $R_{wp} < 10\%$. High measured background can artificially reduce this value since it is easy to subtract out, so careful judgment should be used in order to determine quality of fit. For further information regarding the Rietveld method, see [63].

2.12 References

[1] M.E. Blodgett, *Thermophysical Properties and Structural Evolution of Supercooled Metallic Liquids*, Ph.D. Thesis, Washington University in St. Louis (2015).

[2] N.A. Mauro, *Structural and Thermophysical Property Studies of Metallic Liquids and Glasses Using the Beamline Electrostatic Levitation Technique*, Ph.D. Thesis, Washington University in St. Louis (2011).

[3] A.K. Gangopadhyay, G.W. Lee, K.F. Kelton, J.R. Rogers, A.I. Goldman, D.S. Robinson, T.J. Rathz, R.W. Hyers, *Review of Scientific Instruments* **76**, 073901 (2005).

[4] N.A. Mauro, K.F. Kelton, *Review of Scientific Instruments* **82**, 035114 (2011).

[5] J.C. Bendert, *Thermophysical and Structural Measurements of Liquid Metallic Alloys Using Electrostatic Levitation*, Ph.D. Thesis, Washington University in Saint Louis (2013).

[6] T. Meister, H. Werner, G. Lohoefer, D.M. Herlach, H. Unbehauen, *Control Engineering Practice* **11**, 117 (2003).

[7] M.A. Khan, C. Allemand, T.W. Eagar, *Review of Scientific Instruments* **62**, 392 (1991).

[8] R.C. Bradshaw, D.P. Schmidt, J.R. Rogers, K.F. Kelton, R.W. Hyers, *Review of Scientific Instruments* **76**, 125108 (2005).

[9] S.K. Chung, D.B. Thiessen, W.-K. Rhim, *Review of Scientific Instruments* **67**, 3175 (1996).

[10] T. Ishikawa, P.-F. Paradis, S. Yoda, *Review of Scientific Instruments* **72**, 2490 (2001).

[11] R.W. Hyers, R.C. Bradshaw, J.R. Rogers, T.J. Rathz, G.W. Lee, A.K. Gangopadhyay, K.F. Kelton, *International Journal of Thermophysics* **25**, 1155 (2004).

[12] W.-K. Rhim, K. Ohsaka, P.-F. Paradis, R.E. Spjut, *Review of Scientific Instruments* **70**, 2796 (1999).

[13] J.C. Bendert, K.F. Kelton, *Journal of Non-Crystalline Solids* **376**, 205 (2013).

[14] J.C. Bendert, N.A. Mauro, K.F. Kelton, *Journal of Applied Crystallography* **46**, 999 (2013).

[15] J.C. Bendert, M.E. Blodgett, K.F. Kelton, *Acta crystallographica. Section A, Foundations of crystallography* **69**, 131 (2013).

[16] T. Egami, S.J.L. Billinge, *Underneath the Bragg Peaks - Structural Analysis of Complex Materials*, Pergamon, 2003.

[17] A.P. Hammersley, S.O. Svensson, M. Hanfland, A.N. Fitch, D. Hausermann, *High Pressure Research* **14**, 235 (1996).

[18] B.E. Warren, *X-ray Diffraction*, Dover Publications, New York, 1990.

[19] H. Balyuzi, *Acta Crystallographica Section A* **31**, 600 (1975).

[20] P.F. Peterson, E.S. Božin, T. Proffen, S.J.L. Billinge, *Journal of Applied Crystallography* **36**, 53 (2003).

[21] T.E. Faber, J.M. Ziman, *Philosophical Magazine* **11**, 153 (1965).

[22] D. Waasmaier, A. Kirfel, *Acta Crystallographica Section A Foundations of Crystallography* **51**, 416 (1995).

[23] X.L. Wang, J. Almer, C. Liu, Y. Wang, J. Zhao, a. Stoica, D. Haeffner, W. Wang, *Physical Review Letters* **91**, 265501 (2003).

[24] J.F. Loeffler, W.L. Johnson, *Applied Physics Letters* **76**, 3394 (2000).

[25] E. Pekarskaya, J.F. Löffler, W.L. Johnson, *Acta Materialia* **51**, 4045 (2003).

[26] B.J. Park, H.J. Chang, D.H. Kim, W.T. Kim, *Applied Physics Letters* **85**, 6353 (2004).

[27] J.H. Han, N. Mattern, D.H. Kim, J. Eckert, *Journal of Alloys and Compounds* **509S**, S42 (2011).

[28] N. Mattern, G. Goerigk, U. Vainio, M. Miller, T. Gemming, J. Eckert, *Acta Materialia* **57**, 903 (2009).

[29] A. Guinier, G. Fournet, *Journal of Polymer Science* **19**, 594 (1956).

[30] L. Fan, M. Degen, S. Bendle, N. Grupido, J. Ilavsky, *Journal of Physics: Conference Series* **247**, 012005 (2010).

[31] F. Zhang, J. Ilavsky, G.G. Long, J.P.G. Quintana, A.J. Allen, P.R. Jemian, *Metallurgical and Materials Transactions A* **41**, 1151 (2009).

[32] B.R. Pauw, *Journal of Physics: Condensed Matter* **25**, 383201 (2013).

[33] N.A. Mauro, K. Derendorf, A.J. Vogt, M.L. Johnson, D. Quirinale, A.I. Goldman, K.F. Kelton, *Manuscript in Preparation* (2015).

[34] K. Derendorf, *The Design, Construction, and Implementation of an Electrostatic Levitation Facility for Neutron Scattering Studies of Liquids*, Ph.D. Thesis, Washington University in St. Louis (2013).

[35] A.J. Vogt, *Studies of Structural and Chemical Ordering in Metallic Liquids and Glasses Using Electrostatic Levitation*, Ph.D. Thesis, Washington University in St. Louis (2014).

[36] J. Neuefeind, M. Feygenson, J. Carruth, R. Hoffmann, K.K. Chipley, *Nuclear Instruments and Methods in Physics Research Section B: Beam Interactions with Materials and Atoms* **287**, 68 (2012).

[37] A.J. Dianoux, G.H. Lander, P.L.G. Institut Max von Laue, I. Laue-Langevin, *Neutron Data Booklet*, Second Edition ed., Old City, 2003.

[38] F. Sears, *Neutron News* **3**, 29 (1992).

[39] G. Kresse, J. Furthmüller, *Computational Materials Science* **6**, 15 (1996).

[40] G. Kresse, J. Hafner, *Physical Review B* **47**, 558 (1993).

[41] G. Kresse, D. Joubert, *Physical Review B* **59**, 1758 (1999).

[42] M.S. Daw, M.I. Baskes, *Physical Review B* **29**, 6443 (1984).

[43] M.S. Daw, S.M. Foiles, M.I. Baskes, *Materials Science Reports* **9**, 251 (1993).

[44] R. Soklaski, Z. Nussinov, Z. Markow, K.F. Kelton, L. Yang, *Physical Review B* **87**, 184203 (2013).

[45] R.L. McGreevy, *Journal of Physics: Condensed Matter* **13**, (2001).

[46] O. Gereben, P. Jovari, L. Temleitner, L.G. Pusztai, *Journal of Optoelectronics and Advanced Materials* **9**, 3021 (2007).

[47] J.D. Honeycutt, H.C. Andersen, *Journal of Physical Chemistry* **91**, 4950 (1987).

[48] A.S. Clarke, H. Jonsson, *Physical Review E* **47**, 3975 (1993).

[49] L. Huang, C.Z. Wang, S.G. Hao, M.J. Kramer, K.M. Ho, *Physical Review B* **81**, 014108 (2010).

[50] G. Voronoi, *Journal Fur Die Reine Und Angewandte Mathematik* **134**, 198 (1908).

[51] J.L. Finney, *Nature (London)* **226**, 309 (1977).

[52] J.L. Finney, *Proceedings of the Royal Society of London A* **319**, 479 (1970).

[53] J. Park, Y. Shibutani, *Intermetallics* **23**, 91 (2012).

[54] Y.Q. Cheng, E. Ma, *Progress in Materials Science* **56**, 379 (2011).

[55] F.C. Frank, J.S. Kasper, *Acta Crystallographica* **12**, 483 (1959).

[56] C.H. Rycroft, *Chaos* **19**, 18 (2009).

[57] B.H. Toby, R.B. Von Dreele, *Journal of Applied Crystallography* **46**, 544 (2013).

[58] A.C. Larson, R.B. Von Dreele, *General Structure Analysis System (GSAS)*, Los Alamos national Laboratory Report LAUR 86-748, 2004.

[59] M.I. Aroyo, J.M. Perez-Mato, D. Orobengoa, E. Tasci, G. De La Flor, A. Kirov, *Bulgarian Chemical Communications* **43**, 183 (2011).

[60] M.I. Aroyo, J.M. Perez-Mato, C. Capillas, E. Kroumova, S. Ivantchev, G. Madariaga, A. Kirov, H. Wondratschek, *Zeitschrift für Kristallographie* **221**, 15 (2009).

[61] M.I. Aroyo, A. Kirov, C. Capillas, J.M. Perez-Mato, H. Wondratschek, *Acta Crystallographica* **A62**, 115 (2006).

[62] P. Villars, L.D. Calvert, *Pearson's Handbook of Crystallographic Data for Intermetallic Phases*, American Society for Metals, Metals Park, OH, 1985.

[63] V. Pecharsky, P. Zavalij, *Fundamentals of Powder Diffraction and Structural Characterization of Materials*, 2nd ed., Springer US, 2009.

Chapter 3: Structural evolution in Ni-Nb and Ni-Nb-Ta liquids and glasses – A measure of liquid fragility? [1]

This chapter has been published in the *Journal of Non-Crystalline Solids* in collaboration with N. A. Mauro, J. C. Bendert, and K. F. Kelton [1], and has been adapted to be consistent with the formatting in this dissertation. The author's personal contributions include reduction of detector data into $S(q)$ and $g(r)$ and subsequent analysis, measuring the glass density, running the RMC simulations and analyzing the results, and participating in writing the manuscript. A large portion of the writing was performed by N. A. Mauro. Scattering data were collected during BESL 2010, and liquid density data were acquired by J. C. Bendert (Washington University in Saint Louis, Saint Louis, MO).

3.1 Introduction

Bulk metallic glasses (BMGs), i.e. glasses that can be cast into large sizes due to their low critical cooling rates, form a unique class of functional materials whose properties make them the focus of significant fundamental and technological research. Most BMGs have been discovered in multicomponent alloys; binary alloys are generally considered to have a low glass-forming ability (GFA). Transition metal (TM) binary BMGs have only been reported in a few alloy families [2-7]. One of these families, the Ni-Nb alloys, is reported to form binary bulk metallic glasses at a composition of $Ni_{62}Nb_{38}$ with a critical casting thickness of 2 mm [5]. These glasses are of practical interest since they are reported to have excellent compressive strength and corrosive resistance [8], while retaining a small reduced glass temperature. For several reasons, these glasses are also of fundamental interest. The bulk-forming compositional range for these glasses is extremely narrow [5] and the three empirical rules for BMG formation [9] do not apply. The best bulk glass-forming composition ($Ni_{62}Nb_{38}$) is not at the eutectic composition ($Ni_{59.5}Nb_{40.5}$), in contradiction with usual expectations [10]. Additionally, glass formation is improved with small compositional changes, including the substation of Ta for Nb [11-14].

Glass formability and physical properties are related to local atomic order. However, the precise nature of these relations remains one of the central problems in the study of metallic liquids and glasses. Based on both theoretical and experimental studies, it is generally accepted that the development of atomic order in the liquid that is different from that of energetically accessible crystalline phases raises the nucleation barrier and stabilizes the liquid below the equilibrium liquidus temperature, both aiding glass formation [15, 16]. Supporting this, X-ray [17] and neutron [5, 18-20] diffraction studies show a shoulder on the high-q side of the second peak in the total static structure factor, $S(q)$, that is often taken to be an indication of icosahedral-like short-range order (ISRO) [16, 21, 22], which is incompatible with crystal periodicity. However, diffraction studies of high- and low-GFA liquids and glasses in a range of alloy families show that a developing shoulder on the second peak in $S(q)$ with decreasing temperature is a nearly universal feature. It cannot, therefore, be used as a measure of good GFA. Instead, the rates of evolution with temperature of some structural metrics are emerging as discriminating measures for GFA. Molecular dynamics simulations of low-GFA Cu-Zr [23, 24] liquids indicate that their structures change rapidly near the glass transition, while the structures of high GFA Zr- [25, 26] and Pd- [26, 27] based liquids evolve gradually over a wide temperature range above and through the glass transition temperature. Quantifying this evolution may lead to a better understanding of glass-forming ability. Because of their relative simplicity, binary glasses and liquids, such as the Ni-Nb alloys, provide excellent systems for studying the structural dependence of glass formability in a systematic fashion.

In this manuscript, the results from diffraction studies of containerlessly-processed Ni-Nb liquids and the corresponding glasses are presented. The experimental and analysis techniques used are described in Section 3.2. In Section 3.3, the results of high-energy synchrotron X-ray diffraction studies and thermophysical property measurements of $Ni_{59.5}Nb_{40.5}$, $Ni_{62}Nb_{38}$, and $Ni_{60}Nb_{30}Ta_{10}$ liquids and glasses are presented. In Section 3.4 the results of a structural characterization based on Reverse Monte Carlo fits to experimentally-determined static structure factors are presented and discussed. Trends in the structure factors and pair-correlation functions of the liquids that show evidence for deviations near the glass transition are also discussed. The work is summarized and conclusions are drawn in Section 3.5.

3.2 Experimental

Master ingots (~1.0 g) of all compositions were prepared by arc-melting high-purity elements Ni (99.995%), Nb (99.95% metals basis excluding Ta), and Ta (99.95%) on a water-cooled copper hearth in a high-purity (99.999%) Ar atmosphere. The ingots were crushed and portions were arc-melted to obtain small spherical samples (~2.5 mm diameter) for *in situ* liquid structural studies at the Advanced Photon Source (APS) on 6-ID-D using the Washington University Beamline Electrostatic Levitator (WU-BESL) [28, 29]. WU-BESL is optimized for X-ray diffraction studies of levitated, containerlessly-processed, liquids in a high-vacuum environment (~10^{-7} Torr). Several of the master ingots were melted by RF-induction heating to 1300-1350 °C (well above the liquidus temperature) in a graphite crucible under a high-purity (99.999%) Ar atmosphere and rapidly quenched onto a copper wheel that was rotating at ~70 m/s, producing ribbons that were continuous for 3-10 cm with an average cross section of 1-2 mm by 20-30 μm. Laboratory X-ray diffraction (Rigaku, Cu-K_α, $\lambda = 1.54$ Å radiation) and high-energy synchrotron diffraction studies confirmed that the as-quenched ribbons were amorphous. Synchrotron scattering studies of the glasses were made at the APS in transmission geometry by mounting the ribbon samples on the 6-ID-D beamline goniometer.

The liquid temperature was measured from 160 °C to 2300 °C using two infrared pyrometers with overlapping temperature ranges. A single-color Process Sensors Metis MI18 MB8, operating at a 1.89 µm wavelength, was used for low-temperature measurements (160–800 °C), and a Process Sensors Metis MQ22 two-color ratio pyrometer, operating at 1.40 and 1.64 µm wavelengths, was used for high-temperature measurements (600–2300 °C). Ratio pyrometers provide more accurate measurements of the temperature because emissivity changes with temperature are normalized out [30]. Because of the close measured wavelengths, relative changes in the emissivity at each measured wavelength over a narrow temperature range are expected to be small. Emissivity ratios were calibrated by matching the melt plateau in the time/temperature curve obtained on heating in the ESL (the onset corresponds to the solidus temperature, T_s) to the largest endothermic transition signature measured in a differential thermal analyzer (Labsys™ DTA/DSC, Setaram Instrumentation).

To obtain the maximum supercooling, the levitated samples were heated to 1400 °C, well above the liquidus temperatures (T_L) for the three samples studied, using a fiber-coupled diode laser (980 nm, 50W continuous maximum power output). The samples were subsequently allowed to cool by radiation loss, with the laser power turned off. A constant emissivity ratio was assumed over the entire temperature range for which structural data were acquired. Crystallization from the supercooled metastable liquid was marked by a single large-temperature increase (recalescence). Sample masses were measured before and after ESL processing to determine mass loss during processing, which would indicate a change in composition. In all cases the mass loss was kept negligible.

The temperature measurements were correlated with non-contact volume measurements of the liquid samples. These were made using the shadow method [31, 32] with a Pixelink PL-B741G CMOS camera and a 455 nm collimated microscope LED, which has a total beam power of 240 mW and a beam diameter of 37 mm. The pixel dimensions were calibrated before and after each sample measurement using $2.38125 \pm 7.62 \times 10^{-4}$ mm diameter (grade 3) tungsten carbide standards. The sample volume was determined from the shadow of the backlit levitated sample [33], and the density was then calculated by multiplying the sample mass by the inverse of the volume. The volume is recorded as a video as a function of time and temperature during radiative free-cooling with the heating laser turned off. During free-cooling, the temperature of the sample is described by

$$mC_p \frac{dT}{dt} = -\sigma_B A \varepsilon_T \left(T^4 - T_0^4 \right) , \tag{3.1}$$

where m, C_p, dT/dt, σ_B, A, ε_T, T, and T_0 are the sample mass, specific heat, cooling rate, Stefan-Boltzmann constant, sample surface area, total hemispherical emissivity, sample temperature and ambient temperature, respectively. The video data were taken at a frame rate of 20-25fps. Details of the machine vision volume measurement algorithm are given elsewhere [31]. The relative precision of the density data was ~0.3% over the temperature range studied, with an absolute accuracy of ~0.5%; the measurement error is dominated by errors in the volume and mass calibrations. The densities of the amorphous ribbons at room temperature were determined using Archimedes' method, with toluene as the working fluid; the uncertainties in the values obtained were between 1.2% and 1.5% after error propagation.

High-energy diffraction measurements of the liquids and glasses (E = 129 keV, λ = 0.0969 Å^{-1} for the liquid studies; E = 100 keV, λ = 0.1243 Å^{-1} for the glass studies) were made in a transmission geometry to a momentum transfer, q, of 15 Å^{-1} using a GE Revolution 41-RT amorphous Si flat-panel X-ray detector. The structure factor, $S(q)$, was derived from the scattering data by first applying an appropriate gain map, masking bad pixels, averaging images, subtracting the appropriate dark current, and correcting for oblique incidence, absorption, multiple scattering, fluorescence, Compton scattering, and secondary container scattering contributions using in-house analysis packages written in LabView$^{\text{TM}}$ [22]. Liquid diffraction patterns were obtained at a variety of temperatures by controlling the heating-laser power to keep the temperature constant. A series of measurements of duration 10-20 seconds were made at each temperature step. The total static structure factor was calculated from the scattering data using

$$S(q)=\frac{I(q)-\sum_{i=1}^{n}a_i\left|f_i(q)\right|^2}{\left|\sum_{i=1}^{n}a_i f_i(q)\right|^2}+1\ , \tag{3.2}$$

where $I(q)$ is the measured diffraction intensity, a_i is the atomic fraction of each element, and $f_i(q)$ is the q-dependent atomic form factor for each species. The sums were made over all species and an isotropic and statistically homogeneous atomic distribution was assumed. The total structure factor is related to the total pair-correlation function, $g(r)$, by a Fourier transform as shown in Eqn. 3.3,

$$S(q)=1+4\pi\rho_0\int\left[g(r)-1\right]\frac{\sin qr}{qr}r^2dr\,, \tag{3.3}$$

where ρ_0 is the average number density.

Average atomic structures of the liquids and glasses as a function of temperature were obtained from Reverse Monte Carlo (RMC) fits to the $S(q)$ data (see [34-36] for a discussion of the RMC method). For this study, atoms with appropriate stoichiometric composition were confined to a cubic box with dimensions appropriate to the measured density. Several RMC fits were made for each composition of interest to generate statistical information on the Honeycutt and Andersen (HA) indices [37] used to provide quantitative information about the structures obtained. Each RMC fit was started from a random configuration of 5000 atoms and from a face centered cubic (FCC) lattice of 4000 atoms. The data for one composition ($Ni_{59.5}Nb_{40.5}$) were fit at the same temperature (1386 °C) eight times to gather a statistical distribution on the output. For the RMC fits, the minimum distances (hard-sphere cut-offs) in the partial $g(r)$s were calculated from where $g(r)$ trended to zero on the low-r side of the primary peak and scaled to account for atomic size and bonding length contraction due to enthalpy of mixing. For a given liquid composition the values obtained did not change significantly with temperature, and were, therefore, taken to be constant. Within a given composition, the Ni-Ni, Ni-Nb, and Ni-Ta distances were set approximately the same (denoted as Ni-(Ni,Nb,Ta)), as were the Nb-Nb, Nb-Ta and Ta-Ta distances (denoted as (Nb,Ta)-(Nb,Ta)). These distances were changed between compositions to be consistent with the experimental $g(r)$s. The Ni-(Ni,Nb,Ta) hard-sphere cutoffs were nominally 1.88 ± 0.09 Å; the (Nb,Ta)-(Nb,Ta) hard-sphere cutoffs were nominally 2.25 ± 0.10 Å. For the RMC fits to the data for the glasses, the variability of the cutoff distances was even smaller between compositions. The Ni-(Ni,Nb,Ta) hard-sphere cutoffs were nominally 2.17 ± 0.01 Å; the (Nb,Ta)-(Nb,Ta) hard-sphere cutoffs were nominally 2.61 ± 0.01 Å. As mentioned, the short-range order (SRO) in the atomic structures obtained from the RMC fits was evaluated in terms of the HA indices. For the HA index calculations, the temperature-dependent, nearest-neighbor, cutoff distances were taken to be the location of the minimum in the total $g(r)$ after the first peak. These values did not change significantly with temperature or composition, nominally 3.68 ± 0.02 Å in the liquid and 3.57 ± 0.01 Å in the glass.

The positions and magnitudes of the first peaks in $S(q)$ and $g(r)$ were refined by fitting a cubic spline to the peak. Total uncertainties were estimated by considering perturbations from independent sources of errors, including statistical uncertainties, estimated following the method described by Hammersley [38], and confidence intervals of fitted correction factors (e.g. intensity normalization). Based on this, the precision of the peak heights in both $S(q)$ and $g(r)$ is ~0.5% and the accuracy of the peak heights in $g(r)$ is ~ 4%.

3.3 Results

The representative temperature-time free-cooling curves for the three compositions studied are shown in Figure 3.1 (a). For each composition a single melt plateau is observed which marks the onset of the solidus temperature, T_s. For $Ni_{60}Nb_{30}Ta_{10}$, T_s was determined to be 1191 ± 5 ^oC; for $Ni_{59.5}Nb_{40.5}$ and $Ni_{62}Nb_{38,}$ it was 1175 ± 5 ^oC. These values are consistent with the published phase diagram [39-41]. The amount of supercooling was small for all liquids, approximately 100 ^oC. This was true even for the eutectic Ni-Nb liquid, which could be superheated by ~200 ^oC above the liquidus temperature before Ni evaporation. This is in contrast with reports from previous levitation studies of Ni-Nb liquids [42], where a supercooling of 126 ^oC was reported in one electrostatic levitation study when the liquid was superheated by 200 ^oC [43]. Significant evaporation loss was reported if this amount of superheating was exceeded. There is one report of an extremely large supercooling of 210 ^oC below the solidus, but with a superheating of 400 ^oC [44]. This corresponds to a temperature of 1575 ^oC, where the vapor pressure for Ni is 10^{-2} to 10^{-1} Torr [45]. Evaporation was very likely at such extreme temperatures, suggesting that the actual composition of the supercooled liquid was not the eutectic composition. Taken together, these results suggest that heterogeneous nucleation sites persist even at the highest superheating.

The time/temperature curves for all supercooled liquids showed a single, relatively long (~ 8 s) recalescence event. High-energy X-ray diffraction patterns taken during recalescence for the $Ni_{59.5}Nb_{40.5}$ and $Ni_{62}Nb_{38}$ liquids indicate a phase mixture of the orthorhombic Ni_3Nb and trigonal Ni_6Nb_7 equilibrium crystal phases [46]. The diffraction patterns obtained during recalescence for the $Ni_{60}Nb_{30}Ta_{10}$ liquid were consistent with these phases, but with a random substitution of Ta onto Nb sites.

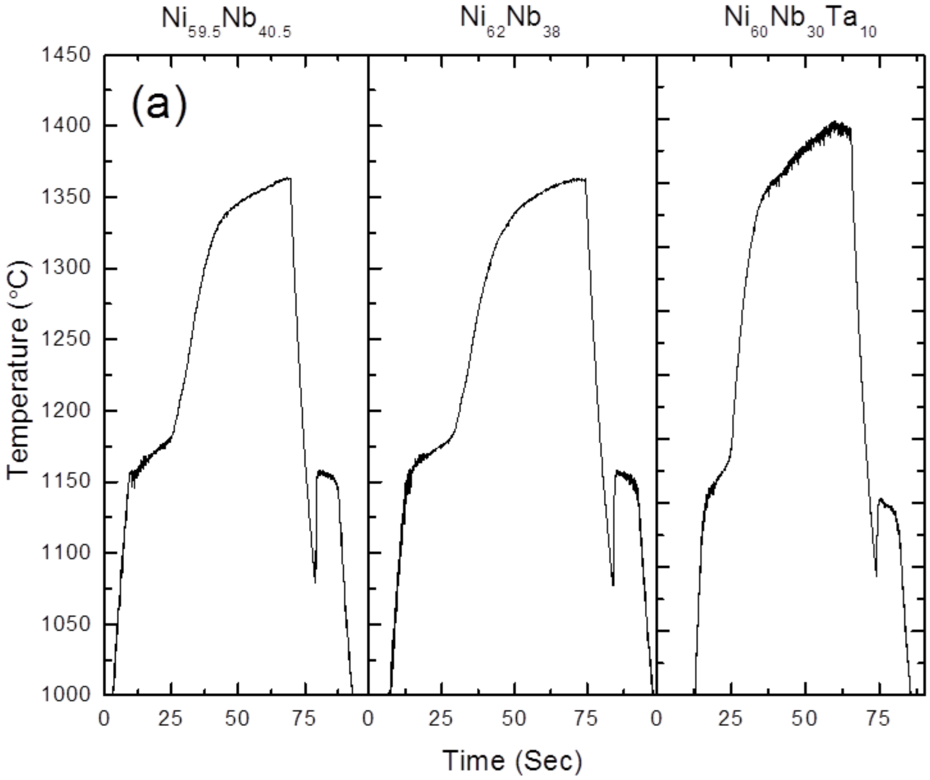

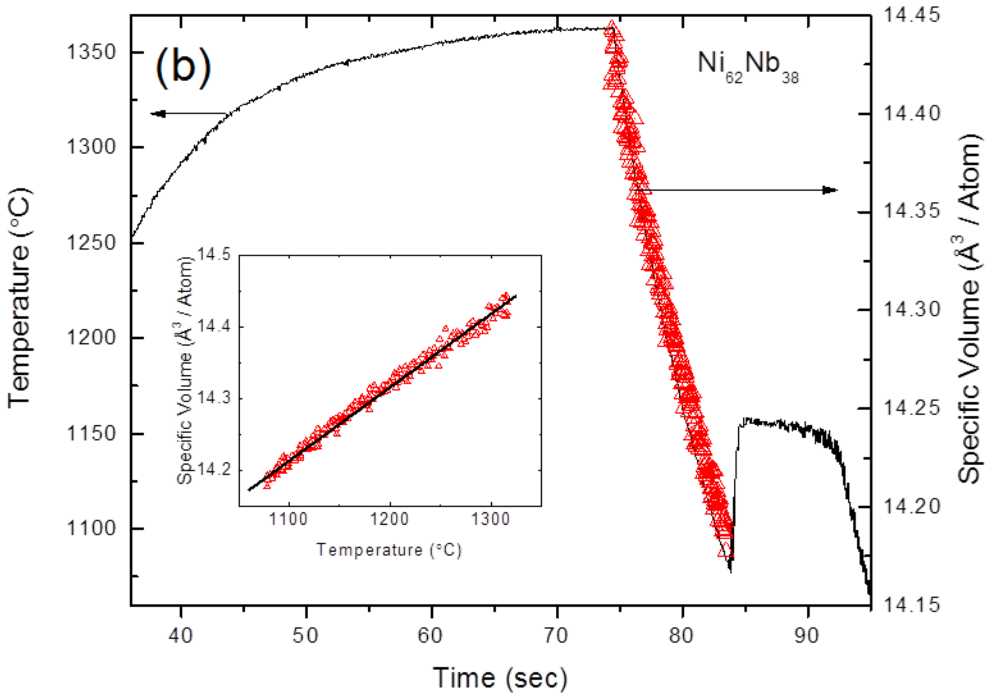

Figure 3.1 (a) Representative temperature-time curves for a typical heating and free-cooling cycle in the three compositions studied. (b) The temperature upon heating and free-cooling (left ordinate axis) and the specific volume (right ordinate axis) as a function of time for one $Ni_{62}Nb_{38}$ cycle. The specific volume as a function of temperature is highly linear, as shown in the insert.

The sample volume was measured as a function of temperature for multiple radiative free-cooling studies for each sample composition. A representative data set is shown in Figure 3.1 (b); the temperature-dependent specific volume (average volume per atom) calculated from these data is shown in the inset to this figure. The rate of change of the number density (β) and the coefficient of thermal expansion ($\alpha = (\partial \ln V / \partial T)_P$) for each liquid composition were determined from linear fits to the density and volume data, respectively, following Eqns. 3.4 and 3.5.

$$\rho(T) = \rho_s\left(1+\beta\left(T-T_s\right)\right) \tag{3.4}$$

$$V(T) = V_s\left(1+\alpha\left(T-T_s\right)\right) \tag{3.5}$$

Here, ρ_s and V_s are the density and volume, respectively, at the solidus temperature, T_s. The fit parameters are listed in Table 3.1. Linear temperature dependencies of both the density and the volume are found for all compositions studied, indicating that the thermal expansion coefficients are constant in the ~ 300 °C temperature range over which the data were taken.

Table 3.1 Fitting parameters for the density and volume for each composition .

Composition	**T_S (°C)**	**Temperature range**	**Density Parameters**		**Volume parameters**	
		T_{max} (°C)	**ρ_S (1/Å^3)**	**β (1/°C)**	**V_S (Å^3)**	**α (1/°C)**
		T_{min} (°C)	**(Uncertainty)**	**(Uncertainty)**	**(Uncertainty)**	**(Uncertainty)**
$Ni_{59.5}Nb_{40.5}$	1175	1400	6.92E-02	-6.18E-05	14.448	6.21E-05
		1170	(± 3.50E-04)	(± 3.09E-06)	(± 7.20E-02)	(± 3.10E-06)
$Ni_{62}Nb_{38}$	1175	1310	6.98E-02	-7.41E-05	14.337	7.39E-05
		1100	(± 3.50E-04)	(± 2.22E-06)	(± 7.10E-02)	(± 3.70E-06)
$Ni_{60}Nb_{30}Ta_{10}$	1191	1400	6.94E-02	-7.98E-05	14.400	7.90E-05
		1090	(± 7.90E-05)	(± 2.39E-06)	(± 1.60E-02)	(± 4.98E-06)

The measured total structure factors, $S(q)$, for the liquids and glasses and the pair-correlation functions, $g(r)$, are shown in Figure 3.2. In all cases, the $S(q)$s (Figure 3.2 (a-c)) oscillate well around unity over the entire q range, indicating the high quality of the experimental data. The lack of high-frequency ripples in the pair-correlation functions (Figure 3.2 (d-f)) indicates that there was little systematic error in the $S(q)$ calculation [47] and that the scattering intensities were measured to sufficiently large q to minimize truncation ripples. For all samples studied, the intensities of the peaks in $S(q)$ increase with decreasing temperature, the widths decrease, and the peak locations shift to higher-q. These trends continue into the glasses. They indicate a growing structural order with cooling towards and through the glass transition. For all liquids, a shoulder on the high-q side of the second peak in $S(q)$, which is typically taken to indicate the development of icosahedral short-range order [16, 21, 22], becomes more pronounced with supercooling and evolves into a splitting of the second peak for each glass.

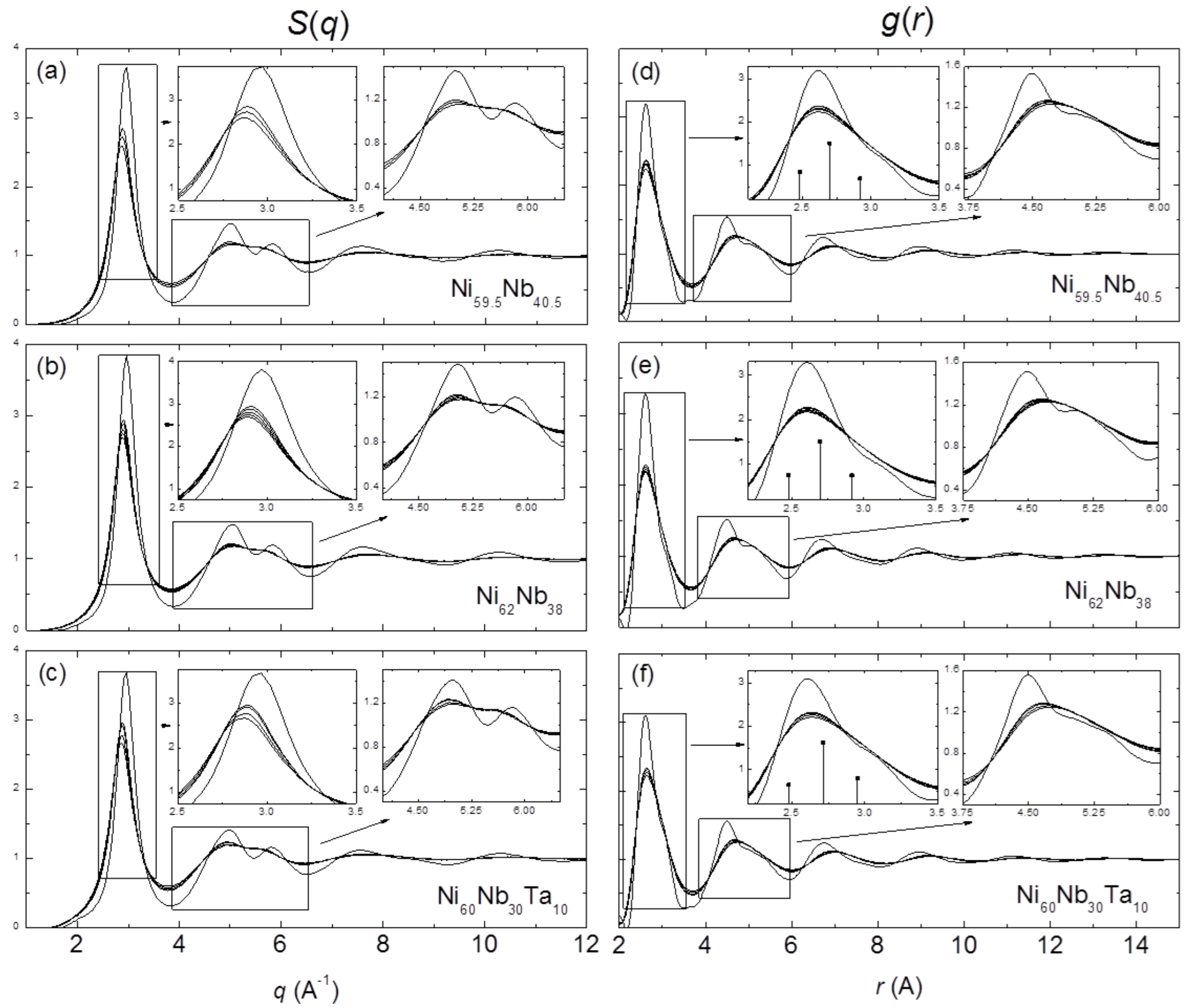

Figure 3.2 The total structure factors, $S(q)$, and the pair-correlation functions, $g(r)$, for the liquids at all temperatures measured and the glass measured at room temperature. The inserts for the $S(q)$s ((a) $Ni_{59.5}Nb_{40.5}$; (b) $Ni_{62}Nb_{38}$; (c) $Ni_{60}Nb_{30}Ta_{10}$) and the $g(r)$s ((d) $Ni_{59.5}Nb_{40.5}$; (e) $Ni_{62}Nb_{38}$; (f) $Ni_{60}Nb_{30}Ta_{10}$) show the evolution of the first and second peaks. For each composition, the insert containing the first peak in $g(r)$ also shows the relative strength of the Ni-Ni, Ni-Nb/Ta, and Nb/Ta-Nb/Ta FZ weighting factors (from Table 3.2) at ~2.48 Å, ~2.70 Å, and ~2.95 Å, respectively.

An asymmetric first peak in the total pair-correlation function is observed for all liquids (inset in Figure 3.2 (d-f)); it continues to develop and becomes more prominent in the glasses. The total pair-correlation function is the weighted average of the chemically specific partial pair-correlation functions (PPCFs). For binary alloys, then, the first peak represents the contributions of three PPCFs (Ni-Ni, Ni-Nb and Nb-Nb); it represents six PPCFs for the ternary liquid/glass (Ni-Ni, Ni-Nb, Ni-Ta, Nb-Nb, Nb-Ta and Ta-Ta).

Within the Faber-Ziman formalism, the total structure factor is the weighted sum of the partial structure factors, $S_{\mathrm{ij}}(q)$,

$$S(q)-1=\sum_{i,j}\gamma_{ij}(q)(S_{ij}(q)-1) \ , \tag{3.6}$$

where the double sum ranges over all of the elemental pairs, the weighting factors are given by [48]

$$\gamma_{ij}(q)=\frac{a_i a_j f_i(q) f_j(q)}{(f(q))^2} \ , \tag{3.7}$$

where a_{i} is the atomic fraction of each element and $f_{\mathrm{i}}(q)$ is the q-dependent atomic form factor for each element. The total PCF is related to the total structure factor by a Fourier transform

$$g(r)=1+\frac{1}{4\pi\rho_0}\frac{2}{\pi}\int[S(q)-1]\frac{\sin(qr)}{qr}q^2dq \, . \tag{3.8}$$

By substituting Eqn. 3.6 in Eqn. 3.8, the total $g(r)$ can be written as

$$g(r)=1+\frac{1}{4\pi\rho_0}\frac{2}{\pi}\int\left[\sum_{i,j}\gamma_{ij}(q)(S_{ij}(q)-1)\right]\frac{\sin(qr)}{qr}q^2dq \, . \tag{3.9}$$

Since the PSFs and the FZ weighting factors are both q-dependent, the construction of the PCF requires the convolution of the Fourier transform of two functions. However, the weighting factors are slowly varying functions and, to a first approximation, the contribution of the partial pair-correlation functions to the total pair-correlation function is given by the $q = 0$ value of the FZ weighting factors [48]. These PPCF weighting factors are listed in Table 3.2. This approximation has been confirmed using known PSFs for related systems; it is a reliable approximation to between 5 and 10%.

Although it was not possible to directly determine the partial PCFs from the X-ray diffraction data, the location of the maxima of the first peaks in the different partial PCFs (corresponding to the first coordination shells) are approximately dictated by the atomic sizes of the constituent elements [49], which are consistent with published data [18, 20]. Table 3.2 summarizes the expected positions of the peaks in the partial PCFs that contribute to the main peak in the total *g*(*r*). The relative weight (from the FZ factors in Table 3.2) and the positions of the partial PCF peaks are shown graphically for each composition in Figure 3.2 (d-f).

Table 3.2 Faber-Ziman (FZ) multiplicative weighting factors for the contributing PPCFs and the estimated bond lengths from atomic size consideration.

Partials	**$Ni_{59.5}Nb_{40.5}$ FZ factors**	**$Ni_{62}Nb_{38}$ FZ factors**	**$Ni_{60}Nb_{30}Ta_{10}$ FZ factors**	**Estimated average bond length (Å)**
Ni-Ni	0.251	0.278	0.213	2.48
Ni-Nb	0.500	0.499	0.312	2.70
Ni-Ta	N/A	N/A	0.185	2.73
Nb-Nb	0.249	0.224	0.114	2.92
Nb-Ta	N/A	N/A	0.136	2.95
Ta-Ta	N/A	N/A	0.040	2.98

The asymmetry observed in the first peaks in *g*(*r*) for the liquids and glasses is the result of the positions of the first peaks in each of the partials being locating at different *r* values. The Ni-Ni contribution to the first peak in *g*(*r*) is small and contributes to broadening observed at low-*r*. The Ni-Nb (or Ni-Nb + Ni-Ta) contribution is large and centered near *r* ~ 2.7 Å, the peak location in the total *g*(*r*). Finally, the Nb-Nb (or Nb-Nb + Nb-Ta + Ta-Ta) contribution is centered near *r* ~ 2.95 Å, causing the peak in *g*(*r*) to spread to high *r*, producing an asymmetry. The similarities in the measured total pair-correlation functions suggest that the chemically specific PSFs and partial PCFs are very similar for the three compositions. The slight differences observed in the total PCFs in Figure 3.2 can be explained by differences in the FZ factors weighting the partial PCFs.

The second peak in the $g(r)$ from all of the glasses shows a pronounced splitting that is much more prominent than in the liquid data. This can be attributed to the development of medium-range order (MRO) in the glass, which has been observed in neutron diffraction studies [18-20]. Depending on the scattering contrast between elements, this MRO can be manifest as a pre-peak in the total structure factor, and, if they are available, can be directly observed in partial structure factors (PSFs). While no PSFs have been measured for the liquids studied here, neutron diffraction studies on $Ni_xNb_{(100-x)}$ (x = 40, 50, 56 and 63) glasses have been made using isotopic substitution [18]. These show evidence for MRO in both the Ni-Ni and Nb-Nb PSFs, for glasses with Ni concentrations larger than 40 at.%. It is likely that MRO is present in the liquids studied here, but the X-ray scattering contrast is insufficient to show a pre-peak in the $S(q)$. The problems associated with insufficient scattering contrast between constituent elements has been recently discussed by Mauro and Kelton [50].

3.4 Discussion

The amplitude of the first peak in $S(q)$ (denoted as $S(q_1)$) is shown as a function of temperature in Figure 3.3. An interesting feature emerges on examining the growth of $S(q_1)$ as the liquid is cooled into the glass. In the liquid, $S(q_1)$ increases approximately linearly with decreasing temperature for all compositions; the best-fit lines are shown with 95% confidence intervals. The liquid structure will continue to change with decreasing temperature, until it reaches the glass transition temperature, T_g, at which point it will become essentially fixed within a narrow temperature range below T_g (except for structural relaxation processes that are slow on the time scale of the cooling). Since it was not possible to supercool the liquid to T_g using the BESL, the data from the glasses measured at room temperature were extrapolated to T_g to compare with the behavior of the liquid, when extrapolated from high temperature. Since the structure of the glass is approximately constant below T_g, changes to $S(q)$ with temperature will be due to atomic vibrations, which can be calculated from the Debye theory [51].

$$\frac{S_{T_2}(q)-1}{S_{T_1}(q)-1}=e^{-2\left[W_{T_2}(q)-W_{T_1}(q)\right]} \tag{3.10}$$

$$W_T(q)=\frac{3}{2}\frac{\hbar^2 q^2}{Mk_B}\frac{T^2}{\theta_D^3}\int_0^{\theta_D/T}\left[\frac{1}{2}+(e^z-1)^{-1}\right]z\,dz \tag{3.11}$$

Here, $W_T(q)$ is the Debye-Waller factor at temperature T, θ_D is the Debye temperature, M is the atomic mass, T_1 is the temperature at which the static structure factor ($S_{T1}(q)$) was measured, and T_2 is the temperature at which the structure factor ($S_{T2}(q)$) is calculated. The Debye temperatures were estimated by a weighted average of the Debye temperatures of the alloy elements [52, 53], giving 37.375 ^{o}C, 39.7 ^{o}C, and 34.5 ^{o}C for $Ni_{59.5}Nb_{40.5}$, $Ni_{62}Nb_{38}$, and $Ni_{60}Nb_{30}Ta_{10}$ respectively. With Eqns. 3.10 and 3.11, the $S(q)$ was estimated near the glass transition temperature for each sample, using the $S(q)$ that was measured at room temperature. Using Eqn. 3.8, the corresponding $g(r)$s were also estimated at T_g, by taking a Fourier transform of the extrapolated $S(q)$.

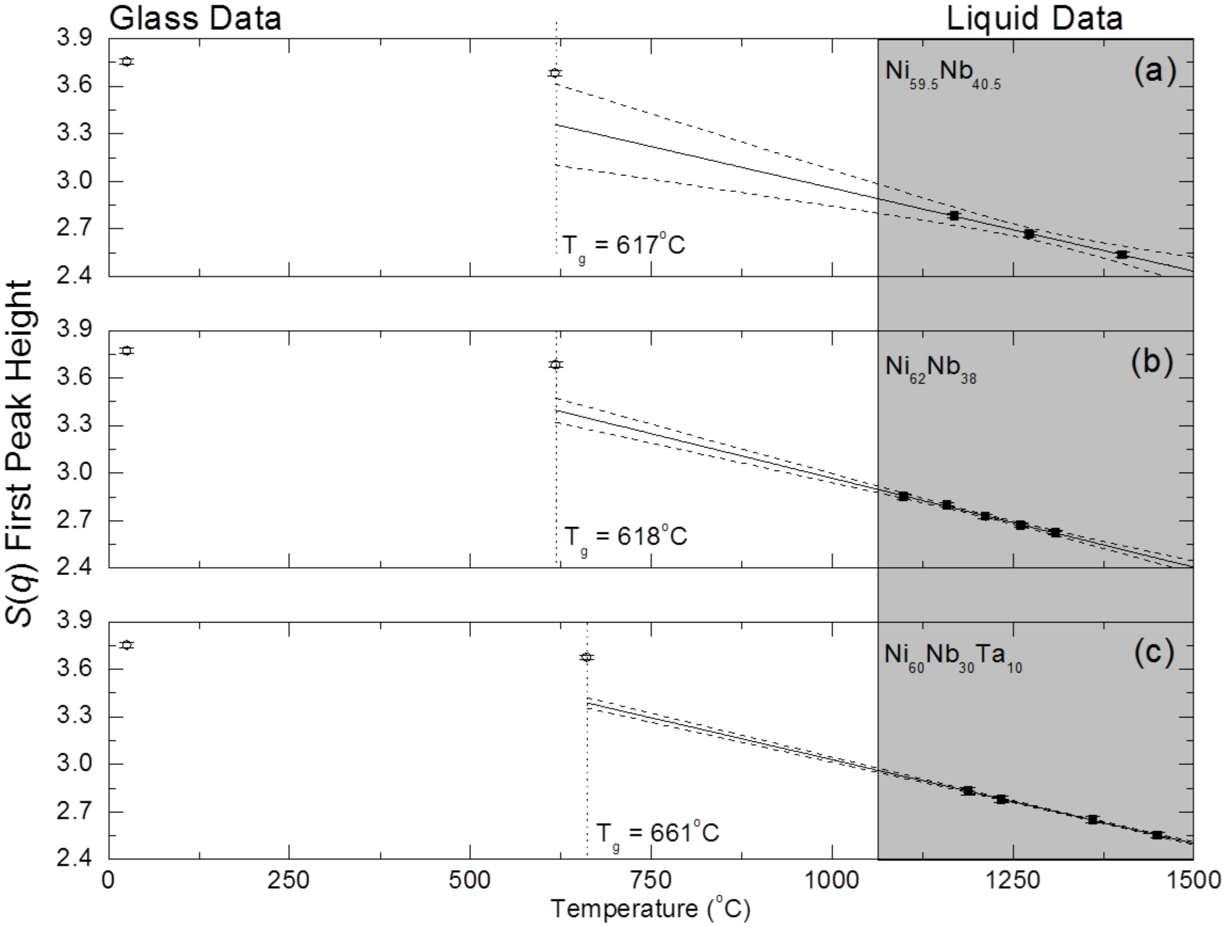

Figure 3.3 Amplitude of the first peak in $S(q)$ as a function of temperature for each composition. The $S(q_1)$ from the Debye-Waller-corrected $S(q)$ for the glasses for each composition are shown at the respective glass transition temperatures. Linear best-fit lines for the $S(q_1)$ liquid data extrapolated down to near T_g are shown with 95% confidence intervals. The data corresponding to the liquid are indicated with solid symbols; those corresponding to glass solid are open symbols.

Linear extrapolations to T_g of the amplitudes of the first peak in $S(q)$ (Figure 3.3) and $g(r)$ (Figure 3.4) for the liquids are considerably smaller than the values extrapolated from the glasses. (It should be noted that the larger range in the extrapolated value for the eutectic composition ($Ni_{59.5}Nb_{40.5}$) than for the other compositions is a consequence of the smaller liquid data set, i.e. measurements at only three temperatures.) These results suggest that the rate of structural ordering in the liquid *accelerates* at some temperature between the lowest one measured in the supercooled liquid and T_g. All liquids show the same trend, not appearing to differentiate the better glass formers ($Ni_{62}Nb_{38}$ and $Ni_{60}Nb_{30}Ta_{10}$) from the poorer one ($Ni_{59.5}Nb_{40.5}$). A qualitatively different behavior was observed for a few high-GFA bulk metallic glass-forming Zr-based and Pd-based bulk metallic glass-forming liquids that have been studied [25-27], which showed no evidence for a sudden change in their structural features determined from scattering studies near T_g. This indicates that the differences between the three liquids studied here may be smaller than the differences between these glass-forming alloys and other glass-forming systems.

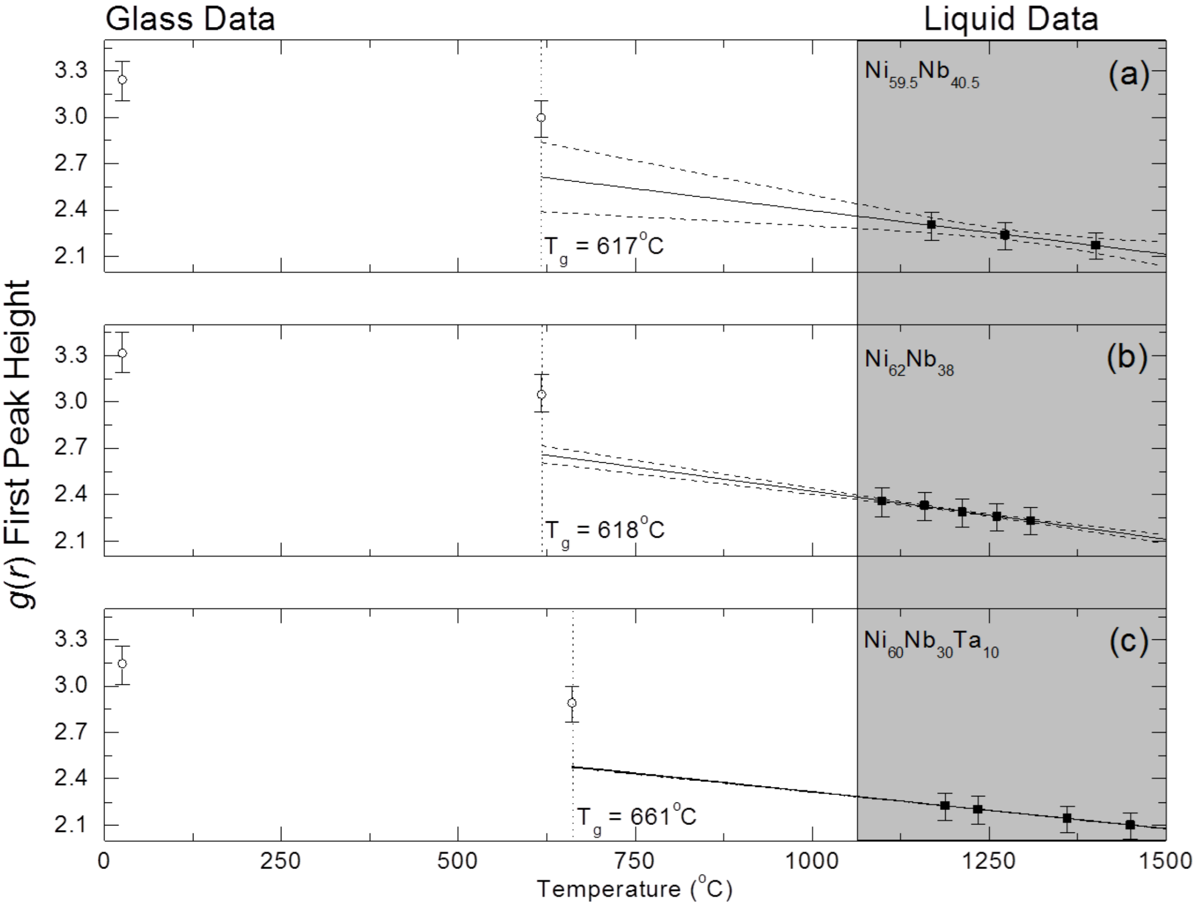

Figure 3.4 Amplitude of the first peak in $g(r)$ as a function of temperature for each composition. The $g(r_1)$ from the Fourier transform of the Debye-Waller corrected glassy $S(q)$ for each composition are shown at the respective glass transition temperatures. Linear best fit lines for the $g(r_1)$ for the liquid for each composition are shown with 95% confidence intervals, extrapolated down to near Tg. The data corresponding to the liquid are indicated with solid symbols; those corresponding to glass solid are open symbols.

For all compositions studied, the position of the first peak in $S(q)$ (located at q_1) shifts to higher-q and thus to shorter length scale with decreasing temperature. This is consistent with the measured average density, which increases with decreasing temperature. The measured q_1 increases approximately linearly with decreasing temperature from the liquid into the glass, with a maximum shift over the entire temperature range measured of about 0.6%. The significant error in this extrapolated value (due to the small temperature range over which liquid data could be obtained and the large separation in temperature between the liquid measurements and those of the glass) makes only a qualitative analysis of this trend possible. The position of the primary peak in $g(r)$, r_1, for each composition in the liquid state shifts by a maximum of 0.1% over the temperature range measured. As with the shift in q_1, a quantitative analysis is not conclusive due to uncertainties in the data.

The atomic structures of the liquids as a function of temperature, and the glasses at room temperature, were obtained from RMC fits to the total structure factor. Extensive discussions of the RMC method and the interpretation of the data obtained can be found elsewhere [53-55]. The large incident X-ray beam size used (.7 mm x .7 mm square) probes a sufficiently large portion of the sample as to obtain information that represents an average of the different local structures. Since RMC is an inverse method that uses one-dimensional scattering information to construct a three-dimensional structure, some caution should be exercised when interpreting the results. This has been explored previously for amorphous metals [56], where it was found that the topological information obtained from a Honeycutt-Anderson analysis of an RMC structure is reliable, both when unconstrained RMC fits were made to X-ray total structure factors and when the fits are constrained by chemically specific partials obtained from *ab-initio* molecular dynamics calculations. However, the quantitative chemically specific information contained in the partial pair-correlation functions is unreliable in unconstrained RMC fits. The partial PCFs show features that are qualitatively consistent with data obtained previously for metallic glasses [19, 57, 58] but the positions of the first peaks differ considerably from the reported values. Therefore, for the liquids and glasses presented here, only the topological structures as characterized by their HA indices are discussed.

Atomic models that were consistent with the experimental scattering data were obtained for the liquid and glass at each composition. RMC fits were also made to the $S(q)$ data from the glasses, which were extrapolated from room temperature to their respective T_g. As noted in Section 3.2, the convergence of the RMC fits was explored for different starting configurations at each temperature, examining both ordered (cubic symmetry) and random initial configurations. In all cases, a good fit was obtained for all scattering momentum transfer, q. Figure 3.5 shows representative RMC fits for $Ni_{59.5}Nb_{40.5}$ at 1400 °C (liquid) and at 25 °C (glass). For all compositions and at all temperatures, the $S(q)$ obtained from RMC fit the first peak almost perfectly, and only slightly under-represent the second peak and shoulder. The higher order peaks were fit well in all cases.

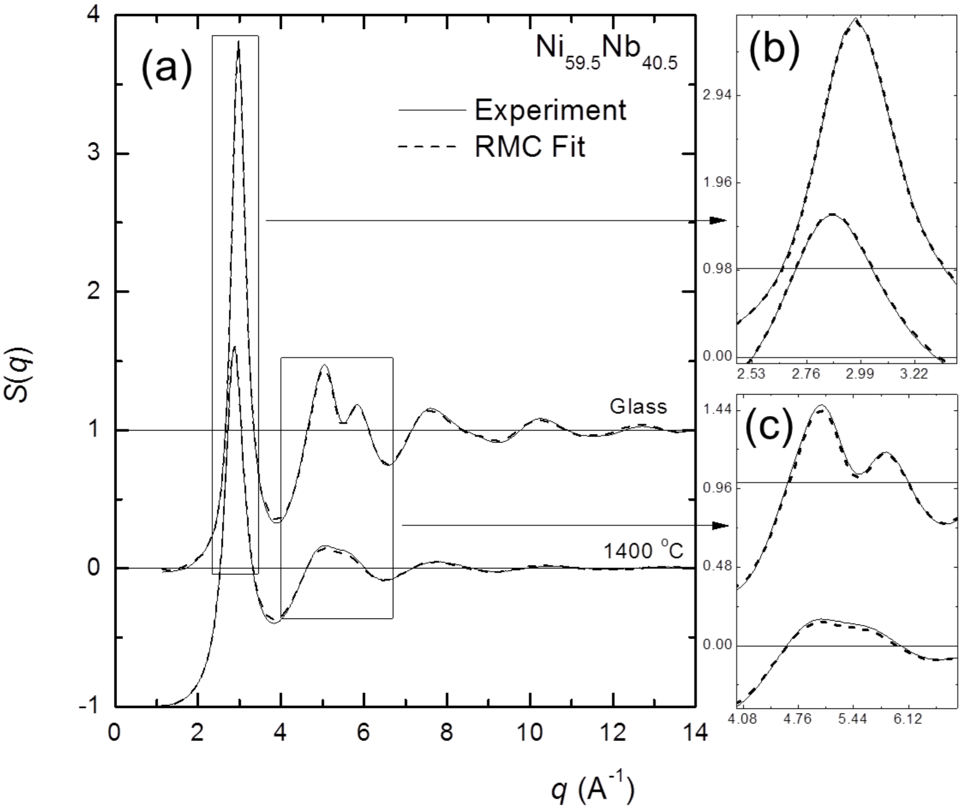

Figure 3.5 Representative RMC fits for $Ni_{59.5}Nb_{40.5}$ at 1400°C (liquid) and 25°C (glass). (a) The RMC fits over the entire *q* range; (b) the RMC fits for the first peaks; (c) the RMC fits for the second peaks.

An HA analysis was made of the structures obtained from the RMC fits; the most relevant indices are shown in Figure 3.6. The variations in HA for the different initial configurations for the RMC fits are reflected in the error bars presented. Liquids and glasses of all compositions show prevalence for icosahedral (1551) and distorted icosahedral (1541+1431) local order, which is common in TM-based metallic liquids and glasses [22, 35, 59]. For the liquids, this order exceeds 30-40% of the sum of all of the HA nearest-neighbor indices, regardless of temperature. However, the fraction of icosahedral and icosahedral-like order becomes even more dominant in the glass, exceeding 60% of the total sum of HA indices. This is due in large part to a dramatic increase in the 1551 index. Only small amounts of BCC-type (1661) and crystal-close-packed-type (1421 +1421) order are observed in the liquids and glasses.

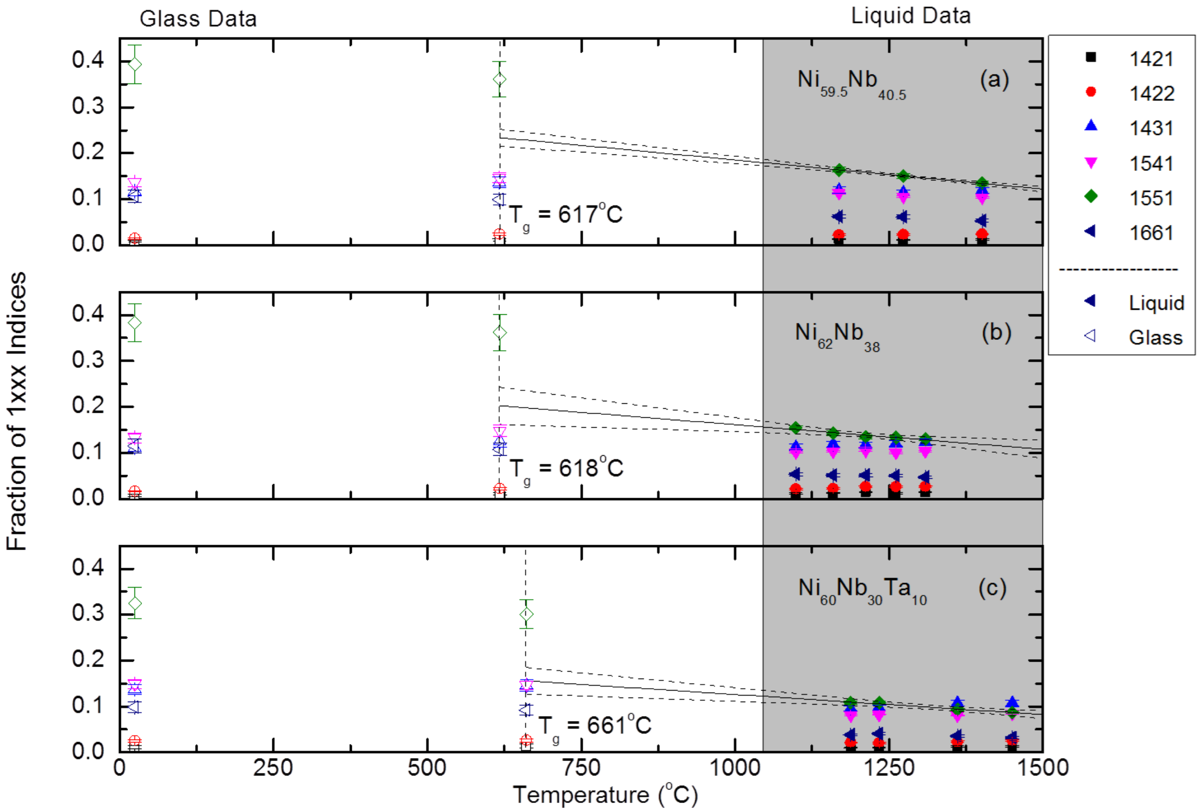

Figure 3.6 HA analysis of the structures obtained from the RMC fits for each composition at each temperature, scaled to the total number of measured 1xxx pairs. The HA indices calculated from the room temperature *S*(*q*) data for the glass after extrapolation to the glass transition temperature. The best fit lines for the 1551 index (liquid only) for each composition are shown with 95% confidence intervals, extrapolated to near T_g. The data corresponding to the liquid HA indices are indicated with solid symbols; those corresponding to the glasses are shown as open symbols.

An interesting feature emerges on examining the growth of the 1551 index. In the liquid, this index increases approximately linearly with decreasing temperature (Figure 3.6); the best-fit lines are shown with 95% confidence intervals. Since upon cooling, the rate of structural change in the glass is arrested near T_g, the number of 1551 indices estimated from the results of a RMC fit to the glass *S*(*q*) data at T_g, extrapolated from the room-temperature data, should correctly reflect the structure at that temperature. A linear extrapolation of the number of 1551 indices in the liquid phase to the glass transition temperature (noted for all compositions in Figure 3.6) is well below that estimated for the glass. Like the trends observed in the *S*(*q*) and *g*(*r*) peak heights, these results suggest that the rate of development of the 1551 index *accelerates* at some temperature between T_g and the lowest temperature at which data were obtained in the supercooled liquid. This acceleration is not observed in the other indices, which is consistent with the results of MD simulations for Cu-Zr liquids and glasses [23], where only some features of the local atomic order accelerate near T_g. Like the experimental results shown here in the Ni-Nb and Ni-Nb-Ta liquids, the MD simulations show that, for Cu-Zr liquids above but near T_g, the 1551 index decreases rapidly with increasing temperature [23].

It might be expected that the rate of increase in the 1551 HA in the liquids would be arrested on cooling toward the glass transition temperature, reflecting a decreasing atomic mobility which should cause a decrease in the rate of structural evolution. Such behavior has been observed in a few bulk metallic glass-formers in the Zr-based family [25, 26] and the Pd-based family [26, 27]. The differences in the structural evolution of these Zr-BMG-forming liquids and the Ni-Nb glass-forming liquids can be understood within the fragility classification (*strong/fragile*) [60]. Quantities such as the viscosity, specific heat, volume, *etc*. change more rapidly near T_g for fragile liquids than for strong liquids. The data presented here suggest that structural properties derived from the X-ray static structure factor also provide a measure of the fragility. Within the framework of fragility, schematically illustrated in Figure 3.7, the structural changes in strong liquids are expected to be more gradual and begin at higher temperatures than in fragile liquids, which would show significant structural changes only near the glass transition temperature.

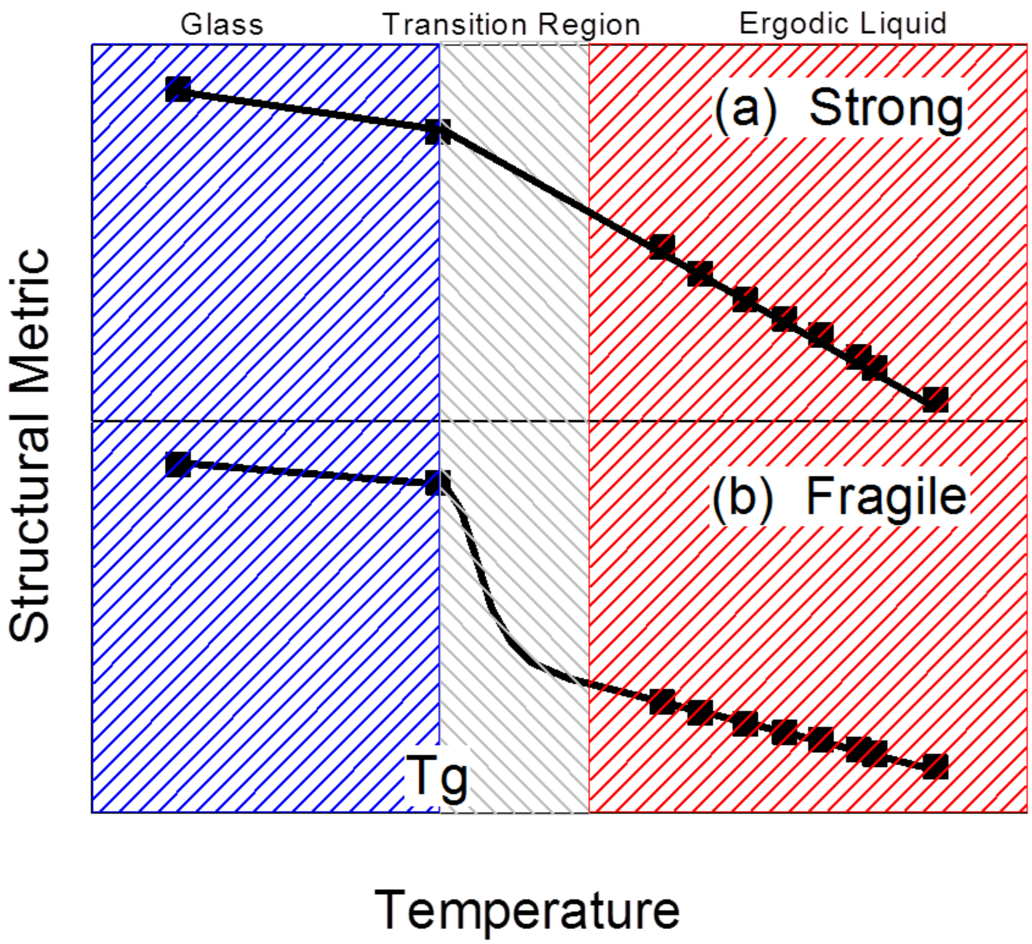

Figure 3.7 Schematic illustration of how structural metrics such $S(q_1)$, $g(r_1)$, HA index, etc. change with temperature for (a) strong and (b) fragile liquids.

Rapid structural ordering in liquids of the type inferred here has been observed in MD simulations. Cu-Zr liquids, for example, show the rapid formation of Cu-centered clusters, near T_g but before vitrification [24]. However, to our knowledge this is the first study of this directly from scattering data. Further, rapid structural ordering in Ni-Nb-based liquids upon approaching T_g has not been observed previously in scattering experiments or MD simulations. The atomic structures of Ni-Nb glasses are believed to be fundamentally different from those of the Zr-rich binary glasses [61]. Yet both are fragile and both indicate rapid structural ordering in the liquid at temperatures near the glass transition temperature. Taken together, then, the MD results for

Cu-Zr liquids and the experimental results presented here indicate that the temperature-dependent structural changes that can be deduced directly from the $S(q)$ and $g(r)$ obtained from X-ray studies could be a universal indicator of liquid fragility. If true, such structural studies could provide an easier method for obtaining fragility information than from viscosity measurements. Since the HA indices for icosahedral ordering are the ones that show the most dramatic change on approaching T_g, this suggests that icosahedral ordering is intimately linked to fragility. It also supports previous work indicating that icosahedral ordering plays an important role the glass transition [30].

3.5 Conclusion

Containerless measurements were made of the density, volume, thermal expansivity and X-ray diffraction for $Ni_{62}Nb_{38}$, and $Ni_{60}Nb_{30}Ta_{10}$ (bulk metallic glass-forming) and for $Ni_{59.5}Nb_{40.5}$ (non-bulk metallic glass-forming) equilibrium and supercooled liquids. Atomic structures were obtained from Reverse Monte Carlo fits to the scattering data. Few experimental data sets exist that include structural measurements for both the supercooled liquids and the glasses at the same composition. Interestingly, the structural and thermophysical properties are similar, despite the different glass-forming abilities of the liquids. This indicates that the signature of glass formability in the liquid far above the glass transition temperature is weak. However, based on the evolution of the amplitude of the primary peak in $S(q)$, the first peak in $g(r)$, and the amount icosahedral order in the structure (in terms of the HA 1551 index), there is an acceleration of the structural change in the liquid near the glass transition temperature. This rapid development of structural ordering is similar to what is observed in the viscosity, specific heat, volume, *etc*., of a fragile liquid. This is in contrast to the behavior observed in a Zr-based bulk metallic-glass-forming strong liquid. There, the growth of the icosahedral 1551 HA index changes linearly in the liquid with decreasing temperature, with the rate of change decreasing near T_g as a consequence of the decreasing atomic mobility. That the 1551 index shows the expected behavior for both strong and fragile glasses, indicates that the evolution of icosahedral order is intimately linked to liquid fragility.

3.6 References

[1] N.A. Mauro, M.L. Johnson, J.C. Bendert, K.F. Kelton, *Journal of Non-Crystalline Solids* **362**, 237 (2013).

[2] D. Wang, Y. Li, B.B. Sun, M.L. Sui, K. Lu, E. Ma, *Applied Physics Letters* **84**, 4029 (2004).

[3] D. Xu, G. Duan, W. Johnson, *Physical Review Letters* **92**, 245504 (2004).

[4] D.H. Xu, B. Lohwongwatana, G. Duan, W.L. Johnson, C. Garland, *Acta Materialia* **52**, 2621 (2004).

[5] L. Xia, W.H. Li, S.S. Fang, B.C. Wei, Y.D. Dong, *Journal of Applied Physics* **99**, 026103 (2006).

[6] P. Jia, J. Xu, *Journal of Materials Research* **24**, 96 (2009).

[7] Y. Wang, Q. Wang, J. Zhao, C. Dong, *Scripta Materialia* **63**, 178 (2010).

[8] A. Kawashima, H. Habazaki, K. Hashimoto, *Materials Science and Engineering: A* **304-306**, 753 (2001).

[9] A. Inoue, *Acta Materialia* **48**, 279 (2000).

[10] M.H. Cohen, D. Turnbull, *Nature* **189**, (1961).

[11] H. Choi-Yim, D. Xu, W.L. Johnson, *Applied Physics Letters* **82**, 1030 (2003).

[12] H. Choi-Yim, D. Xu, W. Johnson, *Journal of Alloys and Compounds* **449-451**, (2007).

[13] M. Lee, D. Bae, W. Kim, D. Kim, *Materials Transactions* **44**, 2084 (2003).

[14] W. Zhang, A. Inoue, *Materials Transactions* **43**, 2342 (2002).

[15] G.W. Lee, A.K. Gangopadhyay, K.F. Kelton, R.W. Hyers, T.J. Rathz, J.R. Rogers, D.S. Robinson, *Physical Review Letters* **93**, 037802 (2004).

[16] K.F. Kelton, G.W. Lee, A.K. Gangopadhyay, R.W. Hyers, T.J. Rathz, J.R. Rogers, M.B. Robinson, D.S. Robinson, *Physical Review Letters* **90**, 195504 (2003).

[17] S. Basak, R. Clarke, S.R. Nagel, *Physical Review B* **20**, (1979).

[18] P. Lamparter, *Physica Scripta* **T57**, 45 (1995).

[19] E. Svab, F. Forgacs, F. Hajdu, N. Kroo, J. Takacs, *Journal of Non-Crystalline Solids* **46**, 125 (1981).

[20] E. Svab, G. Meszaros, G. Konczos, S.N. Ishmaev, S.L. Isakov, I.P. Sadikov, A.A. Chernyshov, *Journal of Non-Crystalline Solids* **104**, 291 (1988).

[21] S. Sachdev, D.R. Nelson, *Physical Review Letters* **53**, 1947 (1984).

[22] N.A. Mauro, V. Wessels, J.C. Bendert, S. Klein, A.K. Gangopadhyay, M.J. Kramer, S.G. Hao, G.E. Rustan, A. Kreyssig, A.I. Goldman, K.F. Kelton, *Physical Review B* **83**, 184109 (2011).

[23] M.I. Mendelev, M.J. Kramer, R.T. Ott, D.J. Sordelet, M.F. Besser, A. Kreyssig, A.I. Goldman, V. Wessels, K.K. Sahu, K.F. Kelton, R.W. Hyers, S. Canepari, J.R. Rogers, *Philosophical Magazine* **90**, 3795 (2010).

[24] Y. Cheng, H. Sheng, E. Ma, *Physical Review B* **78**, 014207 (2008).

[25] Y.T. Shen, T.H. Kim, A.K. Gangopadhyay, K.F. Kelton, *Physical Review Letters* **102**, 057801 (2009).

[26] N. Mattern, J. Sakowski, U. Kühn, H. Vinzelberg, J. Eckert, *Journal of Non-Crystalline Solids* **345–346**, 758 (2004).

[27] N. Mattern, H. Hermann, S. Roth, J. Sakowski, M.-P. Macht, P. Jovari, J. Jiang, *Applied Physics Letters* **82**, 2589 (2003).

[28] N.A. Mauro, K.F. Kelton, *Review of Scientific Instruments* **82**, 035114 (2011).

[29] A.K. Gangopadhyay, G.W. Lee, K.F. Kelton, J.R. Rogers, A.I. Goldman, D.S. Robinson, T.J. Rathz, R.W. Hyers, *Review of Scientific Instruments* **76**, 073901 (2005).

[30] M.A. Khan, C. Allemand, T.W. Eagar, *Review of Scientific Instruments* **62**, 392 (1991).

[31] R.C. Bradshaw, D.P. Schmidt, J.R. Rogers, K.F. Kelton, R.W. Hyers, *Review of Scientific Instruments* **76**, 125108 (2005).

[32] S.K. Chung, D.B. Thiessen, W.-K. Rhim, *Review of Scientific Instruments* **67**, 3175 (1996).

[33] T. Ishikawa, P.-F. Paradis, S. Yoda, *Review of Scientific Instruments* **72**, 2490 (2001).

[34] D.A. Keen, R.L. Mcgreevy, *Nature* **344**, 423 (1990).

[35] T.H. Kim, K.F. Kelton, *The Journal of Chemical Physics* **126**, 054513 (2007).

[36] R.L. Mcgreevy, *Journal of Physics-Condensed Matter* **3**, F9 (1991).

[37] J.D. Honeycutt, H.C. Andersen, *Journal of Physical Chemistry* **91**, 4950 (1987).

[38] A.P. Hammersley, S.O. Svensson, M. Hanfland, A.N. Fitch, D. Hausermann, *High Pressure Research* **14**, 235 (1996).

[39] M. Hansen, K. Anderko, *Constitution of Binary Alloys*, McGraw-Hill, New York, 1958.

[40] Z. Kejun, Z. Xianzhang, J. Zhanpeng, *Journal of Alloys and Compounds* **179**, 177 (1992).

[41] T.B. Massalski, J.L. Murray, J.H. Bennett, H. Baker, in, American Society for Metals, Metals Park, OH, 1986.

[42] B. Predel,

[43] S. Mukherjee, Z. Zhou, W.L. Johnson, W.-K. Rhim, *Journal of Non-Crystalline Solids* **337**, 21 (2004).

[44] M.B. Robinson, D. Li, J.R. Rogers, R.W. Hyers, L. Savage, T.J. Rathz, *Applied Physics Letters* **77**, 3266 (2000).

[45] R.C.o. America, in, 1962.

[46] P. Nash, A. Nash, *Bulletin of Alloy Phase Diagrams* **7**, (1986).

[47] P.F. Peterson, E.S. Božin, T. Proffen, S.J.L. Billinge, *Journal of Applied Crystallography* **36**, 53 (2003).

[48] T.E. Faber, J.M. Ziman, *Philosophical Magazine* **11**, 153 (1965).

[49] F.R.D. Boer, R. Boom, W.C.M. Mattens, A.R. Miedema, A.K. Niessen, *Cohesion In Metals: Transition Metal Alloys (Cohesion And Structure)*, North-Holland, Amsterdam, 1988.

[50] N.A. Mauro, K.F. Kelton, *Journal of Non-Crystalline Solids* **358**, 3057 (2012).

[51] S. Sinha, P.L.L. Srivastava, R.N.N. Singh, *Journal of Physics: Condensed Matter* **1**, 1695 (1989).

[52] C.Y. Ho, R.W. Powell, P.E. Liley, *Journal of Physical Chemistry* **Ref. Data 3**, 1 (1974).

[53] R.L. McGreevy, *Journal of Physics: Condensed Matter* **13**, (2001).

[54] R.L. McGreevy, P. Zetterström, *Current Opinion in Solid State and Materials Science* **7**, 41 (2003).

[55] R.L. McGreevy, *Journal of Non-Crystalline Solids* **156-158**, 949 (1993).

[56] N.A. Mauro, *Structural and Thermophysical Property Studies of Metallic Liquids and Glasses Using the Beamline Electrostatic Levitation Technique*, Ph.D. Thesis, Washington University in St. Louis (2011).

[57] D.K. Belashchenko, G.F. Syrykh, *Inorganic Materials* **40**, 483 (2004).

[58] L. Pusztai, E. Sváb, *Journal of Non-Crystalline Solids* **156-158**, 973 (1993).

[59] V. Wessels, A.K. Gangopadhyay, K.K. Sahu, R.W. Hyers, S.M. Canepari, J.R. Rogers, M.J. Kramer, A.I. Goldman, D.S. Robinson, J.W. Lee, J.R. Morris, K.F. Kelton, *Physical Review B* **83**, 094116 (2011).

[60] C.A. Angell, *Journal of Physics and Chemistry of Solids* **49**, 863 (1988).

[61] H.W. Sheng, W.K. Luo, F.M. Alamgir, J.M. Bai, E. Ma, *Nature* **439**, 419 (2006).

Chapter 4: Structural Evolution and Thermophysical Properties of Zr_xNi_{100-x} Metallic Liquids and Glasses [1]

This chapter has been published in the *Journal of Non-Crystalline Solids* in collaboration with N. A. Mauro, A. J. Vogt, M. E. Blodgett, C. Pueblo, and K. F. Kelton [1], and has been adapted to be consistent with the formatting in this dissertation. The author's personal contributions include the acquisition and analysis of X-ray and thermophysical data and writing the manuscript. Initial data reduction and preliminary results were performed by A. J. Vogt. Some viscosity data were acquired by M. E. Blodgett. Glassy ribbons were prepared by C. Pueblo, who also performed DTA and DSC measurements. All authors participated in the acquisition of high-energy X-ray data during BESL 2013 and significantly contributed in drafting the results.

4.1 Introduction

Since the discovery of metallic glasses [2], considerable effort has gone into understanding the fundamental processes that govern why some metallic liquids can be cooled slowly into a glass, while others must be rapidly-quenched. The rapidly slowing liquid kinetics upon approaching the glass transition temperature, T_g, play a significant role in glass formation, which ultimately hinges on avoiding crystallization. Since the viscosity increases by nearly 15 orders of magnitude from the liquidus temperature to T_g, it is a particularly sensitive property, useful for characterizing liquids. As the temperature is decreased, the viscosity increases with an Arrhenius behavior for those liquids characterized as *strong*. In contrast, *fragile* liquids show highly non-Arrhenius behavior, with a rapid increase in the apparent activation energy upon approaching T_g [3]. Generally strong liquids have a higher glass-forming ability (GFA) than fragile liquids [4-6], making a deeper understanding of fragility of both fundamental as well as practical interest. While fragility is typically defined in terms of the viscosity, it fundamentally reflects ordering in the liquid structure. Improvements in containerless processing and levitation techniques allow this ordering to now be investigated quantitatively. While some structural studies have been possible using containers, structural investigations of glass-forming liquids over a wide compositional range are lacking. The recent development of the Washington University Beamline Electrostatic Levitation facility (WU-BESL) [7, 8] has enabled such studies, allowing high-energy X-ray diffraction studies to be made of metallic liquids and glasses for a wide range of alloy families and compositions. These experiments have provided precise determinations of the X-ray static structure factors, $S(q)$, and pair-correlation functions, $g(r)$, for many glass-forming liquids. With this improved data quality, the link between structural ordering and fragility was recently demonstrated experimentally [9]. As explained later in this section, the Zr-Ni liquids provide an excellent system for exploring these points further and for developing possible correlations between GFA and structural and thermophysical properties.

Both X-ray and neutron scattering experiments have shown that with increased supercooling, metallic liquids develop significant short-range and often medium-range order [10-14]. While the total structure factors and pair-correlation functions are qualitatively similar for almost all metallic liquids and glasses, it has been established recently that there are quantitative differences that may be correlated with GFA [9]. For Ni-Nb [15], Cu-Zr [16, 17], and other fragile metallic glass-forming liquids, studies have shown that the ordering must accelerate as the temperature of the supercooled liquid approaches T_g. In several studies of fragile liquids, Reverse Monte Carlo (RMC) fits to experimental data [15] and molecular dynamics (MD) simulations [18] have demonstrated that the rapid ordering is due to a rapid increase in the number of particular local atomic clusters. Experimentally, the increased ordering manifests as a deviation from an extrapolation of the first peak height in the total structure factor, $S(q_1)$, of the high-temperature liquid to the glass at T_g, leading to the definition of a *structural fragility index* [9]

$$\gamma = 100 * \frac{S(q_1)_{glass} - S(q_1)_{liquid\ extrapolation}}{S(q_1)_{glass}} \text{ at } T_g. \tag{4.1}$$

Like the kinetic fragility parameter, m, γ increases with increasing liquid fragility. The rapid increase in $S(q_1)$ near T_g for fragile liquids is in contrast to the behavior of $S(q_1)$ for stronger Zr- and Pd- based liquids [19]. There, the extrapolated high-temperature liquid values for $S(q_1)$ are nearly the same as for the glass at T_g, indicating a more constant rate of structural ordering over the temperature range from near the liquidus temperature, T_L, to T_g.

Since metallic liquids with high GFA typically contain four or more components, the measured total structure factor is composed of many partial structure factors, making it extremely difficult to unravel the nature of the chemical and topological ordering. The simpler binary liquids and glasses are better suited for such studies, although they have a lower GFA. Zr-Ni is known to form a glass across a wide range of compositions, albeit only when rapidly-quenched at cooling rates of at 10^5-10^6 K/s [20]. These alloys also form the basis of more complex alloys with better GFA. Zr-Ni liquids and glasses have been extensively studied by X-ray [21-25] and neutron scattering [14, 23, 26-31], as well as through simulations [22, 32-34]. The results from these studies have attracted attention because of the evidence for significant chemical ordering in both the liquid and glass [22, 23, 32, 34]. However, to our knowledge, there has never been a comprehensive investigation of the ordering of Zr-Ni across a large compositional range. Furthermore, most structural studies have focused only on the liquid or the glass and not the relationship between the two.

In this work, results from a coordinated study of the structure and thermophysical properties are presented for three Zr-Ni alloys selected to represent a wide compositional range: $Zr_{36}Ni_{64}$, $Zr_{57}Ni_{43}$, and $Zr_{76}Ni_{24}$. Viscosity and density measurements were made over a wide temperature range for all liquids while processing in a containerless environment. Results from high-energy X-ray diffraction studies of the equilibrium and supercooled liquids and the corresponding glasses suggest that distinct asymmetric features in the total pair-distribution function reflect chemical ordering in all three alloys, starting in the high-temperature liquid and increasing into the glass. Based on a quantitative analysis of the temperature dependence of the static structure factor, all three liquids are fragile.

4.2 Experimental procedure

Master ingots for all compositions were prepared by arc-melting high-purity Zr (99.95 at.%, including Hf nominal 3 at.%) and Ni (99.995 at.%) on a Cu hearth in a high-purity (99.999 at.%) Ar atmosphere. A Ti-Zr getter located close to the sample was melted prior to arc-melting to further reduce the oxygen concentration in the chamber. Each ingot was melted three times to ensure that the samples were homogeneous; each melt cycle lasted approximately 60 s. Sample mass loss during arc-melting was negligible (less than 0.1%). The master ingots were subsequently crushed and portions were re-melted to obtain small spherical samples (~2.5 mm diameter) for *in situ* liquid structural studies at the Advanced Photon Source (APS) in sector 6-ID-D, using the Washington University Beamline Electrostatic Levitator (WU-BESL) [7, 8]. WU-BESL is optimized for X-ray diffraction studies of levitated, containerlessly processed liquids in a high-vacuum environment (~10^{-7} Torr). Metallic glasses were prepared by RF induction, melting portions of the master ingot in a graphite crucible under a high-purity (99.998%) Ar atmosphere and then rapidly quenching the liquid onto a copper wheel that was rotating at ~60 m/s. This produced continuous 3-10 cm ribbons with an average cross section of 1-2 mm x 20-30 μm. Studies made using a Rigaku powder diffractometer (Cu K_α, λ = 1.54 Å) and high-energy X-ray diffraction studies made at the APS confirmed that the as-quenched ribbons were fully amorphous.

For the levitation experiments, the liquid samples were heated, melted, and subsequently thermally processed using a fiber-coupled diode laser (980 nm, 50 W continuous maximum power output). Crystallization of the supercooled liquid, marked by a sharp rise in temperature (recalescence), limited the lowest temperature for the X-ray diffraction studies to 230 ^{o}C below the liquidus temperature. Sample masses were measured before and after thermal processing to determine the mass loss during processing, which would indicate a change in composition due to Ni evaporation. Based on measurements of the partial pressure of oxygen in the levitation chamber, the mass change from oxygen absorption or oxidation is negligible. Our evaporation measurements indicate that the large negative heats of mixing between Ni and Zr decrease the evaporation rate significantly below a rule of mixtures estimate, leading to a maximum predicted composition shift of 0.1 at.% during the thermal cycling of these experiments. Care was taken to limit the time each sample was at extreme temperatures, and in all cases the mass loss was negligible.

Single amorphous ribbons were mounted to a resistive heating apparatus in the WU-BESL and held in approximately the same location as the levitated samples. The ribbons were thermally cycled from room temperature to near T_g multiple times, while simultaneously acquiring diffraction images and temperature measurements. The cycling allowed the diffraction patterns to be monitored until they were completely reversible up to T_g, indicating complete structural relaxation before crystallization occurred. The relaxed glasses were then held isothermally for 60 s at a series of temperatures that increased towards T_g. They were then heated at a rate of 40 to 100 K/min through T_g until crystallization was observed. The resistive method used here allowed the samples to be heated quickly and their small size allowed them to cool quickly when the heating current was removed. It is more common to place samples in a quartz capillary, which is then heated with an external furnace. However, this suffers from slow heating and cooling rates. The lack of a capillary greatly reduced the background scattering, allowing the quantitative structural studies presented here.

The temperatures of the amorphous ribbons and levitated liquids were measured from 160 ^{o}C to 2300 ^{o}C using two infrared pyrometers with overlapping temperature ranges. A single-color Process Sensors Metis MI18 MB8, operating at a 1.89 μm wavelength, was used for low-temperature measurements (160-800 ^{o}C) of the liquids and glasses and a Process Sensors Metis MQ22 two-color ratio pyrometer, operating at 1.40 and 1.65 μm wavelengths, was used for high-temperature measurements (600-2300 ^{o}C) of the liquids. Ratio pyrometers provide more accurate measurements of the temperature because emissivity changes with temperature are normalized out [35], since relative changes in the emissivity at each of the two close wavelengths are expected to be small. A constant emissivity ratio was assumed for the entire temperature range over which structural data were acquired. For the liquids, the emissivity ratio was calibrated by matching the melt plateau in the temperature versus time curve measured on heating in the BESL to the largest endothermic signature measured in a differential thermal analyzer (DTA) (Labsys^{TM} DTA/DSC, Setaram). In the ESL measurements, the plateau corresponds to the solidus temperature, T_S. For the amorphous ribbons, the low-temperature pyrometer was calibrated by matching the onset temperature of the appearance of crystal peaks in the X-ray diffraction patterns with the onset temperature for the exothermic crystallization signature in a differential scanning calorimeter (DSC) (PerkinElmer DSC 7). The same heating rates were used for the X-ray and DSC studies.

For the liquid samples, the temperature was correlated with non-contact measurements of the volume. The projected area of the sample was obtained using the shadow method [36, 37] with a Pixelink PL-B74IG CMOS camera and a 455 nm collimated microscope LED, which has a total beam power of 240 mW and a beam diameter of 37 mm. The video data were taken at a frame rate of 20-25 fps. The pixel dimensions were calibrated before and after the set of measurements on each sample using 2.38125 ± 0.00076 mm diameter (grade 3) tungsten carbide standards. The volume was determined from the area data, assuming that the sample was symmetric about the vertical axis [38], and the density was calculated from the product of the inverse of the volume and the measured sample mass. The relative precision of the density data was ~0.3% over the temperature range studied, with an absolute accuracy of ~0.5%; the measurement error is dominated by errors in the calibrations of the volume and mass. A more detailed discussion of the machine vision volume measurement algorithm can be found elsewhere [36]. The densities of the amorphous ribbons were determined at room temperature using Archimedes' method, with toluene as the working fluid. The total uncertainties in the values obtained were between 1% and 2%.

The liquid viscosity was measured as a function of temperature using the oscillating drop technique [39-41], where a perturbing voltage on the top and bottom electrodes caused sample oscillation. The viscosity is related to the decay time in the surface oscillation when the perturbation is removed. The surface oscillations were measured by a Pixelink PL-B74IG CMOS camera operating at a high frame rate (1500 fps). More detail is given elsewhere [41].

The diffraction studies of the liquids and glasses were made in a transmission geometry, using high-energy X-rays (E = 132 keV, λ = 0.0940 Å). Scattering data were obtained to a momentum transfer, q, of 20 Å^{-1} at a sampling rate of 1 Hz using a GE Revolution 41-RT amorphous Si flat-panel X-ray detector. The sample-to-detector distance, detector tilt, and detector center were calibrated by fitting the diffraction pattern of a levitated polycrystalline Si sample. These values were confirmed using a NIST Si standard in a capillary placed at the position of the levitated liquid sample. The scattering data obtained were processed by masking bad pixels, applying a pixel efficiency gain map, averaging the images obtained during the isothermal hold, and subtracting the appropriate detector dark current and scattering background. Images were then corrected for oblique incidence, absorption, multiple scattering, fluorescence, polarization, sample geometry, and Compton scattering contributions using in-house analysis packages written in LabVIEW$^{\text{TM}}$ [42]. A series of measurements were made at each temperature step (15-20 s duration for liquids, up to 60 s for glasses) to obtain the total static structure factor using

$$S(q) = \frac{I(q) - \sum_{i=1}^{n} c_i \left| f_i(q) \right|^2}{\left| \sum_{i=1}^{n} c_i f_i(q) \right|^2} + 1, \tag{4.2}$$

where $I(q)$ is the measured diffraction intensity, c_i is the atomic fraction of each elemental species, and $f_i(q)$ is the q-dependent atomic form factor for each species. The sums were taken over all species and an isotropic and statistically homogeneous atomic distribution was assumed.

The total pair-correlation function, $g(r)$, was computed from a Fourier transform of the structure factor,

$$g(r)-1=\frac{1}{4\pi\rho_0}\frac{2}{\pi}\int(S(q)-1)\frac{\sin(qr)}{qr}q^2dq\,, \tag{4.3}$$

where ρ_0 is the average number density.

The positions and magnitudes of the first peaks in $S(q)$ were refined by fitting a cubic spline to the peak. The total measurement uncertainties were estimated by considering perturbations from independent sources of error (including statistical uncertainties) following the method described by Hammersley [43], and from the confidence intervals of fitted correction factors (e.g. intensity normalization). Based on this, the precision of the peak heights in $S(q)$ was 0.4-1.7% for both liquids and glasses. However, because the scattering from the single-ribbon glasses was weak, the accuracy of the calculated peak heights in $S(q)$ is estimated, at ~6%. The accuracy in the calculated peak heights in $S(q)$ for the liquids is much better, ~1%, due to the high signal-to-noise in the scattering data.

4.3 Results and Discussion

For each composition, a single melt plateau at the solidus temperature, T_S, was observed upon heating. These temperatures were calibrated using DTA measurements of T_S, which gave 1070 ± 5 ^{o}C for $Zr_{36}Ni_{64}$, 1025 ± 5 ^{o}C for $Zr_{57}N_{43}$, and 980 ± 5 ^{o}C for $Zr_{76}Ni_{24}$. Representative temperature-time curves for each composition are shown in Figure 4.1. An inflection was observed during the heating of $Zr_{57}Ni_{43}$ at constant laser intensity (Figure 4.1 (b)), indicating a two-phase solid-liquid region that extended to a liquidus temperature, T_L, of 1180 ± 5 ^{o}C. These temperatures are in reasonable agreement with the best available phase diagram for these alloys

[44]. The accessible temperature range for the liquid studies was limited by the evaporation rate of Ni at high temperatures and the maximum supercooling temperature, which varied with composition.

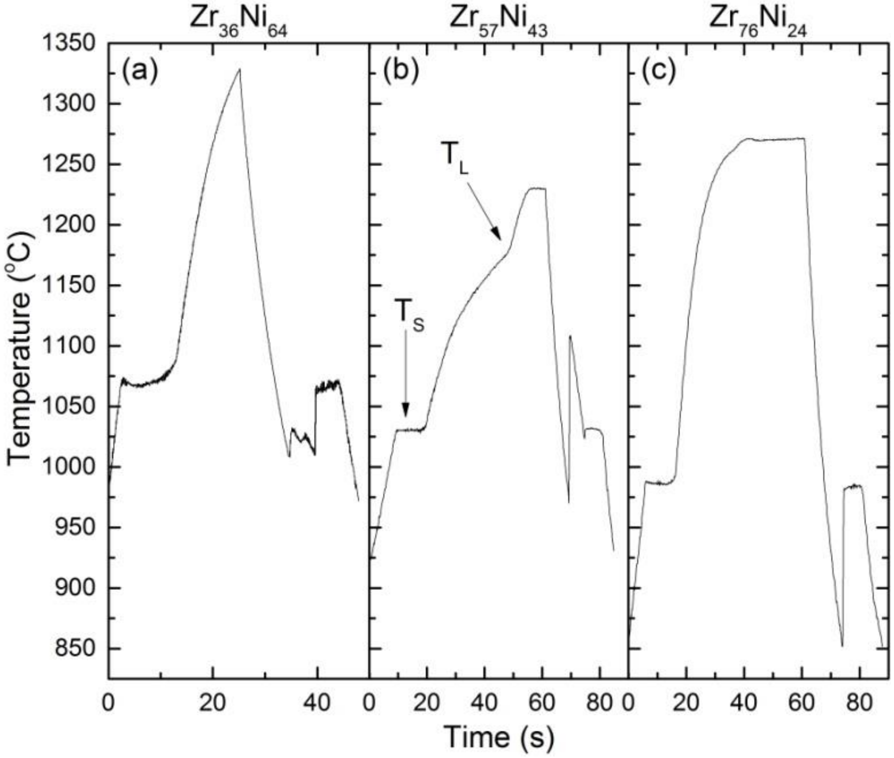

Figure 4.1 Representative temperature-time curves for a typical heating and free-cooling cycle for the three compositions studied: (a) $Zr_{36}Ni_{64}$, (b) $Zr_{57}Ni_{43}$, and (c) $Zr_{76}Ni_{24}$. The solidus temperature, T_S, in each cycle corresponds to the temperature plateau upon heating. An inflection at higher temperature in (b) corresponds to the liquidus temperature, T_L. The absence of an inflection in either Figure 4.1 (a) or (c) indicates that these are eutectic alloys.

The sample volume was measured as a function of temperature for multiple radiative free-cooling cycles and combined with the mass to compute the liquid density. Over the measured temperature range (~400 ^{o}C) the density and volume scale linearly with temperature for all liquid compositions. The density is described by

$$\rho(T) = \rho_S + \frac{d\rho}{dT}(T - T_S)\,, \tag{4.4}$$

where ρ_S is the liquid density at the solidus temperature, T_S. The average density increases with increasing Ni concentration, consistent with the higher density of Ni relative to Zr, and agrees with measurements made in other Zr-Ni glasses [31]. The coefficient of thermal expansion at the solidus temperature, α_S, was calculated for all liquids from a linear fit of the volume as a function of temperature using

$$\alpha_S = \left(\frac{1}{V} \frac{\partial V}{\partial T} \right)_{P,\, T=T_S} . \tag{4.5}$$

The fitting parameters are listed in Table 4.1.

Table 4.1 Fitting Parameters for the Density and Volume for each Liquid Composition[a].

Composition	**T_S (^{o}C)**	**Liquid ρ_S (g cm^{-3})**	**Liquid $d\rho/dT$ (g cm^{-3} ^{o}C^{-1})**	**α_S (^{o}C^{-1})**	**Glass ρ (g cm^{-3})**
$Zr_{36}Ni_{64}$	1070 ± 5	7.50 ± 0.01	-5.09 ± 0.02 E-4	6.87 ± 0.03 E-5	7.87 ± 0.10
$Zr_{57}Ni_{43}$	1025 ± 5	7.02 ± 0.01	-3.51 ± 0.02 E-4	5.08 ± 0.04 E-5	7.21 ± 0.09
$Zr_{76}Ni_{24}$	980 ± 5	6.67 ± 0.01	-2.94 ± 0.02 E-4	4.46 ± 0.03 E-5	6.87 ± 0.13

[a] The solidus temperature, T_S, was determined from DTA measurements; the liquid density at the solidus, ρ_S, rate of change of the liquid density with temperature, $d\rho/dT$, and the coefficient of liquid thermal expansion at the solidus, α_S, were determined using the BESL; the glass density at room temperature, ρ, was determined using Archimedes' method.

The liquid viscosity, η, was measured as a function of temperature for all liquid compositions (Figure 4.2). It is not possible to present the Zr-Ni liquid viscosity in a typical Angell plot [3] since, consistent with previous reports [45, 46], no definitive T_g was observed in our DSC scans for the Zr-Ni glasses despite initially annealing the sample at low temperatures. Over the high temperature range where it could be measured, however, $\log_{10}(\eta)$ scales approximately linearly with inverse temperature, with only a subtle curvature evident (Figure 4.2 (b)). This indicates that the activation energy for flow is approximately constant over this temperature range, as expected for high-temperature metallic liquids [47, 48]. An effective activation energy was calculated from the slope of a linear fit to the Arrhenius region of ln(η) vs. 1/T using the form

$$\ln(\eta) = \ln(\eta_0) + \frac{E_A}{R}\frac{1}{T}, \tag{4.6}$$

where E_A is the activation energy, R is the ideal gas constant, and η_0 is the viscosity at infinite temperature (Table 4.2).

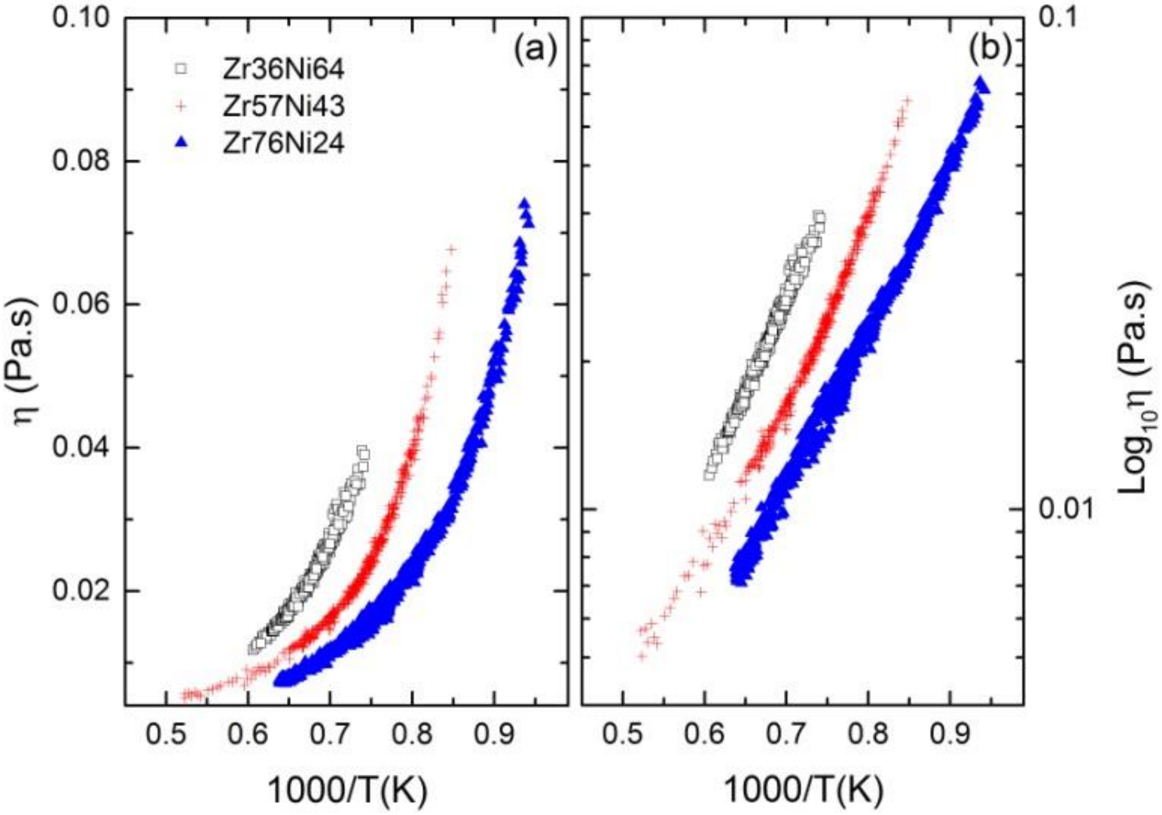

Figure 4.2 (a) Liquid viscosity, η, as a function of reduced inverse temperature. (b) $\log_{10}(\eta)$ versus reduced inverse temperature. In (b) a constant slope is observed over a significant portion of the temperature range studied, indicating a constant activation energy in the high-temperature liquid.

While, as mentioned, T_g is difficult to measure in the Zr-Ni glasses, the crystallization temperature, T_x, is easily measured due to the large enthalpy release. Previous studies have indicated that $T_x - T_g < 10$ K for Zr-Ni alloys [45]. Due to the difficulty in measuring T_g, $T_g \approx T_x$

is used here. DSC measurements of the onset temperature for crystallization were used to calibrate the temperature in the structural studies of the amorphous ribbons. Similar heating and quench rates were used for both measurements. The crystallization temperatures obtained at a heating rate of 40 K/min are presented in Table 4.2.

Table 4.2 DSC Crystallization Temperature and Effective Activation Energy for Viscosity.

Sample	**T_x (40 K/min)**	**Effective Activation Energy (E_A)**
$Zr_{36}Ni_{64}$	568 ± 3 ^oC	72.7 ± 0.4 kJ/mol
$Zr_{57}Ni_{43}$	463 ± 3 ^oC	54.6 ± 0.6 kJ/mol
$Zr_{76}Ni_{24}$	353 ± 3 ^oC	58.4 ± 0.3 kJ/mol

The total structure factors, $S(q)$, for both the liquids and glasses were calculated from the measured intensity, $I(q)$, using Eqn. 4.2; these are shown in Figure 4.3. In all cases, $S(q)$ oscillates well around unity over the entire q-range, indicating the high quality of the experimental data. The amorphous ribbons were not pre-annealed prior to the structural measurements in BESL so that structural relaxation could be studied during heating. The ribbon was initially heated to a temperature well below the estimated glass transition temperature, then cooled to room temperature. In subsequent cycles, the maximum temperatures were increased until reversible behavior in the height of the first peak in the structure factor, $S(q_1)$, was observed. Structural relaxation was observed for all compositions, evidenced by an increase in the height of $S(q_1)$ and a decrease in its full width at half maximum.

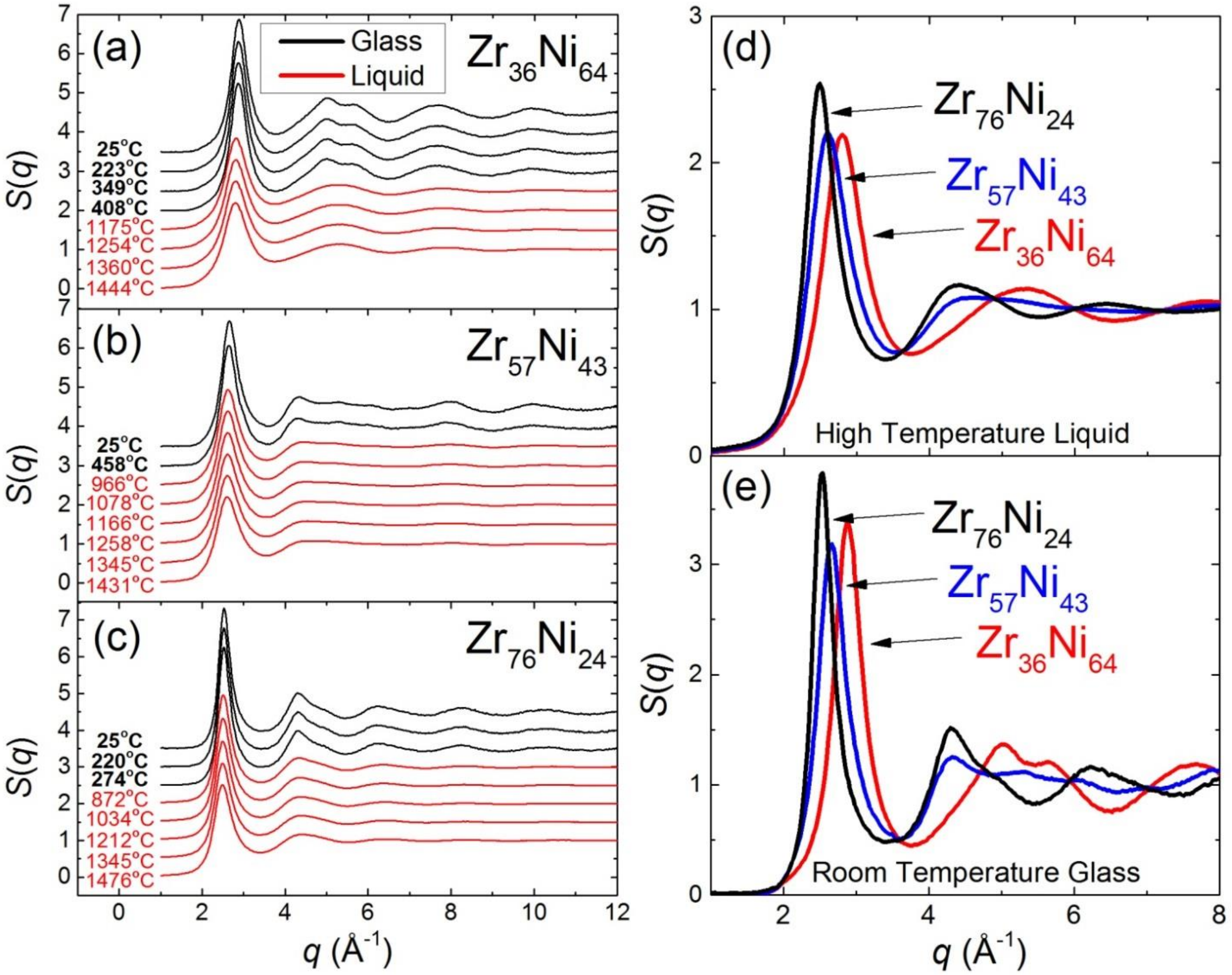

Figure 4.3 Static structure factors for liquids and glasses of (a) $Zr_{36}Ni_{64}$, (b) $Zr_{57}Ni_{43}$, and (c) $Zr_{76}Ni_{24}$. (d) A comparison between the *S*(*q*)s for all three compositions is shown for the liquids at the highest temperature studied (~1435 ^{o}C) and (e) for the glass at room temperature, after structural relaxation. *S*(*q*)s in a-c are each vertically offset by 0.5 for clarity.

For liquids of all compositions, the first peak position shifts towards larger *q* with decreasing temperature, consistent with an increasing density. The first peak also sharpens and increases in amplitude with decreasing temperature, indicating structural ordering in the liquid. The features in the first and higher order peaks in the *S*(*q*)s for the glasses are dramatically sharper than in the liquid, consistent with more structural order in the glass. A large-*q* shoulder on the second peak is often taken as evidence for icosahedral short-range order (ISRO) [10, 13, 49]. However, this is often distorted icosahedral order as is the case in the $Zr_{36}Ni_{64}$ glasses [23].

Further, results from MD simulations of Zr-rich Zr_2Ni [32] and $Zr_{64}Ni_{36}$ [34] have shown that the dominant Zr-centered clusters in the liquid are more closely related to higher-coordinated Frank Kasper (FK) polyhedra (coordination numbers (CN) of 14-16), while the Ni-centered clusters are primarily highly distorted icosahedra (CN of 11-13) with negligible ideal icosahedra (CN of 12). The higher-coordinated FK polyhedra are also present in small amounts in the $Zr_{36}Ni_{64}$ glass, with the relatively reduced population likely due to the smaller Zr concentration. Since the second peak in $S(q)$ varies in shape and position across a wide range of compositions (Figure 4.3 (d-e)), it is possible that there are evolving types of order as Zr is replaced by Ni. This is supported by the differences measured between the partial structure factors obtained from neutron scattering studies with isotopic substitution in the Ni-rich $Zr_{36}Ni_{64}$ glass [23, 50] and from RMC fits to neutron scattering data for the Zr-rich Zr_2Ni glass [31]. There have been numerous reports of a pre-peak in the experimentally measured $S(q)$ obtained from neutron scattering studies of the $Zr_{64}Ni_{36}$ amorphous alloy. This indicates the presence of medium-range order (MRO), attributed to the Ni-Ni correlation for both the high-temperature liquid [26, 30] and the room temperature glass [31]. The pre-peak is also found from *ab initio* MD calculations of the high-temperature liquid [34]. For the $Zr_{36}Ni_{64}$ glass [23, 50] the pre-peak is attributed to both Zr-Zr and Ni-Ni correlations, resulting from pronounced topological and chemical short-range order due to a preferred Zr-Ni bonding. However, the feature is not observed in X-ray diffraction measurements of the room temperature glass [23], consistent with our results. There is no evidence for a pre-peak for the Zr-Ni liquids and glasses studied here, which is expected due to the respective weighting factors of the Zr-Zr, Zr-Ni and Ni-Ni partial structure factors [51].

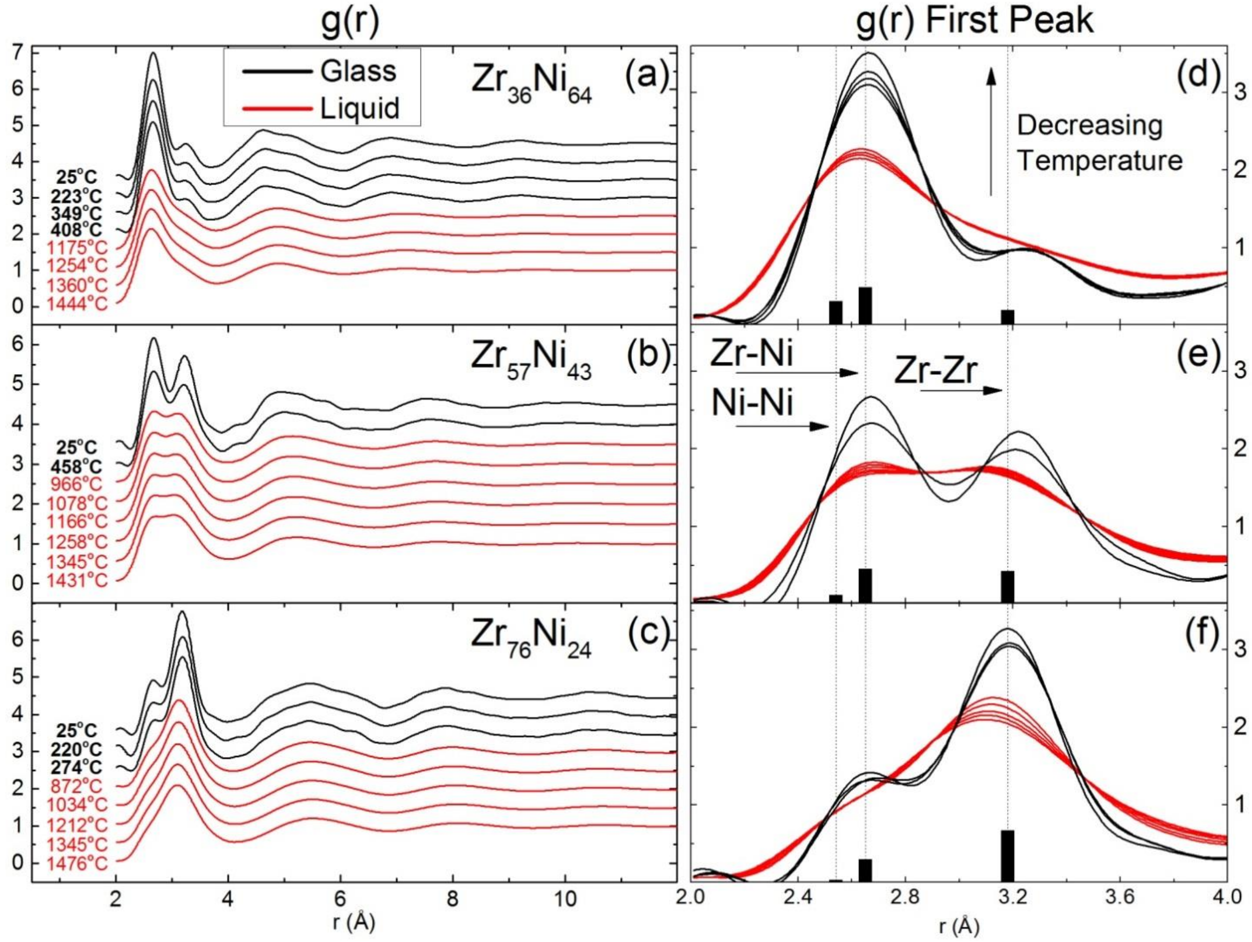

Figure 4.4 Pair-correlation functions, *g*(*r*), calculated from the *S*(*q*)s for the liquids and glasses of (a) $Zr_{36}Ni_{64}$, (b) $Zr_{57}Ni_{43}$, and (c) $Zr_{76}Ni_{24}$. The first peaks, corresponding to the first coordination shell, for each alloy (d-f) show a marked asymmetry or peak splitting corresponding to the positions of the average bond distances, indicated by the dashed lines. The amplitudes of the peaks giving rise to the asymmetry scale with their respective Faber-Ziman weighting, indicated by the height of the solid bars. The *g*(*r*)s in a-c are each vertically offset by 0.5 for clarity. The peaks of the *g*(*r*)s in d-f increase in amplitude as the temperature is decreased.

The pair-correlation function, *g*(*r*), for all liquids and glasses was calculated from the *S*(*q*)s using Eqn. 4.3; these are shown for all liquids and glasses studied in Figure 4.4. The higher order peaks behave in a similar manner for all liquids, increasing in amplitude and shifting towards smaller-*r* with decreasing temperature. These trends indicate an increase in the correlation length for structural order and an increasing density. The smallest-*r* peak (i.e. first peak), however, shows an anomalous expansion, shifting towards larger *r* with decreasing temperature. This is now emerging as common behavior, reported in many metallic glass-forming liquids [52, 53]. The character of the first peak in *g*(*r*) for the different glasses is one of the more interesting features (Figure 4.4 (d-f)). The $Zr_{57}Ni_{43}$ liquid and glass show a distinctly split first peak with the two sub-peaks having nearly equal amplitudes. In contrast, the *g*(*r*) for the $Zr_{36}Ni_{64}$ liquid has an asymmetric first peak that develops into a small shoulder at large-*r* in the glass, consistent with that observed by Georgarakis *et al.* [21]. The $Zr_{76}Ni_{24}$ liquid shows a similar asymmetry, but with the shoulder appearing at small-*r* in the glass. That the sharper features in the *g*(*r*)s for the glasses appear at the same positions as the asymmetries in the liquid *g*(*r*)s suggests that the short-range order in the liquid and glass is similar. An asymmetry was also observed in the first peak in *g*(*r*) in Cu-Zr/Hf liquids and glasses [16, 17, 21], although the features are more subtle than observed here and only become distinct in the glass.

EXAFS [25, 54] and neutron diffraction [27, 29] measurements of room temperature glasses have shown that the Zr-Ni and Ni-Ni bond lengths are almost identical and essentially constant across a range of compositions, while the Zr-Zr bond length is compositionally dependent, increasing to larger *r* as the Zr concentration is decreased. MD calculations of Zr_2Ni liquids indicate a small increase of all bond lengths with decreasing temperature, as well as a separation of the Zr-Ni and Ni-Ni bond lengths similar to what is observed in the glass [32]. Based on these measured average bond distances, the large-*r* feature in the first coordination shell (Figure 4.4 (d-f)) corresponds to the Zr-Zr bond, with the position of this feature shifting to larger *r* as the Zr content decreases. This is consistent with the Zr-Zr bond length increasing with decreasing Zr concentration. The small-*r* feature corresponds to the combined Ni-Ni and Ni-Zr bonds and shifts very little in position across the compositional range studied, consistent with other measurements [25]. The average length of the Zr-Ni bond in other studies is 5-7%

shorter than the sum of their individual atomic radii [21, 25, 32], consistent with the 6-7% decrease observed here. In the Cu-Zr/Hf liquids and glasses, the average length of the Cu-Zr/Hf bond is very close to the sum of the atomic radii, resulting in much more overlap of the distribution of the Cu-Zr/Hf and Zr/Hf-Zr/Hf bond lengths in the first coordination shell. Since the atomic sizes of Cu and Ni are very similar, this difference in behavior is likely due to the higher enthalpy of mixing between Zr and Ni compared with that between Cu and Zr (-49 and -23 kJ/mol, respectively [55]). The reduced average length for the Zr-Ni bonds results in a distinct separation of the peaks of the Zr-Zr and Zr-Ni bond length distributions, indicating an increase in the chemical ordering of Zr with Ni.

The relative amplitudes of the first coordination shell features can be described within the Faber-Ziman formalism [56], where the partial pair-distribution functions (PPDF), $g_{ij}(r)$, are related to the partial structure factors (PSF), $S_{ij}(q)$, by

$$g_{ij}(r) - 1 = \frac{1}{4\pi\rho_0}\frac{1}{\pi}\int (S_{ij}(q) - 1)\frac{\sin(qr)}{qr}q^2 dq \,. \tag{4.7}$$

The total $g(r)$ is related to the partials using the q-dependent Faber-Ziman (FZ) weighting factor, w_{ij}, where, as $q \to 0$,

$$w_{ij}(0) = c_i c_j \frac{Z_i Z_j}{\langle Z \rangle^2}, \tag{4.8}$$

where c_i is the concentration of the i^{th} atomic species and Z_i is the number of electrons in each species. When the features in the partial structure factors vary quickly compared to the atomic form factors, the total pair-correlation function can be approximated as a simple weighted sum of the partial pair-correlation functions,

$$g(r) \cong \sum_i \sum_j w_{ij}(0) g_{ij}(r) . \qquad 4.9$$

This approximation is valid for amorphous metallic alloys and is discussed in more detail elsewhere [16, 57-59]. The relative heights of the peaks and shoulders in the first coordination shell are well correlated with the relative amplitudes of the FZ factors for the corresponding atomic bond distances (Table 4.3). While the small-*r* feature corresponds to the combined first peaks of the Ni-Ni and Ni-Zr PPDFs, the FZ factor for Ni-Ni is small for all alloy concentrations, indicating that the Ni-Ni PPDF contributes very little to the total *g*(*r*). The split peaks in the first coordination shell then correspond primarily to contributions from the Ni-Zr and Zr-Zr PPDFs. Their sharpening indicates an increase in the coherence length and frequency of Zr-Ni and Zr-Zr bonding, signaling chemical ordering for all of the alloys studied. The sharpening of these peaks also indicates an increase in topological ordering, but the well-separated bond lengths show that the change in structure is not chemically random but rather is tied to specific chemical contributions. The chemical ordering in Zr-Ni, then, is not restricted to the glass, but also occurs in the high-temperature liquid. Such chemical ordering is, therefore, not unique to Cu-Zr/Hf liquids, but may be quite common in metallic alloy liquids.

Table 4.3 Faber-Ziman weighting factors for each amorphous alloy.

Composition	$w_{Ni\text{-}Ni}(0)$	$w_{Zr\text{-}Ni}(0)$	$w_{Zr\text{-}Zr}(0)$
$Zr_{36}Ni_{64}$	0.307	0.494	0.199
$Zr_{57}Ni_{43}$	0.120	0.452	0.428
$Zr_{76}Ni_{24}$	0.033	0.296	0.671

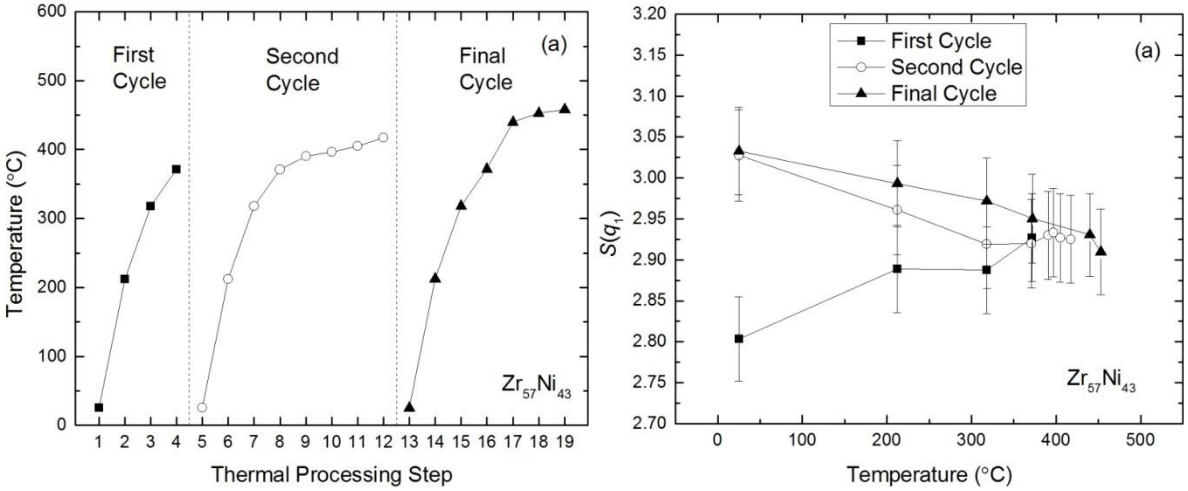

Figure 4.5 (a) The thermal processing program for $Zr_{57}Ni_{43}$ glass. The maximum temperature is slowly increased to observe structural relaxation. (b) The maximum in the first peak in $S(q)$ ($S(q_1)$) in the $Zr_{57}Ni_{43}$ glass as a function of temperature over several processing cycles. The final cycle is fully reversible after a nearly 8% increase in $S(q_1)$ at room temperature from the as-quenched structure to the fully relaxed structure. The error bars reflect the imprecision in the height of the first peak in the static structure factor.

A dramatic sharpening of the first peak in $S(q)$ on going from the liquid to the glass is observed for all alloy compositions (Figure 4.3 (a-c)) and indicates an increase in the ordering of the liquid on a larger scale, accompanying the increasing density. The increasing height of the first peak, $S(q_1)$ is correlated with a decreasing peak width. One benefit of the experimental design is the ability to extract quantitative information from these changes with temperature. As already discussed, the as-quenched glasses were thermally cycled to allow structural relaxation to be measured. For illustration, the processing cycle for $Zr_{57}Ni_{43}$ is shown in Figure 4.5 (a), with the change in $S(q_1)$ shown in Figure 4.5 (b). In the case of $Zr_{57}Ni_{43}$, pronounced changes in $S(q)$ accompany structural relaxation, with $S(q_1)$ increasing by nearly 8% from the as-quenched state to the fully relaxed state (measured at room temperature).

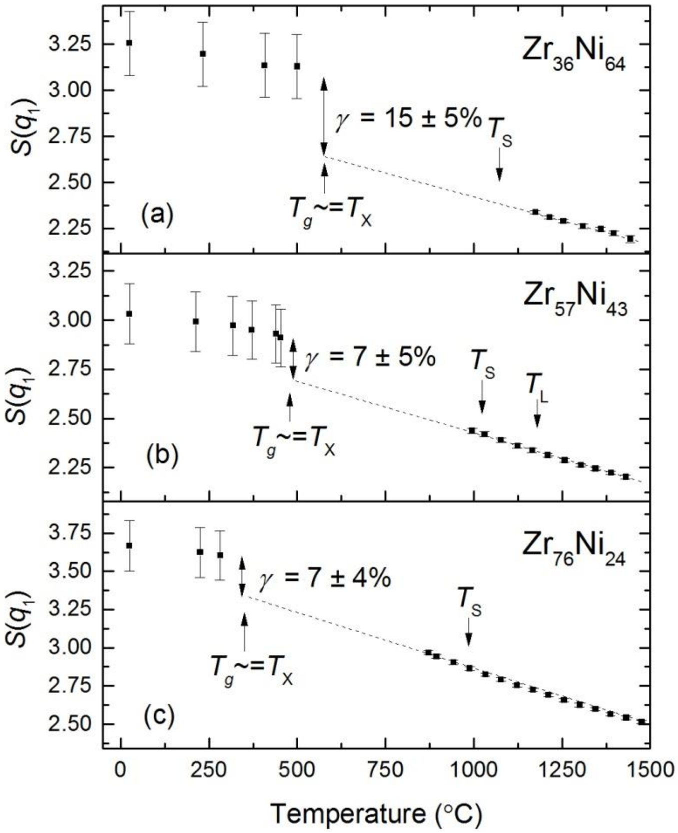

Figure 4.6 The maximum in the first peak in $S(q)$, ($S(q_1)$), in the glass and liquid as a function of temperature for (a) $Zr_{36}Ni_{64}$, (b) $Zr_{57}Ni_{43}$, and (c) $Zr_{76}Ni_{24}$. The glass data were obtained after complete structural relaxation. The respective crystallization (T_x), solidus (T_S), and liquidus (T_L) temperatures are indicated in each panel. When extrapolated to T_g, the liquid $S(q_1)$ values are smaller than those for the relaxed glass. The computed values of the structural fragility, γ, reflect this difference. The error bars reflect the total uncertainty, incorporating estimates of both accuracy and precision.

The temperature dependence of $S(q_1)$ for the liquids and glasses of all three compositions is shown in Figure 4.6. At high temperature, $S(q_1)$ increases linearly with decreasing temperature with very similar rates ($dS(q_1)/dT$) for all liquid alloys. After complete structural relaxation, the temperature dependence of $S(q_1)$ for the glass is small, primarily arising from atomic vibrations, which are described within the Debye theory [60]. For all three alloys studied, a discontinuity is observed between a linear extrapolation to T_g of the $S(q_1)$s for the liquids and the $S(q_1)$s measured for the completely relaxed glasses at T_g. The structurally relaxed state was chosen to ensure consistency of the measurements between glasses prepared using different techniques and with different effective quench rates. From Eqn. 4.1, the calculated structural fragility index, γ, is 15 ± 5% for $Zr_{36}Ni_{64}$, 7 ± 4% for $Zr_{57}Ni_{43}$ and 7 ± 5% for $Zr_{76}Ni_{24}$. These indicate that a large acceleration of structural ordering must occur in the liquid upon approaching the glass transition temperature. This is the behavior expected for fragile liquids [9], with the $Zr_{36}Ni_{64}$ appearing more fragile than the other two Zr-Ni liquids. GFA is often argued to correlate with liquid fragility, consistent with the low GFA and high fragility for these alloy liquids.

4.4 Conclusions

In summary, density, volume, thermal expansivity, viscosity, and high-energy X-ray diffraction studies of Zr_xNi_{100-x} (x = 36, 57, and 76) equilibrium and supercooled liquids were made in a containerless environment using the electrostatic levitation capabilities of the BESL facility. Complementary X-ray data were obtained in the BESL from rapidly-quenched glasses made from these liquids. The smaller background than is possible in capillary measurements gave higher quality data that could be compared with the liquid data. For all alloys, the pair-correlation function, $g(r)$, showed evidence of chemical ordering between Ni and Zr with decreasing temperature that starts in the liquid and becomes more prominent in the glass. This is a manifestation of the strong bonding between Zr and Ni. Similar evidence for chemical ordering was observed earlier by us in Cu-Zr and Cu-Hf liquids and glasses. The results presented here indicate that this may be a common feature in many binary metallic liquids and glasses, hinted at by simulations of Zr-transition metal binary alloys [32]. A deeper experimental investigation of this ordering requires the measurement of the partial structure factors from, for example, neutron diffraction studies. Topological ordering accompanies the chemical ordering. A rapid acceleration in the structural ordering near the glass transition temperature is observed in the temperature evolution of $S(q_1)$, indicating a high fragility for the Zr-Ni liquids [9]. Normally, fragility is determined by the temperature dependence of the viscosity, which is often difficult to measure. The ability to determine fragility from structural studies provides a new avenue for studies of the origin of fragility and for investigating the relationship between fragility and glass-forming ability.

4.5 References

[1] M.L. Johnson, N.A. Mauro, A.J. Vogt, M.E. Blodgett, C. Pueblo, K.F. Kelton, *Journal of Non-Crystalline Solids* **405**, 211 (2014).

[2] W. Klement, R.H. Willens, P. Duwez, *Nature* **187**, 869 (1960).

[3] C.A. Angell, *Journal of Physics and Chemistry of Solids* **49**, 863 (1988).

[4] E.S. Park, J.H. Na, D.H. Kim, *Applied Physics Letters* **91**, 031907 (2007).

[5] H. Tanaka, *Journal of Non-Crystalline Solids* **351**, 678 (2005).

[6] A. Meyer, R. Busch, H. Schober, *Physical Review Letters* **83**, 5027 (1999).

[7] A.K. Gangopadhyay, G.W. Lee, K.F. Kelton, J.R. Rogers, A.I. Goldman, D.S. Robinson, T.J. Rathz, R.W. Hyers, *Review of Scientific Instruments* **76**, 073901 (2005).

[8] N.A. Mauro, K.F. Kelton, *Review of Scientific Instruments* **82**, 035114 (2011).

[9] N.A. Mauro, M.E. Blodgett, M.L. Johnson, A.J. Vogt, K.F. Kelton, *Nature Communications* **5:4616**, (2014).

[10] K.F. Kelton, G.W. Lee, A.K. Gangopadhyay, R.W. Hyers, T.J. Rathz, J.R. Rogers, M.B. Robinson, D.S. Robinson, *Physical Review Letters* **90**, 195504 (2003).

[11] V. Wessels, A.K. Gangopadhyay, K.K. Sahu, R.W. Hyers, S.M. Canepari, J.R. Rogers, M.J. Kramer, A.I. Goldman, D.S. Robinson, J.W. Lee, J.R. Morris, K.F. Kelton, *Physical Review B* **83**, 094116 (2011).

[12] Y.T. Shen, T.H. Kim, A.K. Gangopadhyay, K.F. Kelton, *Physical Review Letters* **102**, 057801 (2009).

[13] N.A. Mauro, V. Wessels, J.C. Bendert, S. Klein, A.K. Gangopadhyay, M.J. Kramer, S.G. Hao, G.E. Rustan, A. Kreyssig, A.I. Goldman, K.F. Kelton, *Physical Review B* **83**, 184109 (2011).

[14] T. Kordel, D. Holland-Moritz, F. Yang, J. Peters, T. Unruh, T. Hansen, A. Meyer, *Physical Review B* **83**, 104205 (2011).

[15] N.A. Mauro, M.L. Johnson, J.C. Bendert, K.F. Kelton, *Journal of Non-Crystalline Solids* **362**, 237 (2013).

[16] N.A. Mauro, A.J. Vogt, M.L. Johnson, J.C. Bendert, R. Soklaski, L. Yang, K.F. Kelton, *Acta Materialia* **61**, 7411 (2013).

[17] N.A. Mauro, A.J. Vogt, M.L. Johnson, J.C. Bendert, K.F. Kelton, *Applied Physics Letters* **103**, 021904 (2013).

[18] Y. Cheng, H. Sheng, E. Ma, *Physical Review B* **78**, 014207 (2008).

[19] N. Mattern, H. Hermann, S. Roth, J. Sakowski, M.-P. Macht, P. Jovari, J. Jiang, *Applied Physics Letters* **82**, 2589 (2003).

[20] Z. Altounian, T. Guo-hua, J.O. Strom-Olsen, *Journal of Applied Physics* **54**, 3111 (1983).

[21] K. Georgarakis, A.R. Yavari, M. Aljerf, D.V. Louzguine-Luzgin, M. Stoica, G. Vaughan, A. Inoue, *Journal of Applied Physics* **108**, 023514 (2010).

[22] S.G. Hao, M.J. Kramer, C. Wang, K. Ho, S. Nandi, A. Kreyssig, A.I. Goldman, V. Wessels, K.K. Sahu, K.F. Kelton, R.W. Hyers, S.M. Canepari, J.R. Rogers, *Physical Review B* **79**, 104206 (2009).

[23] I. Kaban, P. Jóvári, V. Kokotin, O. Shuleshova, B. Beuneu, K. Saksl, N. Mattern, J. Eckert, A.L. Greer, *Acta Materialia* **61**, 2509 (2013).

[24] M.J. Kramer, M. Xu, Y.Y. Ye, D.J. Sordelet, J.R. Morris, *Metallurgical and Materials Transactions A* **39A**, 1847 (2008).

[25] X.J. Liu, X.D. Hui, G.L. Chen, T. Liu, *Physics Letters A* **373**, 2488 (2009).

[26] T. Voigtmann, A. Meyer, D. Holland-Morritz, S. Stuber, T. Hansen, T. Unruh, *Europhysics Letters* **82**, 66001 (2008).

[27] A.F. Lee, G. Etherington, C.N.J. Wagner, *Journal of Non-Crystalline Solids* **61 & 62**, 349 (1984).

[28] T. Mizoguchi, N. Nishioka, S. Yamada, T. Suemasa, S. Yoda, N. Akutsu, H. Narumi, T. Kudo, M. Akimitsu, N. Watanabe, M. Nishi, K. Motoya, *Journal de Physique Colloques* **43**, C9 (1982).

[29] T. Fukunaga, N. Hayashi, N. Watanabe, K. Suzuki, *Rapidly Quenched Metals*, Elsevier, New York, 1985.

[30] D. Holland-Moritz, S. Stüber, H. Hartmann, T. Unruh, T. Hansen, A. Meyer, *Physical Review B* **79**, 064204 (2009).

[31] T. Fukunaga, K. Itoh, T. Otomo, K. Mori, M. Sugiyama, H. Kato, M. Hasegawa, A. Hirata, Y. Hirotsu, A.C. Hannon, *Intermetallics* **14**, 893 (2006).

[32] L. Huang, C.Z. Wang, S.G. Hao, M.J. Kramer, K.M. Ho, *Physical Review B* **81**, 014108 (2010).

[33] F. Li, X.J. Liu, H.Y. Hou, G. Chen, G.L. Chen, M. Li, *Intermetallics* **17**, 98 (2009).

[34] L. Huang, C.Z. Wang, K.M. Ho, *Physical Review B* **83**, 184103 (2011).

[35] M.A. Khan, C. Allemand, T.W. Eagar, *Review of Scientific Instruments* **62**, 392 (1991).

[36] R.C. Bradshaw, D.P. Schmidt, J.R. Rogers, K.F. Kelton, R.W. Hyers, *Review of Scientific Instruments* **76**, 125108 (2005).

[37] S.K. Chung, D.B. Thiessen, W.-K. Rhim, *Review of Scientific Instruments* **67**, 3175 (1996).

[38] T. Ishikawa, P.-F. Paradis, S. Yoda, *Review of Scientific Instruments* **72**, 2490 (2001).

[39] R.W. Hyers, R.C. Bradshaw, J.R. Rogers, T.J. Rathz, G.W. Lee, A.K. Gangopadhyay, K.F. Kelton, *International Journal of Thermophysics* **25**, 1155 (2004).

[40] W.-K. Rhim, K. Ohsaka, P.-F. Paradis, R.E. Spjut, *Review of Scientific Instruments* **70**, 2796 (1999).

[41] J.C. Bendert, K.F. Kelton, *Journal of Non-Crystalline Solids* **376**, 205 (2013).

[42] J.C. Bendert, N.A. Mauro, K.F. Kelton, *Journal of Applied Crystallography* **46**, 999 (2013).

[43] A.P. Hammersley, S.O. Svensson, M. Hanfland, A.N. Fitch, D. Hausermann, *High Pressure Research* **14**, 235 (1996).

[44] H. Okamoto, *Journal of Phase Equilibria and Diffusion* **28**, 409 (2007).

[45] A. Inoue, T. Zhang, T. Masumoto, *Journal of Non-Crystalline Solids* **156-158**, 473 (1993).

[46] J. Saida, M. Kasai, E. Matsubara, A. Inoue, *Annales de Chimie - Science des Matériaux* **27**, 77 (2002).

[47] T. Iwashita, D.M. Nicholson, T. Egami, *Physical Review Letters* **110**, 205504 (2013).

[48] M.E. Blodgett, T. Egami, Z. Nussinov, K.F. Kelton, *Private Communications* (2014).

[49] S. Sachdev, D.R. Nelson, *Physical Review Letters* **53**, 1947 (1984).

[50] A. Lefebvre, A. Quivy, J. Bigot, Y. Calvayrac, R. Bellissent, *Journal of Physics F* **15**, L99 (1985).

[51] N.A. Mauro, K.F. Kelton, *Journal of Non-Crystalline Solids* **358**, 3057 (2012).

[52] A.K. Gangopadhyay, M.E. Blodgett, M.L. Johnson, J. McKnight, V. Wessels, A.J. Vogt, N.A. Mauro, J.C. Bendert, R. Soklaski, L. Yang, K.F. Kelton, *Journal of Chemical Physics* **140**, 044505 (2014).

[53] H. Lou, X. Wang, Q. Cao, D. Zhang, J. Zhang, T. Hu, H.-k. Mao, *Proceedings of the National Academy of Sciences* **110**, 10068 (2013).

[54] R. Frahm, R. Haensel, P. Rabe, *Journal of Physics F: Metal Physics* **14**, 1333 (1984).

[55] F.R.D. Boer, R. Boom, W.C.M. Mattens, A.R. Miedema, A.K. Niessen, *Cohesion In Metals: Transition Metal Alloys (Cohesion And Structure),* North-Holland, Amsterdam, 1988.

[56] T.E. Faber, J.M. Ziman, *Philosophical Magazine* **11**, 153 (1965).

[57] C.N.J. Wagner, *Journal of Non-Crystalline Solids* **76**, 29 (1985).

[58] N. Mattern, A. Schöps, U. Kühn, J. Acker, O. Khvostikova, J. Eckert, *Journal of Non-Crystalline Solids* **354**, 1054 (2008).

[59] N. Mattern, P. Jóvári, I. Kaban, S. Gruner, A. Elsner, V. Kokotin, H. Franz, B. Beuneu, J. Eckert, *Journal of Alloys and Compounds* **485**, 163 (2009).

[60] S. Sinha, P.L.L. Srivastava, R.N.N. Singh, *Journal of Physics: Condensed Matter* **1**, 1695 (1989).

Chapter 5: Measurements of Structural and Chemical Order in $Zr_{80}Pt_{20}$ and $Zr_{77}Rh_{23}$ Liquids

This chapter includes X-ray scattering data acquired during the BESL 2013 experiment and neutron scattering data acquired during the NOMAD 2014 experiment. Some density measurements were performed by M. E. Blodgett, and DTA measurements were performed by N. A. Mauro (Washington University in Saint Louis, Saint Louis, MO). Results from MD simulations were provided by M. Kramer (Ames Laboratory, Ames, IA) and have been published elsewhere [1]. Voronoi analysis was performed using a modified version of Voro++ provided by V. Tran (Washington University in Saint Louis, Saint Louis, MO).

5.1 Introduction

Although lacking long-range order, metallic liquids do have short-range order (SRO) and medium-range order (MRO), which have been heavily studied in recent years through both experiment [2-12] and simulations [13-15]. This SRO and MRO are important for understanding the nucleation and growth of crystalline phases [16] and can provide insight into metastable phase formation and glass formation. Frank predicted that icosahedral SRO, a structure that is highly coordinated but is incompatible with translational periodicity, is dominant in elemental liquids [17] and provides a significant energy barrier to crystallization. Molecular dynamics (MD) simulations of pure Cu have provided evidence that this is the case [18], and it has since been observed in levitated elemental liquids [12, 19, 20]. In one case, the icosahedral order catalyzed the nucleation of a metastable icosahedral quasicrystal phase (*i-phase*) [16], directly demonstrating the impact of order on the nucleation barrier. Rapidly-quenched Zr-rich compositions of Zr-Pt and Zr-Pd liquids are also known to form the *i-phase* [21-23], suggesting that those liquids could also have dominant icosahedral order. Supporting this, amorphous Zr-Pt can be produced by rapid quenching if the oxygen concentration is increased [24], with the *i-phase* as the primary devitrification product [25, 26] followed by the equilibrium hexagonal Zr_5Pt_3 phase [27]. Small changes in Pt-concentration (from 20 at.% Pt to 27 at.% Pt) change the transformation kinetics, giving Zr_5Pt_3 as the primary devitrification product [28] and bypassing the formation of the *i-phase*. While other similar alloys such as Zr-Rh do not directly form the *i-phase*, additions of Rh to Zr-Cu binary alloys does cause quasicrystal formation [29].

Previous X-ray scattering studies of Zr-Pt glasses have shown a pre-peak in the total structure factor, $S(q)$, at small-q, indicating a significant amount of MRO in the amorphous structure [27, 30, 31]. Those studies suggest large amounts of icosahedral and distorted icosahedral SRO in the glass, with the pre-peak arising from Pt-Pt correlations. X-ray scattering studies of supercooled $Zr_{80}Pt_{20}$ liquids suggest that this MRO begins in the high-temperature liquid and persists through quenching into the glass [1]. A pre-peak is also a common feature of Zr-(noble metal) eutectic liquids, such as Zr-Ir/Pt/Au [5]. However, while the noble metals are all similar in size and have similar bonding strengths with Zr, Zr-Rh and Zr-Pd eutectic liquids do not contain a pre-peak. The Faber-Ziman (FZ) weighting factors [32] scale with the square of the atomic number, Z. The lack of a pre-peak in Zr-Rh and Zr-Pd, where Rh and Pd have smaller Z than Ir, Pt, and Au, has then been attributed to the small value of the solute-solute FZ coefficients compared with those for the other two partials [5]. It is of interest to determine the structures of these liquids to further investigate this explanation for the lack of a pre-peak in some Zr-noble metal liquids and the reasons for glass and complex crystal phase formation. Combinations of data from different types of experiments (e.g., anomalous X-ray scattering, wide-angle X-ray scattering, and elastic neutron scattering using isotopic substitution) are typically used to determine the structural and chemical ordering. The number of experiments needed is determined by the number of components in the alloy. For an alloy with n components, $n(n+1)/2$ different experiments are needed to separate the partials.

Here we report the results of combined wide-angle high-energy X-ray diffraction and time-of-flight (TOF) elastic neutron scattering studies on electrostatically levitated $Zr_{80}Pt_{20}$ and $Zr_{77}Rh_{23}$ liquids. These suggest that the lack of a pre-peak is not simply due to the values of the FZ coefficients. An analysis of the data shows that while the topological SRO is similar for both alloys, $Zr_{77}Rh_{23}$ has more prominent chemical SRO. Based on a Voronoi tessellation analysis of the atomic structure obtained from a Reverse Monte Carlo simulation of a $Zr_{80}Pt_{20}$ liquid that is constrained by the results of molecular dynamics simulations, the liquid contains dominant polyhedra that are consistent with structural features of the equilibrium Zr_5Pt_3 crystalline phase. Due to the topological similarity between $Zr_{77}Rh_{23}$ and $Zr_{80}Pt_{20}$, a new phase is predicted, Zr_5Rh_3, and is found as a primary crystallizing phase in the deeply supercooled $Zr_{77}Rh_{23}$ liquid. While the free energies of the stable crystal phases are less, the similarity in structure to that of the liquid lowers the nucleation barrier, favoring the formation of the phase.

5.2 Experimental Details

Master ingots for all compositions were prepared by arc-melting high-purity Zr (99.95 at.%, which contained Hf to a nominal concentration of 3 at.%), Pt (99.95 at.%), and Rh (99.8 at.%) on a Cu hearth in a high-purity (99.999 at.%) Ar atmosphere. A Ti-Zr getter located close to the sample was melted prior to arc-melting to further reduce the oxygen concentration in the chamber. Master ingots were melted three times to ensure that the samples were homogeneous; each melt cycle lasted approximately one minute. Mass loss during arc-melting was negligible (less than 0.1%). The master ingots were subsequently crushed and portions were re-melted to obtain small spherical samples (~2.5 mm diameter) that were processed in a containerless environment using the Washington University Beamline Electrostatic Levitation (WU-BESL) facility [33, 34]. WU-BESL is optimized for X-ray diffraction studies of levitated, containerlessly processed liquids in a high-vacuum environment (~10^{-7} Torr), and was used for *in situ* structural studies of the levitated liquids at the Advanced Photon Source (APS) in sector 6-ID-D. Additional master ingots were crushed and re-melted into slightly larger spherical samples (~3 mm diameter, 100 mg) for *in situ* liquid structural studies at the Spallation Neutron Source (SNS) located at Oak Ridge National Laboratory (ORNL). Elastic neutron scattering studies were made on the Nanoscale-Ordered Materials Diffractometer (NOMAD) beamline [35] using the Neutron Electrostatic Levitator (NESL) [36-38]. The NESL is optimized for time-of-flight (TOF) elastic and inelastic neutron studies of levitated liquid samples in a vacuum environment; the pressure at the sample location was ~8×10^{-6} Torr for these studies.

5.2.1 X-ray Scattering Details

For the X-ray experiments, the liquid samples were heated, melted, and subsequently thermally processed using a fiber-coupled diode laser (980 nm, 50 W continuous maximum power output). Crystallization of the supercooled liquid, marked by a sharp rise in temperature (recalescence), limited the lowest accessible temperature for the X-ray diffraction studies to 190 ^{o}C below the liquidus temperature (T_L). A Process Sensors Metis MQ22 two-color ratio pyrometer, operating at 1.40 and 1.65 μm wavelengths, was used for high-temperature measurements (600-2300 ^{o}C) of the liquids. A constant emissivity ratio was assumed for the entire temperature range over which structural data were acquired. The emissivity ratio was calibrated by matching the onset of the melt plateau (corresponding to the solidus temperature,

T_S, in the temperature versus time curve measured on heating in WU-BESL) to the largest endothermic signature measured in a differential thermal analyzer (DTA) (Labsys^{TM} DTA/DSC, Setaram) [39].

The temperature was correlated with non-contact measurements of the volume, made using the shadow method [40, 41] with a Pixelink PL-B74IG CMOS camera and a 455 nm collimated microscope LED. The relative precision of the density data was ~0.3% over the temperature range studied, with an absolute accuracy of ~0.5%; the measurement error is dominated by errors in the calibrations of the volume and mass. A more detailed discussion of the machine vision volume measurement algorithm and experimental implementation can be found elsewhere [40, 42].

The X-ray diffraction studies of the liquids were made in a transmission geometry using high-energy X-rays (E = 130 keV, λ = 0.0956 Å for $Zr_{80}Pt_{20}$, E = 132 keV, λ = 0.09403 Å for $Zr_{77}Rh_{23}$). Scattering data were obtained to a momentum transfer, q, of 20 Å^{-1} at a sampling rate of 1 Hz using a GE Revolution 41-RT amorphous Si flat-panel X-ray detector. The sample-to-detector distance, detector tilt, and detector center were calibrated by fitting the diffraction pattern of a levitated polycrystalline Si sample. These values were confirmed using a NIST Si standard in a capillary placed at the position of the levitated liquid sample. The scattering data obtained were processed by masking bad pixels, applying a pixel efficiency gain map, averaging the images obtained during the isothermal hold, and subtracting the appropriate detector dark current and scattering background. Images were then corrected for oblique incidence, absorption, multiple scattering, fluorescence, polarization, sample geometry, and Compton scattering contributions using in-house analysis packages written in LabVIEW^{TM} [43]. A series of measurements were made at each temperature step (15-20 s) to obtain the total static structure factor using

$$S(q) = \frac{I(q) - \sum_{i=1}^{n} c_i \left| f_i(q) \right|^2}{\left| \sum_{i=1}^{n} c_i f_i(q) \right|^2} + 1, \tag{5.1}$$

where $I(q)$ is the measured diffraction intensity, c_i is the atomic fraction of each elemental species, and $f_i(q)$ is the q-dependent atomic form factor for each species. The sums were taken over all species and an isotropic and statistically homogeneous atomic distribution was assumed. The total pair-distribution function, $g(r)$, and the reduced pair-distribution function, $G(r)$, were computed from a Fourier transform of the structure factor using

$$G(r) = 4\pi\rho r \left(g(r) - 1 \right) = \frac{2}{\pi} \int q(S(q) - 1) \sin(qr)\, dq\,, \tag{5.2}$$

where ρ_{exp} is the average number density measured as described above.

5.2.2 Neutron Scattering Details

For the neutron experiments, the liquid samples were heated, melted, and subsequently thermally processed using a pair of fiber-coupled diode lasers (980 nm, 110 W continuous maximum power output) on opposite sides of the sample. Two lasers were used to ensure even heating and to minimize the temperature gradient across the larger samples. Temperatures of the levitated NESL samples were measured from 500 ^{o}C to 1800 ^{o}C using a single Process Sensors Metis MQ22 two-color ratio pyrometer. A constant emissivity ratio was assumed for the entire temperature range over which structural data were acquired. The emissivity ratio was calibrated in a similar manner as WU-BESL measurements [39]. Due to long time-scale drift in the positioning lasers, the sample would slowly shift relative to the pyrometer causing an apparent temperature drift in the sample. The melt plateau was measured before and after each measurement and was used to calibrate the isothermal temperature.

The TOF elastic neutron diffraction studies of the electrostatically levitated liquids were made using high-energy neutrons (E = 10 meV – 10 eV, λ = 0.1 – 2.9 Å). Scattering data were obtained to a momentum transfer of 100 $Å^{-1}$ for a series of isothermal measurements (60 min for the $Zr_{80}Pt_{20}$, 30 min for $Zr_{77}Rh_{23}$). Diamond powder contained in a pure vanadium can located in the approximate sample position was used to calibrate the sample-to-detector distances for each ^{3}He linear position sensitive detector covering a scattering angle, 2θ, of 3 – 175 ^{o}. A levitated sample of incoherently scattering vanadium was used to measure the incident distribution of neutron energies for subsequent normalization once coherent Bragg peaks were removed. Both the sample and vanadium measurements were corrected with an empty chamber scan. Absorption and multiple scattering contributions were simulated for both the sample and vanadium measurements based on a spherical sample geometry using the measured sample mass and density and were removed from the scattering data [35].

The $S(q)$s obtained from neutron scattering experiments showed a large overall curvature, causing poor normalization around unity. This feature corresponds to inelastic scattering contributions that are manifest as large unphysical peaks in the small-r region of $G(r)$ (r < 1 Å). The oscillations were replaced with a linear fit to the hard-sphere region where it is expected to go as $G(r) = -4\pi\rho r$. The difference between the experimental ripples and the fit was then Fourier transformed back into q-space and subtracted from the initial $S(q)$. This method produces physically realistic behavior in the hard-sphere region and removes inelastic scattering contributions below the first nearest-neighbor distance [44].

In order to effectively compare two independently measured structure factors, they must both appear on the same absolute scale. Incomplete accounting for secondary scattering, i.e. neutrons scattered by the sample that undergo subsequent scattering from the environment before being detected, is one of the primary causes of incorrect scaling. In practice, it is nearly impossible to properly model the secondary scattering without knowing the precise location and material composition of each part of the sample environment. However, some approximations can be made from the expected physical behavior. The Peterson metric, ΔG_{low} [45] (Eqn. 5.3), quantifies the magnitude of ripples in $G(r)$ below some cut-off before the first peak, r_{low}, which corresponds to the hard-sphere cutoff where no atom may be located.

$$\Delta G_{low} = \frac{\int_0^{r_{low}} \left[rG(r) + 4\pi r^2 \rho_{fit} \right]^2 dr}{\int_0^{r_{low}} \left(4\pi r^2 \rho_{fit} \right)^2 dr} \tag{5.3}$$

The parameter ρ_{fit} is the number density calculated from the slope of a linear fit below r_{low} in $G(r)$. The slope of this region was adjusted to minimize ΔG_{low}, minimizing the deviation from linear behavior. The measured $S(q)$ was then multiplied by a scaling factor, α, according to the method described by Peterson [45] using

$$S'(q) = \alpha S(q) + (1-\alpha)\,. \tag{5.4}$$

Here, $S'(q)$ is the corrected structure factor and the additive constant of $1-\alpha$ is required to maintain oscillation of the structure factor about unity. Since α is a constant, it propagates through a Fourier transform and changes the scaling in real space as well without otherwise changing or distorting the real space features. It was adjusted until the experimentally measured number density, ρ_{exp}, matched ρ_{fit}. This treatment was applied to the $S(q)$s obtained from both the X-ray and neutron measurements and was confirmed to give identical results for measurements of identical alloys at the same temperature from two separate X-ray scattering studies.

5.2.3 Reverse Monte Carlo Fits

Atomic configurations were obtained from the scattering data with the Reverse Monte Carlo (RMC) technique [46] using RMC_POT [47]. By constraining the fits with the results from the X-ray and neutron scattering experiments, the extraction of physically-reasonable, chemically-specific partial structure factors (PSF) could be obtained. In addition, fits to the liquid $Zr_{80}Pt_{20}$ data were constrained using the Zr-Pt partial pair-distribution function (PPDF) obtained from *ab initio* MD simulations [1]. A detailed discussion of the choice of this constraint is given in Section 5.3.2. The starting configurations for the RMC fits contained 10,000 atoms (8,000 Zr, 2,000 Pt) that were randomly distributed in a cubic box with a size constrained by $\rho_{\text{exp}}(T)$ measured in WU-BESL. Minimum PPDF cutoff distances were used to increase the convergence of the fit and were set optimally at 2.2, 2.2, and 2.4 Å for Zr-Zr, Zr-Pt, and Pt-Pt respectively. The atomic configurations obtained from the RMC fits were analyzed with Voronoi tessellation techniques [48, 49] using Voro++ [50]. Recently, the importance of weighted bisectors in the Voronoi analysis has become clear [51]. Elemental Goldschmidt radii [52] were used to calculate more physically realistic bisecting planes between two atoms of different sizes. The effect of weighted bisectors is to create a larger separation in the average coordination numbers (CN) of the large and small atoms by more accurately modeling how much space each individual atom encompasses. Because the liquid structure is already disordered and the local coordination number is continuously changing, the time-averaged atomic configuration will contain many unphysically-sized faces that incorrectly identify an atom as a neighbor. To correct for this effect, faces with an area smaller than 0.25 Å^2 were removed. This cutoff was determined by the maximum face area that caused a histogram of edge sizes to appear to follow Gaussian distribution without altering the shape of the large-edge size. The CRMC fits were performed eight times for each temperature to generate sufficient statistics and determine the error bars in the Voronoi and CN analysis.

5.3 Results and Discussion

5.3.1 Liquid X-ray and Neutron Scattering Measurements

The total structure factors, $S(q)$, were measured for $Zr_{80}Pt_{20}$ and $Zr_{77}Rh_{23}$ liquids from high-energy X-ray and TOF neutron scattering data obtained over a temperature range of 980 - 1300 ^{o}C (Figure 5.1). Since the oscillations in $S(q)$ damp to close to unity by q = 12 Å^{-1} in liquids, the data acquired beyond this are not shown here. As the temperature of $Zr_{80}Pt_{20}$ is decreased below the solidus temperature (T_S = 1177 ^{o}C, measured with DTA) into the supercooled liquid, the primary peak sharpens and the second peak develops two distinct shoulders. These features indicate that the liquid structure is becoming increasingly ordered as preferred length scales emerge during cooling. Due to the limited temperature range over which $Zr_{77}Rh_{23}$ was measured (ΔT = 50 ^{o}C, T_S = 1061 ^{o}C), very little peak evolution was observed. For both alloys, the primary peak from X-ray scattering data is shifted to slightly larger-q than in the neutron scattering experiments; the shift is more noticeable in the broad second peak. These features are due to differences in the weighting of the partial structure factors between the X-ray and neutron scattering, likely revealing chemically specific short-range ordering (CSRO).

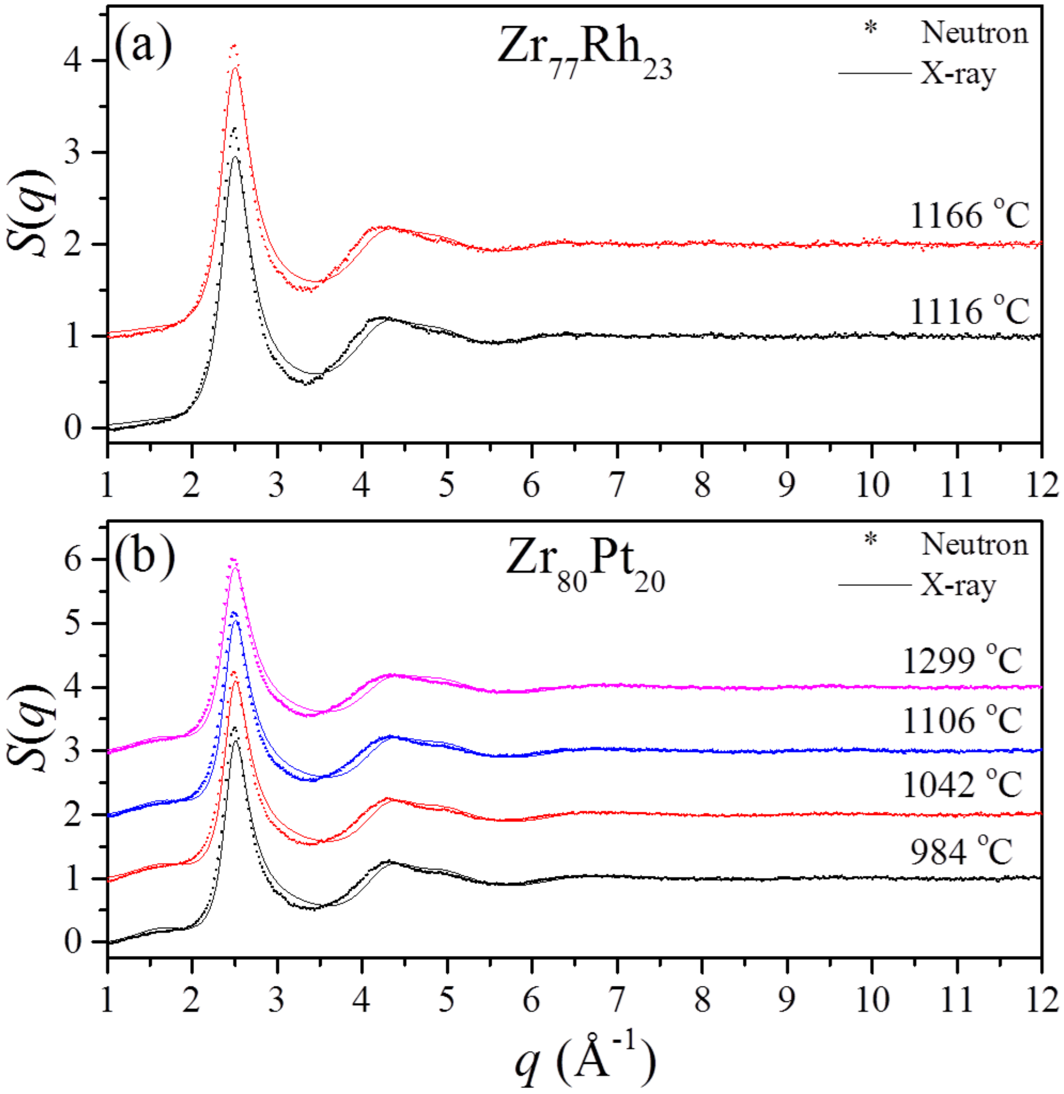

Figure 5.1 Total $S(q)$s measured for levitated liquid (a) $Zr_{77}Rh_{23}$ and (b) $Zr_{80}Pt_{20}$ using both X-ray (solid lines) and neutron (solid symbols) scattering.

The $S(q)$ for $Zr_{80}Pt_{20}$ contains a pre-peak at q~1.6 Å^{-1}, consistent with previous liquid [1, 5] and glass studies [27, 30, 53]. Appearing in both X-ray and neutron data, it is greatly reduced in the latter (Figure 5.2). This feature has been argued to reflect the Pt-Pt correlation between Pt-centered icosahedron-like clusters [1, 30, 54]. It is interesting to note that, while many of the features of the $Zr_{77}Rh_{23}$ and $Zr_{80}Pt_{20}$ $S(q)$s are remarkably similar, the pre-peak is absent in both X-ray and neutron $S(q)$s for $Zr_{77}Rh_{23}$. A previous study of the MRO in Zr-(noble metal) (NM) liquids [5] suggested that the same sort of chemical order is likely present in all of these alloy liquids, but the pre-peak might not appear due to smaller chemical contrast from the Faber-Ziman (FZ) [32] weighting factors.

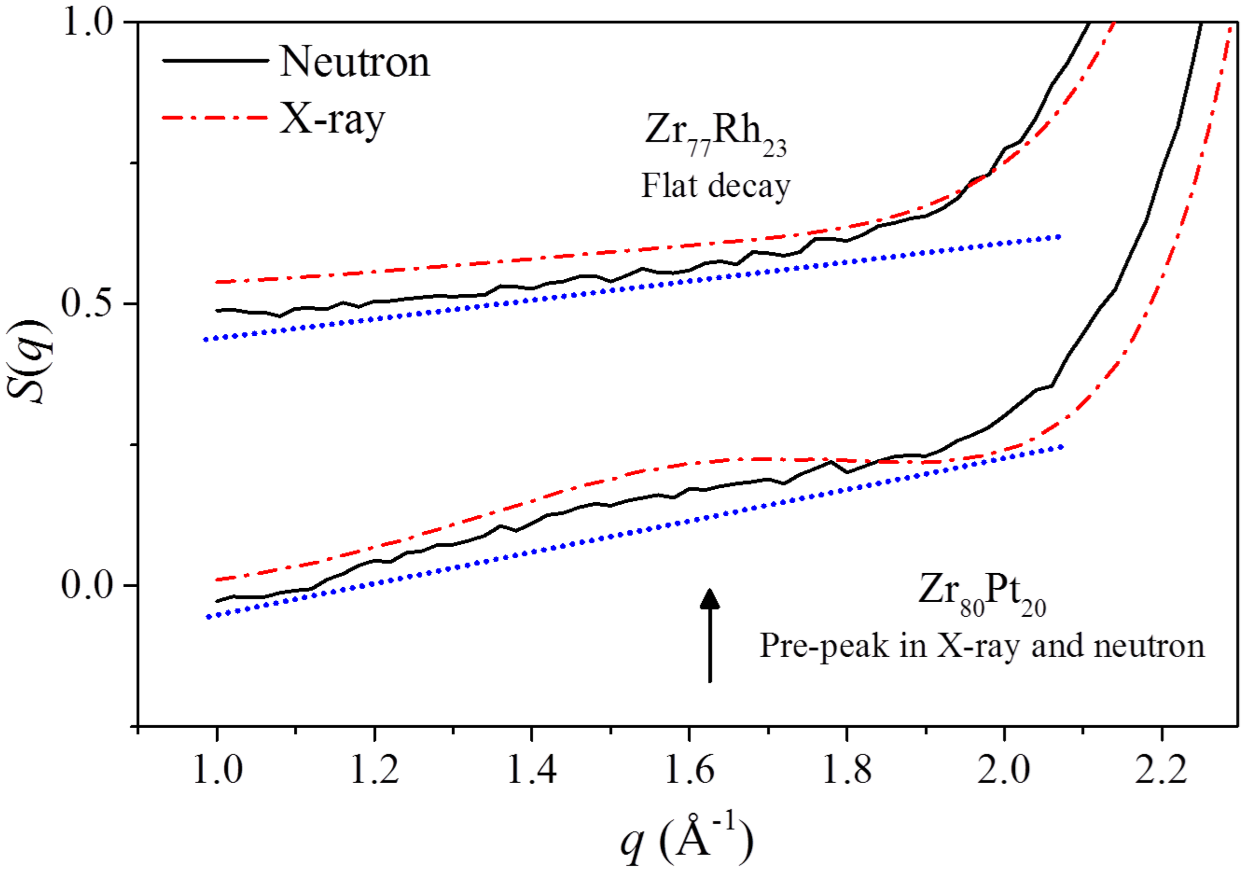

Figure 5.2 Neutron (—) and X-ray (–·–) scattering in the low-q region at ~1100 °C for $Zr_{77}Rh_{23}$ (top) and $Zr_{80}Pt_{20}$ (bottom) liquids (vertically offset by 0.5 for clarity). The dotted blue lines (····) are guides to the eye to emphasize the pre-peak that forms in $Zr_{80}Pt_{20}$.

The relative amplitudes of the first coordination shell features can be described within the Faber-Ziman formalism [32], where the partial pair-distribution functions (PPDF), $g_{ij}(r)$, are related to the partial structure factors (PSF), $S_{ij}(q)$, by

$$g_{ij}(r)-1=\frac{1}{4\pi\rho_0}\frac{1}{\pi}\int(S_{ij}(q)-1)\frac{\sin(qr)}{qr}q^2dq\,. \tag{5.5}$$

Here, ρ_{exp} is the experimentally measured number density (Table 5.1) and is given by

$$\rho_{\mathrm{exp}}(T) = \rho_S + \frac{d\rho}{dT}(T - T_S)\,. \tag{5.6}$$

T_{S} is the solidus temperature and ρ_{S} is the number density measured at T_{S}. The total $g(r)$ is related to the partials using the q-dependent FZ weighting factor, w_{ij}, where, as $q \to 0$,

$$w_{ij}(0) = c_i c_j \frac{Z_i Z_j}{\langle Z \rangle^2}\,. \tag{5.7}$$

Here, c_i is the concentration of the i^{th} atomic species and Z_i is the number of electrons in each species. For neutron scattering, Z is replaced by the neutron scattering length, b. When the features in the partial structure factors vary rapidly with q compared to the atomic form factors, the total pair-correlation function can be approximated as a simple q-independent weighted sum of the partial pair-correlation functions,

$$g(r) \cong \sum_i \sum_j w_{ij}(0) g_{ij}(r)\,. \tag{5.8}$$

This approximation is valid for amorphous metallic alloys and is discussed in more detail elsewhere [3, 55-57]. The equivalent weighting factors for neutron scattering are calculated using Eqn. 5.7 by replacing Z with the neutron scattering length, b. The calculated X-ray weighting factors for $\mathrm{Zr_{77}Rh_{23}}$, $w_{ij}^{X,ZrRh}$, are almost equal to the neutron weighting factors for $\mathrm{Zr_{80}Pt_{20}}$, $w_{ij}^{N,ZrPt}$ (Table 5.2). By the argument given previously [5], since no pre-peak is observed in X-ray measurements for $\mathrm{Zr_{77}Rh_{23}}$, it should not be observable in the neutron scattering data for $\mathrm{Zr_{80}Pt_{20}}$. That it is observed, however, indicates that the two liquids must have different topological and/or chemical ordering, calling into question the previous interpretation of similar structures among Zr-NM liquids [5].

Table 5.1 Measured liquid density and change with temperature (see Eqn. 5.6).

Composition	T_S (°C)	ρ_S (g cm^{-3})	dρ/dT (g cm^{-3} °C^{-1})
$Zr_{80}Pt_{20}$	1177 ± 5	8.38 ± 0.01	-3.30 ± 0.02E^{-4}
$Zr_{77}Rh_{23}$	1061 ± 5	7.22 ± 0.01	-3.24 ± 0.02E^{-4}

Table 5.2 Faber Ziman weighting factors for X-ray and neutron scattering (see Eqn. 5.7).

Alloy	Scattering type	w_{ii}	w_{ij}	w_{jj}
$Zr_{80}Pt_{20}$	X-ray	0.45195	0.44065	0.10741
	Neutron	0.56093	0.37604	0.06302
$Zr_{77}Rh_{23}$	X-ray	0.56022	0.37651	0.06326
	Neutron	0.64397	0.31701	0.03901

5.3.2 Single Partial Subtraction

Previous structural studies of liquid $Zr_{80}Pt_{20}$ were based on RMC fits to experimental X-ray scattering data and constrained by the PPDFs from *ab initio* MD simulations of 100 atoms (80 Zr, 20 Pt) [1]. While these MD-PPDFs are consistent with $g(r)$ from X-ray scattering experiments ($g^X(r)$, Figure 5.3 (a)), they are less consistent with $g(r)$ from neutron scattering experiments ($g^N(r)$, Figure 5.3 (b)). While MD gives $g(r)$s for the higher-order coordination shells consistent with $g^N(r)$, the primary peak, $g(r_1)$, is not well reproduced.

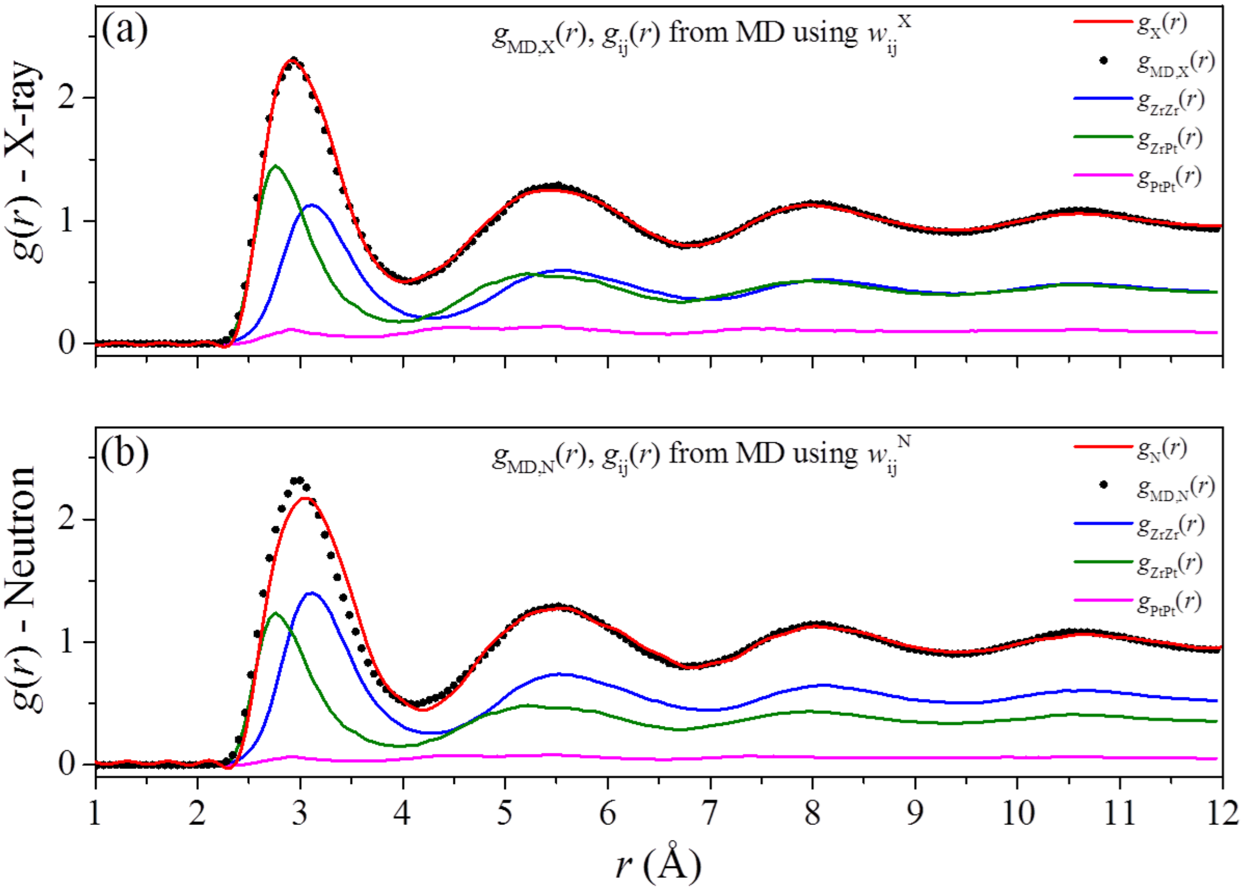

Figure 5.3 Liquid $g(r)$s (red curves) at 1299 °C, showing the results from (a) neutron and (b) X-ray scattering measurements. The partials for $g_{ZrZr}(r)$ (blue), $g_{ZrPt}(r)$ (green), and $g_{PtPt}(r)$ (pink) from MD are weighted by their appropriate FZ weighting factors (Eqn. 5.7). The total $g(r)$s from MD for both types of scattering are also plotted (solid symbols).

If two contrasting scattering experiments are performed, such as using a combination of X-ray and neutron scattering, two independent equations can be constructed from Eqn. 5.8 that contain weighting factors specific to the scatterer (i.e., using $f_i(q)$ for X-rays and b_i for neutrons). Three independent equations are required to completely solve for all $g_{ij}(r)$s in a binary alloy. However, if only two experiments are performed, the individual contribution of any single $g_{ij}(r)$ can be removed using an appropriate linear combination of the two equations [58-60] using:

$$\Delta g_{no-i'j'} = \frac{w^{N}_{i'j'}\left(g^{X}(r)\right) - w^{X}_{i'j'}\left(g^{N}(r)\right)}{w^{N}_{i'j'} - w^{X}_{i'j'}} = \frac{\sum\limits_{i,j\neq i',j'} \left(w^{N}_{i'j'}w^{X}_{ij} - w^{X}_{i'j'}w^{N}_{ij}\right)\left(g_{ij}(r)\right)}{w^{N}_{i'j'} - w^{X}_{i'j'}} . \qquad (5.9)$$

Here the superscripts X and N represent X-ray and neutron scattering, w_{ij} is the weighting factor for the ij^{th} partial (ij = Zr,Pt), and $i'j'$ represents the partial being removed. If experimentally determined $g(r)$s are available, the contribution from a single partial, $g_{i'j'}(r)$, can be removed using the left-hand-side of Eqn. 5.9. Alternatively, an equivalent curve can be calculated if a full set of $g_{\mathrm{ij}}(r)$s are known, such as through MD, using the right-hand-side of Eqn. 5.9.

When compared with the MD results (open circles, Figure 5.4), the best agreement was observed when the contribution from the Zr-Zr partial was removed (Figure 5.4, black curves). The primary peak amplitude in $\Delta g_{\text{no-ZrZr}}$ was underestimated by MD, but the peak position was in approximately the correct location. In contrast, the worst agreement was found when the Zr-Pt contribution was removed ($\Delta g_{\text{no-ZrPt}}$, Figure 5.4, red curves). In this case, there was a large offset between the primary peak positions, with the experimental value located at larger-r. The Zr-Zr partial is ~85% of the total contribution to $\Delta g_{\text{no-ZrPt}}$, suggesting that the main peak position primarily corresponds to the average Zr-Zr bond distance, giving $r_{\text{Zr-Zr}}$ = 3.32 Å. This is in better agreement with EXAFS measurements of a $\mathrm{Zr_{80}Pt_{20}}$ glass [61] (3.26 Å) than with MD (3.14 Å). When the Pt-Pt partial was removed (Figure 5.4, blue curves), there was again a large discrepancy between the MD and experiment. This is also weighted heavily towards the Zr-Zr contribution (~71%), consistent with MD underestimating the Zr-Zr bond length. In all cases, the second- and higher-order peaks were consistent between both experiment and MD. Since the best agreement was found when $g_{\mathrm{ZrPt}}(r)$ was the dominant partial and large inconsistencies were found when $g_{\mathrm{ZrZr}}(r)$ was present, $g_{\mathrm{ZrPt}}(r)$ was chosen as the third constraint for the RMC simulations.

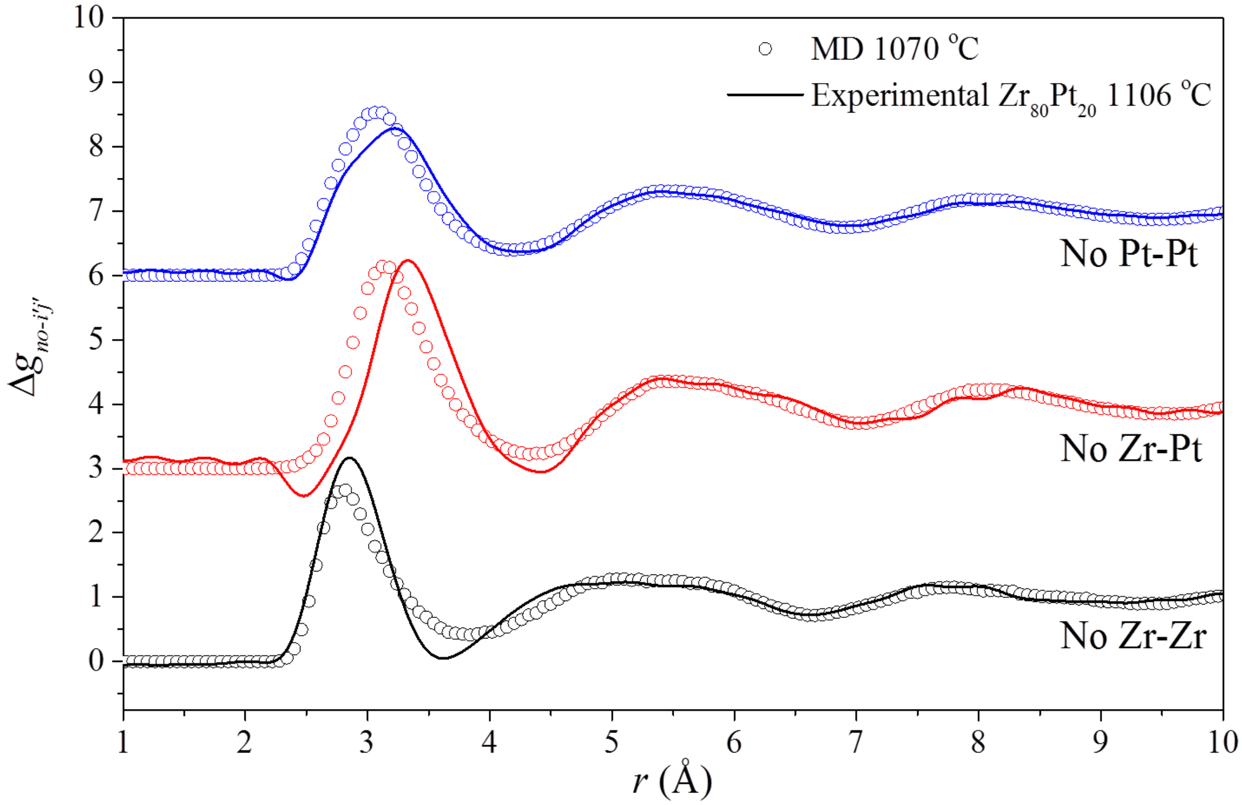

Figure 5.4 Experimental and calculated values of contributions to the total $g(r)$ when a single partial is removed using Eqn. 5.9. Large differences are observed when the Zr-Zr partials dominate. Each curve is offset by 3 for clarity.

5.3.3 Constrained Reverse Monte Carlo

As discussed in Section 5.2.3, atomic configurations for the liquids were generated from the experimental scattering data using the Reverse Monte Carlo technique [46]. It is important to note that, while producing realistic results, RMC structures are not unique. They are the most disordered structures that can describe the experimental data. Since the measured $S(q)$s are already averaged over many liquid configurations due to the rapid dynamics in the liquid and the long acquisition times, the structures obtained from RMC are reasonable approximations to this average. However, while the total structure factor is generally well reproduced, RMC structures obtained from a single experimental X-ray or neutron scattering constraint do not properly capture chemical order, yielding unphysical PPDFs. This can be significantly improved by constraining the RMC fits with multiple experimental inputs, such as from X-ray, neutron, and EXAFS measurements, as well as with PPDFs obtained from MD simulations.

Based on the results from Section 5.3.2, RMC fits to the experimental $S(q)$s from X-ray and neutron scattering, $S^X(q)$ and $S^N(q)$, were additionally constrained with the Zr-Pt partial, $g_{ZrPt}(r)$, obtained from the MD simulations. The constrained fits agreed well with both X-ray and neutron results (Figure 5.5 (a)). $S^X(q)$ was in particularly good agreement. The positions and amplitudes of the first peak in $g(r)$ were consistent with both the neutron and X-ray results (Figure 5.5 (b)). The pre-peak in $S^N(q)$ was not reproduced with the constraints used; only when the RMC fits were constrained with the two experimental measurements and not the MD results did the pre-peak appear. In that case, however, the PPDFs contained unphysical features due to insufficient constraints during the RMC fitting procedure.

When compared with the PPDFs obtained from MD, $g_{ZrPt}(r)$ was well reproduced, since it was one of the input constraints to the CRMC fit (Figure 5.6 (b)). As predicted, the $g_{ZrZr}(r)$ from RMC shifted to slightly larger-r relative to MD (Figure 5.6 (a)). The most significant difference with MD was in $g_{PtPt}(r)$ (Figure 5.6 (c)), where the very small first peak nearly doubled in size and shifted to slightly larger-r. This larger nearest-neighbor Pt-Pt correlation is consistent with previous CRMC results made using EXAFS measurements of $Zr_{80}Pt_{20}$ glasses [62]. The amplitude of the second-neighbor shell (r~4.5 Å) for $g_{PtPt}(r)$ is also increased. The PSFs from the CRMC show very good agreement with the Zr-Pt MD partial (Figure 5.7 (b)), as expected, and while the Zr-Zr partial is very similar to that from MD (Figure 5.7 (a)), all of the peaks show a small shift to lower-q, consistent with a shift to larger-r in the PPDF. The largest differences are again for the Pt-Pt partial (Figure 5.7 (c)). As argued previously, the pre-peak in $S(q)$ near $q = 1.6$ Å^{-1} is due to Pt-Pt correlations beyond those of nearest neighbors. This is consistent with the large feature around 4.5 Å in $g_{\mathrm{PtPt}}(r)$ (Figure 5.6 (c)) and the large peak around 1.6 Å^{-1} in $S_{\mathrm{PtPt}}(q)$ (Figure 5.7 (c)). The peak in g_{PtPt} at r~4.5 Å is significantly reduced if the pre-peak is masked in S_{PtPt}, suggesting that this is the dominant length scale for the medium range Pt-Pt correlation. This is consistent with interatomic distances in different types of interpenetrating Pt-centered icosahedra [30, 54]. The approximate distances between the center Pt atoms for these clusters are 4.55-5 Å in a capped configuration (Figure 5.8 (a)) and 4-4.3 Å in a diagonal configuration (Figure 5.8 (b)). In a highly disordered liquid containing a distribution of icosahedral-like clusters, these distances are likely smeared out, creating the broad peak in $g_{\mathrm{PtPt}}(r)$ centered at 4.5 Å.

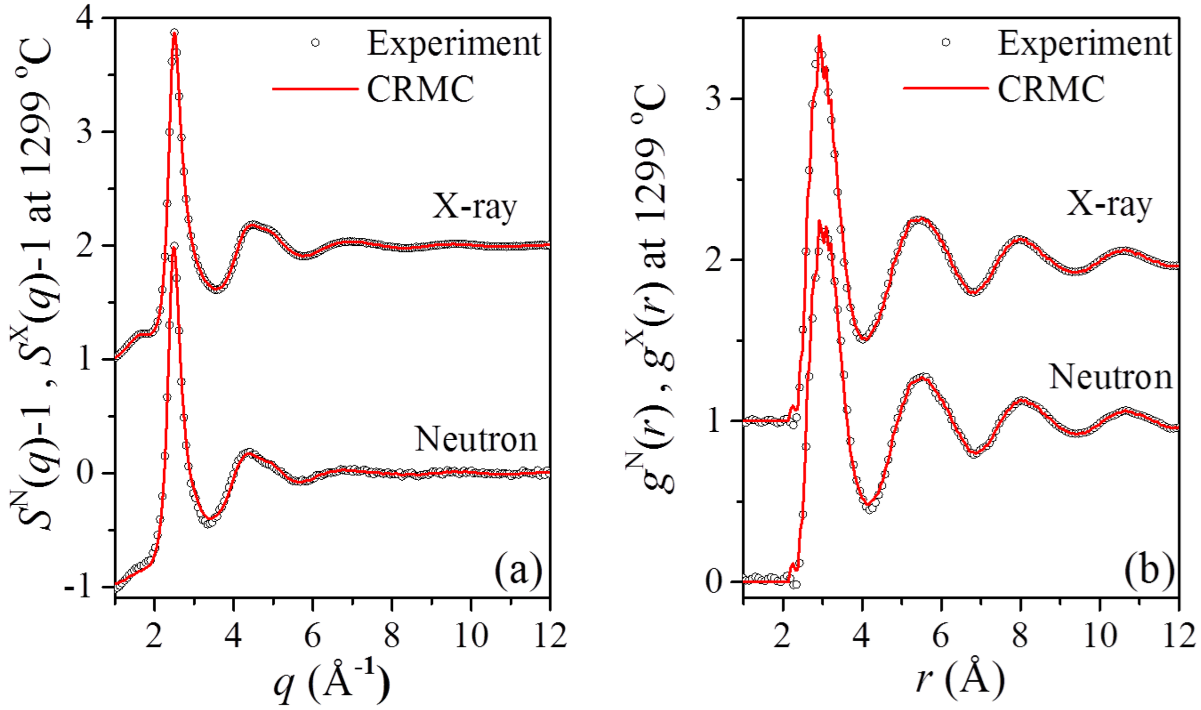

Figure 5.5 Results of CRMC fits to $Zr_{80}Pt_{20}$ liquid at 1299 °C for (a) $S(q)$-1 and (b) $g(r)$ for both X-ray (top curves) and neutron (bottom curves) scattering. In all cases, the CRMC (solid red lines) reproduced the experimental inputs constraints (open symbols) to high accuracy.

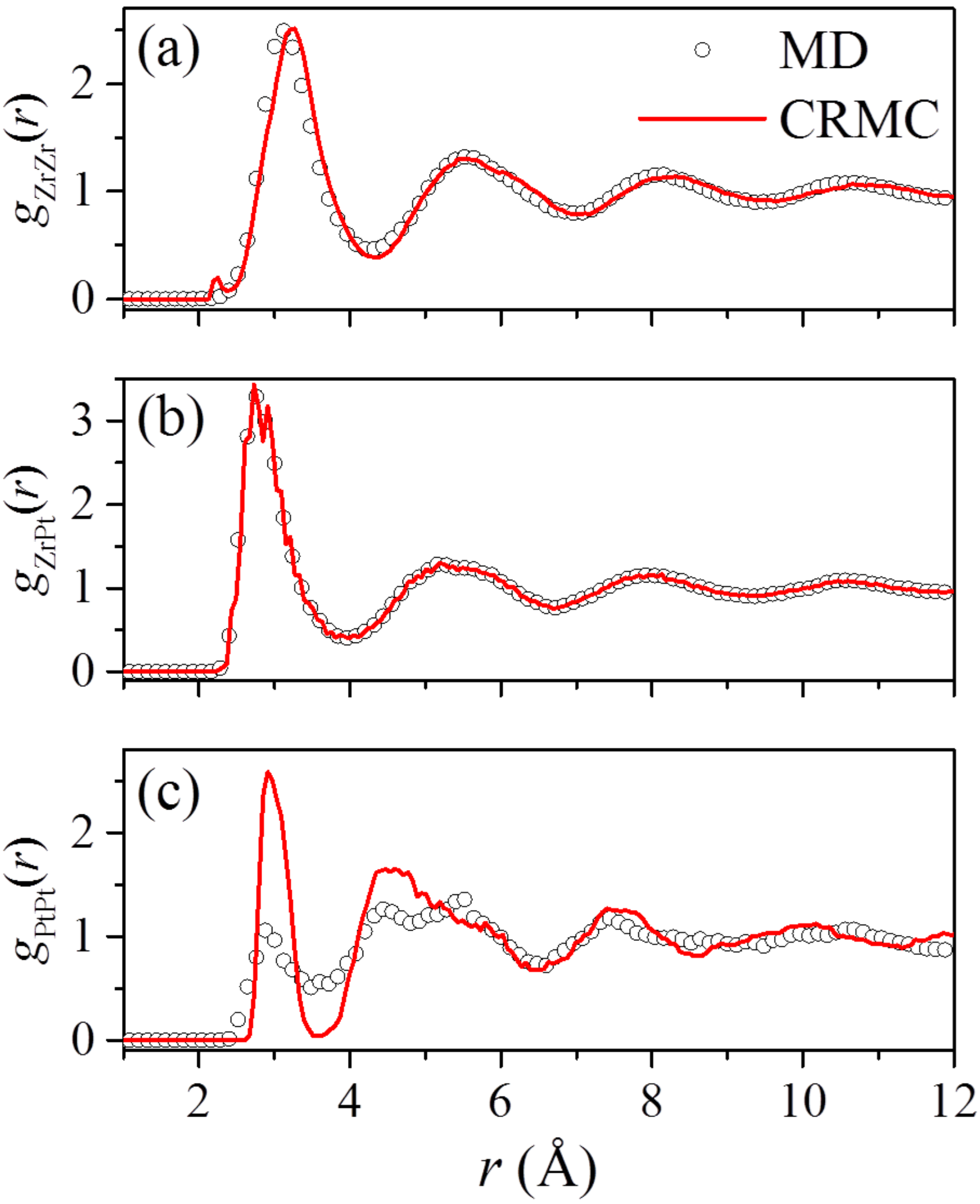

Figure 5.6 Comparisons of the PPDFs from MD (open symbols) and CRMC (red lines) for (a) $g_{ZrZr}(r)$, (b) $g_{ZrPt}(r)$, and (c) $g_{PtPt}(r)$. The largest differences were observed with $g_{PtPt}(r)$.

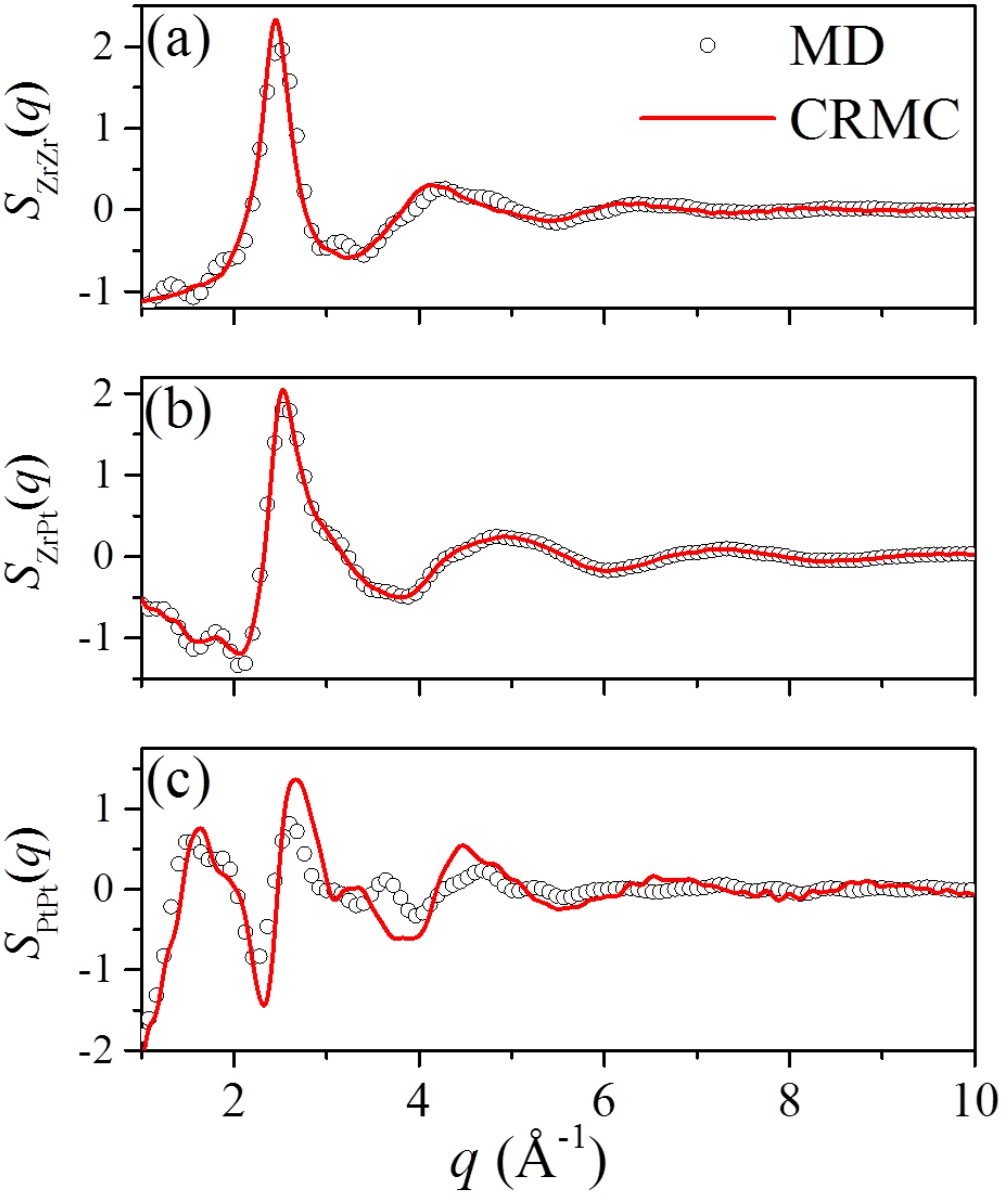

Figure 5.7 Comparisons of the PSFs from MD (open symbols) and CRMC (red lines) for (a) $S_{\mathrm{ZrZr}}(q)$, (b) $S_{\mathrm{ZrPt}}(q)$, and (c) $S_{\mathrm{PtPt}}(q)$. The largest differences were observed with $S_{\mathrm{PtPt}}(q)$.

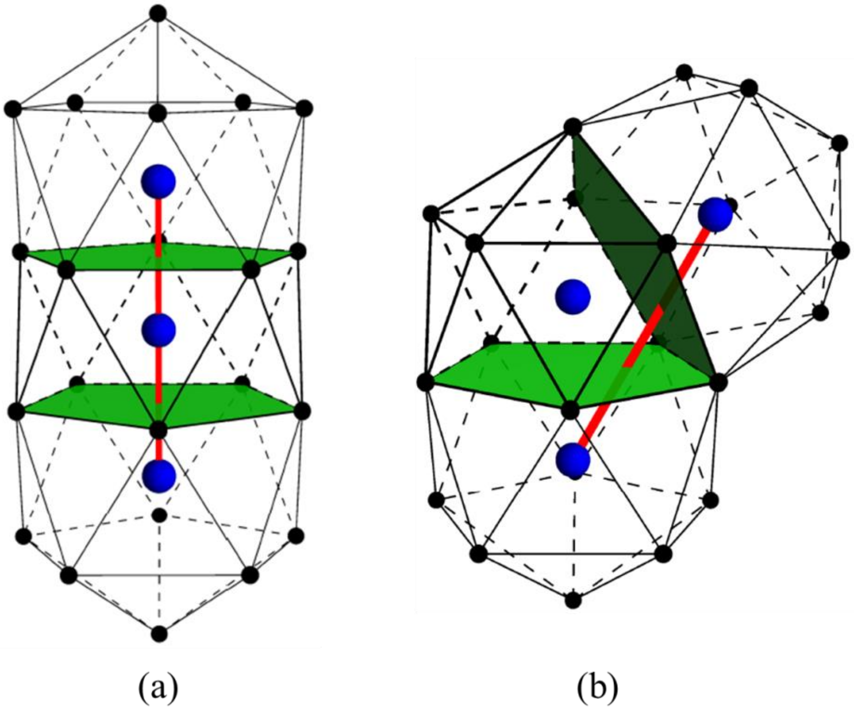

Figure 5.8 (a) Capped and (b) diagonal interpenetrating icosahedra. The center of each icosahedron is represented by a blue sphere. A red line connects the centers of neighboring interpenetrating icosahedra.

5.3.4 Bhatia-Thornton Partial Structures

The total structure factor of a binary alloy can also be expressed within the Bhatia-Thornton formalism [63] (Eqn. 5.10). $S_{BT}(q)$ is described in terms of fluctuations in density (topological order, $S_{NN}(q)$), fluctuations in chemical concentration (chemical order, $S_{CC}(q)$), and the cross-correlation between topological and chemical order ($S_{NC}(q)$):

$$S_{BT}^{N}(q)=\frac{\langle b\rangle^{2}}{\langle b^{2}\rangle}S_{NN}(q)+\frac{2\langle b\rangle\left(b_{i}-b_{j}\right)}{\langle b^{2}\rangle}S_{NC}(q)+\frac{\left(b_{i}-b_{j}\right)^{2}}{\langle b^{2}\rangle}S_{CC}(q)\,. \tag{5.10}$$

Here, b corresponds to the neutron scattering length and i,j correspond to the first and second elements in the binary alloy, respectively. $S_{CC}(q)$ is defined such that at large-q it converges to $c_i c_j$. While the order of b_i-b_j is important for the interpretation of $S_{NC}(q)$, reversing the alloy equation only changes the sign. $S_{BT}(q)$ can be calculated for X-ray scattering by replacing b_i

with the q-dependent atomic form factor, $f_i(q)$, as is done within the FZ formalism. The BT partial structure factors can also be described in terms of the FZ partials:

$$\begin{aligned}
&(a)\quad S_{NN}(q) = c_i^2 S_{ii}(q) + 2c_i c_j S_{ij}(q) + c_j^2 S_{jj}(q)\\
&(b)\quad S_{NC}(q) = c_i^2 c_j S_{ii}(q) + \left(c_i c_j^2 - c_i^2 c_j\right) S_{ij}(q) - c_i c_j^2 S_{jj}(q)\\
&(c)\quad S_{CC}(q) = c_i^2 c_j^2 \left(S_{ii}(q) - 2S_{ij}(q) + S_{jj}(q)\right) + c_i c_j
\end{aligned}\tag{5.11}$$

For $Zr_{80}Pt_{20}$, all three FZ partials were obtained from CRMC and converted to the BT formalism using Eqn. 5.11 (Figure 5.9 (a)). For $Zr_{77}Rh_{23}$, the weighting factor for $S_{CC}(q)$ in both X-ray and neutron scattering was negligible compared to $S_{NN}(q)$ and $S_{NC}(q)$ (less than 1%), so Eqn. 5.10 reduced to an equation with only two unknowns and $S_{NN}(q)$ and $S_{NC}(q)$ could be uniquely determined with two experimental inputs. The equivalent PPDFs, $g_{NN}(r)$, $g_{NC}(r)$, and $g_{CC}(r)$, were then obtained from a Fourier transform of the partial structure factors (Figure 5.9 (b)). While the amplitude of the $Zr_{80}Pt_{20}$ $S_{NN}(q)$ partial is slightly larger than that of $Zr_{77}Rh_{23}$, $S_{NN}(q)$ is virtually identical in all other aspects. Topologically, then, the ordering in the two liquids appears to be very similar, with nearly identical average bond lengths between atomic sites. This similarity is also evident in $g_{NN}(r)$, where again nearly identical peak shapes and positions are found. Perhaps this is not surprising since, in the limit of $c_j \rightarrow 0$, $S_{NN}(q)$ equals $S(q)$ for the pure element and Rh and Pt are of similar size (r_{Pt} = 1.38 Å, r_{Rh} = 1.34 Å) and in adjacent columns and rows on the periodic table. However, $S_{NN}(q)$ in another pair of alloy liquids where the solutes are again in adjacent columns in the periodic table ($Zr_{64}Ni_{36}$ and Zr_2Cu) show very different topological order [64]. This could be a consequence of the lower solute concentrations in the Zr-Pt and Zr-Rh liquids, with the order constrained by the Zr, or it simply indicates that it is possible for alloy liquids with similar atomic sizes to behave quite differently.

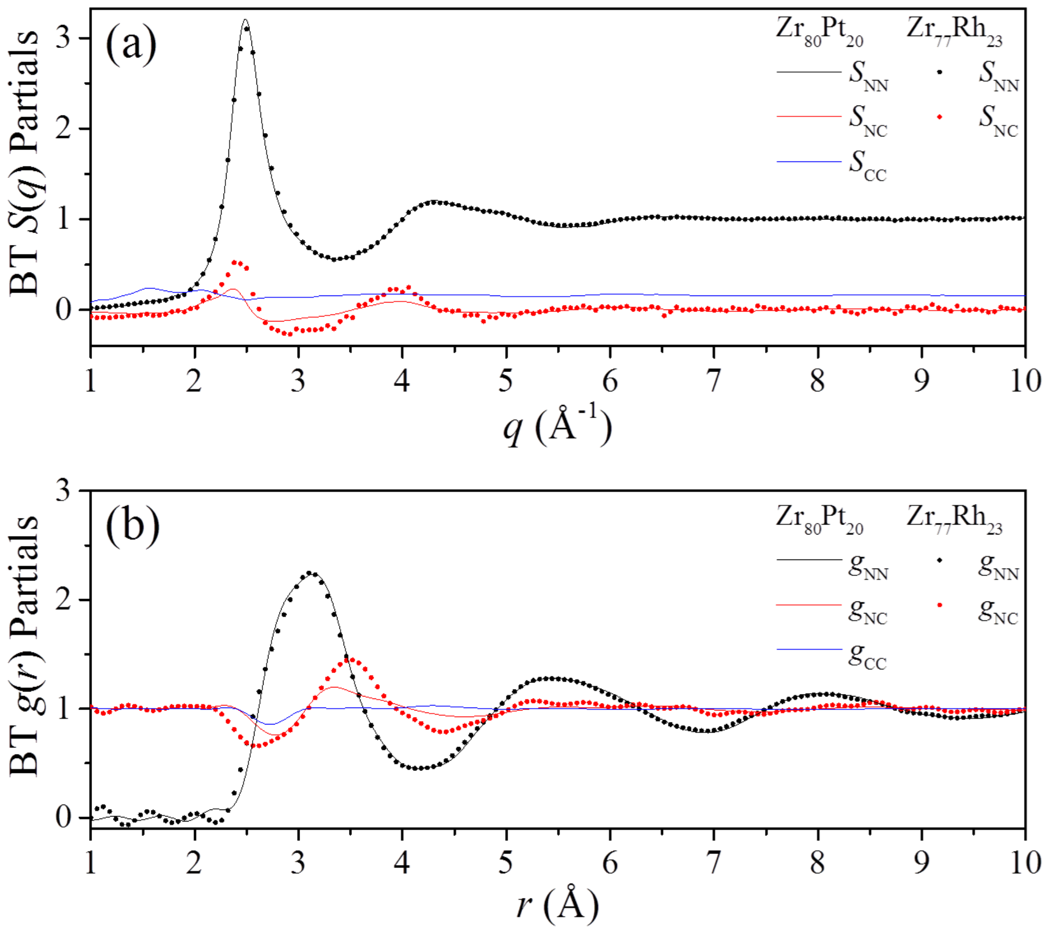

Figure 5.9 (a) $S(q)$ and (b) $g(r)$ Bhatia-Thornton partials for $Zr_{80}Pt_{20}$ (solid lines) and $Zr_{77}Rh_{23}$ (solid symbols) at 1115 °C. The topological order (NN) is very similar between both alloys.

The positive peak in $S_{CC}(q)$ for $Zr_{80}Pt_{20}$ near 1.6 Å^{-1} (Figure 5.9 (a)) suggests that the pre-peak in the total $S(q)$ arises from atoms of the same chemical species that are arranged in a regular pattern within the overall structural topology. Taken with the results of CRMC, this is consistent with a Pt-Pt correlation. There is also a corresponding positive peak in $g_{CC}(r)$ near 4.5 Å, consistent with the Pt-Pt correlation observed in the second coordination shell of $g_{PtPt}(r)$.

The cross-correlation terms, $S_{NC}(q)$ and $g_{NC}(r)$, are often described as representing a "size effect." The negative peak in $g_{NC}(r)$ for $Zr_{80}Pt_{20}$ near 2.75 Å suggests there is a higher density of atoms surrounding Pt atoms at that distance than around Zr. The corresponding negative peak in

$g_{CC}(r)$ suggests that atoms of opposite species tend to associate at this length scale, consistent with the high chemical affinity between Zr and Pt. Similarly the positive peak near 3.2 Å suggests a larger density of atoms surrounding Zr atoms at that distance than around Pt atoms. These results are consistent with fewer atoms packing around the smaller Pt atoms than around the larger Zr atoms. The lack of features in $g_{CC}(r)$ at $r = 3.2$ Å implies that there is no preference for Zr over Pt atoms at this length scale. The negative peak in $g_{NC}(r)$ near 4.5 Å again suggests a higher density of atoms around Pt atoms relative to around Zr, and the corresponding positive peak in $g_{CC}(r)$ is consistent with there being a preference for those atoms to also be Pt. This is consistent with the medium-range correlations previously discussed in the FZ formalism.

It is interesting to note that while $Zr_{80}Pt_{20}$ and $Zr_{77}Rh_{23}$ are nearly identical in their topological order, the size effect is much larger for $Zr_{77}Rh_{23}$, despite Pt and Rh having very similar atomic radii, and suggests that the chemical order in $Zr_{77}Rh_{23}$ is more strongly tied to the topological order than in $Zr_{80}Pt_{20}$. It seems that the stronger heat of mixing between Zr-Pt than between Zr-Rh should at least make up for this difference, if not surpass it. Without $g_{CC}(r)$ available for $Zr_{77}Rh_{23}$, it is impossible to know what chemical order overlays the topological configuration, but it is possible that Zr-Rh forgoes the establishment of medium-range correlations between Rh-atoms in favor of increased chemical short range order. This would explain the lack of pre-peak in $S^X(q)$ for $Zr_{77}Rh_{23}$ while it exists in $S^N(q)$ for $Zr_{80}Pt_{20}$, despite their identical FZ weighting factors.

5.3.5 Coordination Number

The average coordination numbers, $\langle CN \rangle_{BT}$, were calculated from $g_{NN}(r)$ by integrating the topological radial distribution function, $R_{NN}(r) = 4\pi r^2 \rho g_{NN}(r)$, between the minima on either side of the primary peak. The calculated values of $\langle CN_{ZrPt} \rangle_{BT} = 13.5$ and $\langle CN_{ZrRh} \rangle_{BT} =$

13.6 are nearly identical and are significantly larger than the value of 12 for ideal icosahedral packing. The larger numbers reflect the larger size of the dominant species, Zr, allowing more atoms to efficiently pack around it. This is confirmed using the partial coordination number for *j* atoms surrounding a central *i* atom, $\langle CN_{ij} \rangle_{PPDF}$, calculated in a similar fashion by integrating between the minima on either side of the primary peak. On average, each Zr atom ($\langle CN_{Zr} \rangle_{PPDF}$) is surrounded by 14.1 atoms (11.6 Zr and 2.5 Pt), while each Pt atom ($\langle CN_{Pt} \rangle_{PPDF}$) is surrounded by 11 atoms (10 Zr and 1 Pt).

5.3.6 Voronoi Tessellation

To further probe the liquid structures, the Voronoi tessellations were computed for the atomic configurations generated from CRMC (Figure 5.10). The average coordination numbers calculated from the Voronoi Indices (VI) were consistent with those found from the RDF method, with $\langle CN_{Zr} \rangle_{VI} = 13.8$ and $\langle CN_{Pt} \rangle_{VI} = 11.0$. It is not unexpected that the CN as determined by the RDF method overestimates the CN determined from Voronoi cells as there is some overlap between coordination shells which cannot be removed.

The dominant Zr-centered clusters (Figure 5.10 (a)) consist of large-CN Frank-Kasper (FK) polyhedra [65] such as <0 1 10 3 0> (CN 14) and <0 1 10 2 0> (CN 13), along with distorted polyhedra that relieve packing frustrations (<0 2 8 4 0>, <0 3 6 5 0>, and <0 4 4 6 0> for CN = 14, <0 3 6 4 0> and <0 2 8 3 0> for CN = 13). There are a few CN 15 polyhedra as well as a small fraction (~2%) of perfect icosahedral clusters (<0 0 12 0 0>; these are much less preferred because of the large size of Zr). Having a majority of large CN polyhedra (13-15) is consistent with the average $\langle CN_{Zr} \rangle_{PPDF} = 14.1$ determined from the $g_{ij}(r)$. Over the temperature range studied, the number of ideal FK polyhedra (<0 1 10 2 0>, <0 1 10 3 0>, and <0 1 10 4 0>) increases with decreasing temperature reflecting the ordering in the liquid. However, the number of distorted CN 14 and CN 13 FK polyhedra does not decrease, indicating that increased ordering is due to the transformation of strongly-disordered, high-CN polyhedra into more efficiently packed structures. As an example, the equilibrium crystal phase Zr_5Pt_3 contains two distinct Zr-centered clusters with coordination numbers of 14 and 15 [53]. When the <0 1 10 3 0> cluster in the liquid undergoes small distortions, it transforms into the CN 15 Zr-centered cluster in Zr_5Pt_3.

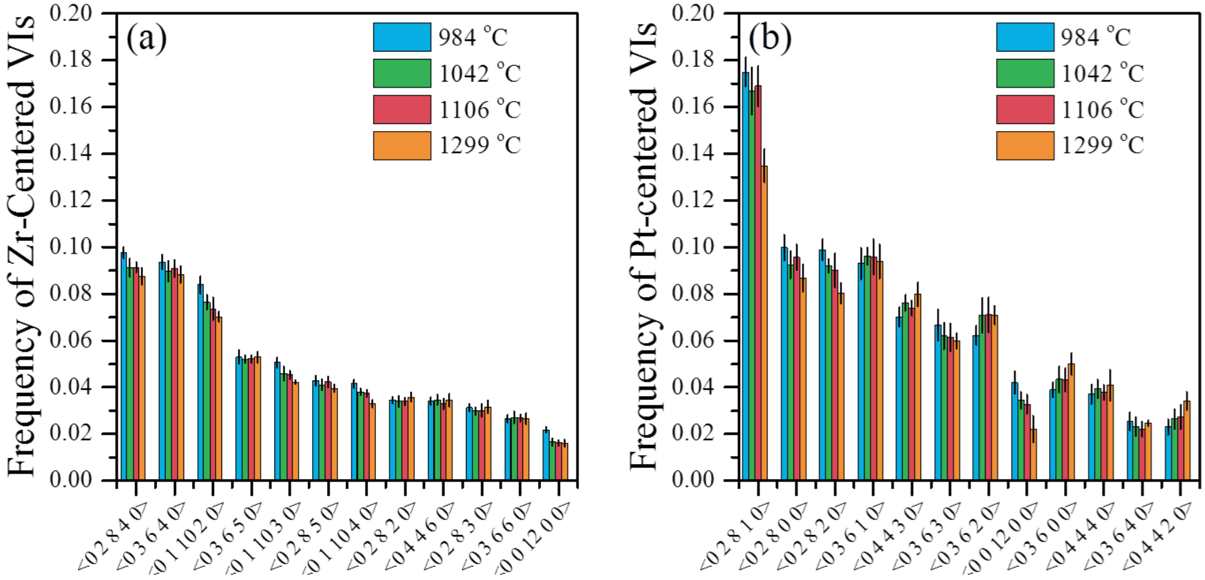

Figure 5.10 Frequency of the dominant Voronoi Indices for (a) Zr-centered and (b) Pt-centered structures.

While no single VI constitutes more than 10% of the total of Zr-centered polyhedra, the Pt-centered clusters are clearly dominated by <0 2 8 1 0> (Figure 5.10 (b)), the CN = 11 FK polyhedron. This structure appears to be very stable, since it was also shown to dominate in $Zr_{80}Pt_{20}$ glasses [30, 53]. This polyhedron corresponds to the Pt-centered cluster in the Zr_5Pt_3 equilibrium crystal phase [66], which is also the second phase to devitrify from amorphous ribbons following the formation of the quasicrystal [27]. While <0 2 8 1 0> clearly dominates, other polyhedra with CN = 10-12 also appear. Interestingly, while perfect icosahedra, <0 0 12 0

0>, are only weakly present in the high-temperature liquids, their frequency nearly doubles upon supercooling. The icosahedral-like clusters, <0 2 8 2 0> and <0 3 6 3>, are among the remaining dominant structures, with the number of <0 2 8 2 0> polyhedra also showing a sizeable increase with decreasing temperature. The rapid increase of these 12-coordinated structures likely aids in the formation of the quasicrystal phase upon cooling.

5.3.7 Crystal Identification

While complete chemical information cannot be extracted for $Zr_{77}Rh_{23}$, the similar coordination numbers with those of $Zr_{80}Pt_{20}$ and the nearly identical $S_{BT}(q)$ and $g_{BT}(r)$ suggest that these two liquids are at least topologically very similar. While there appears to be a much higher correlation between topological and chemical ordering in $Zr_{77}Rh_{23}$, the stability of the <0 2 8 1 0> cluster makes it likely that it is also prevalent in $Zr_{77}Rh_{23}$. Since this polyhedron is also found in the Zr_5Pt_3 crystal phase, it would seem that a similar phase might form in $Zr_{77}Rh_{23}$. It has not been observed in studies of Zr-Rh and Zr-Pd equilibrium phase diagrams [67, 68], but does form in Zr-Ir alloys (Zr_5Ir_3) [69]. Given this, an equivalent Mn_5Si_3-type phase is likely close to equilibrium in all of the Zr-noble metal alloys and may form as a metastable product during the crystallization. This appears to be the case for Zr-Rh. Shown in Figure 5.11 are fits (using GSAS II [70]) to X-ray data taken during recalescence of liquid $Zr_{77}Rh_{23}$ (with more than 200^{o}C supercooling). These indicate the presence of two phases, β-Zr and a hexagonal Mn_5Si_3-type phase, having a space group of $P6_3/mcm$. The most intense peaks are from β-Zr (*), while all remaining peaks belong to the Zr_5Rh_3 phase (o). Starting with lattice parameters found in Zr_5Pt_3 (a = 8.201 Å and c = 5.405 Å) [71, 72], the converged fits gave a = 7.95 Å and c = 5.6 Å for Zr_5Rh_3, closer to those found for Zr_5Ir_3 (a = 8.025 Å and c = 5.488 Å) [69]. While some differences are observed in the lattice parameters, the nonequilibrium conditions during the nucleation and growth of the metastable phase likely introduced chemical disorder within the lattice, slightly distorting the average atomic distances.

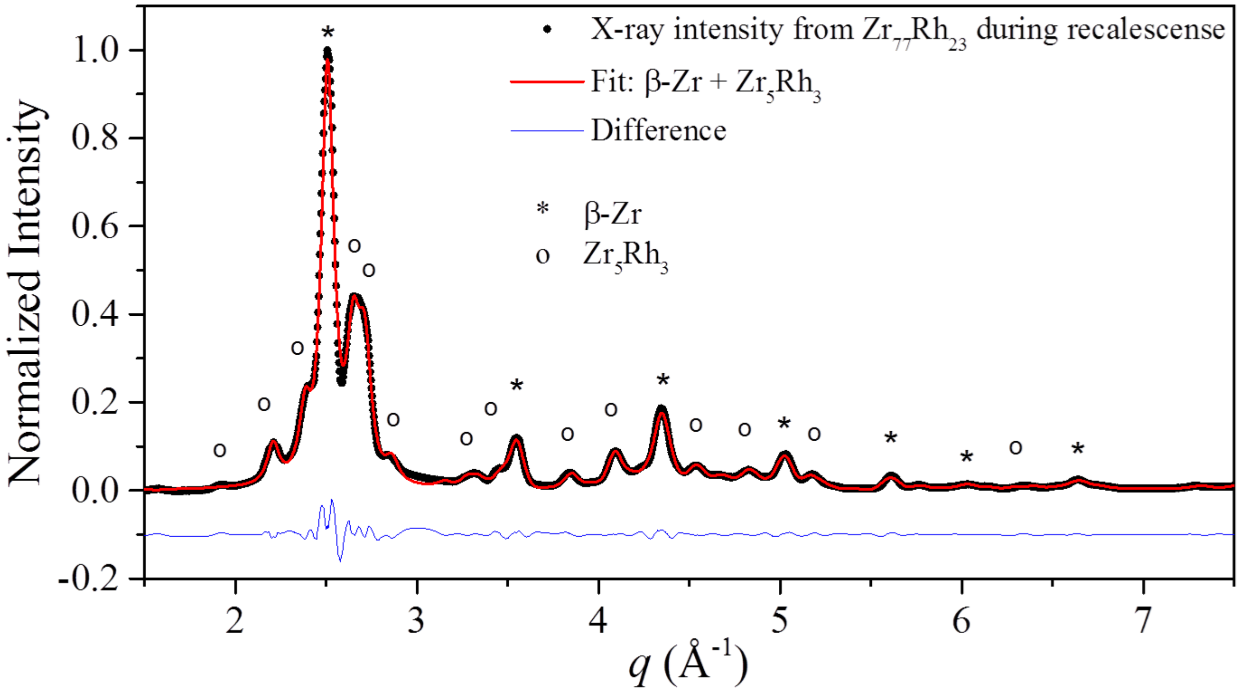

Figure 5.11 Identification of a phase mixture of β-Zr (*) and Zr_5Rh_3 (o) crystalline phases.

5.4 Conclusions

In summary, the first neutron scattering results of liquid and supercooled $Zr_{80}Pt_{20}$ and $Zr_{77}Rh_{23}$, made using a new electrostatic levitation facility [36], are reported. By combining these data with high-energy X-ray scattering studies of these liquids at equivalent temperatures, it is possible to extract topological and chemical ordering information. A comparison of structure factors and pair-distribution functions obtained from molecular dynamics simulations revealed differences between the computed values and those measured from the X-ray and neutron scattering experiments. Partial subtraction methods suggest that the $g_{ZrZr}(r)$ and $g_{PtPt}(r)$ MD partials were least consistent with measured results. The X-ray and neutron structure factors, $S^X(q)$ and $S^N(q)$, were therefore combined with $g_{ZrPt}(r)$ from MD to obtain the partials and the atomic structure for liquid $Zr_{80}Pt_{20}$ using the constrained Reverse Monte Carlo method. A pre-peak in the scattering data for $Zr_{80}Pt_{20}$ is consistent with medium-range ordering, arising from extended Pt-Pt correlations. Bhatia-Thornton partials for $Zr_{77}Rh_{23}$ were obtained by ignoring the CC contribution (less than 1% of the total) and calculating the NN and NC partials using X-ray and neutron scattering measurements. For $Zr_{80}Pt_{20}$, they were calculated directly from the Faber-Ziman partials determined from CRMC. From this, the two liquids were found to be topologically very similar. The larger cross partial, S_{NC}, for $Zr_{77}Rh_{23}$ suggests that the chemical order is more strongly tied to the topology than for $Zr_{80}Pt_{20}$. Combined with the lack of a pre-peak in the diffraction data, it is suggested that there is strong Rh-Rh chemical short-range order, but weaker medium-range order. The Voronoi results for the Zr-Pt liquid showed a mixture of ordered and distorted FK polyhedra, as well as a dominating Pt-centered <0 2 8 1 0> cluster, a structure also found around the Pt atoms in the Zr_5Pt_3 equilibrium crystal phase. A similar metastable phase was found to crystallize from a deeply supercooled (>200 ^{o}C) $Zr_{77}Rh_{23}$ liquid; this phase has not previously been reported in this binary alloy.

In addition to identifying some features of Zr-noble metal liquids, these results, based on multiple types of scattering experiments and combined with MD simulations, demonstrate the ability to follow the chemical and topological ordering of metallic liquids as a function of supercooling. This information is critically important in developing a better understanding of features such as liquid properties, crystal nucleation, possible liquid/liquid phase transitions, and ultimately glass formation.

5.5 References

[1] N.A. Mauro, V. Wessels, J.C. Bendert, S. Klein, A.K. Gangopadhyay, M.J. Kramer, S.G. Hao, G.E. Rustan, A. Kreyssig, A.I. Goldman, K.F. Kelton, *Physical Review B* **83**, 184109 (2011).

[2] N.A. Mauro, M.E. Blodgett, M.L. Johnson, A.J. Vogt, K.F. Kelton, *Nature Communications* **5:4616**, (2014).

[3] N.A. Mauro, A.J. Vogt, M.L. Johnson, J.C. Bendert, R. Soklaski, L. Yang, K.F. Kelton, *Acta Materialia* **61**, 7411 (2013).

[4] S. Klein, D. Holland-Moritz, D.M. Herlach, N.A. Mauro, K.F. Kelton, *Europhysics Letters* **102**, 36001 (2013).

[5] N.A. Mauro, K.F. Kelton, *Journal of Non-Crystalline Solids* **358**, 3057 (2012).

[6] N.A. Mauro, W. Fu, J.C. Bendert, Y.Q. Cheng, E. Ma, K.F. Kelton, *The Journal of Chemical Physics* **137**, 044501 (2012).

[7] V. Wessels, A.K. Gangopadhyay, K.K. Sahu, R.W. Hyers, S.M. Canepari, J.R. Rogers, M.J. Kramer, A.I. Goldman, D.S. Robinson, J.W. Lee, J.R. Morris, K.F. Kelton, *Physical Review B* **83**, 094116 (2011).

[8] G.W. Lee, A.K. Gangopadhyay, R.W. Hyers, T.J. Rathz, J.R. Rogers, D.S. Robinson, A.I. Goldman, K.F. Kelton, *Physical Review B* **77**, 184102 (2008).

[9] D. Holland-Moritz, F. Yang, J. Gegner, T. Hansen, M.D. Ruiz-Martín, A. Meyer, *Journal of Applied Physics* **115**, 1 (2014).

[10] T. Kordel, D. Holland-Moritz, F. Yang, J. Peters, T. Unruh, T. Hansen, A. Meyer, *Physical Review B* **83**, 104205 (2011).

[11] D. Holland-Moritz, O. Heinen, R. Bellissent, T. Schenk, *Materials Science and Engineering: A* **449-451**, 42 (2007).

[12] T. Schenk, D. Holland-Moritz, V. Simonet, R. Bellissent, D. Herlach, *Physical Review Letters* **89**, 1 (2002).

[13] L. Huang, C.Z. Wang, S.G. Hao, M.J. Kramer, K.M. Ho, *Physical Review B* **81**, 014108 (2010).

[14] R. Soklaski, Z. Nussinov, Z. Markow, K.F. Kelton, L. Yang, *Physical Review B* **87**, 184203 (2013).

[15] R. Soklaski, V. Tran, Z. Nussinov, K.F. Kelton, L. Yang, *arXiv:1502.01739[cond-mat.dis-nn]* 1

[16] K.F. Kelton, G.W. Lee, A.K. Gangopadhyay, R.W. Hyers, T.J. Rathz, J.R. Rogers, M.B. Robinson, D.S. Robinson, *Physical Review Letters* **90**, 195504 (2003).

[17] F. Frank, *Proceedings of the Royal Society of London Series A* **215**, 43 (1952).

[18] P. Ganesh, M. Widom, *Physical Review B - Condensed Matter and Materials Physics* **74**, 1 (2006).

[19] G.W. Lee, A.K. Gangopadhyay, K.F. Kelton, R.W. Hyers, T.J. Rathz, J.R. Rogers, D.S. Robinson, *Physical Review Letters* **93**, 037802 (2004).

[20] T.H. Kim, K.F. Kelton, *The Journal of Chemical Physics* **126**, 054513 (2007).

[21] J. Saida, M. Matsushita, A. Inoue, *Applied Physics Letters* **77**, 73 (2000).

[22] B.S. Murty, D.H. Ping, K. Hono, *Applied Physics Letters* **77**, 1102 (2000).

[23] B.S. Murty, D.H. Ping, M. Ohnuma, K. Hono, *Acta Materialia* **49**, 3453 (2001).

[24] D.J. Sordelet, X.Y. Yang, E.A. Rozhkova, M.F. Besser, M.J. Kramer, *Applied Physics Letters* **83**, 69 (2003).

[25] D.J. Sordelet, E. Rozhkova, M.F. Besser, M.J. Kramer, *Journal of Non-Crystalline Solids* **334-335**, 263 (2004).

[26] J. Saida, M. Matsushita, A. Inoue, *Journal of Applied Physics* **90**, 4717 (2001).

[27] D.J. Sordelet, R.T. Ott, M.Z. Li, S.Y. Wang, C.Z. Wang, M.F. Besser, A.C.Y. Liu, M.J. Kramer, *Metallurgical and Materials Transactions A* **39**, 1908 (2007).

[28] M.H. Lee, X. Yang, M.J. Kramer, D.J. Sordelet, *Philosophical Magazine* **86**, 443 (2006).

[29] C. Li, L. Wang, A. Inoue, *Journal of Physics: Condensed Matter* **13**, L803 (2001).

[30] S. Wang, C. Wang, M. Li, L. Huang, R. Ott, M. Kramer, D. Sordelet, K. Ho, *Physical Review B* **78**, 184204 (2008).

[31] M.H. Lee, R.T. Ott, M.F. Besser, M.J. Kramer, D.J. Sordelet, *Scripta Materialia* **55**, 505 (2006).

[32] T.E. Faber, J.M. Ziman, *Philosophical Magazine* **11**, 153 (1965).

[33] A.K. Gangopadhyay, G.W. Lee, K.F. Kelton, J.R. Rogers, A.I. Goldman, D.S. Robinson, T.J. Rathz, R.W. Hyers, *Review of Scientific Instruments* **76**, 073901 (2005).

[34] N.A. Mauro, K.F. Kelton, *Review of Scientific Instruments* **82**, 035114 (2011).

[35] J. Neuefeind, M. Feygenson, J. Carruth, R. Hoffmann, K.K. Chipley, *Nuclear Instruments and Methods in Physics Research Section B: Beam Interactions with Materials and Atoms* **287**, 68 (2012).

[36] N.A. Mauro, K. Derendorf, A.J. Vogt, M.L. Johnson, D. Quirinale, A.I. Goldman, K.F. Kelton, *Manuscript in Preparation* (2015).

[37] K. Derendorf, *The Design, Construction, and Implementation of an Electrostatic Levitation Facility for Neutron Scattering Studies of Liquids*, Ph.D. Thesis, Washington University in St. Louis (2013).

[38] A.J. Vogt, *Studies of Structural and Chemical Ordering in Metallic Liquids and Glasses Using Electrostatic Levitation*, Ph.D. Thesis, Washington University in St. Louis (2014).

[39] J.C. Bendert, C.E. Pueblo, S. Veligati, N.A. Mauro, K.F. Kelton, *International Journal of Thermophysics* **35**, 1687 (2014).

[40] R.C. Bradshaw, D.P. Schmidt, J.R. Rogers, K.F. Kelton, R.W. Hyers, *Review of Scientific Instruments* **76**, 125108 (2005).

[41] S.K. Chung, D.B. Thiessen, W.-K. Rhim, *Review of Scientific Instruments* **67**, 3175 (1996).

[42] J.C. Bendert, K.F. Kelton, *International Journal of Thermophysics* **35**, 1677 (2014).

[43] J.C. Bendert, N.A. Mauro, K.F. Kelton, *Journal of Applied Crystallography* **46**, 999 (2013).

[44] K. Page, C.E. White, E.G. Estell, R.B. Neder, A. Llobet, T. Proffen, *Journal of Applied Crystallography* **44**, 532 (2011).

[45] P.F. Peterson, E.S. Božin, T. Proffen, S.J.L. Billinge, *Journal of Applied Crystallography* **36**, 53 (2003).

[46] R.L. McGreevy, *Journal of Physics: Condensed Matter* **13**, (2001).

[47] O. Gereben, P. Jovari, L. Temleitner, L.G. Pusztai, *Journal of Optoelectronics and Advanced Materials* **9**, 3021 (2007).

[48] J.L. Finney, *Proceedings of the Royal Society of London A* **319**, 479 (1970).

[49] J.L. Finney, *Nature (London)* **226**, 309 (1977).

[50] C.H. Rycroft, *Chaos* **19**, 18 (2009).

[51] J. Park, Y. Shibutani, *Intermetallics* **23**, 91 (2012).

[52] W.F. Gale, T.C. Totemeier, *Smithells Metals Reference Book (8th Edition)*, Elsevier, 2004.

[53] J. Saida, K. Itoh, S. Sato, M. Imafuku, T. Sanada, A. Inoue, *Journal of Physics: Condensed Matter* **21**, 375104 (2009).

[54] H.W. Sheng, W.K. Luo, F.M. Alamgir, J.M. Bai, E. Ma, *Nature* **439**, 419 (2006).

[55] C.N.J. Wagner, *Journal of Non-Crystalline Solids* **76**, 29 (1985).

[56] N. Mattern, A. Schöps, U. Kühn, J. Acker, O. Khvostikova, J. Eckert, *Journal of Non-Crystalline Solids* **354**, 1054 (2008).

[57] N. Mattern, P. Jóvári, I. Kaban, S. Gruner, A. Elsner, V. Kokotin, H. Franz, B. Beuneu, J. Eckert, *Journal of Alloys and Compounds* **485**, 163 (2009).

[58] J. Neuefeind, K.D. Lis, *Ber. Bunsenges. Phys. Chem.* **100**, 1341 (1996).

[59] C.J. Benmore, J.K.R. Weber, S. Sampath, J. Siewenie, J. Urquidi, J.a. Tangeman, *Journal of Physics: Condensed Matter* **15**, S2413 (2003).

[60] M.C. Wilding, M. Wilson, P.F. McMillan, *Philosophical transactions. Series A, Mathematical, physical, and engineering sciences* **363**, 589 (2005).

[61] J. Saida, T. Sanada, S. Sato, M. Imafuku, A. Inoue, *Applied Physics Letters* **91**, 111901 (2007).

[62] J. Saida, K. Itoh, T. Sanada, S. Sato, M. Imafuku, M. Ohnuma, A. Inoue, *Journal of Alloys and Compounds* **509S**, S27 (2011).

[63] A.B. Bhatia, D.E. Thornton, *Physical Review B* **2**, 3004 (1970).

[64] D. Holland-Moritz, F. Yang, T. Kordel, S. Klein, F. Kargl, J. Gegner, T. Hansen, J. Bednarcik, I. Kaban, O. Shuleshova, N. Mattern, A. Meyer, *Europhysics Letters* **100**, 56002 (2012).

[65] F.C. Frank, J.S. Kasper, *Acta Crystallographica* **12**, 483 (1959).

[66] E. Matsubara, T. Nakamura, M. Sakurai, M. Imafuku, S. Sato, J. Saida, A. Inoue, *MRS Proceedings* **644**, (2001).

[67] D. Arias, J.P. Abriata, *Journal of Phase Equilibria* **14**, 110 (1993).

[68] R.M. Waterstrat, a. Shapiro, a. Jeremie, *Journal of Alloys and Compounds* **290**, 63 (1999).

[69] H. Okamoto, *Journal of Phase Equilibria* **13**, 653 (1992).

[70] B.H. Toby, R.B. Von Dreele, *Journal of Applied Crystallography* **46**, 544 (2013).

[71] P. Villars, *Material Phases Data System (MPDS),* SpringerMaterials, CH-6354 Vitznau, Switzerland, 2014.

[72] T. Biswas, K. Schubert, *Zeitschrift für Metallkunde* **58**, 558 (1967).

Chapter 6: Metastable Phase Selection in $Zr_{77}Rh_{23}$

This chapter includes X-ray data that were acquired during the BESL 2013 experiment, as well as at Washington University in St. Louis. Neutron data were acquired on the NOMAD beamline at the Spallation Neutron Source in 2013 in the same configuration as NOMAD 2014. DTA measurements were assisted by C. Pueblo, and crystallography was supported by Prof. P. C. Gibbons (Washington University in Saint Louis, Saint Louis, MO).

6.1 Introduction

While equilibrium crystal phases are thermodynamically favored to form in a supercooled liquid, these phases do not necessarily have the lowest homogeneous nucleation barrier to crystallization [1]. Instead, the nucleation and growth of the metastable phases with a lower nucleation barrier often occurs [2]. To observe the influence of the homogeneous nucleation barrier, however, heterogeneous nucleation must be avoided. By using the electrostatic levitation technique [3] to remove contact with container walls, which serve as potent heterogeneous nucleation sites, the non-equilibrium liquid can be maintained to low temperatures before the onset of crystallization, allowing homogeneous nucleation to be explored. By carefully selecting an alloy composition at a deep eutectic [4], the supercooling can be further enhanced by increasing the reduced glass transition temperature, T_g/T_L, due to the lower liquidus temperature. This reduces the difference in Gibbs free energy between the liquid and the crystal, decreasing the driving force towards crystallization and improving undercooling.

The binary alloy $Zr_{77}Rh_{23}$ is a eutectic alloy that has been of interest due to its superconducting properties [5-8] and its ability to form a metallic glass by rapid quenching [8-

10]. Complex crystal phases, such as the Ti_2Ni-like “big cube” phase [8, 11, 12] and phases with $D0_e$–like structure [11, 12] form upon devitrification of the amorphous phase. These phases disappear upon further annealing in favor of the equilibrium phases. In some instances where the liquid was not quenched quickly enough to form a fully amorphous phase, diffraction peaks from a metastable $L1_2$–type FCC structure were identified [10, 13]. Past studies of metastable phases in this alloy have been limited to the devitrification products, but we have recently reported the identification of a metastable Zr_5Rh_3 (Mn_5Si_3-like) crystalline structure emerging during the recalescence of an undercooled levitated liquid using *in situ* high-energy X-ray diffraction (Chapter 5) [14]. Additional recalescences have been observed, suggesting the non-equilibrium undercooled $Zr_{77}Rh_{23}$ liquid contains many crystallization pathways to different metastable states. The deep undercooling obtained in this alloy (160-280 ^{o}C) increases the amount of time spent crystallizing under non-equilibrium conditions such as occurs when the hypercooling limit is reached [1] and helps facilitate these transformations.

Here we discuss the metastable phase selection of supercooled $Zr_{77}Rh_{23}$ liquids using the electrostatic levitation technique to maximize supercooling. Initial characterization was performed *in situ* using high-energy X-ray and neutron diffraction. Subsequent studies were made using powder diffraction with laboratory CuK_α radiation of crushed samples that were allowed to radiatively free-cool to room temperature after recalescence was observed.

6.2 Experimental Methods

Samples were prepared in a manner consistent with the procedures outlined in Chapter 2. The *in situ* X-ray diffraction measurements were acquired during the “BESL 2013” experiment using WU-BESL [15] and details of the detector setup and configurations are discussed in Section 2.4.3. Liquid diffraction analysis was performed using in-house LabVIEW modules [16] and is discussed in Section 2.5. The *in situ* neutron diffraction measurements were made using the NESL [17-19] on the Nanoscale-Ordered Materials Diffractometer (NOMAD) beamline at the Spallation Neutron Source [20]. Details of the experimental configuration are discussed in Section 2.8.3. Some samples were thermally processed in WU-BESL until the recalescence of interest was observed. The sample was then allowed to radiatively free-cool to room temperature and was subsequently recovered and crushed into a powder. Room temperature powder patterns were acquired using a Rigaku powder diffractometer (CuK$_\alpha$ $\lambda = 1.54$ Å). The details of these measurements are discussed in Section 2.2.2. Crystalline phases were identified using the GSAS II software [21], and the details of this analysis are discussed in Section 2.11.

6.3 Results and Discussion

The melt plateaus in the temperature-time profiles for the $Zr_{77}Rh_{23}$ liquid were matched to the experimental solidus value, T_S, of 1061 ^{o}C, which was in reasonable agreement with the best available phase diagram [22]. Once melted, the temperature was increased until the desired processing temperature was reached. The laser was then turned off and the samples were allowed to radiatively free-cool below the melting temperature. Eventually, a sharp rise in temperature was observed corresponding to the release of latent heat as the sample crystallized. Several representative temperature-time profiles of the processed $Zr_{77}Rh_{23}$ liquid are shown in Figure 6.1. The free-cooling curves are plotted on top of each other; the similar slopes during the free-cools indicate similar cooling rates. Depending on the amount of supercooling observed, three unique regions of maximum undercooling and recalescence temperature were observed (Figure 6.2) corresponding to the three profiles in Figure 6.1. Each type of recalescence was observed from multiple independent samples suggesting that the observations are not sample dependent. None of the combinations of crystalline phases that formed during recalescence were found to be consistent with the equilibrium phase diagram [22].

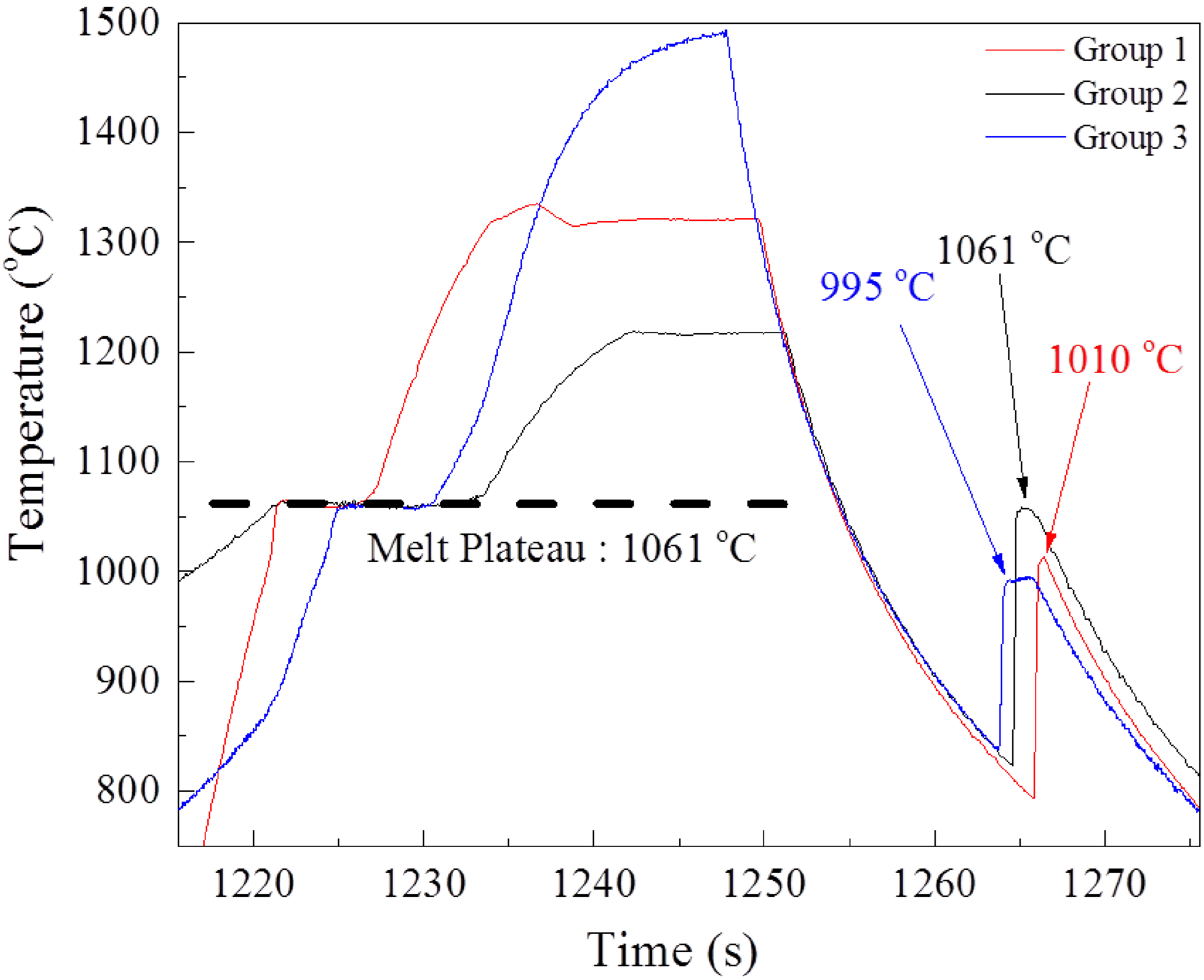

Figure 6.1 Temperature-time profiles corresponding to three unique types of recalescence behavior. All profiles have a melt plateau at 1061 ^{o}C (dashed line) and all times are relative. Each curve was shifted in time so their free-cool behavior would overlay the others.

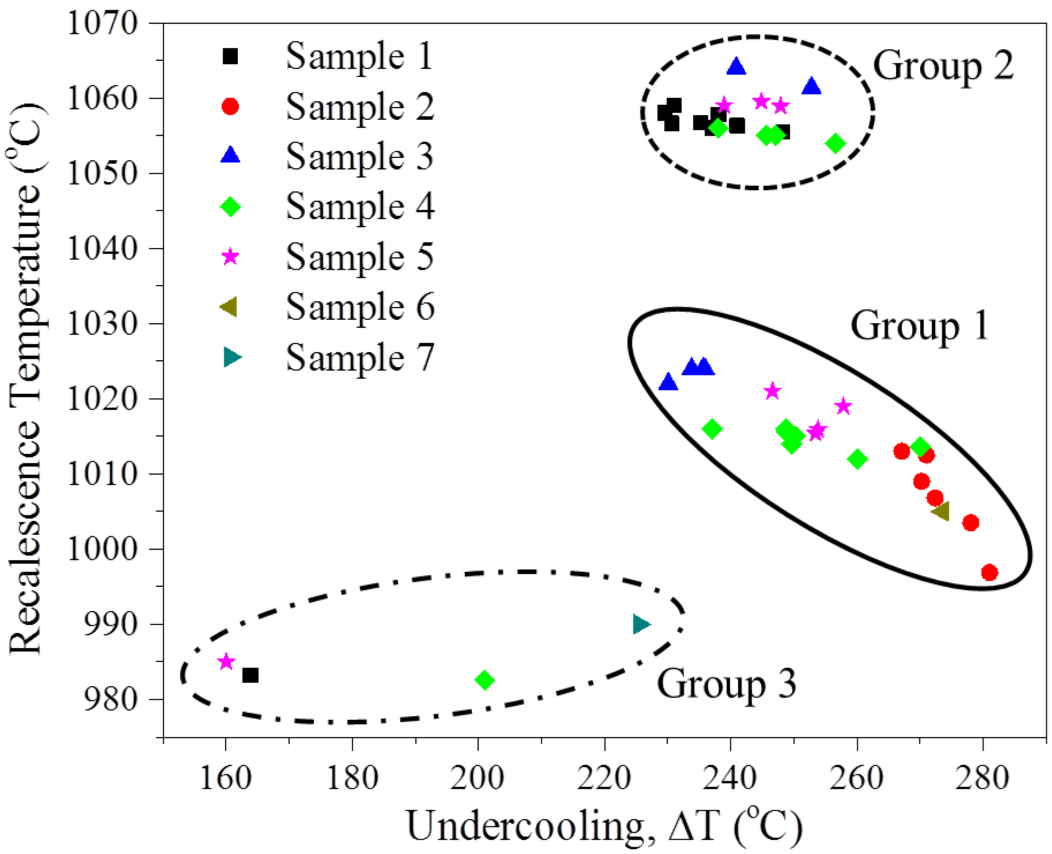

Figure 6.2 Three distinct recalescence behaviors were observed. The smallest undercooling was observed for Group 3 (-.-), while Groups 1 (——) and 2 (- - -) had some overlap. The post-recalescence temperature/time behavior with increased undercooling for Group 1 indicates that it is hypercooled.

The crystalline phases of the sample at the melt plateau prior to melting were observed *in situ* from neutron scattering using the NESL (Figure 6.3 (a)). They were identified as a mixture of the BCC β–Zr and the tetragonal C16 phases, consistent with the equilibrium phases at this temperature [22]. Their lattice parameters (Table 6.2) were in good agreement with the measured values for the equilibrium phases (Table 6.1). If Rh substitutes for Zr in β–Zr, the lattice parameter will shrink due to the smaller size of Rh (r_{Rh} = 1.35 Å, r_{Zr} = 1.61 Å) [23]. At the maximum equilibrium solubility (8%), the lattice parameter shrinks from 3.601 Å to 3.568 Å [9]. The fit value of a = 3.550 Å would suggests that the maximum solubility limit is exceeded, likely signaling that equilibrium solubility is larger than found in the accepted phase diagram.

The fit parameters for the C16 phase ($a = b = 6.556$ Å, $c = 5.595$ Å) are also in reasonable agreement with the expected equilibrium values ($a = b = 6.496$ Å, $c = 5.605$ Å).

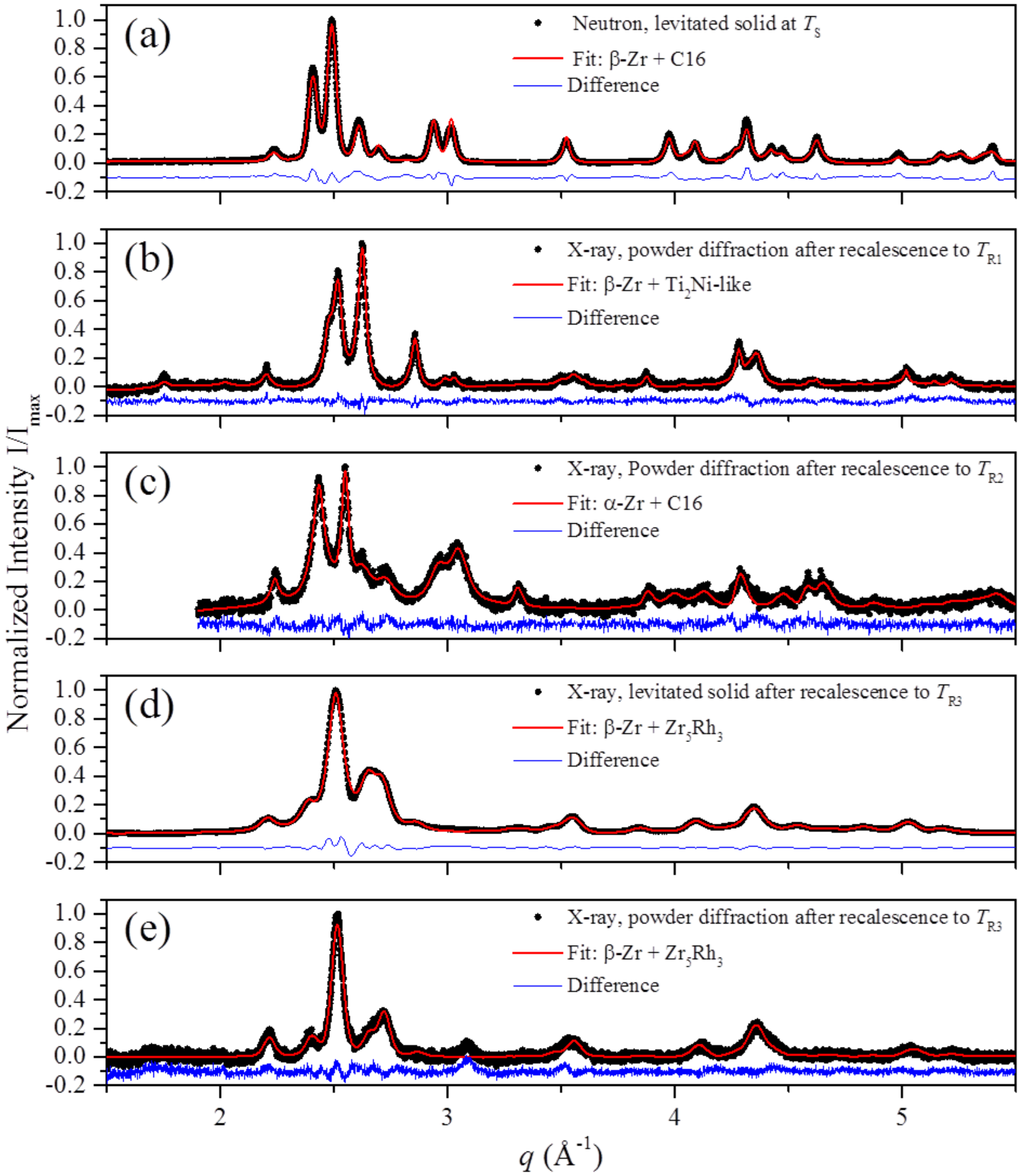

Figure 6.3 Crystalline phase identification of measured intensity (black points) and model fits (red lines) scaled to the maximum intensity recorded. The difference curve is displayed below each fit (blue line). (a) *In situ* neutron diffraction pattern at the melt plateau: β–Zr + Zr_2Rh (C16). (b) Recalescence to $T_{R1} \approx 1020$ °C, measured from powder diffraction: β–Zr + Zr_2Rh (Ti_2Ni-like). (c) Recalescence to $T_{R2} \approx 1060$ °C, measured from powder diffraction: α–Zr + Zr_2Rh (C16). (d) *In situ X-ray* diffraction pattern at the recalescence plateau ($T_{R3} \approx 995$ °C): β–Zr + Zr_5Rh_3 (Mn_5Si_3-like). (e) Recalescence to $T_{R3} \approx 995$ °C, measured from powder diffraction: β–Zr + Zr_5Rh_3 (Mn_5Si_3-like). Unidentified peak near $q = 3.1$ Å appears *in situ* only at low temperatures and is likely a third phase.

Table 6.1 Previously identified equilibrium and metastable phases of Zr-Rh, Zr-Pt, and Zr-Ir. The parameters x_1 and x_2 correspond to the adjustable atomic locations in the Wyckoff site symmetry.

Phase	Type	a (Å) b (Å) c (Å)	Symbol	Wyckoff multiplicity	x	y	z	Ref
β–Zr	W	3.568	*Im3m*	Zr (2a)	0	0	0	[24]
α–Zr	Mg	3.232 5.147	$P6_3/mmc$	Zr (2c)	1/3	2/3	1/4	[24]
Zr_2Rh	Al_2Cu (C16)	6.496 5.605	*I4/mcm*	Rh (4a) Zr (8h)	0 0.1667 (x_1)	0 0.6667 (x_2)	1/4 0	[24, 25]
Zr_2Rh	Ti_2Ni ($E9_3$)	12.536	*Fd3m*	Zr (16d) Rh (32e) Zr (48f)	5/8 0.8381 (x_1) 0.1848 (x_2)	5/8 0.8381 0	5/8 0.8381 0	[11]
Zr_5Pt_3	Mn_5Si_3	8.201 5.405	$P6_3/mcm$	Zr (4d) Zr (6g) Pt (6g)	1/3 0.236 (x_1) 0.5991 (x_2)	2/3 0 0	0 1/4 1/4	[24, 26]
Zr_5Ir_3	Mn_5Si_3	8.025 5.488	$P6_3/mcm$	Zr (4d) Zr (6g) Ir (6g)	-	-	-	[24, 27]

Table 6.2 Phases and their fit parameters identified from experimental X-ray and neutron scattering data. x_1 and x_2 correspond to the adjustable atomic locations in the Wyckoff site symmetry.

Group	Undercooling (ΔT_S) (^{o}C)	Recalescence Temperature (ΔT_S) (^{o}C)	Phases	Phase 1 a (Å) b (Å) c (Å)	Phase 2 a (Å) b (Å) c (Å)	x_1 x_2	Observation
-	Melt Plateau	Melt Plateau	β–Zr + Zr_2Rh (C16)	3.550	6.556 5.595	0.1653 0.6653	*in situ*: NESL
1	780-830 (281-230)	997-1024 (64-37)	β–Zr + Zr_2Rh (Ti_2Ni)	3.550	12.506	0.8431 0.1874	Powder
2	804-830 (257-230)	1054-1064 (7-(-3))	α–Zr + Zr_2Rh (C16)	3.239 5.160	6.521 5.602	0.1667 0.6667	Powder
3	835-901 (226-160)	983-990 (78-71)	β–Zr + Zr_5Rh_3 (Mn_5Si_3)	3.539	7.968 5.685	0.2376 0.5880	*in situ:* WU-BESL, Powder

A single sharp recalescence to $T_{R1} \approx 1020$ ^{o}C was observed for the deepest level of undercooling obtained (Figure 6.2, Group 1). The small width of the recalescence suggests that the deep undercooling (>230 ^{o}C below T_S) was in or close to the hypercooling limit, with nonequilibrium crystallization occurring. This was the most common recalescence behavior observed and was seen in nearly all samples processed. The diffraction peaks were identified as a combination of β–Zr (BCC solid solution) and metastable Zr_2Rh (Ti_2Ni-like FCC, or "big cube") (Figure 6.3 (b)). The Zr_2Rh phase has been previously identified as a primary devitrification product [8]. While this is an equilibrium phase for many alloys [28], in Zr-Rh it is only observed for a short time after devitrification, transforming to equilibrium phases with continued annealing. The fit parameters (a = 3.550 Å and a = 12.506 Å for β–Zr and Zr_2Rh, respectively, Table 6.2) are in good agreement with previously measured values. The Ti_2Ni-like phase has been shown to be a precursor to the icosahedral quasicrystal phase (*i-phase*) in Ti, Zr, and Hf alloys [29] and is often known as the Kuo crystalline approximant phase to the *i-phase* [30]. While the Zr-Rh alloy does not directly form the *i-phase*, additions of Rh to $Zr_{70}Cu_{30}$ facilitate its formation [31, 32]. The Ti_2Ni-like phase is also known to be stabilized by the addition of oxygen. However, all materials used in this study had low reported oxygen content, and while extended liquid processing will slowly consume remaining oxygen in the chamber, no dependence on processing time was observed in the formation of this phase.

With at least 230 ^{o}C of undercooling, a single recalescence at $T_{R2} \approx 1061$ ^{o}C was observed, the same temperature as the melt plateau (Figure 6.2, Group 2). From the measured diffraction peaks (Figure 6.3 (c)), a phase mixture of the low-temperature α–Zr solid solution phase and the equilibrium tetragonal C16 phase forms on recalescence in Group 2 (Table 6.2). Based on the equilibrium phase diagram, β–Zr should form instead of α–Zr. In equilibrium, the solid-solid phase transition from β–Zr to α–Zr occurs at 735 ^{o}C, while the minimum temperatures prior to recalescence were between 804 and 830 ^{o}C. It has been observed in pure Zr that the α–Zr can be formed directly from the liquid through rapid quenching [33-35], aided by interstitial oxygen. However, similar experiments performed on Zr-Nb alloys with up to 5.5 at.% Nb did not produce α–Zr directly from the liquid [35]. Attempts at rapidly quenching by dropping the sample immediately after recalescence, placing it in thermal contact with the rest of the levitation chamber, also contained a mixture of the α–Zr and C16 phases. Since samples from Groups 1 and 3 that were also quenched after recalescence contained the β–Zr phase, it is unlikely that Group 2 samples initially formed the β–Zr phase and transformed into the α–Zr phase during cooling. Instead, it appears that deep undercooling close to the hypercooling limit provides a non-equilibrium crystallization pathway that leads to the formation α–Zr. Since the Group 1 samples recalesce to the melting temperature of the C16 phase, that is likely the first phase to form. However, this was not observed during the *in situ* measurements and could not be verified. The rapid growth of the C16 phase could lead to chemical segregation, forming Zr-rich regions within the liquid which create an environment similar to the pure element and allowing the nucleation and growth of the α–Zr phase.

When the amount of undercooling observed was 226 ^{o}C or less, a single recalescence plateau was observed at $T_{R3} \approx 995$ ^{o}C (Figure 6.2, Group 3). The diffraction peaks indicated a mixture of β–Zr and the metastable Zr_5Rh_3 (Mn_5Si_3-like) phase (Table 6.2). This phase was previously identified from comparisons of the $Zr_{80}Pt_{20}$ and $Zr_{77}Rh_{23}$ liquid structures, for which the SRO for both liquids are nearly identical (Chapter 5) [14]. The Pt-centered Voronoi clusters of the high-temperature $Zr_{80}Pt_{20}$ liquid were dominated by the <0 2 8 1 0> index, a structural unit of the Pt-centered atoms in the Zr_5Pt_3 equilibrium phase (Table 6.1) [36]. Although the Zr_5Rh_3 phase is not a known equilibrium phase in the Zr-Rh system, a similar intermetallic phase appears in Zr-Ir alloys (Table 6.1) [24, 27]. While this phase is observed in both Zr-Ir and Zr-Pt, the Zr-Ir lattice parameter a is noticeably smaller than in Zr-Pt (8.025 vs. 8.201 Å, respectively). The lattice parameters for a Zr_5Rh_3 phase that was fit to the *in situ* X-ray diffraction data were consistent with those observed in the Zr-Ir alloy (a = 7.968 and c = 5.685 Å, Figure 6.3 (d)). Consistent results were found between *in situ* BESL experiments (Figure 6.3 (d)) and room temperature powder samples (Figure 6.3 (e)). An additional diffraction peak was observed at room temperature ~3.1 Å^{-1} (Figure 6.3 (e)). This peak was not observed during high-temperature *in situ* measurements, but appeared as the sample cooled after recalescence. It is likely that this signals the formation of a third phase that grows as the sample cools.

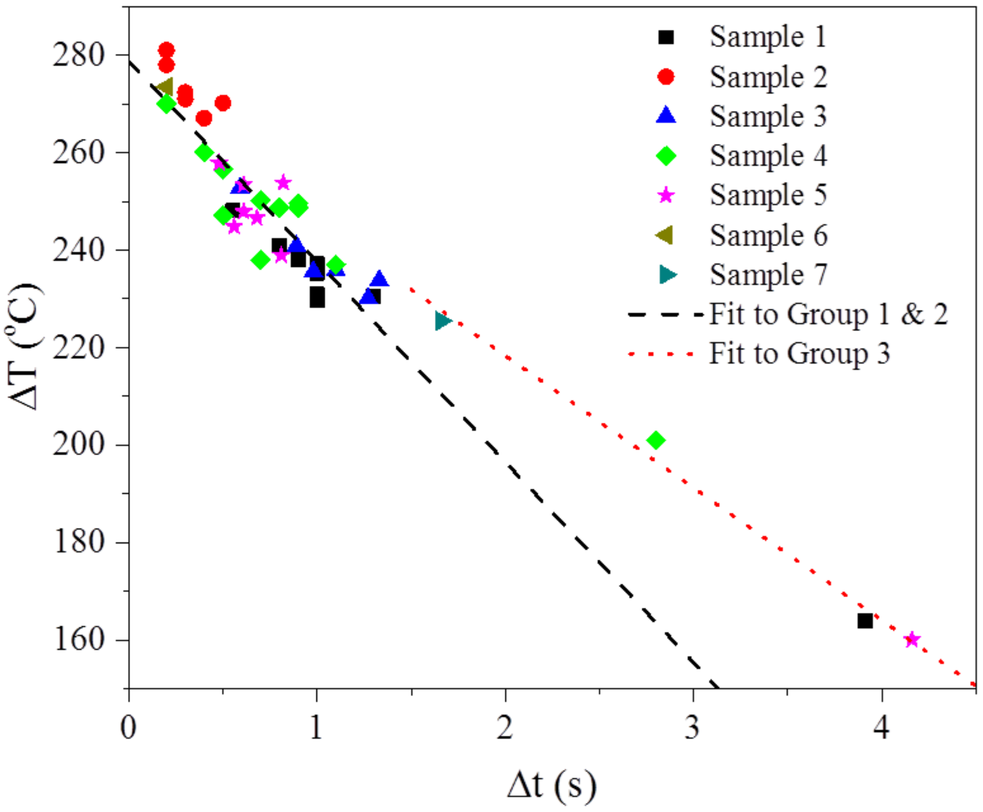

Figure 6.4 Amount of undercooling (ΔT) vs. width of recalescence plateau (in time, Δt). The best fit to Groups 1 and 2 is represented by the dashed black line, and the best fit to Group 3 is represented by the dotted red line.

A significant width (in time) of the recalescence plateau was observed for all Group 3 samples. In Group 1 and Group 2, the width of the plateau (Δt in s) was highly correlated with the amount of undercooling observed (ΔT relative to T_S, in °C). Despite very different phases forming, both followed a very linear trend (Figure 6.4, dashed black line). All occurrences of Group 3 behavior, while consistent within their group, had a very different rate of decay of recalescence width (Figure 6.4, dotted red line). The recalescence temperature is much lower than in Groups 1 and 2 indicating that the kinetics are likely much slower. Since it does not transform during the extended isothermal crystallization, it is suggested that the metastable phase is somewhat close to equilibrium with the metastable liquid at those temperatures, consistent with the stability of the Zr_5Pt_3 phase observed in $Zr_{80}Pt_{20}$ [14].

The observations of multiple metastable phases crystallizing from the supercooled $Zr_{77}Rh_{23}$ liquid were not fully categorized at the time of the initial *in situ* experiments. As such, the identification of Groups 1 and 2 could not be performed *in situ* and were investigated after they had already cooled to room temperature. There are more metastable phenomena that occurred during the processing of in-house samples such as multiple recalescences (Figure 6.5 (a-b) and metastable melt plateaus (Figure 6.5 (c)). Due to the short lifetime of some of these features, (Figure 6.5 (a-b)) it was impossible to study with powder diffraction after processing the sample. In addition to multiple recalescences, samples that recalesced to T_{R3} would sometimes re-melt at the same temperature rather than at the usual melting temperature. While this was only occasionally observed, it was more common to see a discontinuity during re-heating corresponding to T_{R3} followed by a melt plateau at 1061 ^{o}C. *In situ* experiments at high-flux X-ray sources such as the Advanced Photon Source are well suited to study the growth of these phases as well as to identify the primary nucleating phase that forms during recalescence.

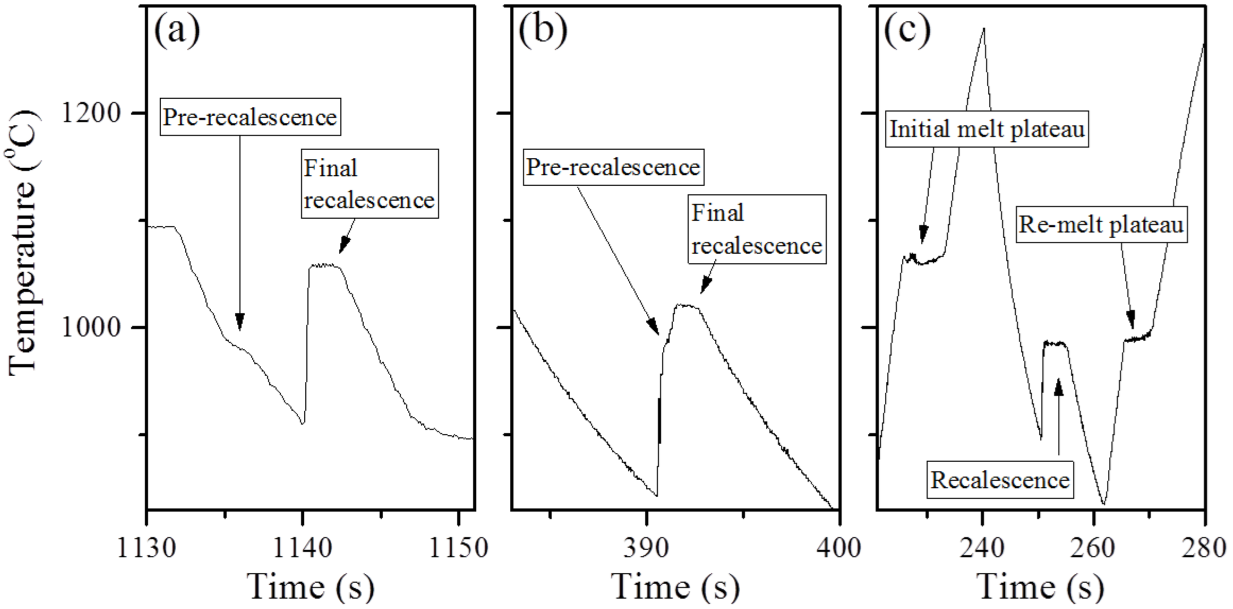

Figure 6.5 Other metastable recalescence behavior featuring (a) a minor recalescence before maximum undercooling is obtained, (b) a pair of recalescences after maximum undercooling, and (c) metastable melting plateaus.

6.4 Conclusions

In summary, the crystallization behavior and metastable phase selection were studied for deeply supercooled $Zr_{77}Rh_{23}$ alloy liquids. The Zr_5Rh_3 phase was first identified from a structural comparison of $Zr_{80}Pt_{20}$ and $Zr_{77}Rh_{23}$ liquids (Chapter 5), and is further characterized here. Three separate crystallization patterns were identified, corresponding to β–Zr + Zr_2Rh (Ti_2Ni-like), α–Zr + Zr_2Rh (C16), and β–Zr + Zr_5Rh_3 (Mn_5Si_3-like). The close similarity of Zr_5Rh_3 phase with the liquid structure likely inhibits this alloy's glass-forming ability. The crystallization pathways are tied to the amount of supercooling obtained prior to crystallization. Several of the identified metastable phases (α–Zr and Zr_2Rh (Ti_2Ni-like)) are known to be stabilized by interstitial oxygen. Further characterization of these phases is needed, including *in situ* observations of the diffraction patterns as they form from the liquid. Additional insight into the topological and chemical structure of the liquid can in turn provide valuable information on the metastable pathways that must be avoided for glass formation. In addition, understanding the behavior and formation of metastable phases is important for determining processing techniques to select for specific phases and mechanical properties for future applications.

6.5 References

[1] D. Herlach, Materials Science and Engineering R **12**, 177 (1994).

[2] B. Feuerbacher, Materials Science Reports **4**, 1 (1989).

[3] A.K. Gangopadhyay, G.W. Lee, K.F. Kelton, J.R. Rogers, A.I. Goldman, D.S. Robinson, T.J. Rathz, R.W. Hyers, Review of Scientific Instruments **76**, 073901 (2005).

[4] D. Turnbull, Transactions of the Metallurgical Society of AIME **221**, 422 (1961).

[5] C.J. Raub, C.A. Andersen, Zeitschrift für Physik **175**, 105 (1963).

[6] S.T. Zegler, Journal of Physics and Chemistry of Solids **26**, 1347 (1965).

[7] M. Tenhover, W.L. Johnson, Physical Review B **27**, 1610 (1983).

[8] A.J. Drehman, W.L. Johnson, in, 1979, pp. 499.

[9] K. Togano, K. Tachikawa, Journal of Applied Physics **46**, 3609 (1975).

[10] X.L. Yeh, K. Samwer, W.L. Johnson, Applied Physics Letters **42**, 242 (1983).

[11] J.S. Cantrell, J.E. Wagner, R.C. Bowman Jr, Journal of Applied Physics **57**, 1985 (1985).

[12] J.E. Wagner, R.C. Bowman, J.S. Cantrell, Journal of Applied Physics **58**, 4573 (1985).

[13] X.L. Yeh, E.J. Cotts, Journal of Materials Research **2**, 173 (1987).

[14] M.L. Johnson, M.E. Blodgett, K. Lokshin, N.A. Mauro, J. Neuefeind, C. Pueblo, D.G. Quirinale, A.J. Vogt, A.I. Goldman, K.F. Kelton, Manuscript in Preparation (2015).

[15] N.A. Mauro, K.F. Kelton, Review of Scientific Instruments **82**, 035114 (2011).

[16] J.C. Bendert, N.A. Mauro, K.F. Kelton, Journal of Applied Crystallography **46**, 999 (2013).

[17] N.A. Mauro, K. Derendorf, A.J. Vogt, M.L. Johnson, D. Quirinale, A.I. Goldman, K.F. Kelton, Manuscript in Preparation (2015).

[18] K. Derendorf, The Design, Construction, and Implementation of an Electrostatic Levitation Facility for Neutron Scattering Studies of Liquids, Ph.D. Thesis, Washington University in St. Louis (2013).

[19] A.J. Vogt, Studies of Structural and Chemical Ordering in Metallic Liquids and Glasses Using Electrostatic Levitation, Ph.D. Thesis, Washington University in St. Louis (2014).

[20] J. Neuefeind, M. Feygenson, J. Carruth, R. Hoffmann, K.K. Chipley, Nuclear Instruments and Methods in Physics Research Section B: Beam Interactions with Materials and Atoms **287**, 68 (2012).

[21] B.H. Toby, R.B. Von Dreele, Journal of Applied Crystallography **46**, 544 (2013).

[22] H. Okamoto, Journal of Phase Equilibria & Diffusion **25**, 486 (2004).

[23] W.F. Gale, T.C. Totemeier, Smithells Metals Reference Book (8th Edition), Elsevier, 2004.

[24] P. Villars, L.D. Calvert, Pearson's Handbook of Crystallographic Data for Intermetallic Phases, American Society for Metals, Metals Park, OH, 1985.

[25] H. Ko, Structural and electronic investigations of complex intermetallic compounds, Ph.D. Thesis, Iowa State University (2008).

[26] P. Villars, Material Phases Data System (MPDS), SpringerMaterials, CH-6354 Vitznau, Switzerland, 2014.

[27] H. Okamoto, Journal of Phase Equilibria **13**, 653 (1992).

[28] M.V. Nevitt, J.W. Downey, R.A. Morris, Transactions of the Metallurgical Society of AIME **218**, 1019 (1960).

[29] K.H. Kuo, D.W. Deng, Journal of Alloys and Compounds **342**, 174 (2002).

[30] S. Ranganathan, A. Inoue, Acta Materialia **54**, 3647 (2006).

[31] C. Li, L. Wang, A. Inoue, Journal of Physics: Condensed Matter **13**, L803 (2001).

[32] C. Li, L. Wang, A. Inoue, The European Physical Journal of Applied Physics **18**, 109 (2002).

[33] S. Banerjee, B. Cantor, in: International Conference on Martensite, MIT Press, Boston, 1979, pp. 195.

[34] S. Banerjee, G.K. Dey, Journal of Materials Science **39**, 3985 (2004).

[35] G.K. Dey, S. Banerjee, Bulletin of Materials Science **15**, 543 (1992).

[36] E. Matsubara, T. Nakamura, M. Sakurai, M. Imafuku, S. Sato, J. Saida, A. Inoue, MRS Proceedings **644**, (2001).

Chapter 7: Devitrification Behavior in $Zr_{52.5}Cu_{17.9}Ni_{14.6}Al_{10}Ti_5$ (Vit105) Using Simultaneous Wide-Angle and Small-Angle X-ray Scattering

This chapter includes X-ray data that were acquired during the SAXS 2014 experiment. DSC and DTA measurements were performed by C. Pueblo (Washington University in Saint Louis, Saint Louis, MO).

7.1 Introduction

Phase separation in the supercooled liquid is a phenomenon that has been observed in silicate glasses for many years [1, 2]. More recently, it has been reported in a variety of metallic glass systems including Ni-based [3-5], Cu-based [6], Zr-based [7, 8], Mg-based [9], and many other alloys [10]. This is of practical interest since phase separation can produce hierarchical microstructures involving chemically and topologically diverse length scales [11]. The formation of these features can hinder the inhomogeneous flow that is typical of metallic glasses, improving their plasticity [12-14]. In addition to phase separation, the formation of dispersed nanocrystals within the amorphous or supercooled liquid state could also provide similar benefits [11].

If phase separation occurs in the supercooled liquid, this implies the existence of a miscibility gap where two liquids of distinct composition can coexist. In order to phase separate in this manner, elements with a repulsive interaction (i.e., positive heats of mixing) can be added to an alloy. This is in direct opposition with the typical rules of bulk glass formation, which require elements with large negative heats of mixing [15]. In some alloys, however, it has been found that the addition of elements with small positive heats of mixing can sometimes aid glass formation [16-18]. Alternatively, a short-lived phase separation could occur. While the homogeneous supercooled liquid has a single liquidus temperature (T_L), decomposing into two compositionally distinct amorphous regions could cause T_L to increase relative to the glass transition temperature (T_g) in at least one phase [19, 20]. In other words, the reduced glass transition temperature, $T_{RG} = T_g / T_L$, decreases. According to the Turnbull criteria [21], nucleation is suppressed for large values of T_{RG}, so a decrease in T_{RG} during decomposition could trigger the onset of crystallization in one of the regions. By understanding the crystallization pathways in these kinds of materials, the development of new and better bulk glass-forming materials may be realized.

7.2 Motivation

A study was undertaken to search for liquid-liquid phase separation in the supercooled liquid through simultaneous wide-angle (WAXS) and small-angle X-ray scattering (SAXS) measurements (denoted in this dissertation as SAXS 2014, Section 2.4.4). A number of bulk glass-forming alloys known to phase separate when annealed close to T_g were examined. A pseudo-binary phase diagram calculated using CALPHAD for one such alloy ($Ni_{58.5}Nb_{20.25}Y_{21.25}$) [4] suggested the presence of a miscibility gap in the high-temperature liquid, and was also investigated. In preparation for this experiment, WAXS data were acquired from levitated liquid samples during BESL 2013 (Section 2.4.3). When the height ($S(q_1)$) and width (full-width at half-max, (FWHM)) of the primary peak in the structure factors ($S(q)$) were compared for a collection of alloy liquids, $Ni_{58.5}Nb_{20.25}Y_{21.25}$ did not cluster with the rest. Instead, the primary peak was shorter and wider than for other liquids (Figure 7.1). While scattering data for

$Ni_{58.5}Nb_{20.25}Y_{21.25}$ were obtained at relatively high temperatures, this temperature range overlapped with that of the other alloy liquids, suggesting that the different peak shape was not solely due to increased disorder. The data suggested, then, that a broad distribution of length scales could result from the formation of two compositionally distinct liquid phases, due to the overlap of widely separated partial structure factors.

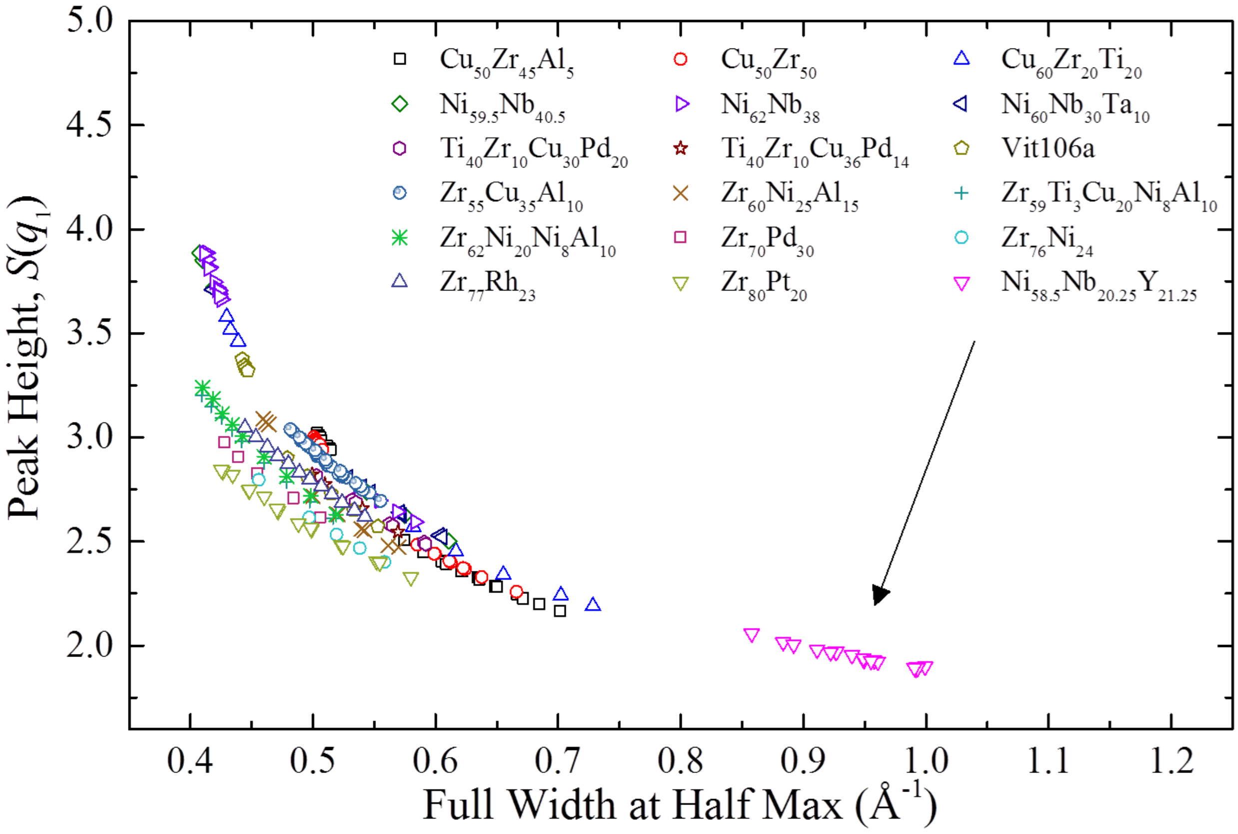

Figure 7.1 $S(q_1)$ vs. FWHM for a variety of liquid alloys measured with high-energy X-ray diffraction in WU-BESL experiments. The primary peak in $Ni_{58.5}Nb_{20.25}Y_{21.25}$ (magenta triangles) was significantly shorter and wider than the rest, suggesting that two separate phases could have overlapping structure factors.

Unfortunately, attempts at observing phase separation in the high-temperature supercooled liquid prior to crystallization were unsuccessful for all alloys studied in SAXS 2014. The SAXS measurements were limited to a q-range of 0.01 – 0.025 $Å^{-1}$ (corresponding to correlation lengths of 1.2 – 62.8 nm) and recorded a flat background. An increase in intensity at very small-q was observed after crystallization, corresponding to a "tail" from much longer-range correlations inaccessible in our configuration. In all cases, this feature appeared simultaneously with the formation of crystal peaks in WAXS. Due to the rapid kinetics in the high-temperature liquid, any nanoscale compositional fluctuations that might form would quickly grow beyond the experimentally accessible length scales in SAXS, preventing studies of the earliest stages. In order to successfully observe liquid-liquid phase separation, the liquid must either be cooled to significantly lower temperatures where the kinetics are much slower, or the acquisition rate must be increased. In the temperature range near T_L, even 1 s scans are probing a time-averaged structure and do not have the resolution to capture such short time-scale fluctuations.

Despite the lack of evidence for phase separation in the supercooled liquid near T_L, however, clear SAXS signals were observed upon heating into the supercooled liquid region in a glassy $Zr_{52.5}Cu_{17.9}Ni_{14.6}Al_{10}Ti_5$ (Vit105) alloy that was quenched *in situ*. Vit105 has been studied in the past with small-angle scattering (SAS), WAXS, DSC, and TEM measurements [20, 22, 23]. When annealed close to T_g, a SAS signal near 0.025 $Å^{-1}$ began to grow. Simultaneous *in situ* SAXS and WAXS measurements revealed that the SAXS intensity began to increase before the WAXS intensity increased when annealed at T_g [23]. This was observed separately using TEM and WAXS, where the sample annealed near T_g for 30 minutes showed clear density fluctuations in TEM and SANS but no crystal peaks appeared in WAXS [20]. Both studies concluded that phase separation likely occurred prior to crystallization. However, later experiments found contradicting results. Nanobeam electron diffraction (NBD) of samples annealed at T_g revealed crystalline diffraction patterns in the density fluctuations observed in

TEM [24]. Similarly prepared samples exhibited a SAXS signal, while no crystal peaks were observed in X-ray diffraction.

The results presented in this chapter seek to clarify these conflicting results in past work. This study was performed in a containerless environment to remove the influence of heterogeneous nucleation sites from a container. The high-flux X-rays available at the Advanced Photon Source (APS) allowed for observation of the crystallization behavior in real-time (acquisition times of 1 s rather than 1 min [23]). In addition, the high stability of this alloy allowed us to examine the crystallization behavior in the supercooled liquid region well above T_g.

7.3 Experimental Methods

Samples were prepared in a manner consistent with the procedures outlined in Chapter 2. The WAXS and SAXS data were acquired during the “SAXS 2014” experiment using WU-BESL [25] and details of the detector setup and configurations are discussed in Section 2.4.4. WAXS analysis was performed using in-house LabVIEW modules [26] and is discussed in Section 2.5. SAXS analysis was performed using Matlab scripts developed by the beamline scientist at Station 1-ID-E at the Advanced Photon Source and is discussed in Section 2.6.

7.4 Results and Discussion

7.4.1 Thermal Analysis

The glass transition (T_g) and crystallization (T_x) temperatures were determined from DSC measurements at a heating rate of 20 ^oC/min (Figure 7.2). T_g was determined to be 389 ^oC, which is within 20 ^oC of other reported values at similar heating rates [20, 23, 27-30]. Vit105 exhibits one or two crystallization events, depending on the oxygen concentration of the sample

[24]. With low oxygen concentration, two crystallization events are seen. The first corresponds to the formation of the tetragonal Zr_2Ni phase, and the second to the formation of the Ti_2Ni-like big cube phase which is known to be stabilized by oxygen. With high oxygen concentration, only the second crystallization event is observed. Two crystallization events were observed in our samples, confirming the high-quality material used in sample preparation. For our samples, T_x was 449 ^{o}C.

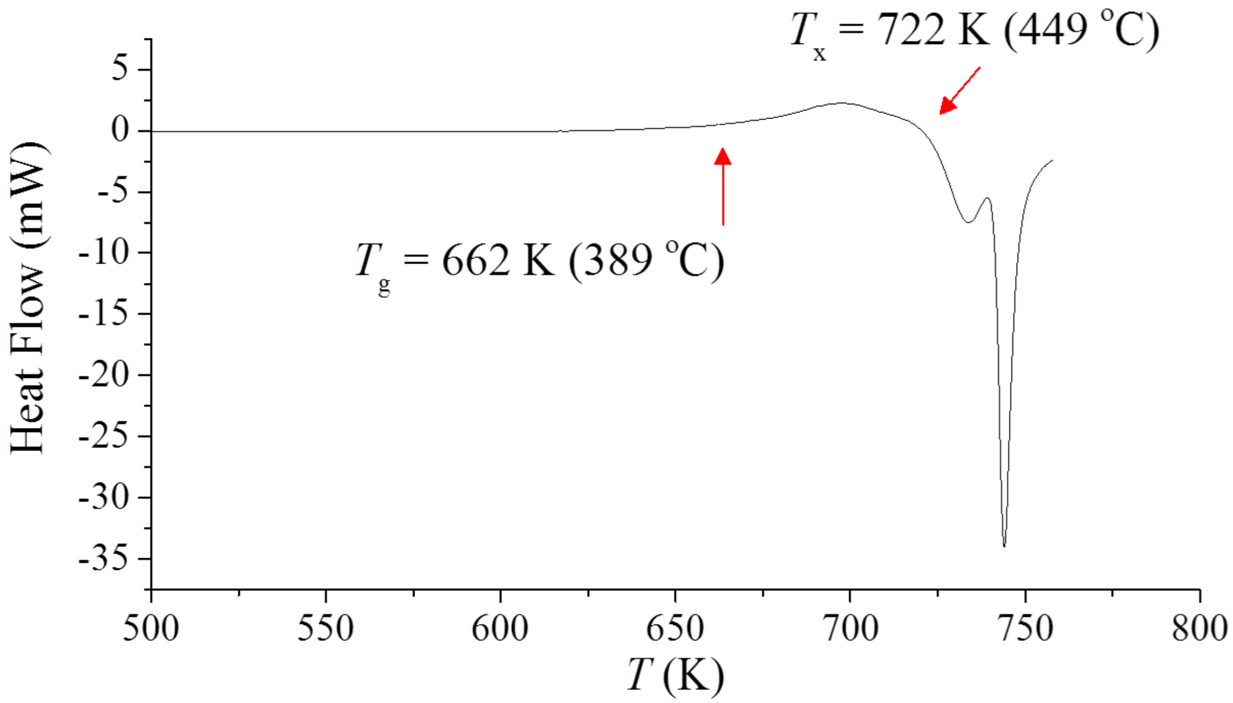

Figure 7.2 DSC curve of Vit105 at 20 ^{o}C/min. T_g and T_x are indicated by the red arrows (389 and 449 ^{o}C, respectively).

The solidus temperature, T_S, was determined from DTA measurements at a heating rate of 5 ^{o}C/min. A single feature is observed at T_s = 799 ^{o}C, suggesting this alloy is near a eutectic composition (Figure 7.3). This temperature was used to calibrate the temperature/time measurements in the high-temperature liquid.

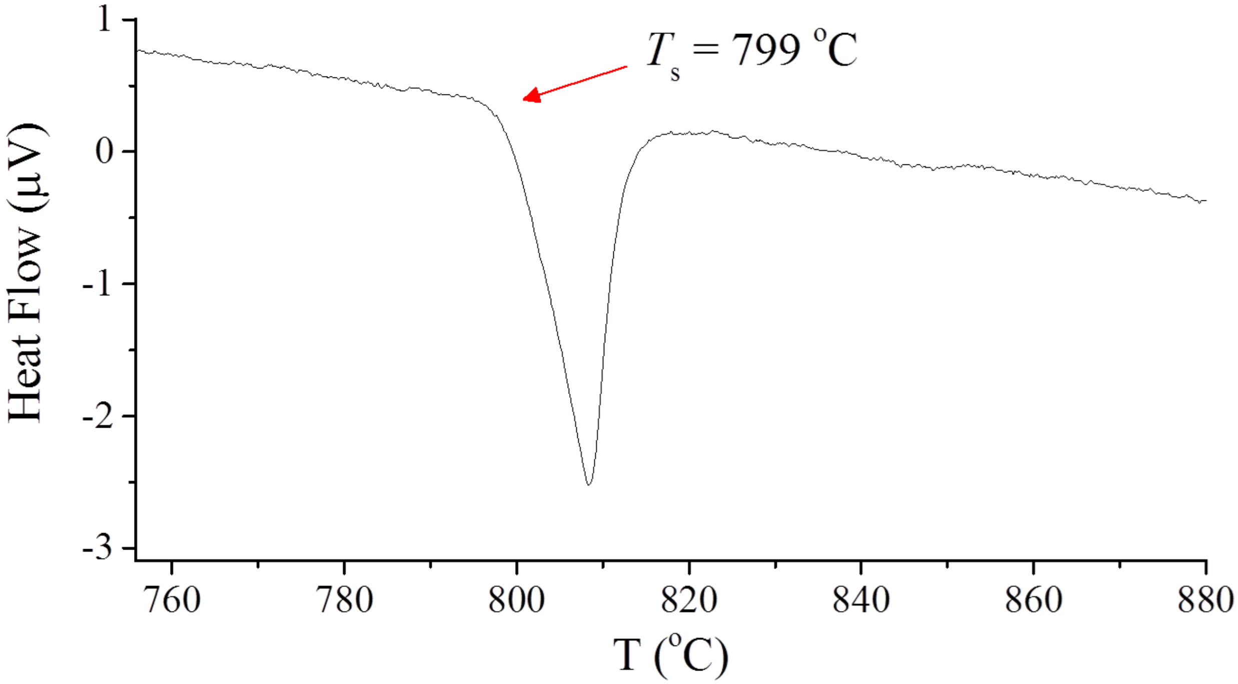

Figure 7.3 DTA scan of Vit105 at 5 °C/min. T_S is indicated by a red arrow (799 °C).

7.4.2 High-Temperature Liquid

Liquid structure factors were acquired for a variety of temperatures both above and below T_S during isothermal holds (10 s, Figure 7.4). For all temperatures, $S(q)$ oscillates smoothly around 1 indicating the high quality of the experimental data. As the temperature decreases, a shoulder develops on the high-q side of the second peak. This feature has been commonly attributed to icosahedral-like structures [31, 32], but it has been found to be a common feature in most metallic liquids [33]. The height of the first peak, $S(q_1)$, increases linearly with decreasing temperature (Figure 7.5). The peak position, q_1, shifts to larger-q with decreasing temperature, consistent with an increasing average density. As mentioned before, simultaneous SAXS measurements recorded a flat signal for all liquid temperatures, picking up no sign of phase separation in the high-temperature liquids.

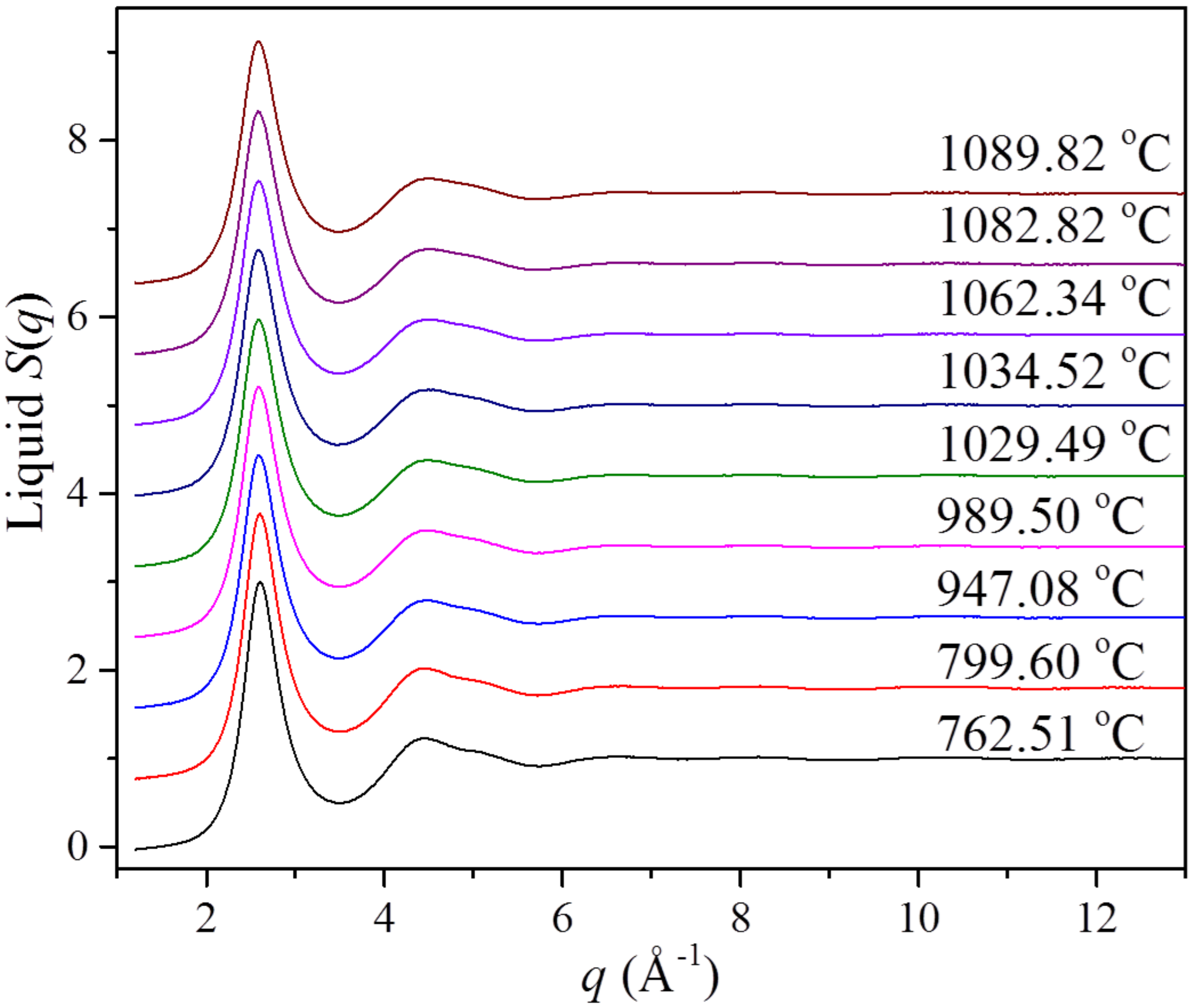

Figure 7.4 Liquid and supercooled liquid structure factors for Vit105.

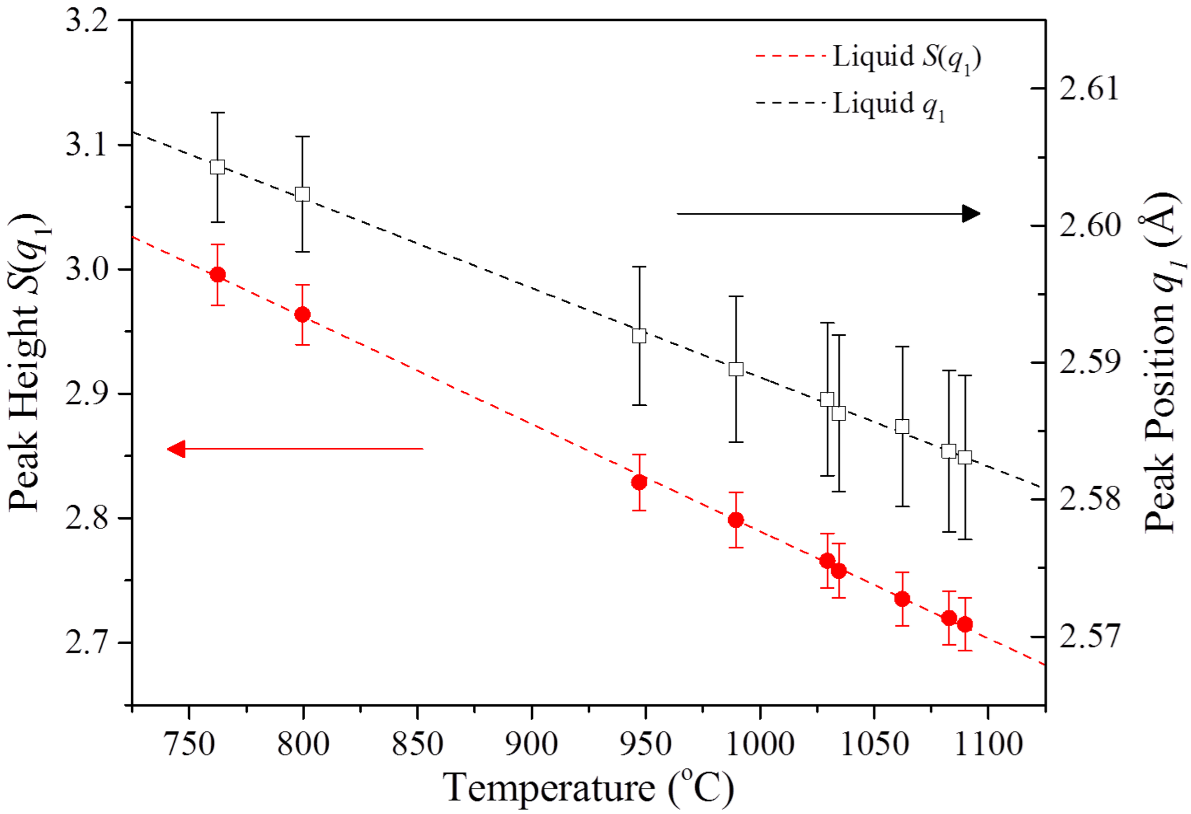

Figure 7.5 Height, $S(q_1)$, and position, q_1, of the main peak in liquid $S(q)$s.

A comparison of $S(q_1)$ and the full-width at half-max (FWHM) reveals that Vit105 does not group with the phase-separating alloy $Ni_{58.5}Nb_{20.25}Y_{21.25}$, contrary to previous predictions discussed in Section 7.2 (Figure 7.6). Instead, it is grouped with the majority of compositions studied and does not appear to have any unique characteristics. This could indicate that the anomalous behavior for $Ni_{58.5}Nb_{20.25}Y_{21.25}$ signals the presence of a liquid-liquid miscibility gap near the melting temperature for that liquid. If phase separation does indeed occur in Vit105, it must be near or below T_g. Alternatively, the anomalous behavior for $Ni_{58.5}Nb_{20.25}Y_{21.25}$ could be due not to phase separation, but simply to large atomic size differences. Y has a much larger Goldschmidt radius (r_Y 1.81 Å) than Ni and Nb (r_{Ni} = 1.25 Å, r_{Nb} = 1.47 Å) [34], which would result in very diverse bond lengths within the alloy, broadening the primary peak in $S(q)$. While the atomic sizes in Vit105 are also very diverse, the largest atom, Zr, is significantly smaller than Y (r_{Zr} = 1.61 Å), limiting the bond size diversity.

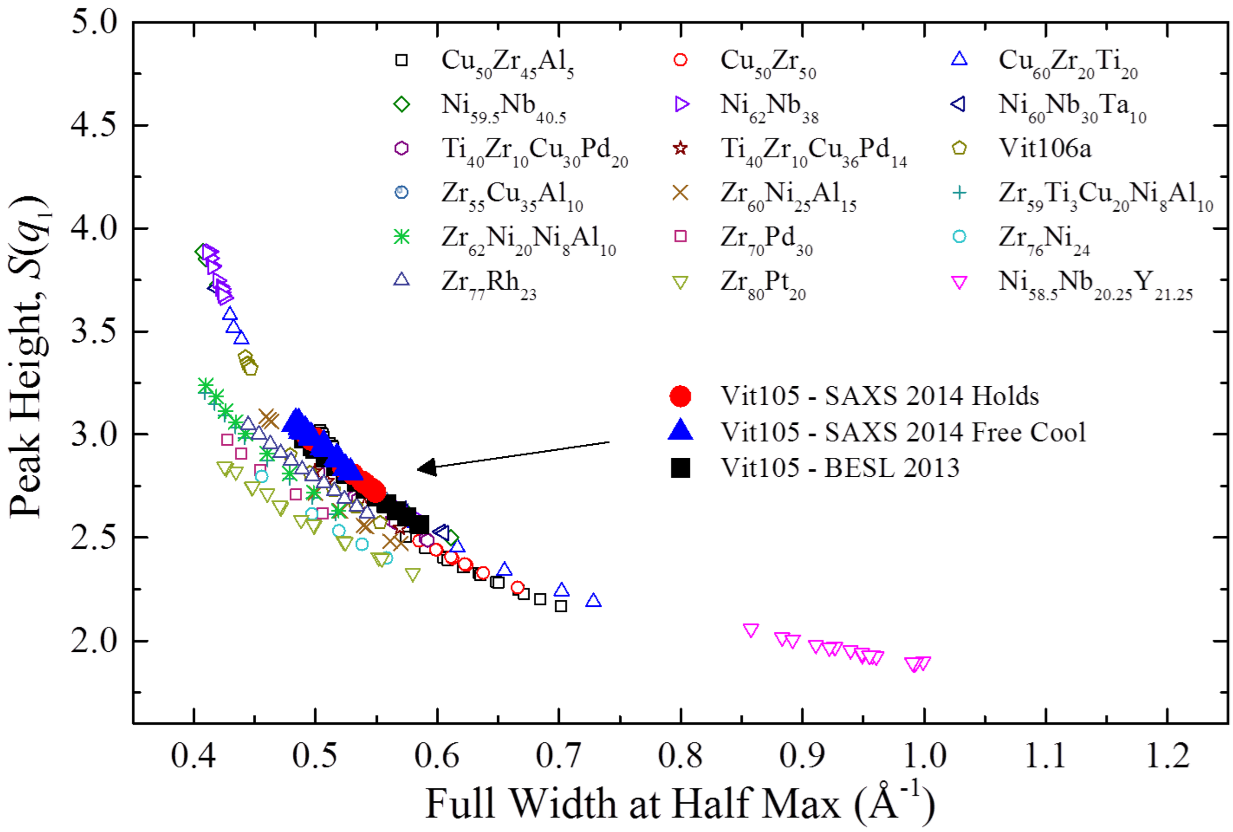

Figure 7.6 $S(q_1)$ vs. FWHM for a variety of liquid alloys. The solid symbols represent the values calculated for Vit105 from BESL 2013 and SAXS 2014 liquid measurements.

Simultaneous WAXS and SAXS diffraction patterns were also acquired every 1 s during a radiative free-cooling cycle. The maximum undercooling obtained was 100 ^{o}C before the sample recalesced. Once crystallized, many sharp diffraction peaks were observed in WAXS (Figure 7.7 (b)). Simultaneously, an increase in intensity was observed at very small-q in SAXS (Figure 7.7 (a)). This “tail” is typical of crystallization and corresponds to a macroscopic correlation length much larger than accessible q-range. The small tail observed prior to crystallization was constant for all liquid temperatures and is likely an artifact from background subtraction. The temperature cycle during the free-cool is presented in Figure 7.8 (a).

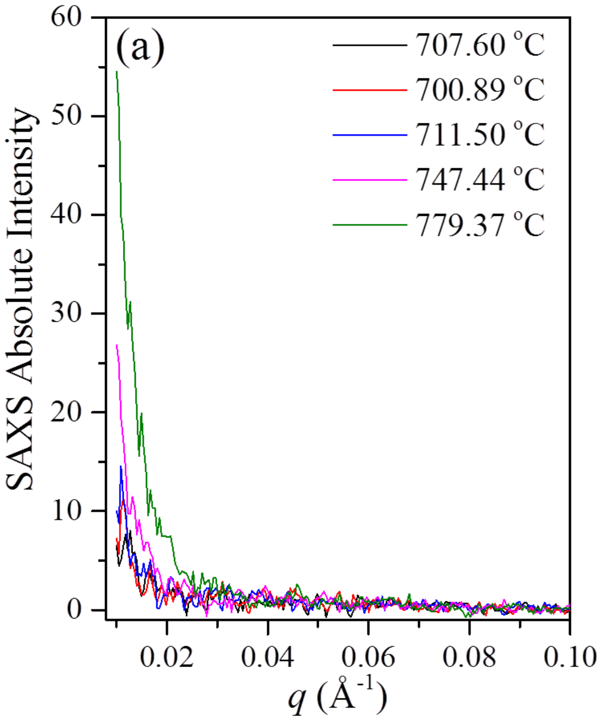

Figure 7.7 (a) SAXS absolute intensity as a function of *q* for 5 temperatures during recalescence. (b) WAXS *S*(*q*) for the same temperatures. *S*(*q*)s are offset by 1 for clarity.

To determine if compositional fluctuations preceded crystallization, the SAXS intensity was summed as a function of time. The growth of any features in SAXS will result in an increase in the overall measured intensity. The integrated WAXS intensity was not a practical parameter for comparison, since the increase in intensity due to crystallization is offset by the reduced scattering from the amorphous material. This is evident in Figure 7.8 (b), where the intensity at q = 2.47 Å^{-1} decreased while the intensity at the locations of crystalline peaks (q = 2.52 and 2.66 Å^{-1}) increased. As such, the amplitude in $S(q)$ at the latter two positions (denoted as $S(q_x)$, i.e. $S(2.52)$ and $S(2.66)$) was used to determine the onset of crystallization. All parameters were normalized by their maximum and minimum values, scaling them between 0 and 1. No change was observed in these parameters throughout the free-cool, but *S*(*2.52*), *S*(*2.66*), and the SAXS intensity (Figure 7.8 (b)) rapidly increased as the sample began to recalesce (Figure 7.8 (a)). All changes occurred simultaneously, indicating that the increase in the SAXS signal corresponds to scattering from large crystals that form within the amorphous matrix.

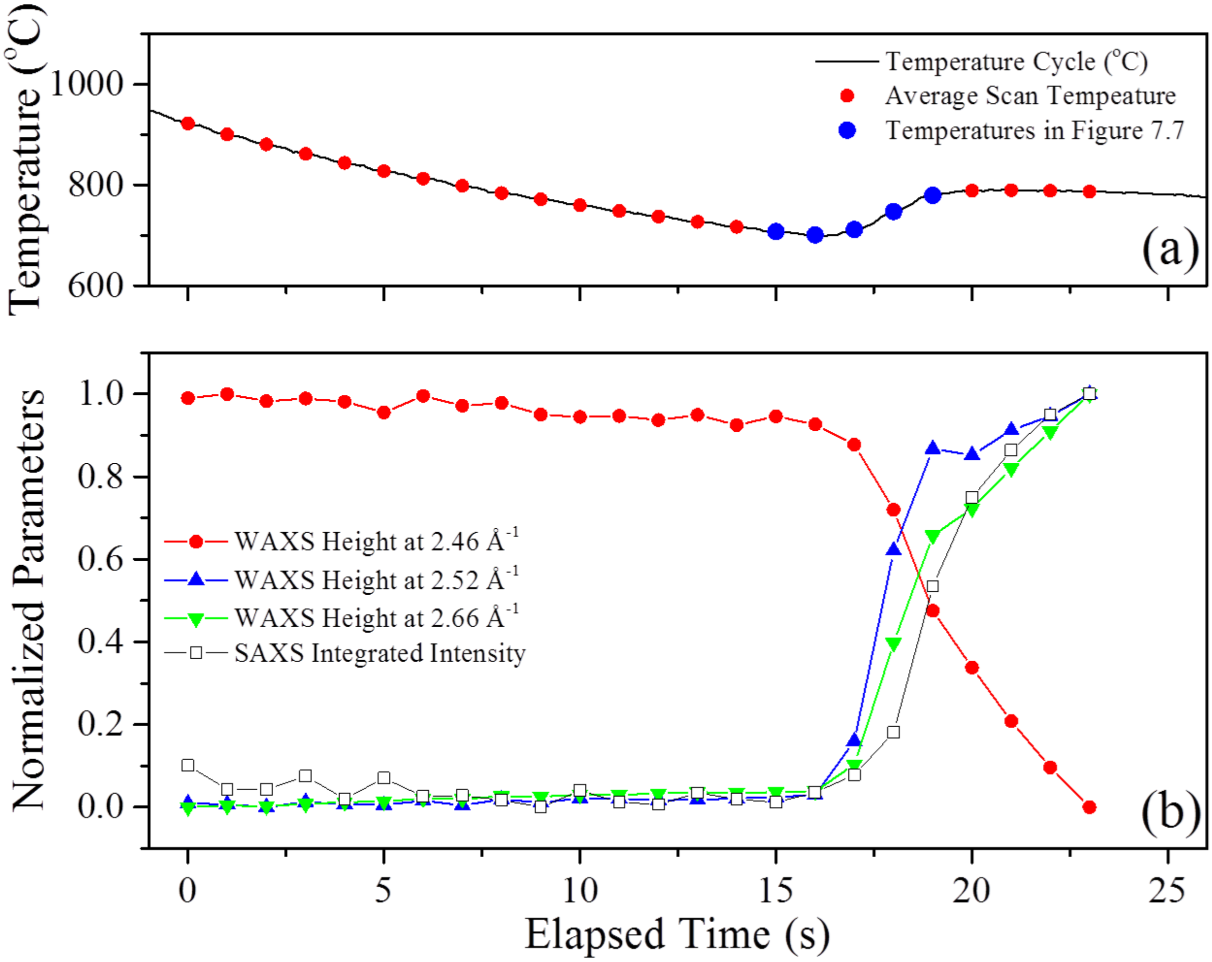

Figure 7.8 (a) Temperature-time cycle during the free-cool. The average temperature for each scan is marked by a red circle, and the scans from Figure 7.7 are marked by blue circles. (b) Normalized parameters for both WAXS and SAXS measurements. The open symbol represents the total sum of SAXS intensity. The solid symbols represent the amplitude of $S(q)$ at specific values of q; the largest crystalline peaks that developed during recalescence correspond to q = 2.52 and 2.66 Å^{-1}, and a region where no crystalline peaks developed corresponds to q = 2.47 Å^{-1}. All parameters are normalized between 0 and 1.

7.4.3 Devitrification

Due to the excellent glass-forming ability of Vit105, sufficient quench rates for glass formation could be achieved *in situ* by dropping molten samples onto the bottom electrode. The quenched samples were re-levitated and confirmed to be fully amorphous. The sample was heated into the supercooled liquid region, above T_g, and held near 450 ^oC while acquiring simultaneous 1 s WAXS (Figure 7.9) and SAXS (Figure 7.10) data. While this temperature is higher than our measured T_x, it is lower than the values reported by others, suggesting that there may have been some small error in our temperature calibration. However, the central point is that the measured temperature is above T_g as measured here; ours are, then, the first measurements made in the supercooled liquid and not the glass.

The $S(q)$s initially contained broad, amorphous features (Figure 7.9, 54 elapsed seconds). They began to sharpen (Figure 7.9, 128 and 253 s) until crystalline peaks were observed in the data (Figure 7.9, 365 s). This sharpening could simply be due to structural relaxation since the sample was not annealed after quenching. Alternatively, the sharpening could be due to the formation of nanocrystals. The crystalline peaks do not grow rapidly at first, but they are clearly visible by 479 s. These peaks are consistent with a tetragonal Zr_2Ni phase.

The SAXS intensity gradually increased during the early stages of the measurements, signaling the formation of compositional fluctuations. Eventually, a peak formed that was centered around 0.025 Å^{-1}, giving a correlation length ($d = 2\pi / q$) of 251 Å (25.1 nm). Whether these fluctuations were due to phase separation or nanocrystals is unclear upon initial examination; the details of the decomposition will be discussed in further detail below. These features are likely the source of sharpening in $S(q)$.

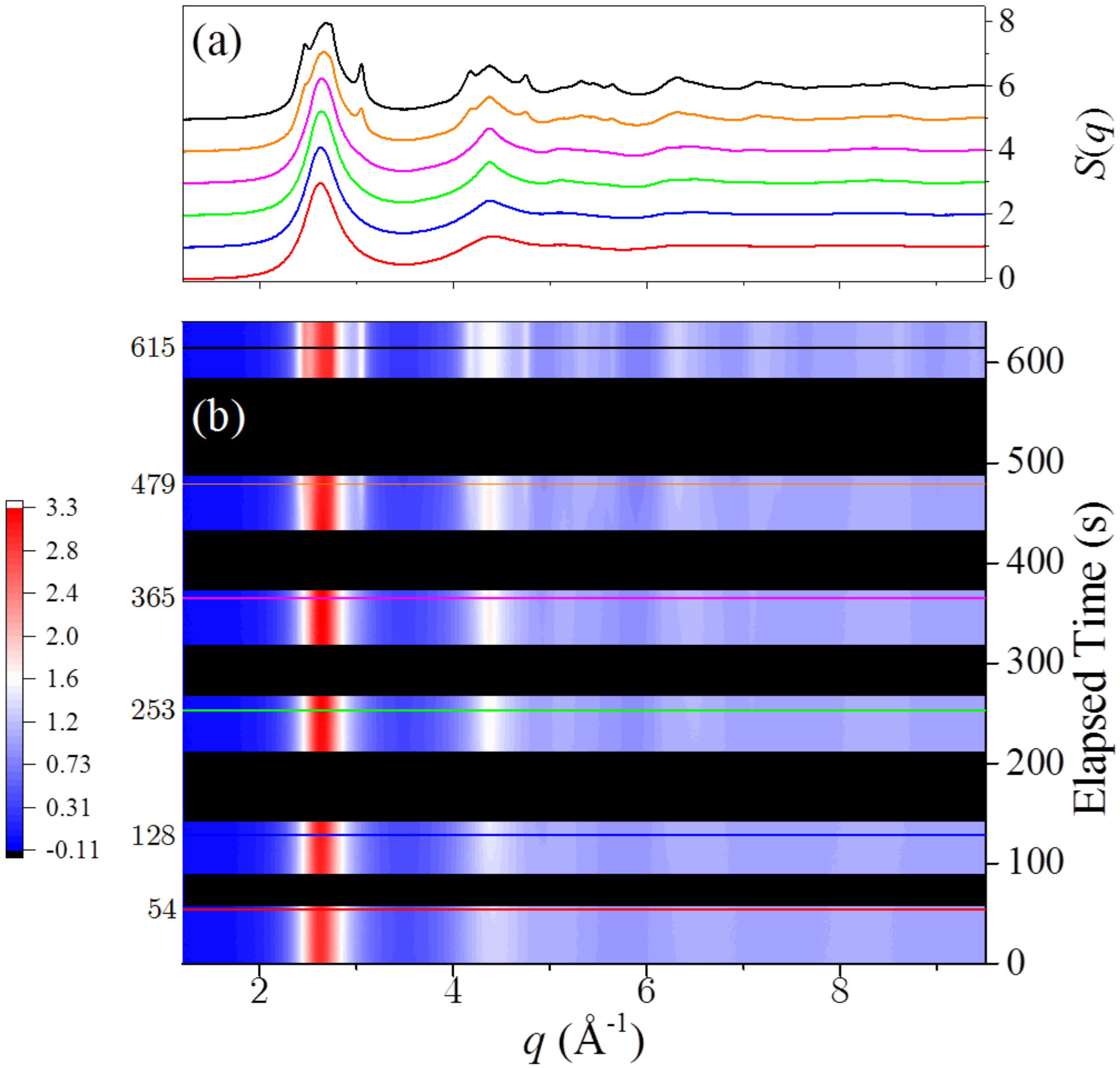

Figure 7.9 WAXS measurements during isothermal holds near 450 °C. (a) $S(q)$s during devitrification (each offset by 1). (b) Intensity contour plot from the entire isothermal experiment. The black regions indicate where the X-ray beam was shuttered between scans. The horizontal lines and corresponding time (displayed on the left) correspond to the $S(q)$s in (a).

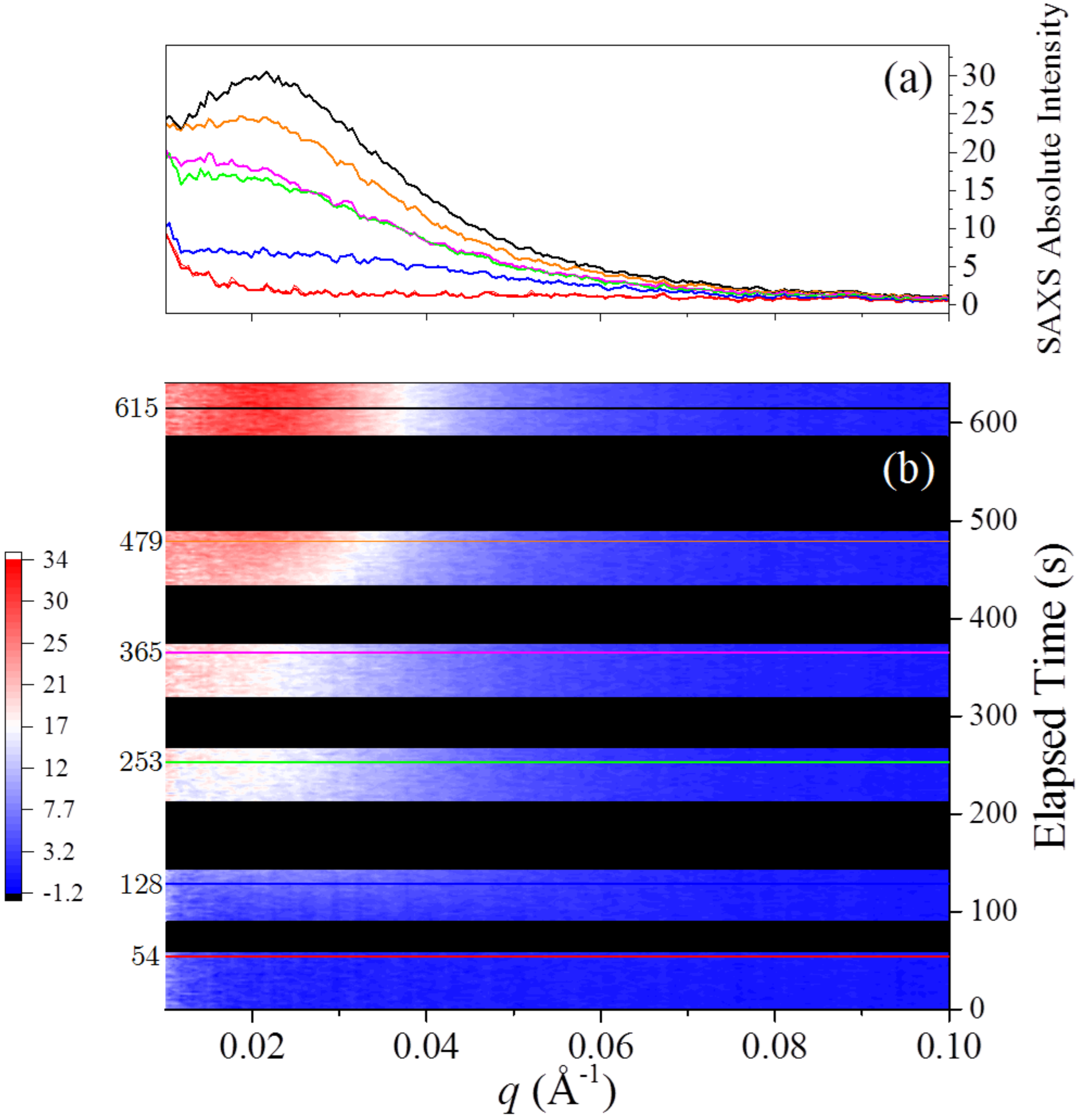

Figure 7.10 SAXS measurements during isothermal holds near 450 °C. (a) *I*(*q*) during devitrification. (b) Intensity contour plot from the entire isothermal experiment. The black regions indicate where the X-ray beam was shuttered between scans. The horizontal lines and corresponding time (displayed on the left) correspond to the *I*(*q*)s in (a).

In order to quantify the evolution of these features, several parameters were tracked in a similar manner as in Section 7.4.2. The integrated SAXS intensity was used to quantify changes in the SAXS signal, but it should be noted that the features in the data were qualitatively different than those observed in the high-temperature liquid. Devitrification was tracked by recording the height in $S(q)$ at positions where crystalline peaks eventually develop (i.e., $S(q_x)$). However, as $S(q_1)$ increases prior to crystallization, the peak also narrows, resulting in a decrease in the amplitude on the shoulder ($S(q_x)$) (Figure 7.11 (a)). While amorphous, $S(q_x)$ follows a linear relationship with $S(q_1)$ (Figure 7.11 (b)). Since $m = (y - b)/x$ is a constant, where y is $S(q_x)$, x is $S(q_1)$, and m and b are the slope and y-intercept from the best fit line in Figure 7.11 (b), plotting $(S(q_x) - b)/S(q_1)$ reveals when the crystalline peaks actually begin to grow.

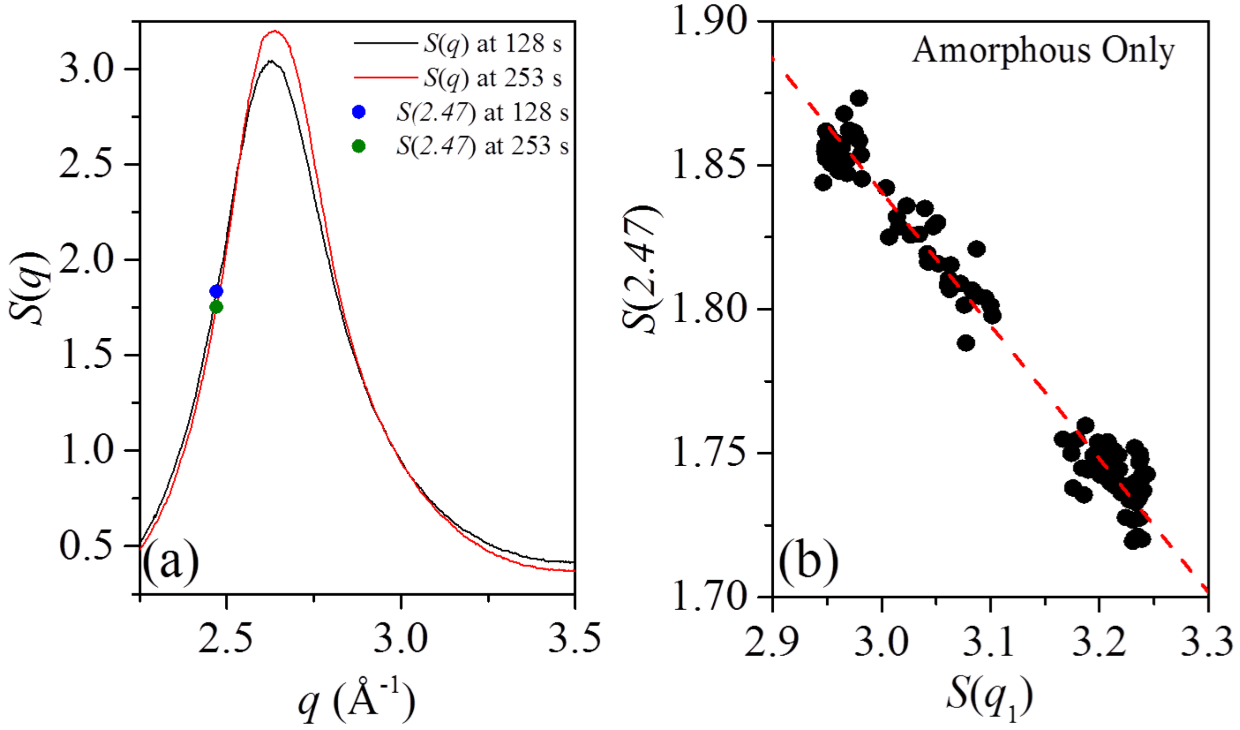

Figure 7.11 (a) Change in amplitude of $S(q)$ at 2.47 Å^{-1} as the primary peak sharpens. (b) $S(2.47)$ follows a linear relationship with $S(q_1)$.

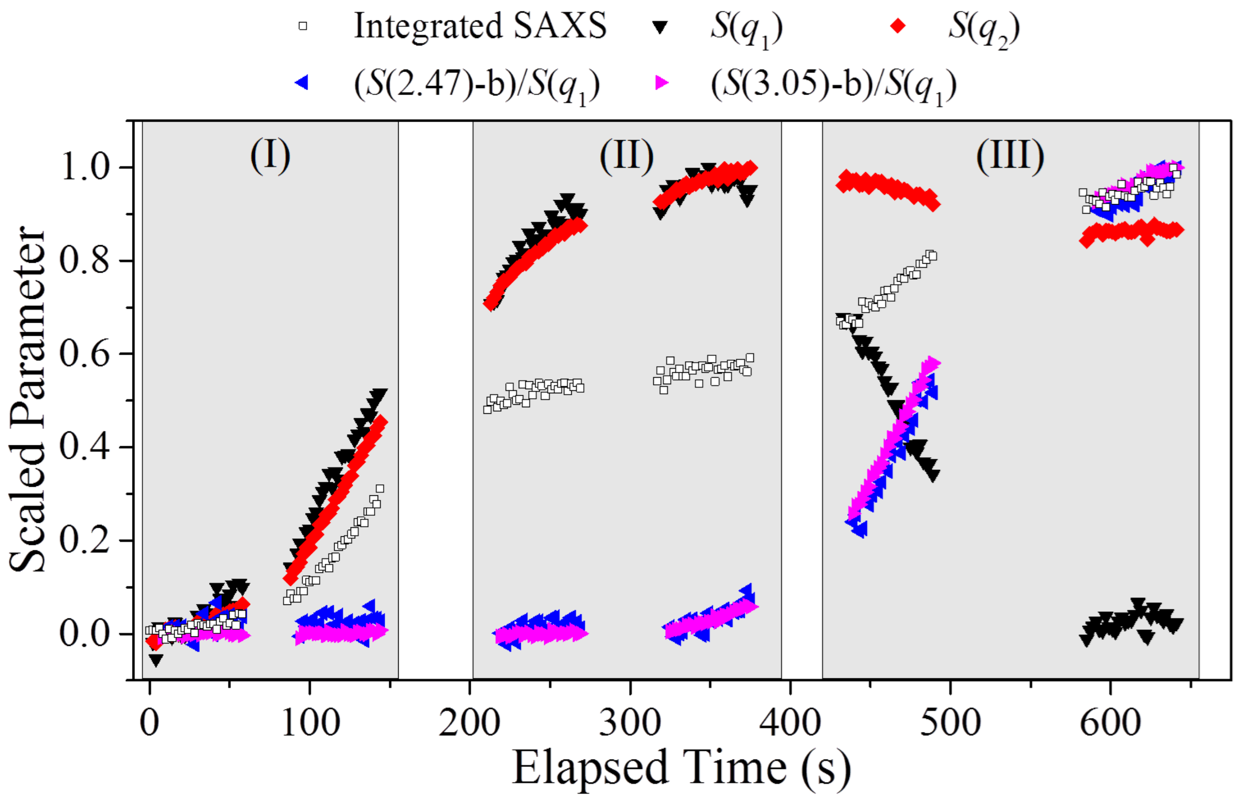

Figure 7.12 Scaled parameters as a function of elapsed time. Parameters are scaled between 0 and 1.

For clarity, all structural parameters were scaled between 0 and 1 using their minimum and maximum values (Figure 7.12). During the initial stages (Figure 7.12, region I), $S(q_1)$ (solid black) and $S(q_2)$ (solid red) grew rapidly. This behavior was visually observed in WAXS (Figure 7.9). The integrated SAXS intensity (open black) also increased during the same time span. However, *S*(*2.47*) (solid blue) and *S*(*3.05*) (solid magenta) both showed no change. If the growth in $S(q_1)$ and $S(q_2)$ is only due to structural relaxation, the sample should remain largely homogeneous. Instead, the simultaneous growth of a SAXS signal indicates that compositional fluctuations are beginning to develop. In the past, this has been interpreted as evidence of two distinct liquid phases forming. However, the sharpened features in the WAXS signal suggest that it may instead be due to the formation of nanocrystals. Previous studies found Zr_2Ni

nanocrystals began to form after annealing near T_g [24]. However, the features in the second peak in the WAXS data share characteristics with the Ti_2Ni-like crystal phase. This is consistent with the appearance of Ti_2Ni-like nanocrystals identified from samples that were heated quickly to 468 ^oC [24]. At that heating rate, the formation of Zr_2Ni nanocrystals was not observed. Annealing close to 450 ^oC possibly suppresses the nucleation rate of Zr_2Ni nanocrystals and the SAXS signal is instead dominated by the formation of Ti_2Ni-like nanocrystals.

After the initial rapid growth of a SAXS signal in region I, the intensity temporarily stabilized (Figure 7.12, region II). By this point, a distinct peak had formed in the SAXS signal at ~0.017 Å^{-1} ($d \approx 370$ Å (37 nm)). At the same time, the growth of $S(q_1)$ and $S(q_2)$ began to slow, eventually leveling off. There was very little additional growth to the SAXS signal, suggesting that the continued changes in the WAXS signal were due to structural rearrangement or relaxation as the nanocrystals stabilized. The intensities at q_x = 2.47 and 3.05 Å^{-1} remained stable in the early stages of this region, but they eventually began to grow. This suggests that the primary crystalline phase began to grow well after the first SAXS signal was observed.

Once nucleated, the Zr_2Ni crystalline phase rapidly grew (Figure 7.12, region III). The SAXS intensity also increased, with the peak shifting to larger-q (q = 0.021 Å^{-1}, d = 299 Å (29.9 nm)). The nucleation and growth of the Zr_2Ni phase was likely induced by chemical segregation wherein the Ti, Cu, and Al atoms were removed from the bulk by the formation of the Ti_2Ni-like nanocrystals. The chemical fluctuations leading to the nucleation of Ti_2Ni-like nanocrystals were likely initially driven by the preferential bonding between Ni and Zr due to their large negative heat of mixing (-49 kJ/mol), leading to locally ordered fluctuations that expelled Ti, Cu, and Al [35]. This could lower the nucleation barrier as these regions become closer in structure and composition to their corresponding crystal phases, promoting nucleation. While nucleation could occur in either the Ti-rich or Ti-poor regions, the features reflected in the WAXS signal suggest that the nucleation rate for the Ti_2Ni-like phase is much higher than for Zr_2Ni at this temperature.

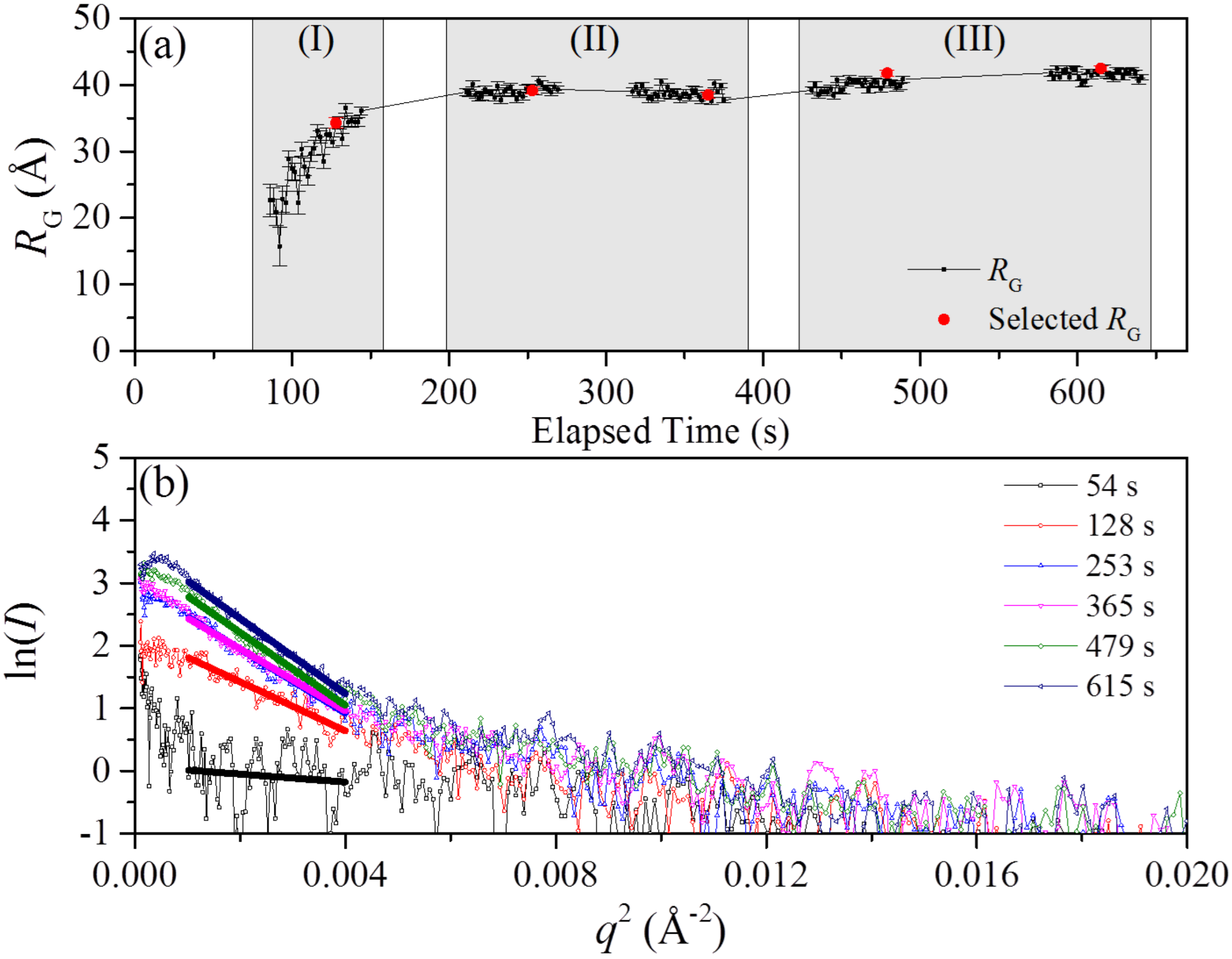

Figure 7.13 (a) Calculated R_G from the measured SAXS curves. The symbols in red are calculated from the select SAXS curves in (b).

In order to characterize crystal growth, the radius of gyration (R_G) was calculated from the SAXS intensity. In the limit as $q \to 0$, the macroscopic cross section follows the well known Guinier relationship [36]:

$$\lim_{q\to 0}\frac{d\Sigma}{d\Omega} = N_v \left|\Delta\rho\right|^2 V^2 \exp\left[-\frac{1}{3}(q\,R_G)^2\right]. \tag{7.1}$$

Here, N_v is the density of the second region within the first, V is the volume of the second region, $\Delta\rho$ is the difference in electron density between the two regions, and R_G is the region's radius of gyration (i.e., the mass distribution around a central axis). R_G was extracted from the slope of $\ln(I)\ vs\ q^2$, providing information on the physical size of the scattering regions (Figure 7.13).

R_G was calculated between q = 0.032 and 0.063 Å^{-1} and is presented in Figure 7.13 (a). Due to the lack of definition in the SAXS signal during the initial stages (0 – 75 s), accurate slopes could not be computed (Figure 7.13 (b), black curve). The R^2 values from the fit were ~0-0.2, lending little statistical meaning to the slope. As the SAXS intensity began to grow (Figure 7.13 (b), red curve, 128 s), sufficient statistics were available for accurate determinations of R_G. Throughout region I, R_G quickly grew, eventually stabilizing around 38.9 ± 0.7 Å by the end of region II. Once crystallization began (end of region II, Figure 7.12), very little change was observed in R_G, eventually stabilizing around 41.7 ± 0.7 Å. This suggests that the increase in absolute intensity was due to an increasing number of crystalline regions rather than growth of existing ones, with their size limited by the dimensions of the compositional fluctuations that developed. The primary crystallization likely did not extend into the second region since the compositional difference between the two phases would restrict growth by limiting the availability of the appropriate chemical elements.

While early studies of Vit105 suggested liquid-liquid phase separation was responsible for the SAXS signal, much of the evidence presented here is consistent with the more recent study where nanocrystals were observed after annealing at T_g [24]. Based on a combination of atom probe tomography, X-ray diffraction, and TEM studies, Kündig *et al.* found evidence of nanocrystals within the inhomogeneous regions corresponding to either the tetragonal Zr_2Ni phase or the oxygen-stabilized Ti_2Ni-like “big cube” phase, depending on the heating rate and amount of oxygen present [24]. The X-ray diffraction peaks in their low-oxygen sample were matched to the Zr_2Ni phase and are consistent with the diffraction peaks observed upon primary crystallization in this study. The results of X-ray diffraction studies of their high-oxygen sample, in particular the features that develop in the second amorphous peak, were remarkably similar to the sharpening that was observed in our WAXS data in region I (Figure 7.9). However, none of the most intense diffraction peaks were observed in our data. This suggests that the compositional fluctuations that develop are likely due to the nucleation of Ti_2Ni-like nanocrystals [24]. As Ti, Cu, and Al are integrated into the nanocrystals, crystallization is induced in the remaining liquid as it becomes compositionally similar to Zr_2Ni, reducing its T_{RG}.

7.5 Conclusions

In summary, simultaneous wide-angle (WAXS) and small-angle (SAXS) X-ray scattering measurements were performed on a levitated $Zr_{52.5}Cu_{17.9}Ni_{14.6}Al_{10}Ti_5$ (Vit105) alloy in the liquid and supercooled liquid state. Vit105 had comparable primary peak heights and widths to similar alloys, and did not display the anomalous behavior found in $Ni_{58.5}Nb_{20.25}Y_{21.25}$. This may indicate that no miscibility gap exists at high temperatures for Vit105. Alternatively, the anomalous behavior observed in $Ni_{58.5}Nb_{20.25}Y_{21.25}$ could instead reflect the large size differences of the constituent elements between Ni/Nb and Y.

Compositional fluctuations were observed in the supercooled liquid, well above T_g, during annealing of an amorphous sample produced *in situ*. While previous studies have suggested these features were due to decomposition into two amorphous phases prior to crystallization, the simultaneous peak sharpening observed in WAXS shared some similarities with low-intensity features observed during the formation of Ti_2Ni-like crystals in a high-oxygen sample. While the high-intensity peaks were not visible, the sharpening in the WAXS signal is likely due to the nucleation of Ti_2Ni-like nanocrystals. Once nucleated, the nanocrystals grow until the appropriate elements are no longer available. At this point, the change in composition in the remaining liquid initiates nucleation of the Zr_2Ni phase, which quickly grew. The growth of the primary crystal phase was restricted by the initial boundary formed between the two regions resulting in a maximum R_G of ~42 Å.

This crystallization pathway is significantly different from that observed from the liquid when cooled to ~100 ^oC below T_L. Just above T_g, crystallization is induced by the nucleation and growth of Ti_2Ni-like nanocrystals, changing the composition of the bulk and reducing T_{RG}. In the high-temperature liquid, nucleation occurs as the sample is cooled below T_L resulting in the formation of a very different crystalline phase(s). In both cases, heterogeneous nucleation from container walls was eliminated, but it is possible that the boundary formed between the nanocrystals and the liquid regions also lowered the energy barrier required for crystallization.

In conclusion, this experiment highlights that a combination of techniques is very useful for examining multiple distinct length scales in a single experiment and sorting out details of complicated phase transitions. The high flux at the APS allows for real-time observations of the crystallization process. While successful measurements of liquid-liquid phase separation in the high-temperature liquid were not possible, the ability to study crystallization in the supercooled liquid near T_g over short timescales provides insight that would otherwise require multiple separate experiments on separate samples. By understanding the crystallization pathways in bulk glass-forming alloys, the structural and kinetic parameters responsible for glass formation can be studied, leading to improvements in bulk glass formability.

7.6 References

[1] P.F. James, *Journal of Materials Science* **10**, 1802 (1975).

[2] D.R. Uhlmann, A.G. Kolbeck, *Physics and Chemistry of Glasses* **17**, 146 (1976).

[3] N. Mattern, U. Vainio, B. Schwarz, J.M. Park, D.H. Kim, J. Eckert, *Intermetallics* **18**, 1842 (2010).

[4] N. Mattern, U. Kühn, A. Gebert, T. Gemming, M. Zinkevich, H. Wendrock, L. Schultz, *Scripta Materialia* **53**, 271 (2005).

[5] N. Mattern, G. Goerigk, U. Vainio, M. Miller, T. Gemming, J. Eckert, *Acta Materialia* **57**, 903 (2009).

[6] N. Mattern, U. Vainio, J.M. Park, J.H. Han, A. Shariq, D.H. Kim, J. Eckert, *Journal of Alloys and Compounds* **509S**, S23 (2011).

[7] S. Schneider, P. Thiyagarajan, W.L. Johnson, *Applied Physics Letters* **493**, 493 (1995).

[8] X.H. Du, J.C. Huang, K.C. Hsieh, Y.H. Lai, H.M. Chen, J.S.C. Jang, P.K. Liaw, *Applied Physics Letters* **91**, 2005 (2007).

[9] Y.L. Ren, R.L. Zhu, J. Sun, J.H. You, K.Q. Qui, *Journal of Alloys and Compounds* **493**, L42 (2010).

[10] D.H. Kim, W.T. Kim, E.S. Park, N. Mattern, J. Eckert, *Progress in Materials Science* **58**, 1103 (2013).

[11] B.J. Park, H.J. Chang, D.H. Kim, W.T. Kim, K. Chattopadhyay, T.A. Abinandanan, S. Bhattacharyya, *Physical Review Letters* **96**, 245503 (2006).

[12] L.Q. Xing, Y. Li, K. Ramesh, J. Li, T. Hufnagel, *Physical Review B* **64**, 1 (2001).

[13] M.H. Lee, J.Y. Lee, D.H. Bae, W.T. Kim, D.J. Sordelet, D.H. Kim, *Intermetallics* **12**, 1133 (2004).

[14] E.S. Park, D.H. Kim, T. Ohkubo, K. Hono, *Journal of Non-Crystalline Solids* **351**, 1232 (2005).

[15] A. Takeuchi, A. Inoue, *Materials Transactions* **46**, 2817 (2005).

[16] D. Xu, G. Duan, W. Johnson, *Physical Review Letters* **92**, 245504 (2004).

[17] M. Lee, D. Bae, W. Kim, D. Kim, *Materials Transactions* **44**, 2084 (2003).

[18] E.S. Park, H.J. Chang, D.H. Kim, T. Ohkubo, K. Hono, *Scripta Materialia* **54**, 1569 (2006).

[19] J.F. Löffler, W.L. Johnson, *Applied Physics Letters* **76**, 3394 (2000).

[20] E. Pekarskaya, J.F. Löffler, W.L. Johnson, *Acta Materialia* **51**, 4045 (2003).

[21] D. Turnbull, *Metallurgical Transactions B* **12**, 217 (1981).

[22] J.F. Löffler, S. Bossuyt, S.C. Glade, W.L. Johnson, W. Wagner, P. Thiyagarajan, *Applied Physics Letters* **77**, 525 (2000).

[23] X.L. Wang, J. Almer, C. Liu, Y. Wang, J. Zhao, a. Stoica, D. Haeffner, W. Wang, *Physical Review Letters* **91**, 265501 (2003).

[24] A.A. Kündig, M. Ohnuma, T. Ohkubo, K. Hono, *Acta Materialia* **53**, 2091 (2005).

[25] N.A. Mauro, K.F. Kelton, *Review of Scientific Instruments* **82**, 035114 (2011).

[26] J.C. Bendert, N.A. Mauro, K.F. Kelton, *Journal of Applied Crystallography* **46**, 999 (2013).

[27] K. Kajiwara, M. Ohnuma, T. Ohkubo, D.H. Ping, K. Hono, *Materials Science and Engineering: A* **375-377**, 738 (2004).

[28] M. Baricco, S. Spriano, I. Chang, M.I. Petrzhik, L. Battezzati, *Materials Science and Engineering A* **304-306**, 305 (2001).

[29] W.H. Jiang, F.X. Liu, H. Choo, P.K. Liaw, *Materials Transactions* **48**, 1781 (2007).

[30] R.J. Xue, D.P. Wang, Z.G. Zhu, D.W. Ding, B. Zhang, W.H. Wang, *Journal of Applied Physics* **114**, 123514 (2013).

[31] K.F. Kelton, G.W. Lee, A.K. Gangopadhyay, R.W. Hyers, T.J. Rathz, J.R. Rogers, M.B. Robinson, D.S. Robinson, *Physical Review Letters* **90**, 195504 (2003).

[32] S. Sachdev, D.R. Nelson, *Physical Review Letters* **53**, 1947 (1984).

[33] N.A. Mauro, M.E. Blodgett, M.L. Johnson, A.J. Vogt, K.F. Kelton, *Nature Communications* **5:4616**, (2014).

[34] W.F. Gale, T.C. Totemeier, *Smithells Metals Reference Book (8th Edition),* Elsevier, 2004.

[35] L. Yang, M.K. Miller, X.L. Wang, C.T. Liu, A.D. Stoica, D. Ma, J. Almer, D. Shi, *Advanced Materials* **21**, 305 (2009).

[36] A. Guinier, G. Fournet, *Journal of Polymer Science* **19**, 594 (1956).

Chapter 8: Summary and Conclusions

The experiments presented in this dissertation are part of a larger effort seeking to understand the liquid and supercooled liquid structure in terms of its thermodynamic and kinetic properties to ultimately answer why some glasses form more easily than others. To this extent, the structural evolution in the liquid is shown to be intimately tied to its viscosity and ability to form a glass. Through the use of containerless environments, the liquid structure well below its melting temperature was studied using X-ray and neutron scattering techniques. The structural features present in the liquid have enabled predictions of previously unknown metastable phases. Careful understanding of the crystallization pathways provided insight into devitrification methods characteristic of good and poor glass-forming alloys.

In Chapter 3, the structural evolution of Ni-Nb(-Ta) liquid alloys was discussed. The structure factors were measured as a function of temperature in the liquid, while the amorphous ribbons were studied at room temperature. The structure of the glass, characterized by the height in the first peak of $S(q)$, was extrapolated to its glass transition temperature by modeling thermal vibrations within the Debye theory. The height of $S(q)$ for the liquid samples was also extrapolated to T_g with a linear fit. A discontinuity was revealed between these two extrapolations, implying that the structural order must accelerate at some point before the glass transition. Reverse Monte Carlo simulations revealed that one of the Honeycutt-Andersen indices related to icosahedral structures also showed the same temperature evolution. The rapid acceleration required is similar to that observed in viscosity, which is typically used to classify a liquid's fragility. Ni-Nb(-Ta) alloys, while considered bulk metallic glasses, are known to be fragile. The rapid acceleration in structural ordering required is in contrast to the observed behavior in previous studies of a very strong alloy, $Pd_{40}Cu_{30}Ni_{10}P_{20}$ [1]. This was the first observation that an acceleration of the rate of structural ordering near T_g was required for fragile liquids and provided the groundwork for a future, more detailed classification of structure and fragility [2].

In Chapter 4, the structure and thermophysical properties of three Zr-Ni alloys were discussed ($Zr_{76}Ni_{24}$, $Zr_{57}Ni_{43}$, $Zr_{36}Ni_{64}$). While the Zr-Ni system has a large glass-forming region, these alloys do not display a glass transition temperature in differential scanning calorimetry studies and are considered to be extremely fragile. Rather than using the predictive models presented in Chapter 3, the structural evolution of the glass was directly measured as a function of temperature up to T_g and found to have a very large discontinuity relative to the liquid, consistent with extremely fragile systems. This experiment highlights the usefulness of the WU-BESL chamber. The chemical ordering was also investigated. The primary peak in the pair-distribution function, $g(r)$, was extremely asymmetric. In alloys at extreme compositions ($Zr_{76}Ni_{24}$ and $Zr_{36}Ni_{64}$), the primary peak contained a shoulder at either large- or small-q. The intermediate alloy, $Zr_{57}Ni_{43}$, consisted of two peaks of approximately equal amplitude. The positions of these peaks were shown to be consistent with appropriate bond-lengths, and the amplitudes scaled with the Faber-Ziman weighting factors. The lack of quality (measured or simulated) partial structure factors limited the characterization of chemical ordering, and highlighted the need for combining multiple scattering experiments with sufficient chemical contrast.

In Chapter 5, the first liquid neutron scattering data of $Zr_{80}Pt_{20}$ and $Zr_{77}Rh_{23}$ acquired using the newly commissioned NESL levitator at the Spallation Neutron Source were discussed in combination with X-ray experiments acquired using WU-BESL. In order to compare two independently obtained $S(q)$s, new data reduction techniques were developed to properly compare both measurements on an absolute scale by constraining to physical parameters. Constrained Reverse Monte Carlo (CRMC) simulations were constrained using $Zr_{80}Pt_{20}$ X-ray and neutron $S(q)$s as well as a single partial pair-correlation function (PPCF) calculated using MD. The atomic configurations were used to calculate the Voronoi indices prevalent in the liquid. It was found that the Pt-centered <0 2 8 1 0> index was dominant and highly stable for all temperatures. The PPCFs from the CRMC were used to study the topological and chemical contributions within the Bhatia-Thornton (BT) formalism. Equivalent BT partials were calculated for the $Zr_{77}Rh_{23}$ alloy by eliminating the smallest contribution (the chemical-chemical was less than 1% of the total) and numerically solving for the rest. The topological order was found to be very similar, while the chemical contributions in $Zr_{77}Rh_{23}$ were found to have much stronger ties to the topology. The similarity in their topology enabled the prediction that the stable <0 2 8 1 0> Voronoi index, a structural unit of the Zr_5Pt_3 crystalline phase, may also be present in $Zr_{77}Rh_{23}$ liquids, and therefore Zr_5Rh_3 might be a metastable phase for $Zr_{77}Rh_{23}$. From this prediction, a previously unobserved metastable Zr_5Rh_3 phase was successfully identified crystallizing from a deeply undercooled liquid.

In Chapter 6, the crystallization behavior of a supercooled $Zr_{77}Rh_{23}$ alloy was discussed. The metastable Zr_5Rh_3 discovered in Chapter 5 was characterized and found to be one of many possible metastable phases that can form. Depending on the maximum supercooling achieved, three different crystallization pathways were observed. Many of these pathways are likely stabilized by the presence of oxygen, such as the Ti_2Ni-like “big cube” phase and the direct formation of $\alpha - Zr$. Understanding the metastable crystallization pathways can lead to the development of materials with carefully selected material properties based on the microstructure of the crystallized phase as well as improving the design and glass formability of new alloys.

In Chapter 7, attempts were made to observe liquid-liquid phase separation in high-temperature bulk metallic glasses using a combination of wide-angle (WAXS) and small-angle X-ray scattering (SAXS). The identification of nanoscale compositional fluctuations in the high-temperature liquid was unsuccessful. However, a SAXS signal was observed during an isothermal measurement of a glassy Vit105 alloy that was quenched *in situ*. It was revealed that compositional fluctuations began well before primary crystallization was observed. Past studies have presented conflicting interpretations of this data. This investigation sought to clarify whether the SAXS signal was the result of liquid-liquid phase separation, or if it corresponded to the formation of nanocrystals. While no crystalline peaks were found in the WAXS data during the growth of a SAXS signal, the broad amorphous peaks began to sharpen with characteristics similar to the previously observed Ti_2Ni-like phase. While direct imaging of the compositional fluctuations in the supercooled liquid were impossible, the evidence suggests that the SAXS signal is not, in fact, from liquid-liquid phase separation, but rather the rapid growth of nanocrystals driven by structural and chemical ordering. The investigation of the crystallization pathways in excellent BMGs such as Vit105 is crucial to understanding not only how such BMGs form, but also provide insight into methods of altering the microstructure to select for specific mechanical properties useful in future applications.

While past speculations have made a structural connection to fragility, clear evidence has not been previously observed. This connection was demonstrated for the first time in this dissertation, based on the measurements of structural evolution presented. In addition, a connection between structural and chemical ordering was found in some, but not all, of the high-temperature liquids studied. Two similar liquids, based on atomic sizes and binding enthalpies of the constituent elements, were found to contain very different local chemical environments despite similar topological order. Based on their local order, a metastable phase was predicted and later discovered and characterized in one of these liquids. Using the capabilities of the newly commissioned NESL levitator, future experiments will further explore the extent of these connections between structural evolution, chemical order, and thermophysical and kinetic properties. By developing a clear understanding of these relationships, a greater understanding of glass formation can be reached.

8.1 References

[1] N. Mattern, H. Hermann, S. Roth, J. Sakowski, M.-P. Macht, P. Jovari, J. Jiang, *Applied Physics Letters* **82**, 2589 (2003).

[2] N.A. Mauro, M.E. Blodgett, M.L. Johnson, A.J. Vogt, K.F. Kelton, *Nature Communications* **5:4616**, (2014).

Appendix A: Neutron Analysis User Guide

This appendix discusses the details involved in reducing the time-of-flight (TOF) neutron scattering data that were performed on the Nanoscale-Ordered Materials Diffractometer (NOMAD) discussed in Section 2.8.3. The IDL and Python scripts that were used for initial reduction are described in detail (Sections A.1-A.6), as well as the methods developed to correct the data post-reduction (Section A.7). Additional details for generic forms of the IDL scripts are covered in Appendix B and detailed descriptions of the LabVIEW programs that were used are covered in Appendix C.

A.1 Data Storage at ORNL

Reduction from neutron counts to $S(q)$ was performed on the Spallation Neutron Source (SNS) servers by remote connection using a free program called NX client. A configuration file is provided by the SNS from their general analysis website, http://analysis.sns.gov. Running the provided configuration file connects the user to their login server. It can be accessed with the account that each user set up prior to the experiment. As of July 27, 2015, the NX client is no longer supported for remote desktop access to the SNS servers. Instead, a new browser-based connection can be used. Since this is a relatively new procedure, the details will not be discussed here. More information can be found at https://analysis.sns.gov/. In order to access any folders on the server, the user's ID must be associated with the experiment number (IPTS number). This can be accomplished by contacting the PI or SNS contact for the experiment of interest, or can be requested from https://neutronsr.us/accounts/request-sns.html. All neutron data used in this dissertation were taken from the experiment designated as IPTS-11941. All data can be found under the following path on the SNS servers:

~/SNS/NOM/IPTS-11941/shared

with the analysis stored under:

~/SNS/NOM/IPTS-11941/shared/abskorr

Temperature-time data were collected on the NESL computers and the data were uploaded to

~/SNS/NOM/IPTS-11941/shared/TemperatureData

Examples and templates were stored in the folder:

~/SNS/NOM/IPTS-11941/shared/GeneralScripts_OctoberNOMAD_20150430

Raw temperature files and processed neutron data were transferred from the SNS servers to a local computer using the FTP software Cyberduck, connecting to *analysis.sns.gov* on *port 22* using an *FTP-SSL (Explicit AUTH TLS)* connection. Information on downloading and connecting to the SNS servers is also contained at http://analysis.sns.gov. As of the writing of this dissertation, the web page is formatted such that hovering over each icon will reveal a description of the program as well as a link to downloading it. The files can be transferred via Cyberduck by right-clicking on the appropriate file or highlighted files and selecting *download to*. There have been issues with the program crashing if this method is used on a second set of files while the first transfer is still in progress.

The reduction of raw neutron counts to final corrected and normalized $S(q)$ and $g(r)$ requires a large number of steps (Figure A.1) and each will be discussed in turn. There are three primary sections that the analysis can be broken into: Initial preparation, use of IDL scripts, and final LabVIEW reduction techniques. The current topic will be highlighted in red in the flow chart as it is discussed within the text.

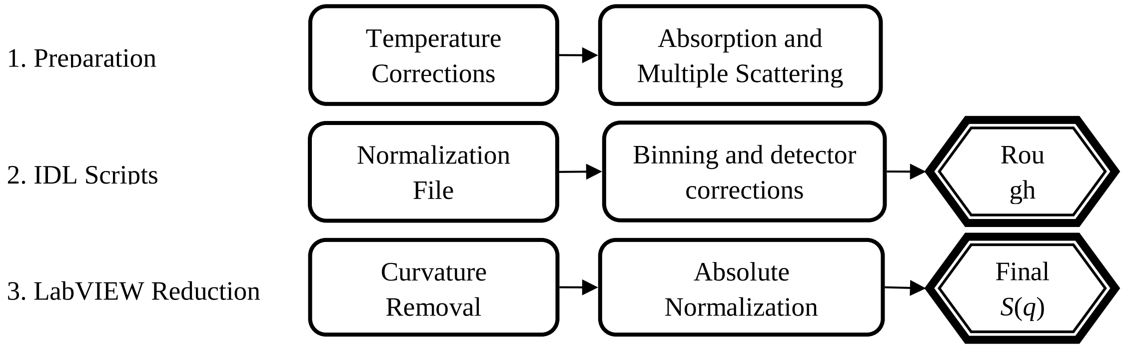

Figure A.1 Sequence of analysis steps for reduction of neutron scattering data.

A.2 Required Files

All corrections were made using a sequence of Python and IDL scripts developed by J. Neuefeind and modified for final use by myself. Python scripts were executed by preceding the script name with the command *python*, and IDL scripts were executed by preceding the script name with the command *idl*. The scan number corresponding to each calibration file is listed in Table A.1.

Table A.1 Calibration files used in NOMAD 2014.

Run ID	Standard Type	Mass (mg)	Diameter (mm)	Scan Length (min)
33228	Empty Chamber	--	--	60
33263	Pure Vanadium	365.23	4.85	60
33278	Diamond Powder	--	--	31
33279	Vanadium Can	--	--	31

Several standard files are required for proper data reduction (Table A.2). Many of them are created by the beamline scientist as part of the automatic reduction and are likely located in the experimental sub folder ~/shared/autoNOM. The relevancy of these automatically generated files for future experiments should be discussed with the beamline scientist to ensure their accuracy. These files include *aqdep33278*, *mask33278.dat*, *nomad_33278.calfile*, and *idlstart.pro*, where *33278* is the scan number of the diamond calibration standard. The file *norm33263_010_290_sm.dat* is the vanadium normalization file specific for NOMAD 2014; instructions on creating this file are discussed in Section A.5. It is possible the automatically reduced normalization file will be sufficient, but in NOMAD 2014 it did not fully remove all coherent vanadium peaks and had to be modified. The creation of the absorption and multiple scattering files *afsample.dat* and *sample.msdat* is discussed in Section A.3 and the use and modification of the standard binning file, *bingr_abs_9999.bat*, is discussed in Section A.6.

Table A.2 Files necessary for data reduction used in NOMAD 2014.

Filename	Description
aqdep33278	Describes the *q*-dependence of the neutron detectors
mask33278.dat	Describes bad pixels and banks to mask out of data analysis
nomad_33278.calfile	Describes detector calibrations necessary for analysis
norm33263_010_290_sm.dat	Normalization file created from the vanadium standard (λ = 0.10 - 2.90 Å) with extraneous peaks manually removed
idlstart.pro	Standard IDL initialization file
afsample.dat	Absorption and multiple scattering correction file
sample.msdat	Sample information used in creation of absorption and multiple scattering files. Generated from sample.ini inputs
bingr_abs_9999.bat	Binning template for NOMAD 2014

A.3 Temperature Corrections

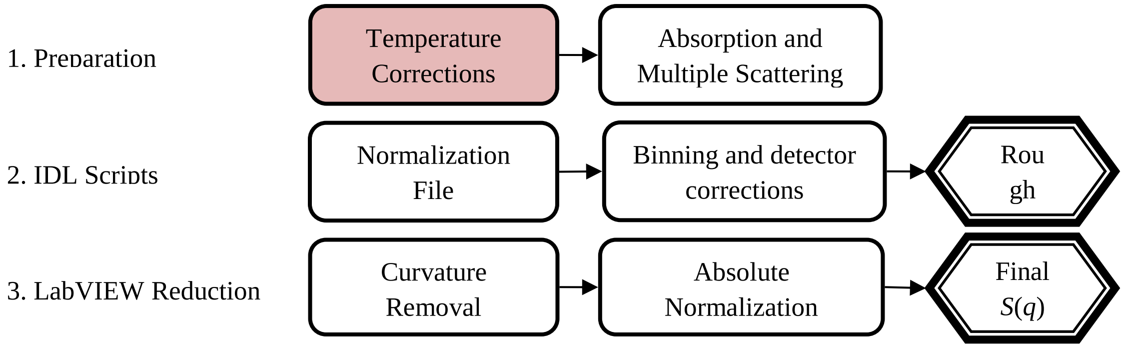

The raw temperature-time files were transferred from the SNS servers to a local PC for emissivity corrections and further reduction. Each isothermal measurement was preceded by a free-cool from the liquid and re-melted. Solidus (T_S) temperatures were determined for each sample from the largest endothermic signature measured in a differential thermal analyzer (DTA) (Labsys^{TM} DTA/DSC, Setaram) and were matched to this melt plateau using a modified version of *EMCorrectTempData.vi* [1]. There was significant drift in the He-Ne positioning lasers resulting in an apparent shift in temperature over time. As a result, the "constant" temperatures could drift by ~50 ^{o}C over 30 min.

Temperature averages were performed using Origin 9 over regions of relatively constant temperature close to the preceding melt plateau. The Origin function *Statistics on Columns* was used, with the beginning and end points determined visually from an inspection of the temperature-time graph. An adequate fit was also obtained using the *Statistics – Mean* gadget, but the error on the mean was not output using this method. The final temperature was calibrated using the melt plateaus before and after each scan. For example, in Figure A.2 (a), Run 33243 was first corrected to the plateau preceding the measurement. Over the first 206.5 s it averaged to 1293.19 ± 0.51 ^{o}C with a standard deviation of 23.09 ^{o}C, where the error represents the standard error of the mean. Similarly, in Figure A.2 (b), the same temperature data was corrected to the melt plateau following the measurement, and the final 560.5 s of the hold averaged to 1293.49 ± 0.16 ^{o}C with a standard deviation of 11.63 ^{o}C. This confirmed that the temperature remained constant throughout the measurement despite the apparent drift. The temperature is typically fairly well defined (Figure A.3 (a-b)) giving the low standard error, but due to sample motion and issues with pyrometer alignment, there was often a spread to the data resulting in a large standard deviation. A typical dataset had a standard deviation of 4-10 ^{o}C (Figure A.3 (b)).

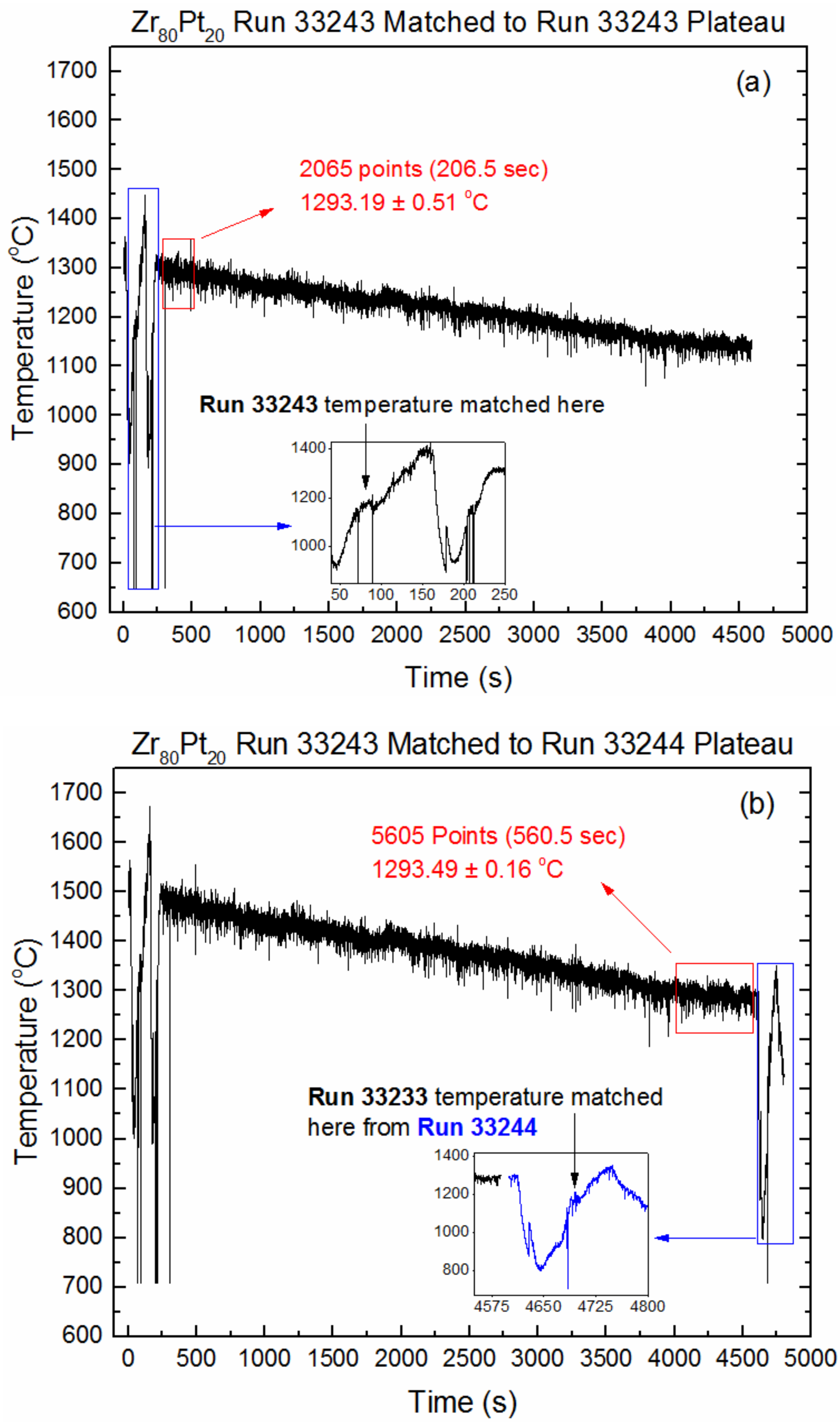

Figure A.2 Temperature-time graphs of $Zr_{80}Pt_{20}$ Run 33243 corrected by (a) matching to the melt plateau in Run 33243 and (b) matching to the melt plateau in Run 33244.

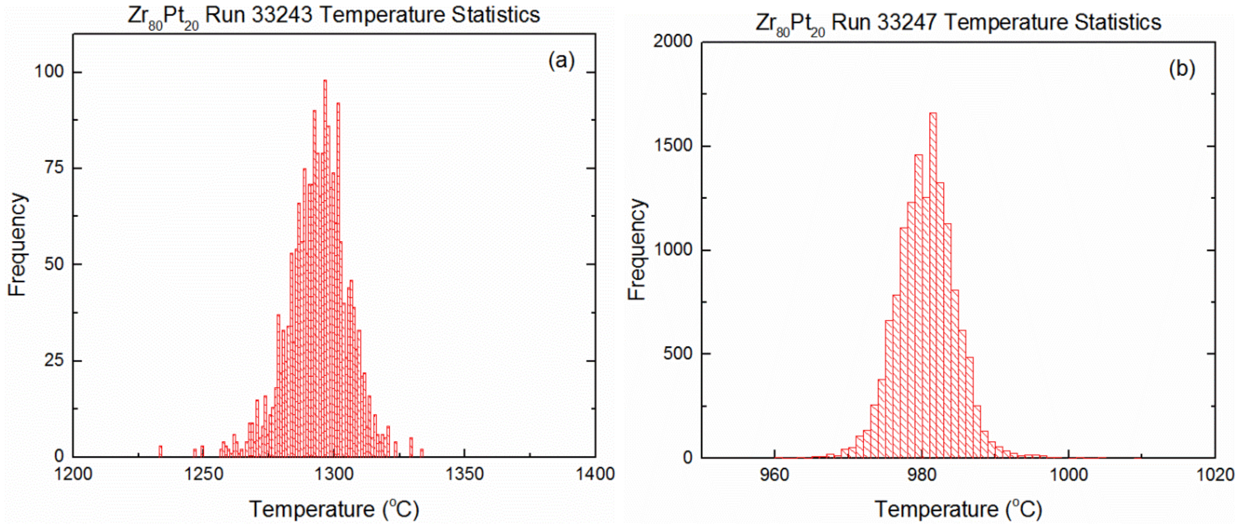

Figure A.3 Statistics on the temperature-time average of (a) Run 33243 matched to the melt plateau prior to the hold and (b) Run 33247.

A.4 Absorption and Multiple Scattering Simulations

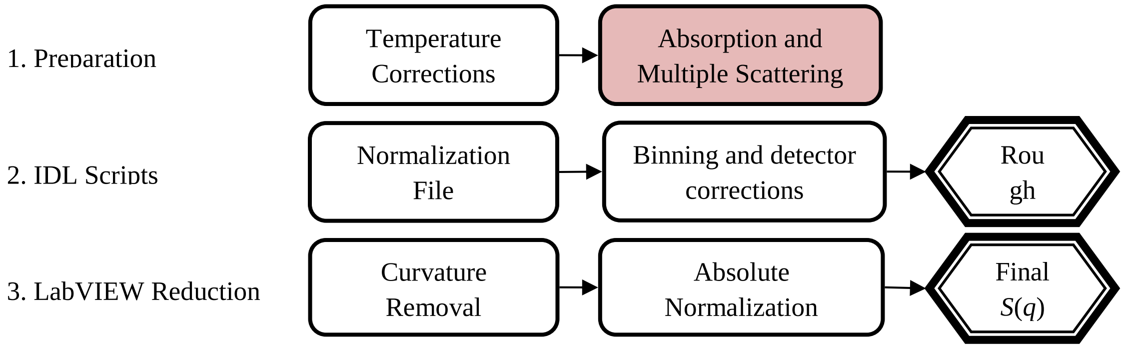

Simulations of absorption and multiple scattering were performed for each sample using temperature-dependent liquid density acquired with WU-BESL at Washington University in Saint Louis. An initialization file was used to define the appropriate radius (in cm) and density (in g/cm^3) of each sample (Figure A.4).

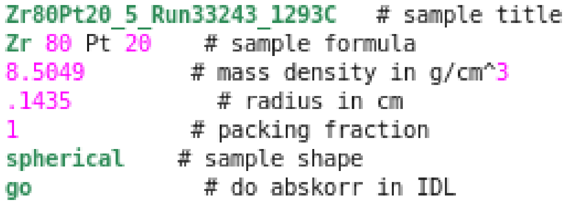

```
Zr80Pt20_5_Run33243_1293C   # sample title
Zr 80 Pt 20    # sample formula
8.5049        # mass density in g/cm^3
.1435           # radius in cm
1             # packing fraction
spherical    # sample shape
go             # do abskorr in IDL
```

Figure A.4 *Zr80Pt20_5_Run33243_1293C.ini* initialization file that seeds the absorption and multiple scattering simulation.

The initialization file can be created or modified using the *gedit* text editor through a Linux terminal using:

```
$ gedit filename.ini
```

where the *$* symbol indicates the start of the entry box in a Linux terminal and is not input by the user. If a file named *filename.ini* exists, it will open in *gedit*. If the file does not exist, it will open an empty text document and name it *filename.ini*. The sample formula requires a space between each element and its corresponding atomic weight (in at.%*100). All samples in this dissertation were calculated using a *spherical* sample shape, but a *cylindrical* shape is also available. The simulation is executed by running the following code in a terminal in the same folder as the initiation file:

```
$ python ~zjn/pytest/define_sample.py –f filename.ini
```

As mentioned in Section 2.9.2, it is generally assumed that the absorption coefficient for neutron scattering behaves linearly with neutron wavelength, commonly known in literature as a *1/v* scaling, where *v* is the velocity of the neutron. When the above command is executed, the absorption coefficients are approximated using Eqn. 2.31. The *define_sample.py* script is also capable of performing an energy-dependent simulation of the absorption coefficient for the cases where an absorption resonance appears in the energy range used at NOMAD. Using $Zr_{77}Rh_{23}$ as an example (Chapter 5 and Chapter 6), rhodium contains a resonance near 0.3 Å (Figure A.5), resulting in a large increase in absorption that deviates from the 1/*v* relationship. The previous command can be modified to read in the measured absorption as a function of wavelength by applying a modifier:

```
$ python ~zjn/pytest/define_sample.py –f filename.ini –R True
```

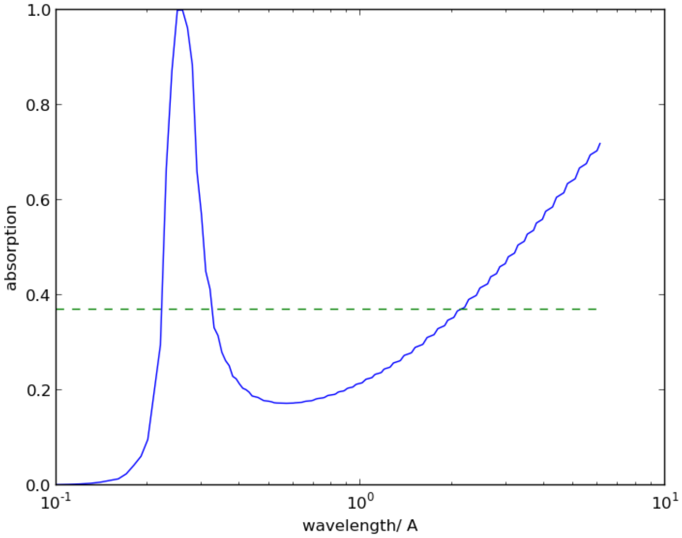

Figure A.5 Rhodium absorption resonance peak. Normal 1/*v* behavior is represented by the linear tail at large wavelength. The range of data presented here spans the accessible wavelengths available at NOMAD.

Due to the very good linear approximation that most materials exhibit in the appropriate energy range, in most experiments it has not been necessary to take into account wavelength-dependent absorption. With the increase in computing power and available data, it is now feasible to start implementing this type of correction. Due to time constraints, this feature was not extensively tested and was not implemented in this dissertation. Instead, the absorbing wavelengths were filtered out. Details of performing wavelength filtering are described in Section B.2.2, Table B.3.

Once completed, these scripts produce a file containing all absorption and multiple scattering information named *afsample.dat*, where *sample* is replaced with a unique filename specific to the composition, run number, and temperature. A second file, named *sample.msdat*, is also generated, containing sample specific information including mass, radius, density, and scattering length based on information provided in the initiation file.

A.5 Normalization File

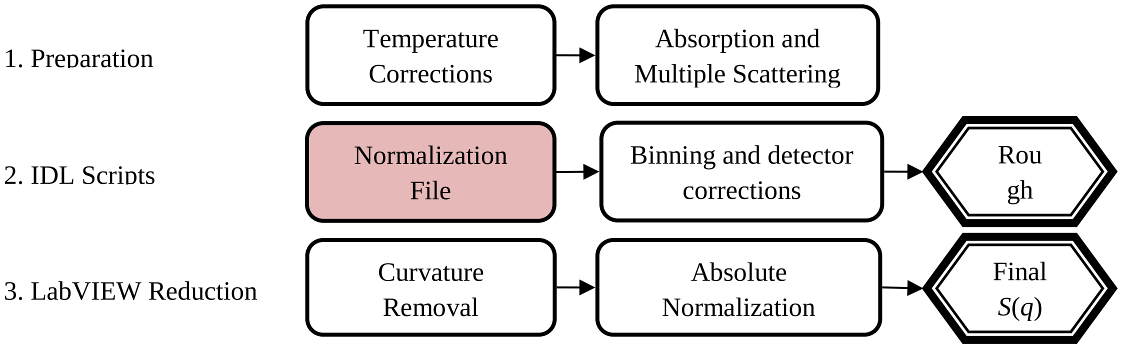

The standard reduction of pure vanadium during NOMAD 2014 had issues removing all Bragg peaks from Run ID 33263. Modified scripts were created to properly correct the data. To begin, both the background and pure vanadium data (Run IDs 33228 and 33263) were reduced using separate batch files (Figure A.6 and Figure A.7). For future experiments, the values *33278* and *33228* can be replaced with the corresponding run numbers for the diamond calibration and empty chamber.

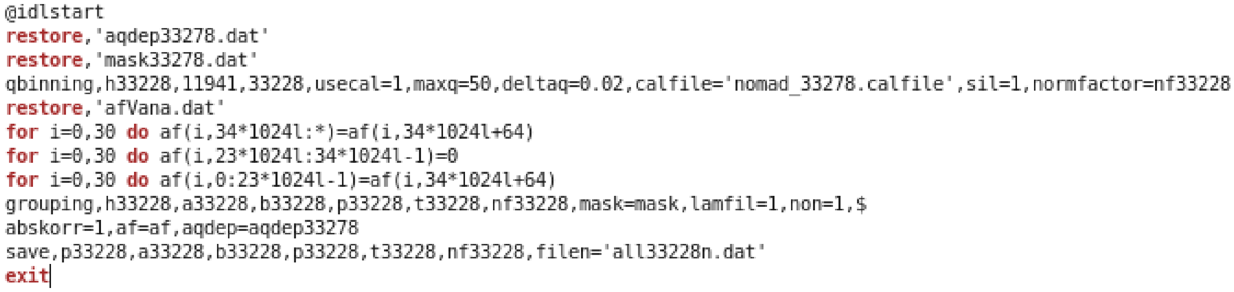

```
@idlstart
restore,'aqdep33278.dat'
restore,'mask33278.dat'
qbinning,h33228,11941,33228,usecal=1,maxq=50,deltaq=0.02,calfile='nomad_33278.calfile',sil=1,normfactor=nf33228
restore,'afVana.dat'
for i=0,30 do af(i,34*1024l:*)=af(i,34*1024l+64)
for i=0,30 do af(i,23*1024l:34*1024l-1)=0
for i=0,30 do af(i,0:23*1024l-1)=af(i,34*1024l+64)
grouping,h33228,a33228,b33228,p33228,t33228,nf33228,mask=mask,lamfil=1,non=1,$
abskorr=1,af=af,aqdep=aqdep33278
save,p33228,a33228,b33228,p33228,t33228,nf33228,filen='all33228n.dat'
exit
```

Figure A.6 IDL binning script for the empty chamber (Run ID 33228).

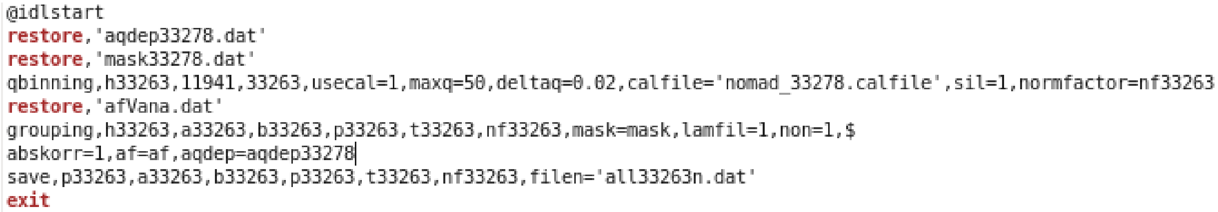

```
@idlstart
restore,'aqdep33278.dat'
restore,'mask33278.dat'
qbinning,h33263,11941,33263,usecal=1,maxq=50,deltaq=0.02,calfile='nomad_33278.calfile',sil=1,normfactor=nf33263
restore,'afVana.dat'
grouping,h33263,a33263,b33263,p33263,t33263,nf33263,mask=mask,lamfil=1,non=1,$
abskorr=1,af=af,aqdep=aqdep33278
save,p33263,a33263,b33263,p33263,t33263,nf33263,filen='all33263n.dat'
exit
```

Figure A.7 IDL binning script for the vanadium standard (Run ID 33263).

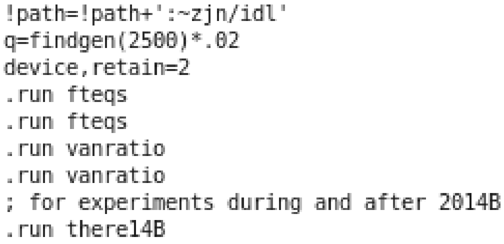

```
!path=!path+':~zjn/idl'
q=findgen(2500)*.02
device,retain=2
.run fteqs
.run fteqs
.run vanratio
.run vanratio
; for experiments during and after 2014B
.run there14B
```

Figure A.8 IDL Script *@idlstart* defines the path of all other scripts used.

These scripts create Run ID-specific files (*all33228n.dat* and *all33263n.dat*, respectively) containing all of the acquired intensity information. The command *@idlstart* is an IDL subroutine that points IDL to the proper directory where all reduction subroutines are stored on the SNS servers (Figure A.8). The command *restore* reads the specified file and imports the data into correctly named variables according to file-type. The command *qbinning* requires an input of Run ID, IPTS number (NOMAD 2014 is considered IPTS-11941), maximum *q*, *q*-spacing, and a reference to the diamond powder calibration file. The file *afVana.dat* that is restored on line 5 in Figure A.6 and Figure A.7 contains the simulated absorption and multiple scattering data for the Vanadium standard. The command *grouping* combines all of the imported information onto the defined *q*-grid. The input *abskorr=1* tells the program to perform the absorption and multiple scattering correction. The command *save* combines the variables created by *grouping* and outputs a text file, typically titled *all#####.dat*. This file contains the run information, where ##### represents the run number of interest. Further information on all of the relevant commands is contained in Appendix B.

The IDL script *run_norm.bat* was then executed to create a normalization file that is properly background subtracted and corrected for absorption and multiple scattering (Figure A.9).

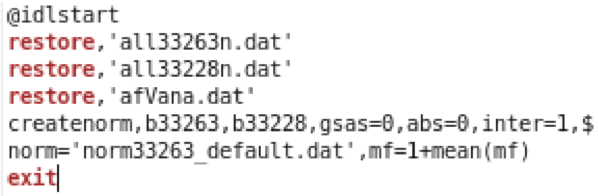

```
@idlstart
restore,'all33263n.dat'
restore,'all33228n.dat'
restore,'afVana.dat'
createnorm,b33263,b33228,gsas=0,abs=0,inter=1,$
norm='norm33263_default.dat',mf=1+mean(mf)
exit
```

Figure A.9 IDL script *run_norm.bat*, which performs proper background subtraction, absorption, and multiple scattering corrections.

This script first restores the binned and grouped files previously created by the binning scripts (Figure A.6 and Figure A.7) as well as the simulated absorption and multiple scattering corrections (*afVana.dat*). During normalization, the data from each bank is fit to a Gaussian near each coherent Vanadium peak (Figure A.10).

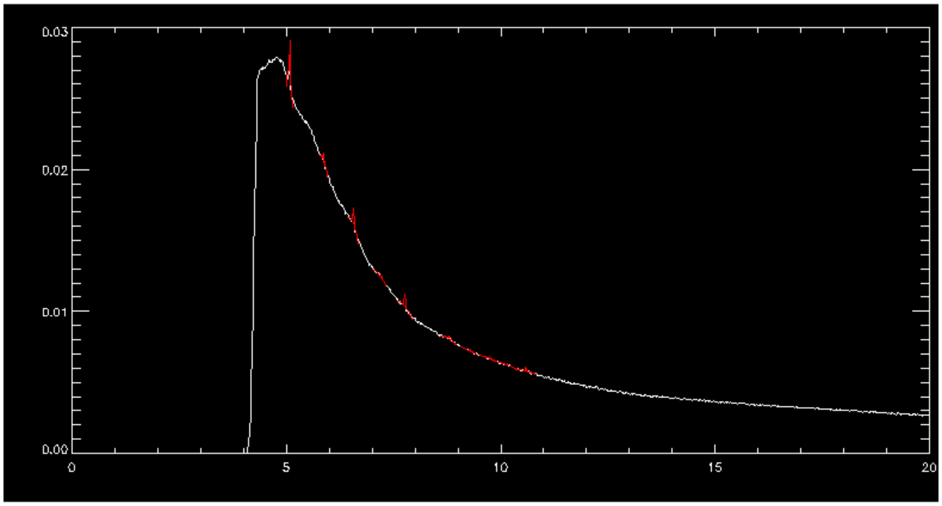

Figure A.10 Vanadium peak removal from Bank 5 of NOMAD. The white curve is the background-subtracted vanadium scattering signal from Run 33263. The red curves are the fits to Bragg peaks from vanadium.

Once all six banks are successfully fit, the peaks are subtracted out and replaced with a smooth curve in that region (Figure A.11).

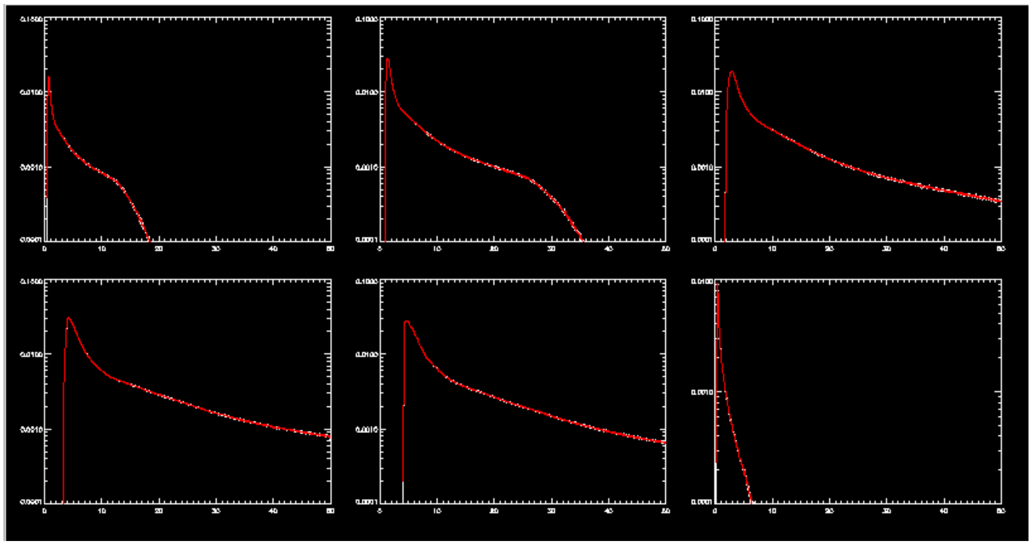

Figure A.11 Each detector bank with vanadium peaks successfully subtracted out.

When this peak-subtracted normalization file was used to normalize the original vanadium scan, the result was a sequence of very small coherent peaks above a flat background (Figure A.12), indicating any signature of the incident spectrum was successfully removed.

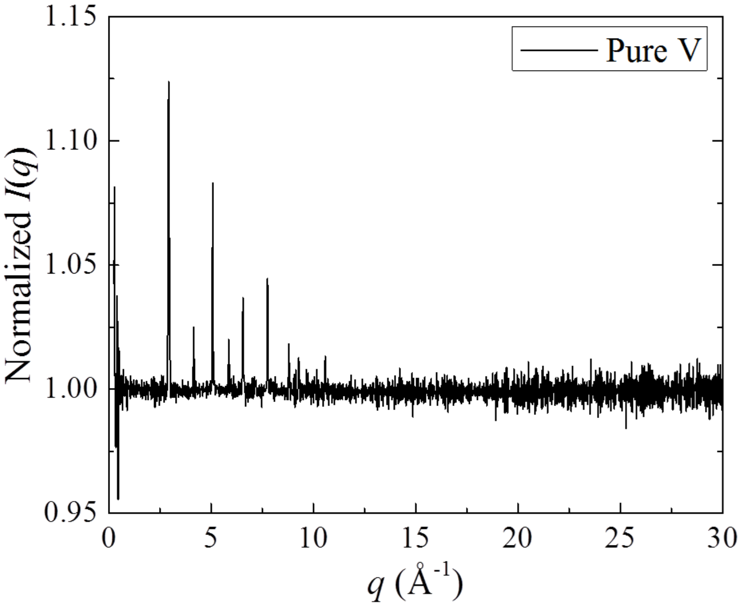

Figure A.12 The vanadium scan normalized to the Bragg-subtracted vanadium normalization factor.

This procedure generally removes all features from the vanadium, but in the data acquired during NOMAD 2014 there was a small feature that was not properly subtracted near q = 5 Å^{-1}, corresponding to the 211 vanadium reflection (q_{211} = 5.079 Å). This feature was quite small, but problematically appeared in the middle of the second peak in $S(q)$ (Figure A.13).

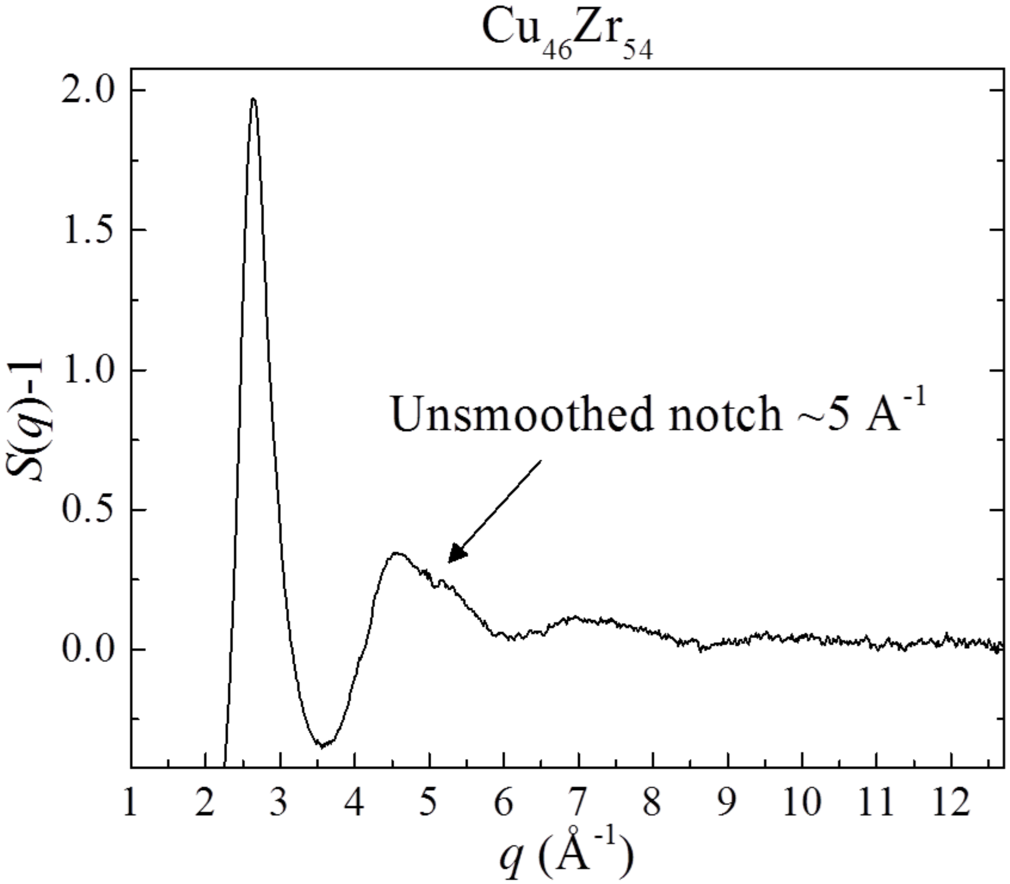

Figure A.13 Liquid $Cu_{46}Zr_{54}$ at 774 °C. The arrow indicates a jagged notch in the second peak of $S(q)$-1 near the 211 Vanadium reflection.

In practice, the bank-averaged sample intensity is divided by the variable *normall* contained in the normalization file. The variable *normall* was extracted using the IDL script *SaveNormall.pro*, shown in Figure A.14.

```
@idlstart

restore,"norm33263_default.dat"
wstd,q,normall,'normall_default.dat',comment='normall with spurrious peak'

exit
```

Figure A.14 IDL script *SaveNormall.pro*, extracting the *normall* parameter from the file *norm33263_default.dat*.

This script restores the normalization file named *norm33263_default.dat*, then writes the variable *normall* to a text file using the command *wstd*. When executed, *normall*(*q*) was written to a user-named file (here, *normall_default.dat*). *Normall* was fit using a cubic spline in Origin with 2500 points (the same number of points in *normall*) using linear and apparent interpolation. Eight points were masked out from the fit from q = 5.0 - 5.14 Å^{-1} and were replaced with the spline fit (Figure A.15).

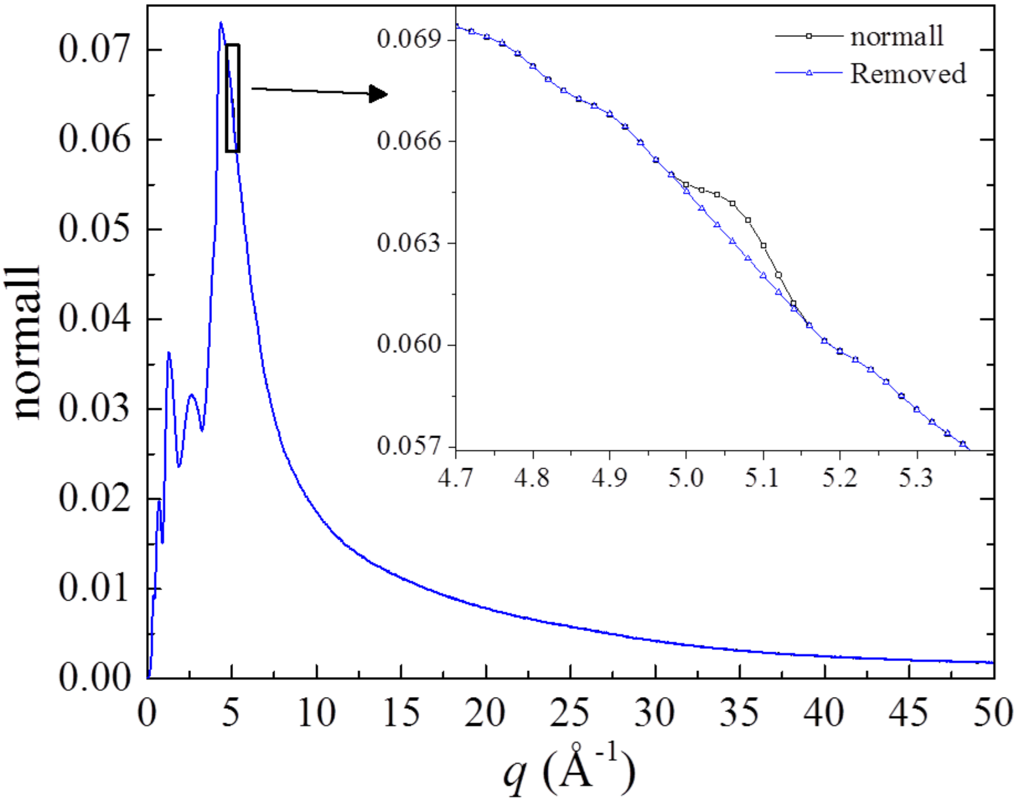

Figure A.15 The normalization factor *normall* both before (black) and after (blue) a residual vanadium peak was masked by hand.

The data were then exported from Origin to a text file, designated as *normall_sm.dat*. The IDL script *VPeakRem_norm.pro* was used to convert *normall_sm* back to the proper format for a normalization file (Figure A.16).

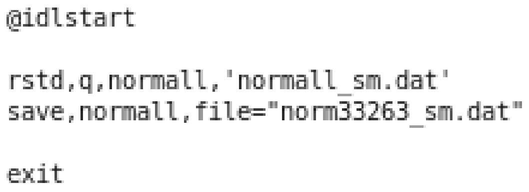

```
@idlstart

rstd,q,normall,'normall_sm.dat'
save,normall,file="norm33263_sm.dat"

exit
```

Figure A.16 IDL script *VPeakRem_norm.pro*. Re-saves *normall* as a normalization file.

With the new normalization factor, *norm33263_sm.dat*, the notch in *S*(*q*)-1 that appeared in Figure A.13 was successfully removed, smoothly spanning the gap and providing a more realistic *S*(*q*)-1 (Figure A.17).

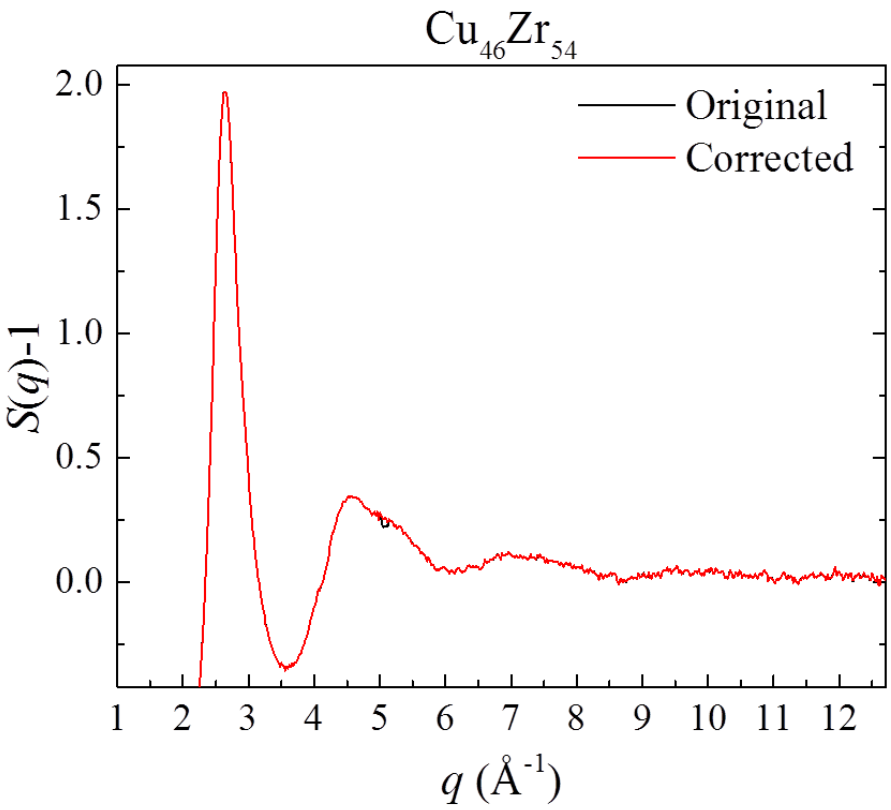

Figure A.17 Liquid $Cu_{46}Zr_{54}$ at 774 °C. The black curve represents a typical *S*(*q*)-1 produced using a normalization file without proper vanadium peak removal. The red curve represents *S*(*q*)-1 with a proper normalization.

A.6 Obtaining *S*(*q*)

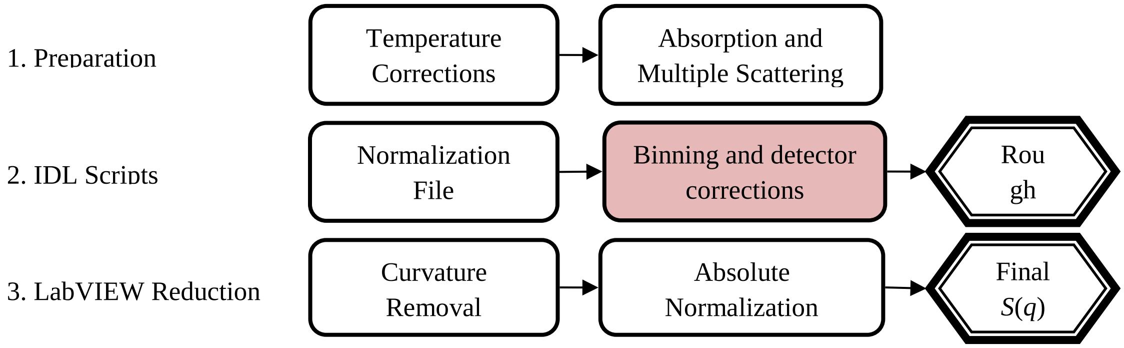

With a proper normalization file, a total *S*(*q*) was generated from the time-of-flight (TOF) data using all of the standard files listed in Table A.2. A binning script was generated for each run number using a standard template, bingr*_abs_9999.bat* (Figure A.18). A detailed description of each function is described in detail in Appendix B. There are two pre-set values that can be easily replaced using *find-replace* in a standard text editor, accessed by *ctrl+h* in *gedit*. The run number is represented by *9999*, and the filename for the absorption correction is represented by *sample*.

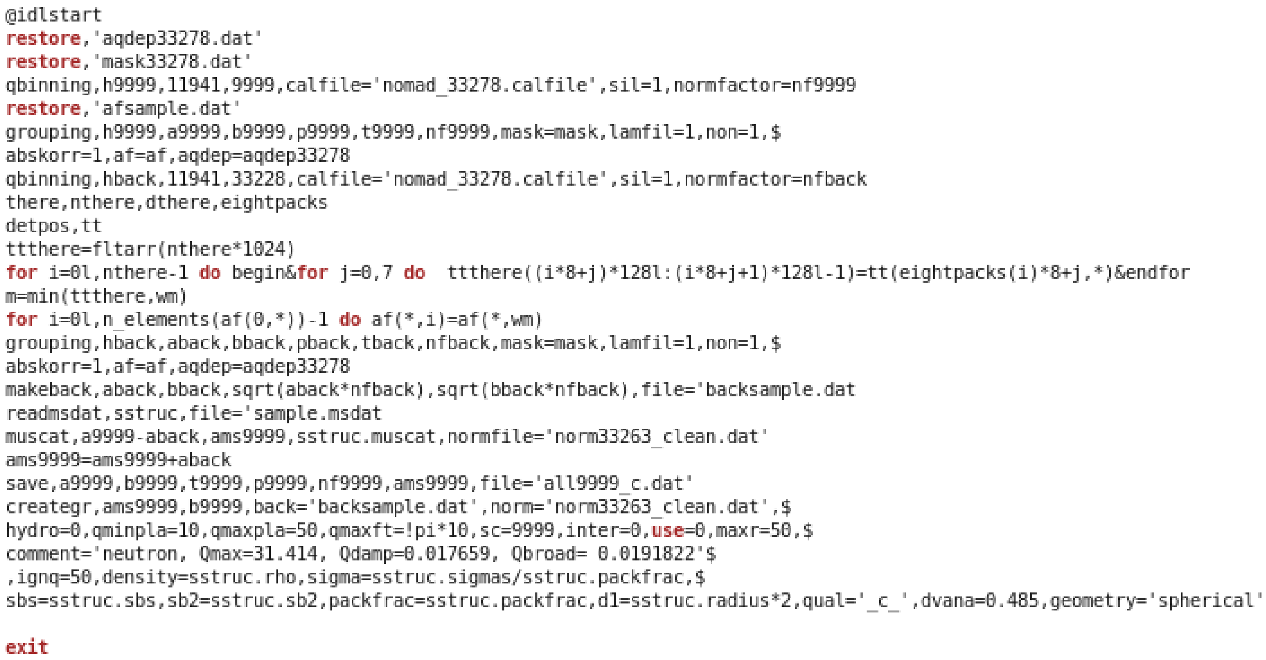

```
@idlstart
restore,'aqdep33278.dat'
restore,'mask33278.dat'
qbinning,h9999,11941,9999,calfile='nomad_33278.calfile',sil=1,normfactor=nf9999
restore,'afsample.dat'
grouping,h9999,a9999,b9999,p9999,t9999,nf9999,mask=mask,lamfil=1,non=1,$
abskorr=1,af=af,aqdep=aqdep33278
qbinning,hback,11941,33228,calfile='nomad_33278.calfile',sil=1,normfactor=nfback
there,nthere,dthere,eightpacks
detpos,tt
ttthere=fltarr(nthere*1024)
for i=0l,nthere-1 do begin&for j=0,7 do  ttthere((i*8+j)*128l:(i*8+j+1)*128l-1)=tt(eightpacks(i)*8+j,*)&endfor
m=min(ttthere,wm)
for i=0l,n_elements(af(0,*))-1 do af(*,i)=af(*,wm)
grouping,hback,aback,bback,pback,tback,nfback,mask=mask,lamfil=1,non=1,$
abskorr=1,af=af,aqdep=aqdep33278
makeback,aback,bback,sqrt(aback*nfback),sqrt(bback*nfback),file='backsample.dat
readmsdat,sstruc,file='sample.msdat
muscat,a9999-aback,ams9999,sstruc.muscat,normfile='norm33263_clean.dat'
ams9999=ams9999+aback
save,a9999,b9999,t9999,p9999,nf9999,ams9999,file='all9999_c.dat'
creategr,ams9999,b9999,back='backsample.dat',norm='norm33263_clean.dat',$
hydro=0,qminpla=10,qmaxpla=50,qmaxft=!pi*10,sc=9999,inter=0,use=0,maxr=50,$
comment='neutron, Qmax=31.414, Qdamp=0.017659, Qbroad= 0.0191822'$
,ignq=50,density=sstruc.rho,sigma=sstruc.sigmas/sstruc.packfrac,$
sbs=sstruc.sbs,sb2=sstruc.sb2,packfrac=sstruc.packfrac,d1=sstruc.radius*2,qual='_c_',dvana=0.485,geometry='spherical'

exit
```

Figure A.18 Standard binning template, *bingr_abs_9999.bat*. Standard find-replace components include *9999* for the sample run number and *sample* for the filename designating absorption and multiple scattering information.

In the example in Figure A.18, the normalization file is input in two places, designated here as *norm33263_clean.dat.* For the purposes of NOMAD 2014, a single normalization file was prepared using the techniques described in Section A.5. There are several other parameters that must be modified for data taken on future experimental runs. A more general template, *bingr_abs_9999_general.bat*, contains several other generic parameters for replacement which are described in detail in Appendix B.

Once a proper binning file is created, it is executed using the command:

```
$ idl bingr_abs_9999.bat
```

This script generates a series of files beginning with *NOM_9999_* including standard *g*(*r*) and *S*(*q*) files. A complete description of the output files are given at http://neutrons.ornl.gov/sites/default/files/How-to-reduce-NOMAD-data.pdf. The only output used from this is the $S(q)$ file, which technically outputs $S(q)$-1. This $S(q)$ has been corrected for all standard detector corrections as well as absorption and multiple scattering. It does not yet properly account for secondary scattering from the chamber or remove non-physical features. These corrections are discussed in Section A.7.

A.7 Curvature Removal and Absolute Normalization

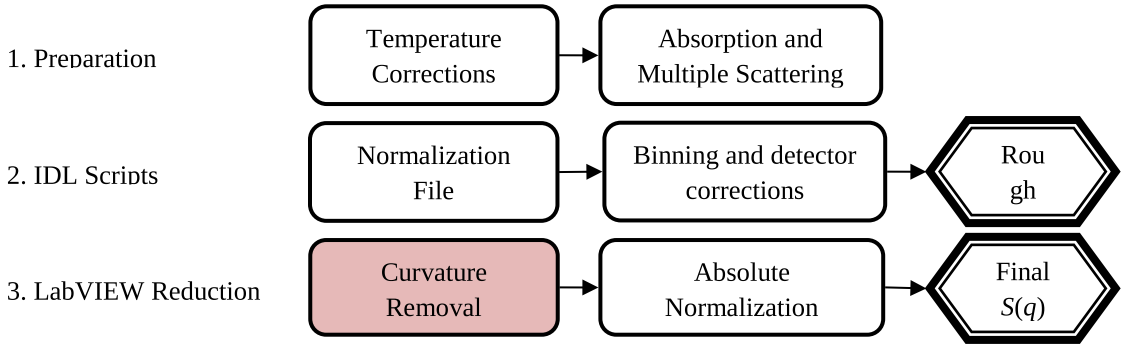

The $S(q)$ produced in the preceding steps is still not fully reduced. Using only those corrections, there is often a sizeable amount of curvature that prevents $S(q)$ from oscillating smoothly around 1 for smaller-q values (5-10 Å^{-1}), as is the expected behavior (Figure A.19). This is typically attributed to inelastic scattering, where the incident neutron transfers noticeable energy to the scattering atom, thereby reducing its velocity and increasing the resulting measured TOF to the detector. These neutrons become incorrectly binned and must therefore be accounted for.

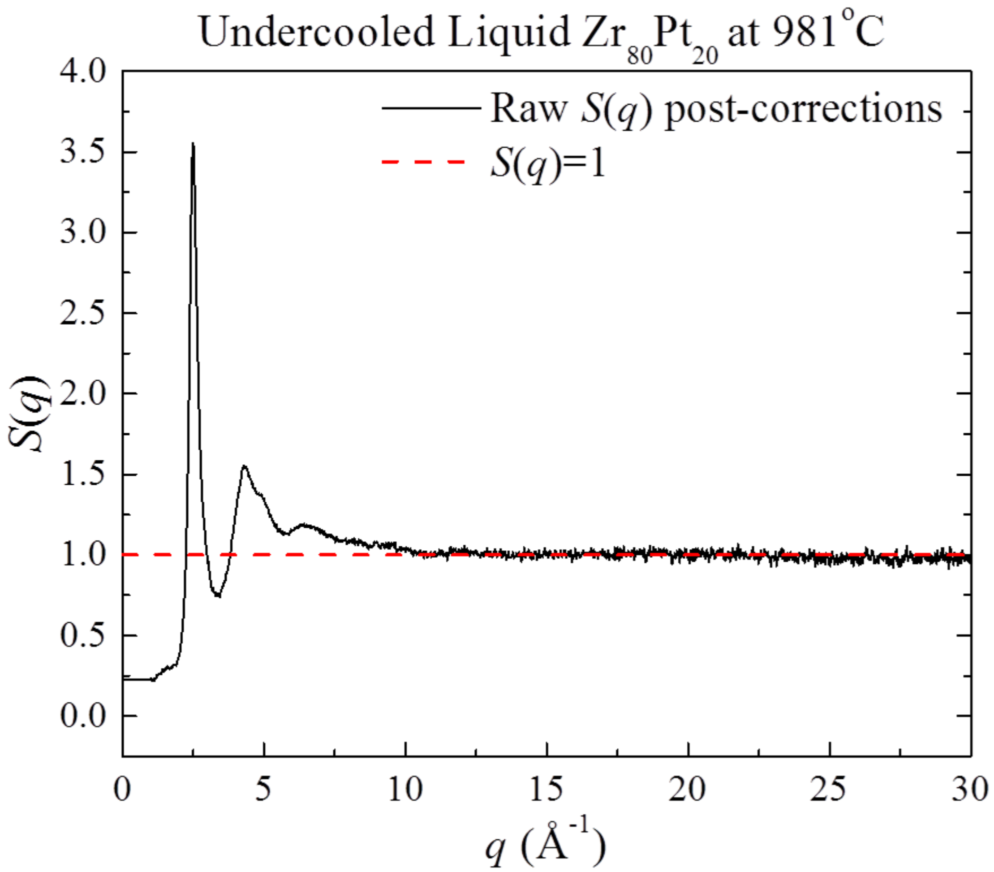

Figure A.19 Initial $S(q)$ post-corrections of undercooled liquid $Zr_{80}Pt_{20}$ at 981°C. The red line indicates $S(q) = 1$.

There are several possible ways of dealing with this excess curvature. The first method is to calculate the estimated effect using the method developed by Placzek [2]. This correction is strongest at small-q, but calculations always severely overestimate its effect. It has been integrated into popular PDF reduction software such as PDFgetN [3], but due to the difficulty of properly calculating this effect over all q-ranges, it is of limited practical use [4]. Other methods are in development using phonon models to directly calculate the inelastic contributions, but are currently not implemented. A method has been developed by Page *et al*. [5] which attempts to account for this effect in q-space by fitting a weighted background to $S(q)$ from each bank of data. The background is weighted within a small window in q-space to ignore contributions from coherent peaks and place more emphasis on determining an appropriate baseline. This method is reasonably effective with high amounts of inelastic scattering of crystalline materials, but due to the broad peaks in liquid structure factors presented in this dissertation, the automatic weighting for the effective background is not expected to accurately fit the data.

A method commonly used in *r*-space assumes that below some minimum *r*-cutoff, $r_{\min}$, the reduced pair-distribution function, $G(r)$, is represented by a straight line with the slope proportional to the number density:

$$G(r) = 4\pi r \rho_0 (g(r) - 1) = \frac{2}{\pi}\int_0^\infty q\left(S(q) - 1\right)\sin(qr)\,dq\,. \tag{A.1}$$

Here, $g(r)$ is the pair-distribution function and ρ_0 is the average number density. The pair-distribution function is a measure of the likelihood of finding another atom a distance *r* away from any given atom. Therefore, there is a hard-sphere limit below which it is unphysical to place two atoms. In this region, $g(r) = 0$ and $G(r) = -4\pi r\rho_0$. If there are any features in the Fourier transform from $S(q)$ to $G(r)$ in this region, then they must be unphysical and can be removed. Features in this region are assumed to produce only low-amplitude, low-frequency oscillations in $S(q)$. The best-fit line can be subtracted from the data and Fourier transformed back to *q*-space where it is then subtracted from $S(q)$. However, this method cannot account for any inelastic scattering contributions to $G(r)$ that occur beyond the first coordination shell. One of primary disadvantages of this method is that it makes assumptions based on the expected structure. However, both $G(r)$ and $g(r)$ are minimally affected above $r_{\min}$ so the real-space distance correlations are preserved.

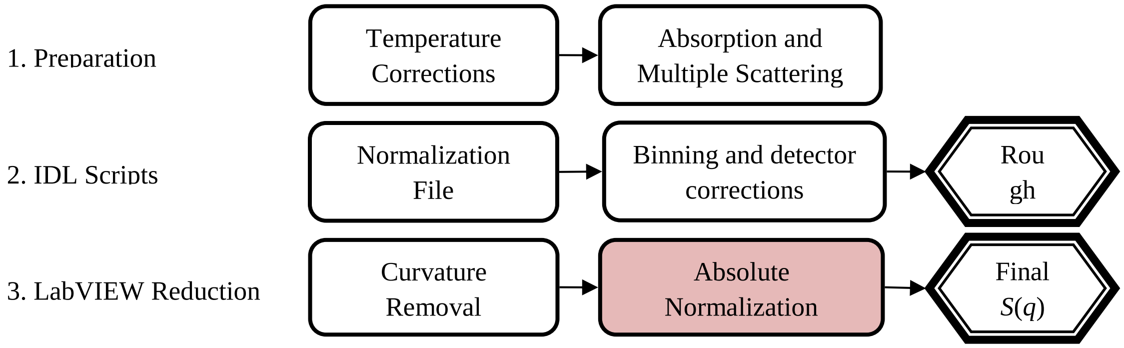

Multiple scattering events are those wherein a neutron that scatters off of a nucleus within the sample is scattered a second time within the same sample. This correction has already been discussed, but it does not account for those neutrons that first scatter from the sample and then scatter a second time from the environment. These events are called *secondary scattering*. The NESL has many components and takes up a large footprint, so there are many opportunities for secondary scattering. Since these events only occur when a sample is present in the beam, an empty chamber scan cannot properly account for these extra counts. An exact calculation of secondary scattering, then, depends upon the precise geometry and elemental composition of the surrounding equipment. This is a nearly impossible task to undertake, but approximations can be made based on expected physical behavior.

The previous discussion involving subtracting out the unphysical ripples in $G(r)$ in the *hard-sphere* region does not guarantee that $g(r) \rightarrow 0$ at $r = 0$ Å. If $g(r)$ at small-r is not 0, this unphysically implies that there are still real-space correlations at distances smaller than interatomic distances and results in a slope in the small-r region of $G(r)$, $4\pi\rho_{\text{fit}}$, that does not match the experimentally measured number density, $\rho_{0.}$ According to Peterson [6], one of the most common systematic errors is a scaling error where the reduced $S(q)$ requires an additional scaling factor:

$$S'(q) = \alpha S(q) + (1-\alpha)\,. \tag{7.3}$$

Here, α is a multiplicative scaling constant and $S'(q)$ is the modified $S(q)$. The addition of (1-α) is necessary to maintain proper normalization about $S(q) = 1$. If the liquid density is known to sufficient accuracy, α can be adjusted until ρ_{fit} calculated from $G(r)$ matches the experimentally determined value. The combination of these two corrections is not unique to neutron scattering measurements, and can also be applied to X-ray measurements in order to put them on the absolute scale.

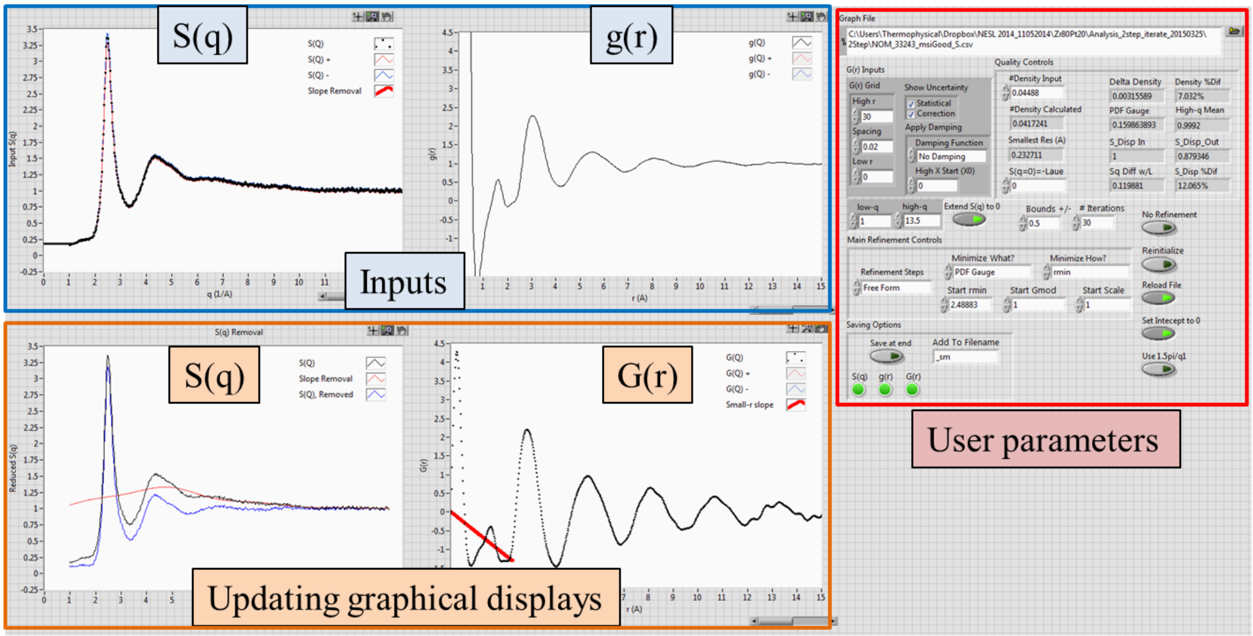

Graph File
C:\Users\Thermophysical\Dropbox\NESL 2014_11052014\Zr80Pt20\Analysis_2step_iterate_20150325\2Step\NOM_33243_msiGood_S.csv

G(r) Inputs
G(r) Grid
High r: 30
Spacing: 0.02
Low r: 0
Show Uncertainty
☑ Statistical
☑ Correction
Apply Damping
Damping Function: No Damping
High X Start (X0): 0

Quality Controls
#Density Input: 0.04488
#Density Calculated: 0.0417241
Smallest Res (A): 0.232711
S(q=0)=-Laue: 0
Delta Density: 0.00315589
PDF Gauge: 0.159863893
S_Disp In: 1
Sq Diff w/L: 0.119881
Density %Dif: 7.032%
High-q Mean: 0.9992
S_Disp_Out: 0.879346
S_Disp %Dif: 12.065%

low-q: 1
high-q: 13.5
Extend S(q) to 0
Bounds +/-: 0.5
Iterations: 30
No Refinement

Main Refinement Controls
Refinement Steps: Free Form
Minimize What?: PDF Gauge
Minimize How?: rmin
Start rmin: 2.48883
Start Gmod: 1
Start Scale: 1
Reinitialize
Reload File
Set Intecept to 0
Use 1.5pi/q1

Saving Options
Save at end
Add To Filename: _sm
S(q) ● g(r) ● G(r) ●

Figure A.20 Custom LabVIEW VI *Sq_Curvature.vi* used for curvature removal and absolute normalization. Displayed data is for a $Zr_{80}Pt_{20}$ liquid $S(q)$ from neutron scattering at 1293 ^{o}C.

The neutron data in this dissertation were reduced using a modified version of the real-space method described above using the LabVIEW program *Sq_Curvature.vi* (Figure A.20, Section C.2). Since the output from the IDL scripts described in Section A.6 produces a non-uniform *space*-delimited file, the output **.dat* must first be converted to the proper format using the custom LabVIEW program *NOMAD_File_Convert.vi* (described in more detail in Section C.1). This VI converts the IDL results into a format consistent with the output from *X-ray Batch.vi*. As a result, *Sq_Curvature.vi* is compatible with structure factors measured from both types of experiments. *Sq_Curvature.vi* has a wide array of options included in the *user parameter* section, but ideal values were found for the majority and do not require adjustment. The details of all possible options are described in detail in Section C.2. The value of $r_{\min}$ is optimally determined by either visually observing the minimum before the first peak in $G(r)$ or by using the minimum bond length expected between the constituent elements. This can be approximated using combinations of the Goldschmidt radii of each species or by chemically specific techniques such as isotopic substitution neutron scattering or extended X-ray absorption fine structure (EXAFS) measurements. For the liquids measured from neutron scattering in this dissertation, $g(r)$ was quite noisy, making it difficult to accurately determine the minimum before the primary peak. In order to minimize arbitrary determination of $r_{\min}$, a golden section search [7] is used to minimize the Peterson metric [6], denoted as *PDFGauge* in this work:

$$PDFGauge = \Delta G_{low} = \frac{\int_0^{r_{\min}} \left[rG(r) + 4\pi r^2 \rho_{fit} \right] dr}{\int_0^{r_{\min}} \left(4\pi r^2 \rho_{fit} \right)^2 dr} . \tag{7.4}$$

Here, ρ_{fit} is determined from the slope of a linear fit to the small-r data with $G(r = 0)$ fixed at 0. Within the program, set *Refinement Steps* to *PDFGauge – rmin*. When the program is run, *Minimize What?* and *Minimize How?* automatically adjust to *PDF Gauge* and *rmin*, respectively (Figure A.21). This particular metric is already implemented in our in-house reduction of X-ray data in order to properly normalize $S(q)$ at large-q and minimize the ripples present in $G(r)$ below some $r_{\min}$ [8].

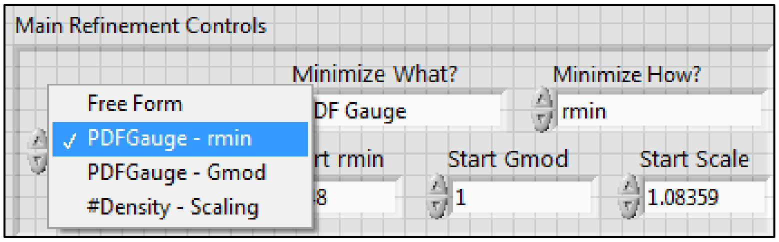

Minimize What? DF Gauge
Minimize How? rmin
rt rmin 8
Start Gmod 1
Start Scale 1.08359

Figure A.21 Refinement control setting to change (subsection of User Parameters from Figure A.20) for fitting r_{min}. *What?* and *How?* are automatically adjusted to the proper settings when the program is run.

As is apparent in Figure A.22 (a), the experimental $G(r)$ is very nonlinear with a large number of unphysical oscillations in the hard-sphere region. The linear fit to $G(r)$ (red line) is subtracted from the experimental data in this region below r_{min} and back-transformed into q-space using the inverse of Eqn. A.1 (red curve, Figure A.22 (b)). When subtracted from the initial $S(q)$ (black curve), the final $S(q)$ (blue curve) now oscillates well around $S(q) = 1$. If this corrected $S(q)$ is Fourier transformed to $G(r)$, the small-r region matches that of the previous fit with small additional ripples added due to termination error (Figure A.22 (c)), and the behavior of $G(r)$ above r_{min} is not altered.

It should be noted that curvature removal is performed during all stages of analysis within *Sq_Curvature.vi*, not just when the value of r_{min} is set. Once the unphysical features are removed from $G(r)$, any best fit to this now smoothed line results in approximately the same line. As a result, each of the steps described below begin with the original input $S(q)$ and an appropriate curvature removal is performed at the end. The previous discussion highlights this process in the context of setting a single parameter.

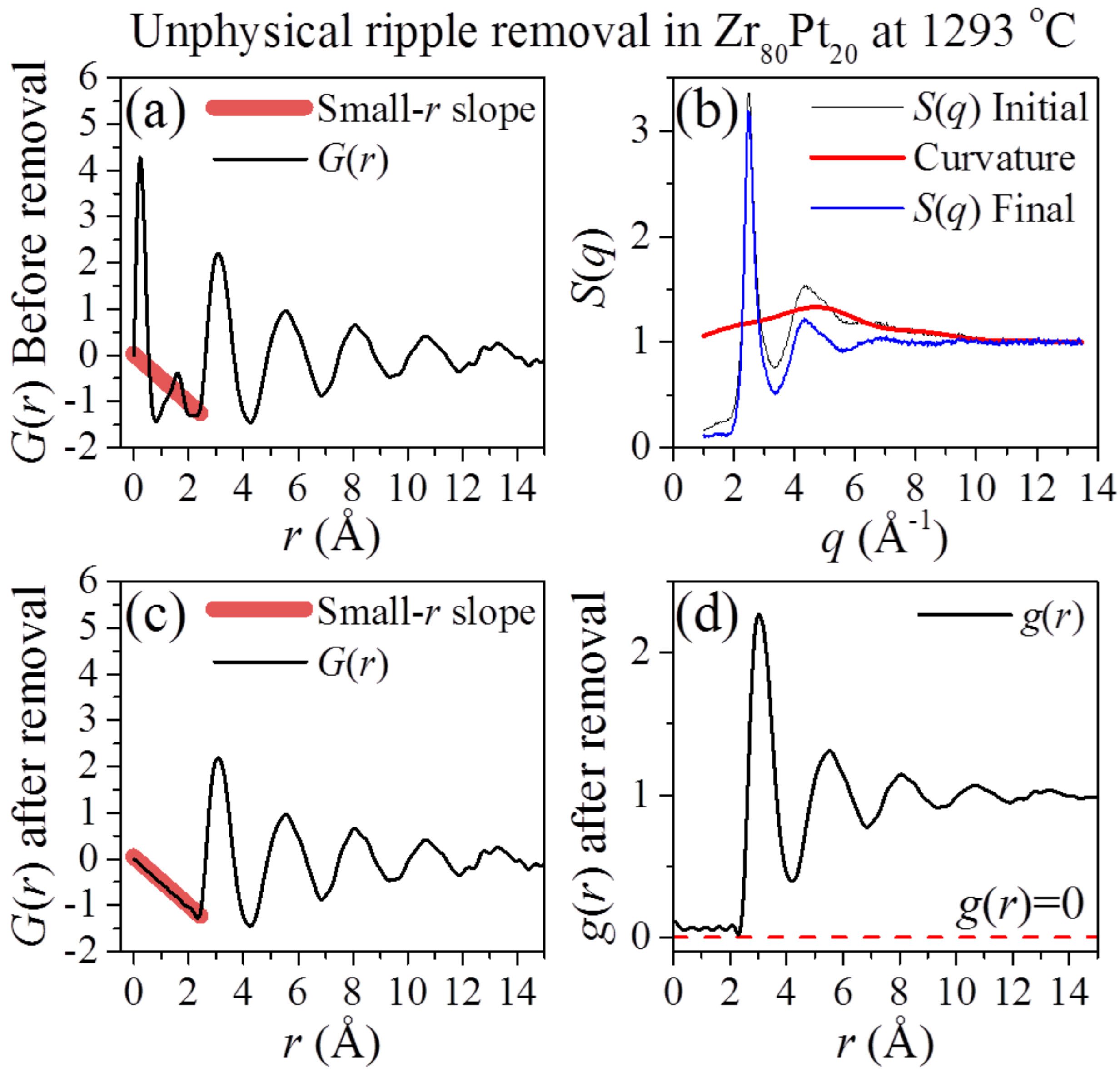

Figure A.22 (a) $G(r)$ transformed from the initial $S(q)$ of liquid $Zr_{80}Pt_{20}$ at 1293°C using Eqn. A.1. The red line is a linear fit to the small-r region below r_{min} determined from a minimization of *PDFGauge*. (b) Initial $S(q)$ (black line) with the Fourier transformed unphysical ripples from (a) (red line) and final $S(q)$ with the curvature subtracted (blue). (c) $G(r)$ from Fourier transform of $S(q)$ after unphysical ripples have been subtracted. (d) $g(r)$ after unphysical ripples have been subtracted.

If Fourier transforms are performed on this $S(q)$ using the experimentally measured density, $g(r)$ often does not oscillate around $g(r) = 0$ (Figure A.22 (d)). This deviation can be attributed to the secondary scattering of neutrons from the environment, as previously discussed. In order to fully remove this contribution and put the data on an absolute scale, a two-step sequence is performed (Figure A.23).

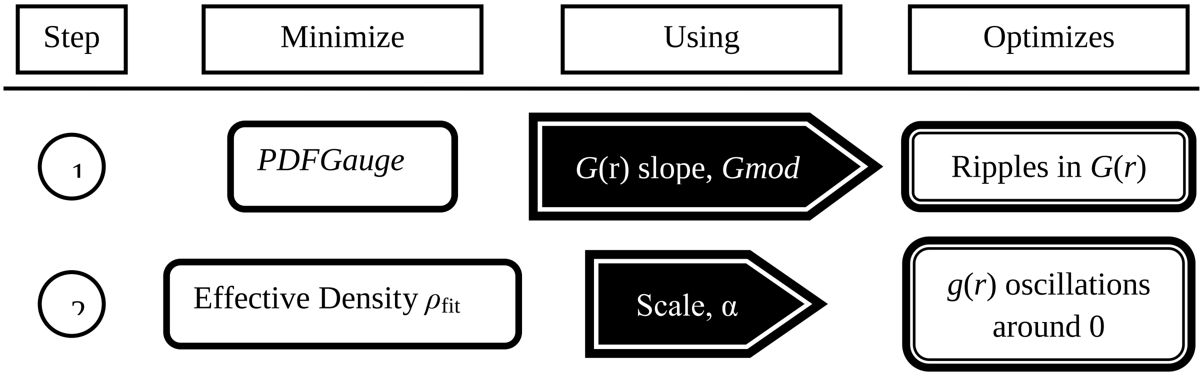

Step	Minimize	Using	Optimizes
1	*PDFGauge*	*G*(r) slope, *Gmod*	Ripples in *G*(*r*)
2	Effective Density ρ_{fit}	Scale, α	*g*(*r*) oscillations around 0

Figure A.23 Two steps used in properly scaling *S*(*q*).

The first step applies a multiplicative factor, *Gmod*, to the small-*r* slope of G(*r*) such that below r_{min}, $G(r) = -4\pi r\rho_0 \times G_{\text{mod}}$. This modifies the effective density calculated from the slope of this region. By minimizing *PDFGauge* with respect to *Gmod*, a best fit line is found that minimizes the magnitude of the ripples. Within the program, set *Refinement Steps* to *PDFGauge – Gmod*. When the program is run, *Minimize What?* and *Minimize How?* will automatically adjust to *PDF Gauge* and *Gmod*, respectively (Figure A.24). *Gmod* starts at a value of 1, representing an unmodified slope.

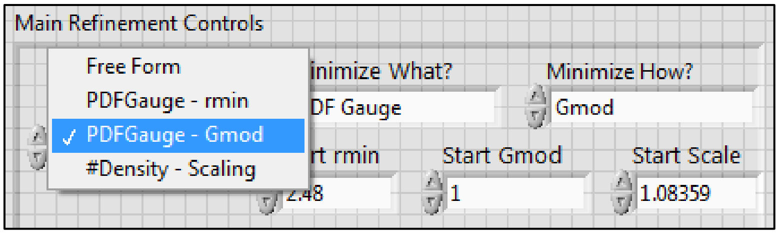

inimize What? DF Gauge
Minimize How? Gmod
rt rmin 2.48
Start Gmod 1
Start Scale 1.08359

Figure A.24 Refinement control setting to change (subsection of User Parameters from Figure A.20) to minimize small-*r* ripples in *G*(*r*) using a scaling factor on the slope, *Gmod*. *What?* and *How?* are automatically adjusted to the proper settings when the program is run.

Once the ripples are minimized by manually adjusting the slope of *G*(*r*), the second refinement step applies a multiplicative scaling factor, α, to *S*(*q*). This factor propagates through into *g*(*r*). This parameter is adjusted until the difference between the effective density, ρ_{fit}, and the experimental density, ρ_0, is minimized, forcing *g*(*r*) to oscillate around *g*(*r*)=0 below r_{min}. Within the program, set *Refinement Steps* to *#Density – Scaling*. When the program is run, *Minimize What?* and *Minimize How?* will automatically adjust to *PDF Gauge* and *rmin*, respectively (Figure A.25).

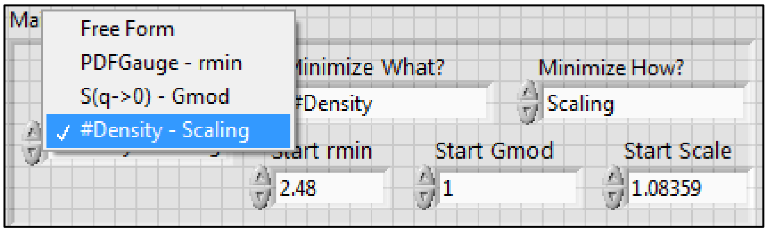

inimize What? #Density
Minimize How? Scaling
art rmin 2.48
Start Gmod 1
Start Scale 1.08359

Figure A.25 Refinement control setting to change (subsection of User Parameters from Figure A.20) to force *g*(*r*) to oscillate around 0 using a scaling factor on the total *S*(*q*), α. *What?* and *How?* are automatically adjusted to the proper settings when the program is run.

With all corrections implemented, the final output is presented in Figure A.26. Both *S*(*q*) and *g*(*r*) now display the expected physical behaviors with *S*(*q*) oscillating around 1 for the entire

q-range with little to no curvature evident, and $g(r)$ oscillating around 0 in the hard-sphere region.

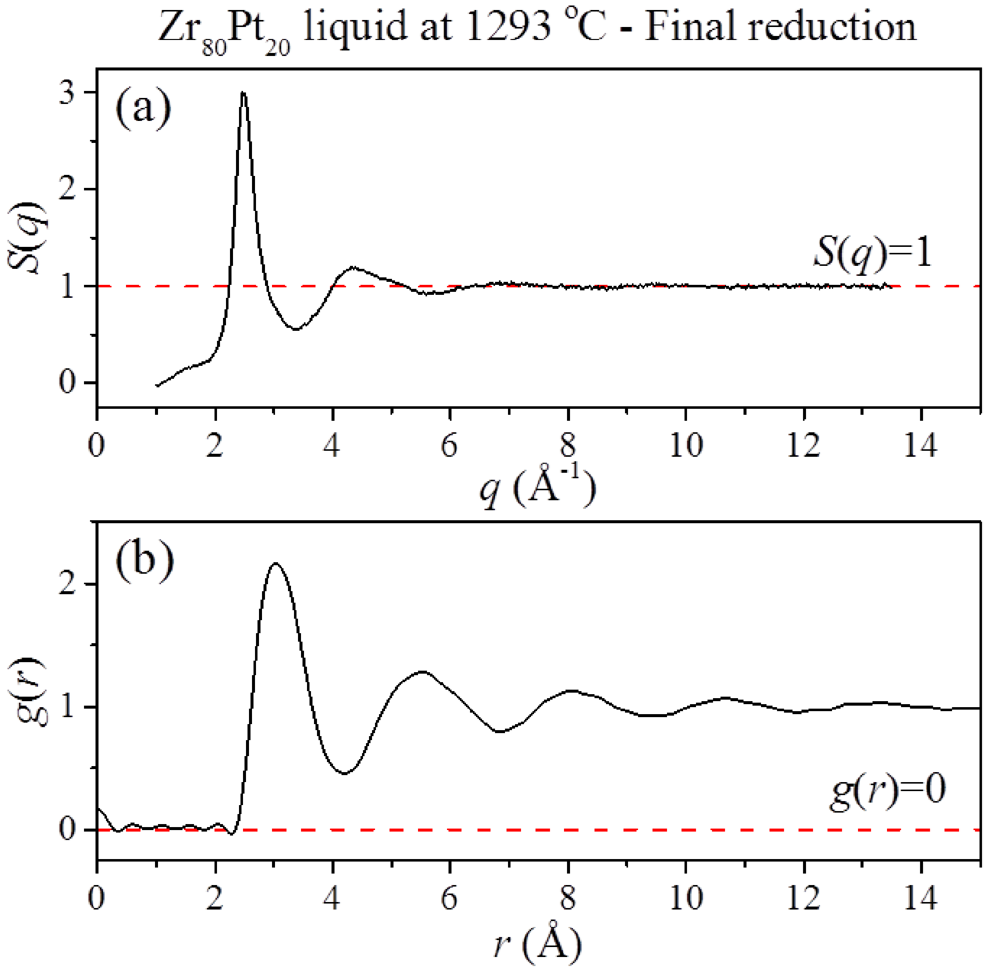

Figure A.26 Final output of Zr$_{80}$Pt$_{20}$ liquid from neutron scattering after all refinement steps for (a) $S(q)$ and (b) $g(r)$. $S(q)$ oscillates around 1 at large-q with no apparent curvature; $g(r)$ oscillates around 0 at small-r.

These techniques are not exclusive to the neutron analysis, but are also useful for correcting high-energy X-ray scattering as well. In order to test the consistency of this method, these steps were performed on Zr$_{76}$Ni$_{24}$ liquid structures at 1085 °C that were acquired on two separate WU-BESL experiments (BESL 2010 and BESL 2013). After using *X-ray Batch.vi* to reduce these data, a discrepancy was noted in the amplitudes of $S(q)$ of what should be identical structure factors (Figure A.27 (a)). Similarly, neither *g*(*r*) oscillated around 0 and furthermore, neither oscillated around the same value (Figure A.27 (b)). When using data from the same experiment, these deviations are likely similar in all scans, but in order to compare between separate experiments, this is not sufficient. Using the steps described in Figure A.23, the two independent measurements were nearly identical when placed on the same absolute scale. Only minimal deviations are observed when a difference is taken between the two final outputs (blue curves in Figure A.27 (c-d)).

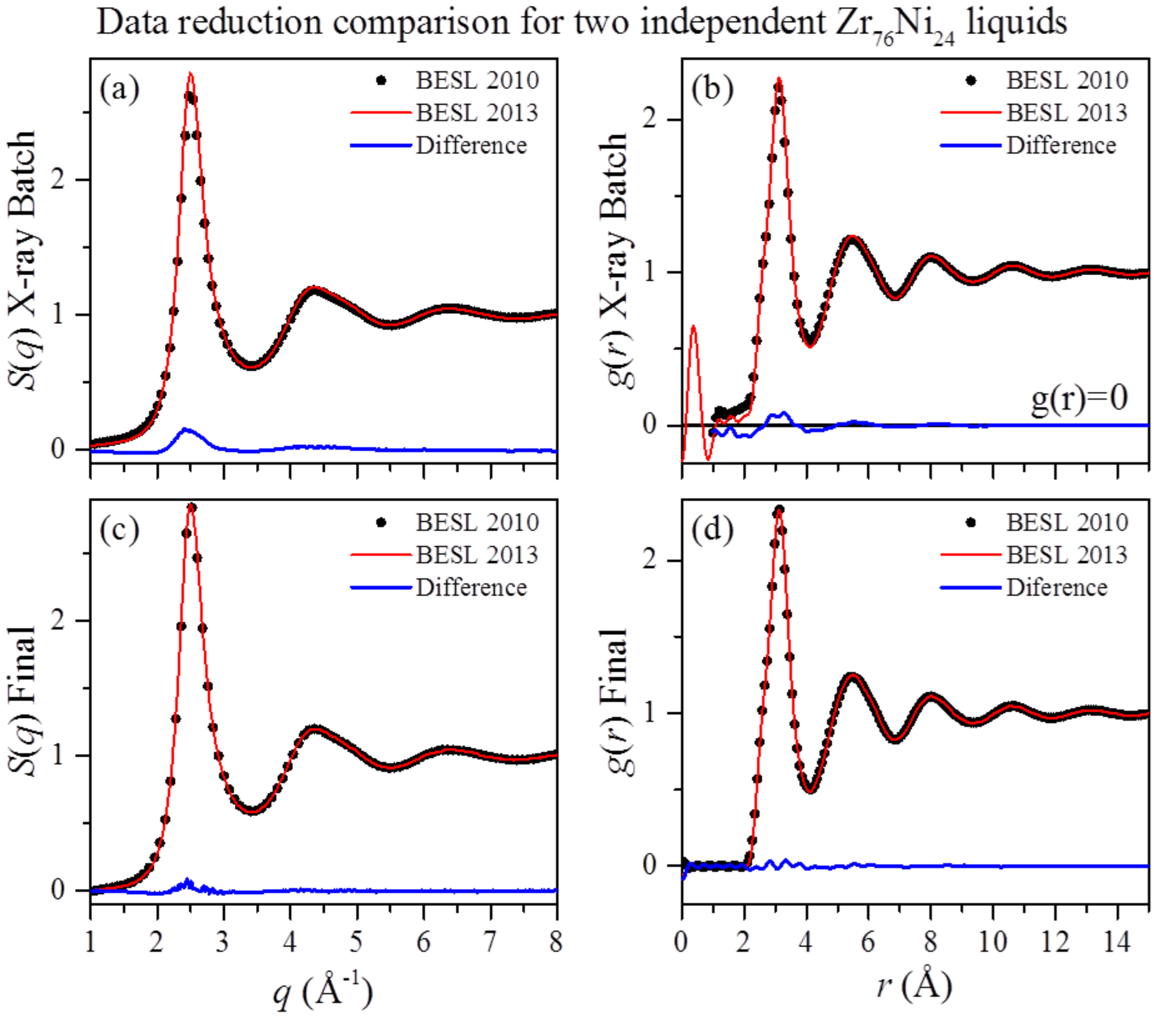

Figure A.27 Reduction of a $Zr_{76}Ni_{24}$ liquid at 1085 ^{o}C from two independent levitation experiments. (a) *S*(*q*) and (b) *g*(*r*) using only X-ray Batch. (c) *S*(*q*) and (d) *g*(*r*) after using the steps in Figure A.23 to put both experimental data sets on an absolute scale.

A.8 References

[1] J.C. Bendert, C.E. Pueblo, S. Veligati, N.A. Mauro, K.F. Kelton, *International Journal of Thermophysics* **35**, 1687 (2014).

[2] G. Placzek, *Physical Review* **86**, 377 (1952).

[3] P.F. Peterson, M. Gutmann, T. Proffen, S.J.L. Billinge, *Journal of Applied Crystallography* **33**, 1192 (2000).

[4] T. Egami, S.J.L. Billinge, *Underneath the Bragg Peaks - Structural Analysis of Complex Materials*, Pergamon, 2003.

[5] K. Page, C.E. White, E.G. Estell, R.B. Neder, A. Llobet, T. Proffen, *Journal of Applied Crystallography* **44**, 532 (2011).

[6] P.F. Peterson, E.S. Božin, T. Proffen, S.J.L. Billinge, *Journal of Applied Crystallography* **36**, 53 (2003).

[7] J. Kiefer, *Proceedings of the American Mathematical Society* **4**, 502 (1953).

[8] J.C. Bendert, N.A. Mauro, K.F. Kelton, *Journal of Applied Crystallography* **46**, 999 (2013).

Appendix B: Generic Templates for Neutron Analysis

The details in this appendix describe the scripts used in the NOMAD 2014 data reduction. A majority of these scripts were written by J. Neuefeind and are described here for clarity.

B.1 General Templates

Templates specific to NOMAD 2014 have been described in Section A.6, but for future experiments there are many other parameters that may require modification than just those described in those sections. Example templates are stored under:

~/SNS/NOM/IPTS-11941/shared/GeneralScripts_OctoberNOMAD_20150430

~/SNS/NOM/IPTS-12581/shared/abskorr/GeneralScripts_OctoberNOMAD_20150430

B.1.1 Initial Data Reduction Template

Figure B.1 represents the template *bingr_abs_9999_general.bat*. In addition to the standard parameters described in Section 2.10.7, there are several additional required parameters that are specific to each individual experiment (listed in Table B.1).

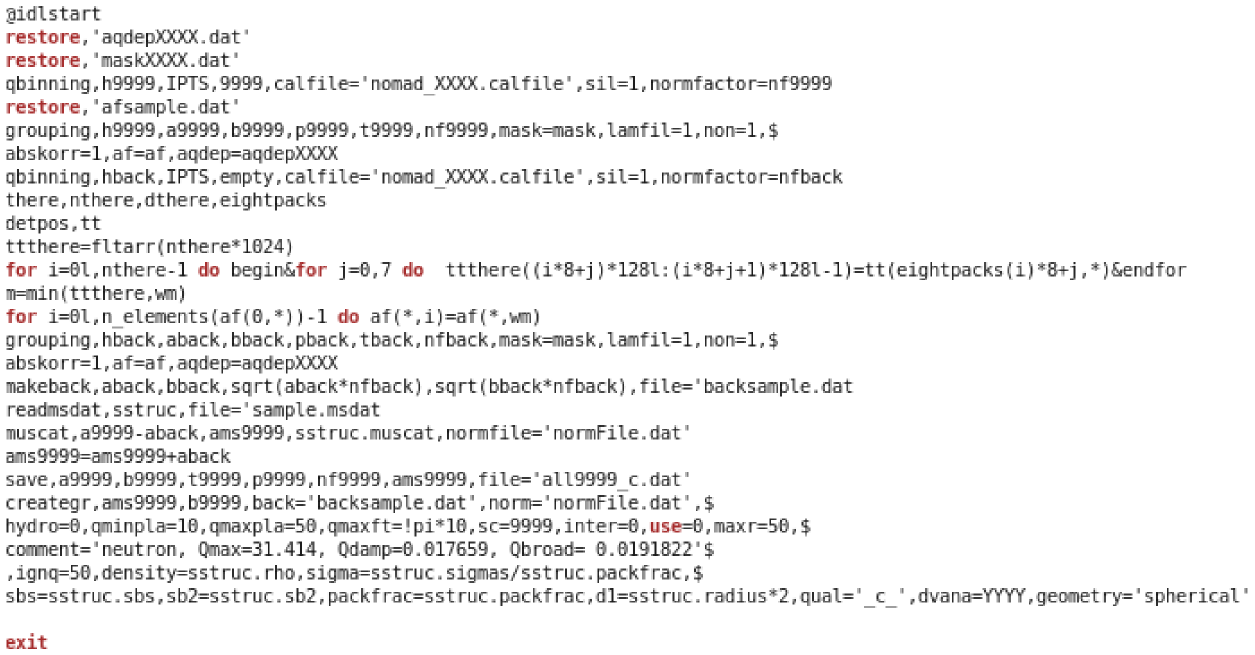

```
@idlstart
restore,'aqdepXXXX.dat'
restore,'maskXXXX.dat'
qbinning,h9999,IPTS,9999,calfile='nomad_XXXX.calfile',sil=1,normfactor=nf9999
restore,'afsample.dat'
grouping,h9999,a9999,b9999,p9999,t9999,nf9999,mask=mask,lamfil=1,non=1,$
abskorr=1,af=af,aqdep=aqdepXXXX
qbinning,hback,IPTS,empty,calfile='nomad_XXXX.calfile',sil=1,normfactor=nfback
there,nthere,dthere,eightpacks
detpos,tt
ttthere=fltarr(nthere*1024)
for i=0l,nthere-1 do begin&for j=0,7 do  ttthere((i*8+j)*128l:(i*8+j+1)*128l-1)=tt(eightpacks(i)*8+j,*)&endfor
m=min(ttthere,wm)
for i=0l,n_elements(af(0,*))-1 do af(*,i)=af(*,wm)
grouping,hback,aback,bback,pback,tback,nfback,mask=mask,lamfil=1,non=1,$
abskorr=1,af=af,aqdep=aqdepXXXX
makeback,aback,bback,sqrt(aback*nfback),sqrt(bback*nfback),file='backsample.dat
readmsdat,sstruc,file='sample.msdat
muscat,a9999-aback,ams9999,sstruc.muscat,normfile='normFile.dat'
ams9999=ams9999+aback
save,a9999,b9999,t9999,p9999,nf9999,ams9999,file='all9999_c.dat'
creategr,ams9999,b9999,back='backsample.dat',norm='normFile.dat',$
hydro=0,qminpla=10,qmaxpla=50,qmaxft=!pi*10,sc=9999,inter=0,use=0,maxr=50,$
comment='neutron, Qmax=31.414, Qdamp=0.017659, Qbroad= 0.0191822'$
,ignq=50,density=sstruc.rho,sigma=sstruc.sigmas/sstruc.packfrac,$
sbs=sstruc.sbs,sb2=sstruc.sb2,packfrac=sstruc.packfrac,dl=sstruc.radius*2,qual='_c_',dvana=YYYY,geometry='spherical'

exit
```

Figure B.1 Template *bingr_abs_9999_general.bat*. Parameters for quick-replacement for future experiments are listed in Table B.1.

Table B.1 Parameters for quick-replacement in *bingr_abs_9999_general.bat* (Figure B.1).

Template Representation	Description
9999	Run number for appropriate sample scan
XXXX	Run number for appropriate diamond scan
IPTS	Proposal number for the experiment of interest – do not include decimal points
sample	Filename of the appropriate absorption/multiple scattering simulation
empty	Run number for appropriate empty chamber scan
normFile	Filename of the appropriate vanadium normalization (case sensitive)
YYYY	Diameter of the vanadium standard used in normFile

Due to the consistency of the majority of these parameters across a single experiment, once these parameters are set there is very little need to change them. These parameters are listed in the order in which they appear in the template.

The run number (*9999*) is typically a 5-digit value that is incremented by one each time the secondary neutron shutter is opened. In principle, this script can be run on any scan including empty chamber and diamond scans, but this script is specifically designed with the assumption that *9999* represents a sample acquisition.

The diamond scan (*XXXX*) is typically measured once over the course of an experiment. It should be noted that the standard filenames used in data reduction (Table A.2) are named according to the file-naming convention in use during the end of 2014. It is possible that the standard filenames will be redefined in the future, in which case the user is advised to find all instances of *XXXX* and take note when a filename is being called instead of a run number. If it is a filename, it will be bracketed by single quotes and should be updated to the new naming convention.

The proposal number (*IPTS*) is a 4-5 digit number which represents the ID number associated with the beamtime proposal. If the IPTS number is unknown, this can be accessed from the ORNL guest portal (http://user.ornl.gov) under *proposals*. The ID number listed next to the individual proposals will often have a decimal value in addition to the 4-5 digit number which represents a specific visit. Typically, this value is listed as ".1" as most experiments are completed in a single site visit. For example, the ID number 11941.1 represents the data taken during NOMAD 2014 in September, and 11941.2 represents the data taken in October. For the purposes of replacing *IPTS* in the template, only the base value is used (11941).

The *sample* filename represents the base filename used in creating an absorption and multiple scattering correction file from an initialization file named *sample.ini*. This parameter has already been discussed elsewhere (Section A.4).

The value of *empty* represents the scan number of the empty chamber used to correct the data, again typically a 5-digit number. In the case of NOMAD 2014, a single sample carousel was loaded and the NESL never broke vacuum. As such, the sample environment did not change and only a single empty chamber scan was acquired for the experiment. During future experiments, it is possible multiple pumping cycles will occur. In this case, it is advised to use a separate *empty* run corresponding to the most recent scan during the same pumping cycle. This value should also be updated when producing a normalization file (Section A.5).

The normalization file, *normFile*, should be updated for the individual vanadium standard used in correcting the data. During NOMAD 2014, a single vanadium standard was acquired so only one normalization file was created. If the *q*-range or energy filter is modified to try to remove absorption features, a new normalization file needs to be created for each setting.

The diameter of the vanadium standard, *YYYY*, should be updated to match the vanadium scan used to create *normFile*.

B.2 Standard IDL Functions

Throughout the templates described in this dissertation, many different functions are called to assist with the data reduction. Some of these are standard functions that are automatically associated with the IDL language, but many have been developed by J. Neuefeind specifically for use with NOMAD data reduction.

B.2.1 Using IDL Functions

Most of the scripts described in this dissertation are written in a text editor (typically gedit) and are saved as either *batch* (**.bat*) or *program* (**.pro*) files. For the purposes of executing scripts in IDL in the context of standard data reduction, it makes no difference which extension is used. However, program files can be more easily called within a higher-order IDL script.

In order to execute a prepared IDL script, the following commands are used:

```
$ idl script.bat
```

or

```
$ idl script.pro
```

These commands are entered into a traditional linux terminal where the current directory matches that of the file of interest, and the symbol *$* represents the end of a traditional command prompt. No leading space is required to be input by the user as in the following more detailed example:

```
[mjohnson@biganalysis05 Zr80Pt20_5_Run33243_1293C]$ idl script.bat
```

The use of *$* simplifies the representation of using the terminal command line. If working within the program IDL (accessed by $ idl), the leading symbol will instead be *IDL>* .

Within an IDL script, other scripts can be called by prefixing the filename with @ and excluding the file extension. For example, the majority of the scripts described within this dissertation begin with the line:

```
@idlstart
```

Once the main script is loaded using the commands described above, the script idlstart.pro is run (Figure B.2). This script adds a second path accessible by the remainder of the scripts by including the location where all of the NOMAD-specific reduction scripts are stored (~zjn/idl).

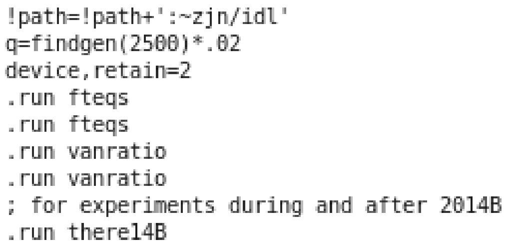

```
!path=!path+':~zjn/idl'
q=findgen(2500)*.02
device,retain=2
.run fteqs
.run fteqs
.run vanratio
.run vanratio
; for experiments during and after 2014B
.run there14B
```

Figure B.2 IDL script *idlstart.pro*.

The second line of this script defines the default values of *q* to be used in subsequent data reduction. The command *.run* compiles the subsequent functions and loads their dependencies into memory for more rapid access. The command *;* is the IDL designator for code commenting. This startup script will typically be created by the instrument scientist of the experiment and can be found in the *autoNOM* folder after the experiment is underway. There should not be a reason to modify this script, but the details are described here to provide greater understanding of the entire process.

It should be noted at this point that spaces are never used to distinguish between a function and its callees. For example, in order to print a value to the screen during operation, the command *print* is used in the following format:

```
IDL> x=1
IDL> print,x
     1
IDL>
```

In this case, the command is not *x*, *print x*, or *print(x)*, but instead contains a comma between the command and the variable of interest.

In order to import IDL-generated files, the command *restore* is used with the filename enclosed in single quotes, as discussed in Section B.1.1. This is a common method built into IDL to recreate a sequence of variables that were saved from the IDL interface, remembering their names in addition to their values. In order to see a list of variables imported when using *restore*, the qualifier */ver* can be added to the end to produce a *verbose* output following the command:

```
IDL> restore,'all33243_c.dat',/ver
% RESTORE: Portable (XDR) SAVE/RESTORE file.
% RESTORE: Save file written by mjohnson@biganalysis05.sns.gov, Fri Mar 13 10:08:43 2015.
% RESTORE: IDL version 7.1.1 (linux, x86_64).
% RESTORE: Restored variable: A33243.
% RESTORE: Restored variable: B33243.
% RESTORE: Restored variable: T33243.
% RESTORE: Restored variable: P33243.
% RESTORE: Restored variable: NF33243.
% RESTORE: Restored variable: AMS33243.
IDL>
```

If more information is needed about the individual functions restored, further information can be gained using the *help* command:

```
IDL> help,A33243
A33243          FLOAT     = Array[2500]
IDL>
```

In this case, the variable A33243 restored from *all33243_c.dat* contains an array of 2500 float values.

In order to plot in IDL, the command *plot* is used. In order to make a plot of Y vs. X, the following command is used:

IDL> plot,X,Y

There are many qualifiers that can be added to the function call, far too many to detail in this appendix. The commonly used qualifiers used in this dissertation are described here, but the online help files at www.exelisvis.com contain more detailed information.

Of particular interest while reducing data as described in this dissertation is the ability to add a second plot on top of the first. This is done using the command *oplot*. This function will take most of the qualifiers that *plot* uses with the exception of axis parameters.

When adding additional curves to a plot, it is necessary to be able to distinguish between each of them. This can be accomplished by altering the point style (*ps*=*integer*) or line color (*color*=*integer* or *color*=’*hexcode*’x). The value of *integer* is an integer value that selects from a pre-determined table of either point styles or colors to use. A point style of *integer* = 0 represents a line, while a color of *integer* > 0 scales the color from white to red (higher values are darker) and *integer* < 0 scales the color from white into blue (more negative values are darker) and can range into the hundreds. Alternatively, a *hexcode* can be specified if more than 3 colors are necessary. A list of exact hexcodes are given for IDL from the description of *!COLOR* (http://www.exelisvis.com/docs/constant_system_variable.html), but the values listed there do not match the output using the tables defined at NOMAD. If the *hexcode* listed online is “rotated” by 2, then the values will work in the NOMAD context (i.e., gold is FFD700 from the reference, but in practice it requires the code *color*=’00FFD7’x).

Another qualifier commonly used in visualizing the data during reduction involves properly scaling the axes. This is accomplished using *xra* = [min,max] and *yra* = [min,max] to set the x and y axis ranges, respectively.

Using the parameters described above, a combined example is given as follows:

```
IDL> restore,'all33243_c.dat'
IDL> @idlstart
IDL> plot,q,A33243,xra=[0,20],yra=[0,0.025]
IDL> oplot,q,A33243/2+.01,color='00D7FF'x,ps=1
IDL>
```

This produces the plot shown in Figure B.3. The first line restores a previously saved file named *all33243_c.dat*. The second line runs the script *idlstart.pro* contained within the operating folder. This script, as described in Figure B.2, creates the variable *q* containing the same number of data points as the variables restored from *all33243_c.dat*. The third line plots the variable *A33243* for $0 < X < 20$ and $0 < Y < 0.025$ using the default white line. The fourth line adds a second curve to the plot using mathematical operators to modify the variable *A33243*, changing the color to gold, and changing the point style to “+”.

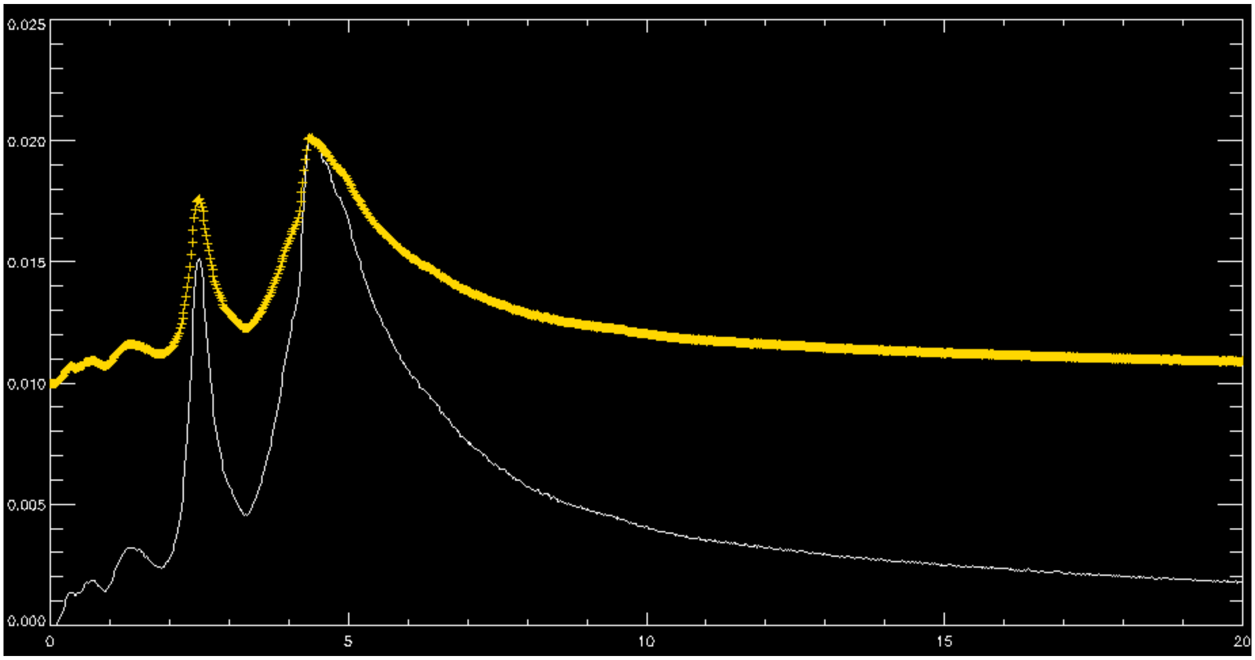

Figure B.3 Example of plotting options commonly used in data reduction scripts.

B.2.2 NOMAD Specific Functions

The previous section described general functions used in the NOMAD data reduction process. In this section, specific functions developed by J. Neuefeind are described. There are several scripts described throughout this dissertation, but the majority of the functions are contained within *bingr_abs_9999_general.bat* script (Figure B.1) and exceptions will be dealt with on an individual basis. Some functions take many inputs and as such will not fit on a single line in a text editor. Those that overflow have an extra *$* symbol on the end of the line signifying that the following line is a continuation of the previous (see examples of *qbinning* and *grouping*). If the information described here is insufficient, the functions are all stored on the ORNL servers under ~SNS/users/zjn/idl. Many also have defined help files, which can be accessed using

```
IDL> function,/help
```

where *function* is the function name of interest.

The function *qbinning* performs automatic binning according to the pre-defined reduction procedures. In order of listing in Figure B.1, the variables are described in Table B.2:

Table B.2 Parameters used in *qbinning*.

Parameter	Description
h9999	Output histogram variable name. In the case of the background *qbinning*, this is replaced with *hback*
IPTS	Proposal number of the experiment
9999	Sample scan number. This is replaced by the background scan number during the second call of *qbinning*
calfile	Calibration file based on the diamond sample from scan number *XXXX*
sil	Silent or verbose output (only affects visual displays during processing)
normfactor	Output normalization factor specific for scan *9999*. This value is an internal calculation and is used in combination with subsequent scripts

Within *bingr_abs_9999_general.bat*, *qbinning* is called twice. The first time requires an input of the sample scan of interest, while the second call performs similar operations on the specified background file. In the case of the background file, the value *nf9999* when calling *normfactor* is replaced by *nfback*.

The function *grouping* combines all of the detected events in the detector file and puts them into several appropriate variables. As a result, there are multiple “outputs” from this function. This is also the function that performs the absorption correction as well as filters by wavelength or *q*. Each of the parameters designated in Figure B.1 is described in Table B.3, as well as some of the other common additions:

Table B.3 Parameters used in *grouping*.

Parameter	Description
h9999	Input histogram generated from *qbinning*
a9999	All neutron events not excluded by mask summed together as a function of the predefined *q* vector. This is the most-used variable generated by *grouping*
b9999	Intensity sorted by bank. NOMAD typically uses 6 generic banks, which are defined as a series of packs of tubes
p9999	Intensity sorted by packs as a function of *q*. Each pack consists of a number of individual tubes.
t9999	Intensity sorted by tubes as a function of *q*. This is the smallest unit of division
nf9999	Normalization factor generated from *qbinning*
mask	Detector mask file based on the variable mask restored from *maskXXXX.dat*
lamfil	Filter by wavelength on (1) or off (0). Only used if *lamlim* is defined.
lamlim	Defines the wavelength range to use. Default values are *lamlim=[0.1,2.9]* in Angstroms
non	Specifies nonlinear treatment of banks
abskorr	Perform an absorption correction or not
multkorr	Perform a multiple scattering correction or not. Currently this function in *grouping* is not utilized and the multiple scattering correction is performed elsewhere. If undefined in the function call as is usual, it is turned off
af	Input parameter of the absorption factor. The variable name *af* is restored from *restore,'afsample.dat'* previously
aqdep	Input parameter of the standard detector file *aqdepXXXX*, previously restored
hz30	A parameter never used during NOMAD 2014, but appears to be related to the maximum wavelength range accessible in the detectors.

Similar to *qbinning*, *grouping* needs to be performed for both the sample and the background file. For the background, all parameters are the same as for the sample except with *9999* replaced with *back*.

The function *there*, *detpos*, and subsequent *for* loops are standard functions that search for which tubes are present in the experiment and determine their relative positions. The limits shown in Figure B.1 were correct during the NOMAD 2014 run, but this is a parameter that may change with time. The details should be discussed with the instrument scientist for future experiments.

The function *makeback* takes variables generated from *grouping* and saves a copy of the generated background file for future use so the calculation doesn't need to be performed every time. The variables are defined in Table B.4:

Table B.4 Parameters used in *makeback*.

Parameter	Description
aback	Variable generated by *grouping* containing the background from all detectors
bback	Variable generated by *grouping* containing the background by bank
sqrt(aback*nfback) = ebacka	Error estimate of *aback*
sqrt(bback*nfback) = ebackb	Error estimate of *bback*
file='backsample.dat	Specifies output filename based on the sample filename

The function *readmsdat* simply reads in a file of the form **.msdat*, which contains all of the sample specific information generated during the processing of the absorption and multiple scattering simulation. The variables are defined in Table B.5:

Table B.5 Parameters used in *readmsdat*.

Parameter	Description
sstruc	Desired variable name generated by *readmsdat*
file='sample.msdat	Defines the filename to be opened

The function *muscat* performs the multiple scattering and secondary scattering corrections on the sample. If a parameter for secondary scattering, *msi*, is not specified, then the default value of *msi* = 0.25 is used. This value is based on measurements of a typical sample environment used at NOMAD. The variables are defined in Table B.6:

Table B.6 Parameters used in *muscat*.

Parameter	Description
a9999–aback	Background-subtracted scattering intensity
ams9999	Output variable containing the modified scattering intensity
back=’backsample.dat’	Filename of the previously defined background file
norm=’normFile.dat’	Filename of the vanadium normalization file
msi=#	A specified value for secondary scattering. A value of 0 turns the correction off completely, and a value of 0.25 is based on a generic sample environment

The output *ams9999* from the multiple scattering function has been background subtracted. The subsequent functions do not assume a background correction has been performed, so when saving the data to file it is added back in. The background file is already saved, so it is a convenient way of storing the data. This is done using the command *ams9999=ams9999+aback*, and the command *save* takes any number of inputs to specify which variables should be stored. The final qualifier of *save* specifies the filename. If this filename is subsequently restored using *restore*, all of the variable names used in the inputs of *save* will be available for use.

The final function, *creategr*, takes all of the previously performed corrections and does the final normalizations required to build $S(q)$ and $g(r)$. In general, the majority of the parameters do not need to be adjusted. If a wavelength filter was applied, however, the maximum q must not be greater than that obtainable by backscatter ($2\theta=180^{\circ}$) at the minimum wavelength, $\lambda_{\min}$ given by:

$$q_{\max} = \frac{4\pi}{\lambda_{\min}} \sin\left(\frac{2\theta = 180^o}{2}\right) \qquad \text{B.1}$$

The variables for *creategr* are defined in Table B.7.

Table B.7 Parameters used in *creategr*.

Parameter	Description
ams9999	Scattering intensity with all corrections but not background subtracted
b9999	Scattering intensity by bank
back='backsample.dat'	Filename of the corrected background file
norm='normFile.dat'	Filename of the vanadium normalization file
hydro	Hydrogen correction for inelastic scattering as defined by Placzek [1]. A value of 0 turns this off
qminpla	Minimum *q* value used in fitting self scattering background, typically 10 Å
qmaxpla	Maximum *q* value used in fitting self scattering background, typically 50 Å but must be modified if a wavelength filter was used as specified in Eqn. B.1
qmaxft	Maximum *q* to Fourier transform. Typically 10π, but must be modified if a wavelength filter was used
sc	Scan number used in naming output files
inter	Interactive plotting during reduction on (1) or off (0). Adds many interruptions and is typically on only for debugging purposes
use	Specifies normalization behavior. use=1 uses high-*q* normalization while use=0 uses absolute normalization. A value of 0 is usual
maxr	Specifies the maximum *r* value in the Fourier transforms
comment ='text string'	Specifies a text string to include in a comments section in the output files
ignq	Specifies the minimum *q* to ignore. A value of 50 ignores up to $q = 1$ Å^{-1}. This is useful for cutting out extra noise
density	Specifies sample density for use in final conversion to *S*(*q*). The command *sstruc.rho* calls the defined variable *sstruc* from *readmsdat* and specifies the sub-parameter *rho*
sigma	Defines effective scattering cross section, scaled by the packing fraction. This is a variable stored in the msdat file as *sstruc.sigmas*
sbs	Effectively $<b>^2$ in units understood by *creategr*. This is a variable stored in the msdat file as *sstruc.sbs*
sb2	Effectively $<b^2>$ in units understood by *creategr*. This is a variable stored in the msdat file as *sstruc.sb2*
packfrack	Defines the packing fraction of the sample. This is a variable stored in the msdat file as *sstruc.packfrac* and is typically 1

d1	Diameter of the sample. This is a variable stored in the *msdat* file as *sstruc.radius*
qual	Defines a string to add to the output filenames. Standard formatting is to use qual=’_c_’
dvana	Defines the diameter of the vanadium standard used. Defined as *YYYY* in the template
geometry	A string defining the geometry of the vanadium standard. This will accept either ‘*spherical’* or ‘*cylindrical’*

It should be noted that the units of $<b>^2$ and $<b^2>$ stored in the *msdat* file are not consistent with values obtained from standard tables. If the standard units are calculated with *b* in units of femtometers (fm), then $<b>^2$ is larger by 10^4 and $<b^2>$ is larger by 10^2.

Some additional standard functions created specifically for NOMAD include both reading and writing standard text files. The function *rstd* takes inputs of *X*, *Y*, and a *filename*. This function loads the specified file and assigns the first column encountered to the variable *X*, and the second column to the variable *Y*. In a similar manner, the function *wstd* will take inputs of *X*, *Y*, and *filename*. In this case, the variables *X* and *Y* are existing variables within the workspace and *filename* is the specified output filename. *Y* can either be a single array or a mathematical function. In the following example, the file named *testIn.dat* is imported, creating the parameters *column1* and *column2*. They are then modified and saved to the file *testOut.dat*, specifying the output should be twice the input:

```
IDL> rstd,column1,column2,’testIn.dat’
IDL> wstd,column1,2*column2,’testOut.dat’
```

These functions are used extensively in the template *ress_9999.dat* to load in the original *S*(*q*)-1 file created by *creategr* and output a new *S*(*q*)-1 modified by secondary scattering.

B.3 References

[1] G. Placzek, *Physical Review* **86**, 377 (1952).

Appendix C: LabVIEW Programs

This appendix describes in detail the various LabVIEW tools that I have designed and created to aid in data reduction and analysis. Information on things such as expected file formatting and the intended procedure will be laid out. All programs were written using 64-bit LabVIEW 2014 and are not compatible with earlier versions. The compatibility with 32-bit LabVIEW 2014 has not been tested but it is expected to work.

C.1 *NOMAD_File_Convert.vi*

The data files that are output from the procedures and scripts used to reduced time-of-flight (TOF) neutron diffraction from the NOMAD beamline [1] are saved in a **.SQ.dat* format that are not compatible with existing file importing protocols used in our in-house LabVIEW analysis suite for X-ray diffraction [2]. Rather than modifying the import protocols, this program was designed to import NOMAD output files and convert them into appropriate **.S*.csv formatted files.

In brief, this program allows for specific file extension filtering and imports a single or multiple NOMAD formatted file containing two columns (q and $S(q)$-1), that are un-evenly *space*-delimited. It converts them into a comma-delimited file containing three columns: q, $S(q)$, and a user specified percent error. It saves three header lines to be consistent with X-ray $S(q)$ file formatting: the first contains the run number, the second contains only a #, and the third contains the column labels.

This program expects an input file name in the following format:

NOM_#####_TextQualifiers_SQ.dat ,

where *#####* represents a 5-digit *run number* corresponding to a specific scan. *TextQualifiers* are specified in the *bingr* scripts (Section A.6, Appendix B). The run numbers must be the first set of sequential digits in the filename.

As of the writing of this dissertation, NOMAD files are saved with exactly 5 header lines (all starting with a # symbol). The second line of the header contains the filename and is specifically used during the file conversion. Following the header, there are two columns of data. The first column is the momentum transfer, *q* (Å^{-1}), and the second is the total structure factor, *S*(*q*)-1, which oscillates around 0. The delimiting between column 1 and column 2 is a non-standard sequence of spaces which varies by row.

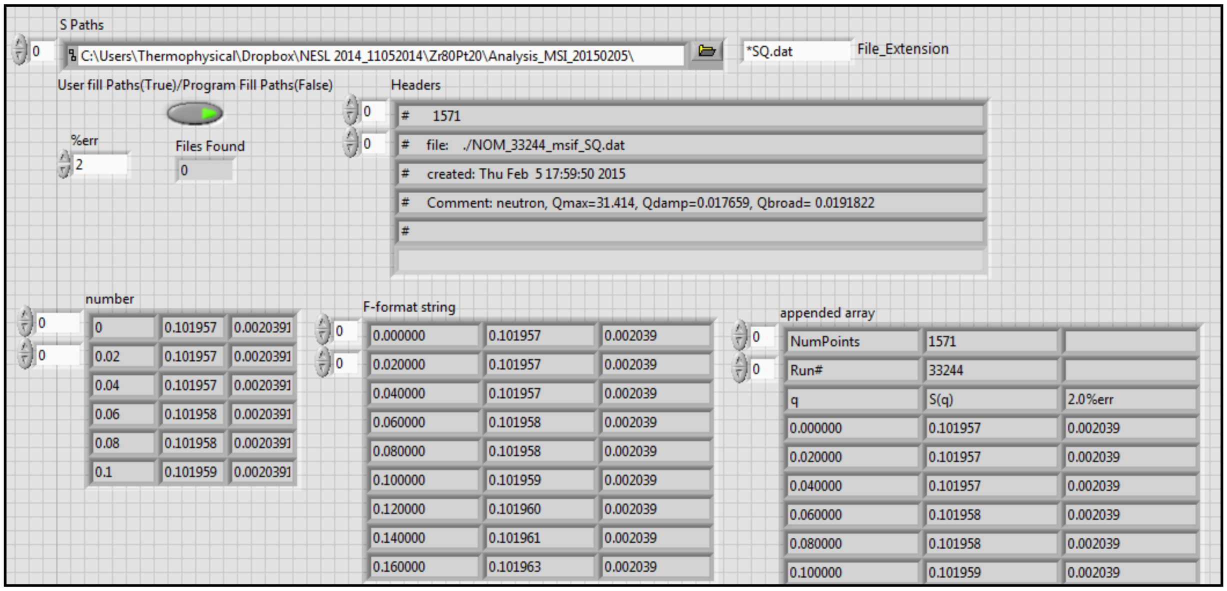

S Paths: C:\Users\Thermophysical\Dropbox\NESL 2014_11052014\Zr80Pt20\Analysis_MSI_20150205\

File_Extension: *SQ.dat

User fill Paths(True)/Program Fill Paths(False)

%err: 2

Files Found: 0

Headers

```
#    1571
#    file:    ./NOM_33244_msif_SQ.dat
#    created: Thu Feb  5 17:59:50 2015
#    Comment: neutron, Qmax=31.414, Qdamp=0.017659, Qbroad= 0.0191822
#
```

number

0	0.101957	0.0020391
0.02	0.101957	0.0020391
0.04	0.101957	0.0020391
0.06	0.101958	0.0020391
0.08	0.101958	0.0020391
0.1	0.101959	0.0020391

F-format string

0.000000	0.101957	0.002039
0.020000	0.101957	0.002039
0.040000	0.101957	0.002039
0.060000	0.101958	0.002039
0.080000	0.101958	0.002039
0.100000	0.101959	0.002039
0.120000	0.101960	0.002039
0.140000	0.101961	0.002039
0.160000	0.101963	0.002039

appended array

NumPoints	1571	
Run#	33244	
q	S(q)	2.0%err
0.000000	0.101957	0.002039
0.020000	0.101957	0.002039
0.040000	0.101957	0.002039
0.060000	0.101958	0.002039
0.080000	0.101958	0.002039
0.100000	0.101959	0.002039

Figure C.1 Example front panel of *NOMAD_File_Convert.vi*. Possible inputs are single or multiple file paths, a file extension filter, and an amount of relative error to consider for each point.

During the import process, the exact file extension can be specified (Figure C.1, upper right). This will filter file-types by specific sequence of characters, where * represents any text allowed. For instance, specifying **SQ.dat* will filter out all files that do not end with *SQ.dat*.

Once imported, the first 5 lines are separated from the data and the first sequence of numbers is extracted from the second line. If the filename follows the format indicated above, this should represent the *run number*. Due to inconsistent delimiters between data points in the two input columns, sequences of numbers are searched for and separated using regular expressions rather than a delimiter-based search. Once two columns have been successfully separated, $S(q)$-1 is converted into $S(q)$ and a relative amount of error specified by the user is included as a third column.

The output filename is modified from the input filename. The extension is stripped off and the final three characters are removed (representing "_SQ") and replaced with ".S.csv", consistent with the formatting of our in-house software for X-ray analysis.

C.2 *Sq_Curvature.vi*

This program contains the bulk of the neutron data reduction steps and has a large array of options to adjust for the interested user. The final analysis techniques described in this dissertation (Section A.7) have fixed most of the parameters as they were found to be self-consistent, however the whole array of options are left available for future testing and characterization.

This program expects an input file ending in **.S.csv* containing exactly three lines of header and at least two *comma*-delimited columns that contain q and an $S(q)$ that oscillates around 1 (i.e., specifically NOT $S(q)$-1). If there is a third column, this program expects it to contain the absolute error associated with each point in $S(q)$.

The outputs from this program are $S(q)$, $G(r)$, and $g(r)$ files containing three lines of header. The first line contains the final values of all refined parameters (described below). The second line contains a single “#”. The third line contains column header names. All files are output as *InputFilenameQualifier.type.dat*, where *InputFilename* is the full filename of the input file without file extensions, Qualifier is the user defined parameter *Add To Filename*, and type is either *S*, *G*, or *pdf*. The data are tab delimited with a file extension of **.dat*.

This program’s primary utility is to perform golden section searches [3] to optimize user-specified parameters by minimizing a user-specified constraint. Another key component of this program is the removal of unphysical oscillations in the small-r region of $g(r)$, as described in more detail in Section A.7. During the reduction, all output $S(q)$ files are re-scaled to a constant q-spacing of 0.02 Å^{-1} for proper subtraction of the Fourier transformed small-r ripples. The following sub-sections describe all of the possible input parameters as well as some of the details potentially relevant to the user.

C.2.1 User Parameters

There are many input parameters in this program, as shown in Figure C.2. Each parameter as named on the front panel will be given a brief description.

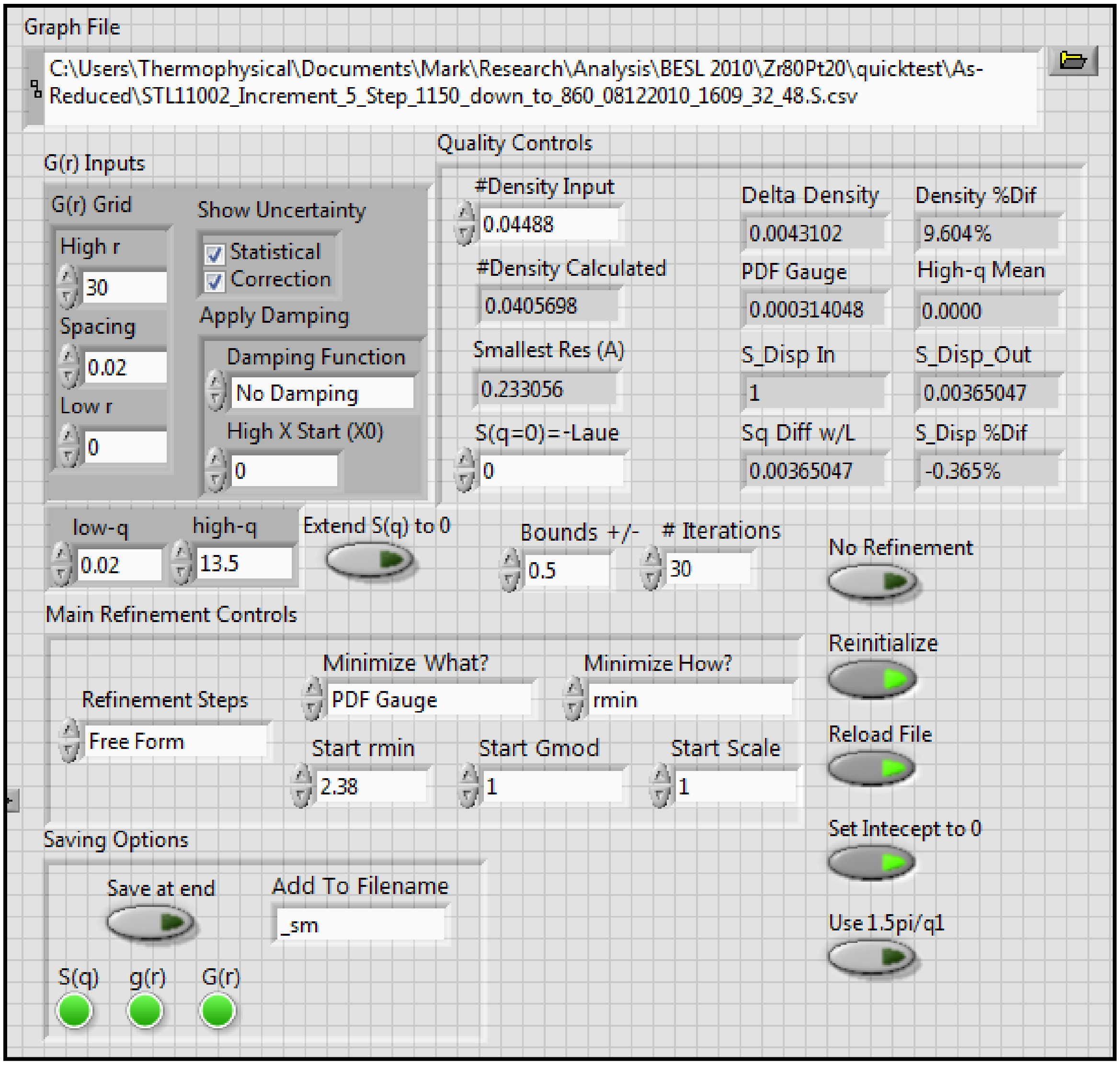
Graph File
C:\Users\Thermophysical\Documents\Mark\Research\Analysis\BESL 2010\Zr80Pt20\quicktest\As-Reduced\STL11002_Increment_5_Step_1150_down_to_860_08122010_1609_32_48.S.csv

G(r) Inputs
G(r) Grid
High r: 30
Spacing: 0.02
Low r: 0
Show Uncertainty
☑ Statistical
☑ Correction
Apply Damping
Damping Function: No Damping
High X Start (X0): 0

Quality Controls
#Density Input: 0.04488
#Density Calculated: 0.0405698
Smallest Res (A): 0.233056
S(q=0)=-Laue: 0
Delta Density: 0.0043102
Density %Dif: 9.604%
PDF Gauge: 0.000314048
High-q Mean: 0.0000
S_Disp In: 1
S_Disp_Out: 0.00365047
Sq Diff w/L: 0.00365047
S_Disp %Dif: -0.365%

low-q: 0.02
high-q: 13.5
Bounds +/-: 0.5
\# Iterations: 30

Main Refinement Controls
Refinement Steps: Free Form
Minimize What?: PDF Gauge
Minimize How?: rmin
Start rmin: 2.38
Start Gmod: 1
Start Scale: 1

Saving Options
Add To Filename: _sm

Figure C.2 User input parameters in *Sq_Curvature.vi*.

Graph file: An input *comma*-delimited $S(q)$ file described above containing q, $S(q)$, and optionally $S(q)$ error with exactly three lines of header.

G(r) inputs – G(r) grid: Specifications for the min, max, and spacing used in calculating $G(r)$ during the analysis. These are calculated directly from the input $S(q)$ and are not sensitive to adjustment.

G(r) inputs – Show Uncertainty: Options to show specified errors in the output $G(r)$s. They are typically turned off.

G(r) inputs – Apply Damping: Provides the user with several options to systematically damp $S(q)$ at larger-q to attempt to correct for termination errors, as well as an option to input a value where the damping begins. This can have a large effect on the output $g(r)$ but may not be physically meaningful, as it is possible to damp down actual correlations. The user is warned to use caution if these options are implemented.

Low-q / High-q: Inputs to specify the maximum and minimum q-values to use from the input data. Problems will occur if either is outside of the range of data contained in the file.

Quality controls - #Density Input: Experimental or otherwise known number density of the sample in question. This is used in the calculation of $g(r)$ and is also a refinement parameter.

Quality controls - S(q=0)=-Laue: Another possible input constraint. As q goes to 0, $S(q)$ should go to $-L$ (the Laue diffuse scattering term).

Extend S(q) to 0: This performs a linear extrapolation from the smallest q-value in the input array to q=0. This is not a physical extrapolation and it is not recommended to be used.

Bounds +/-: The amount that the specified input parameter can vary during a golden section search. For instance, if *Gmod* is being varied from an initial value of 1, a bound of “0.5” would result in the maximum and minimum final values being 1.5 and 0.5

 # Iterations: The number of cycles for each golden section search. It typically converges within 15-20 iterations. With a typical computer, 30 cycles does not significantly extend the analysis time.

C.2.2 Refinement Controls

There are many options for refinement available to the user. The final analysis used in this dissertation is described in Section A.7 and is also briefly described in this section.

Currently there are three values that can be minimized to attempt to improve the reduction. Only one can be selected at a time by changing *Minimize What?*:

PDFGauge: The algorithm minimizes the "Peterson Metric" [4]. This value represents the deviation from linearity in the *hard-sphere* region in $G(r)$. A large value indicates significant deviations from linearity. This is one of the primary methods used for fitting fluorescence and scaling parameters during X-ray data reduction.

S(q)|q=0: The algorithm minimizes the difference between the input parameter *S(q=0)=-Laue* and the actual value at the first data point in the input array. The user should be aware that if *low-q* ≠ 0, then the algorithm compares the first data point in the input array to the input parameter, which may not necessarily be the value at q=0.

#Density: The algorithm minimizes the difference between the input parameter *#Density Input* and the actual value estimated from the slope in the *hard-sphere* region of $G(r)$.

There are three primary parameters that can be adjusted to help improve the refinement of the input $S(q)$. Only one can be selected at a time by changing *Minimize How?*:

Start rmin: Specifies the cutoff value used in the estimation of the slope in the *hard-sphere* region of $G(r)$. There is an option (*Use 1.5pi/q1* true/false) to perform a manual estimate, but this can result in unphysical bumps before the primary peak.

Start Gmod: Specifies a multiplicative modifier to the slope calculated from the *hard-sphere* region of $G(r)$. A value of *Gmod* = 1 represents an unmodified slope.

Start Scale: Specifies a multiplicative modifier to the input $S(q)$, equivalent to Peterson's α [4] using $S'(q) = \alpha S(q)+\beta$. To ensure proper normalization, $\beta=1-\alpha$.

There are several *Refinement Steps* available to the user for commonly used combinations of constraint+parameter. If *Free Form* is selected, *Minimize What?* and *Minimize How?* can be freely modified by the user. The other options specify constraint+parameter pairs. The best method found to reduce the data is as follows:

1) Optimize *rmin* by minimizing *PDFGauge*

2) Optimize *Gmod* by minimizing *PDFGauge*

3) Optimize α by minimizing *#Density*

C.2.3 Saving Options and Additional Boolean Buttons

Once reduction is complete, the button *Save at end* will save the data to files formatted similarly to the input $S(q)$ files. The buttons between $S(q)$, $G(r)$, and $g(r)$ allow the user to select which output curves are saved. *Add To Filename* will automatically attach the specified string to the end of the filename prior to the file extension. If an underscore is desired after the input filename, it must be specified by the user. All files are saved within the input directory and will overwrite existing files. The output format is: InputFilenameQualifier.type.dat, where up to five input file extensions are removed. The data are saved as tab-delimited files.

There are several Boolean buttons available to the user that can affect the analysis:

No Refinement: Skips all golden section searches, but still performs small-*r* oscillation removal

Reinitialize: regularly used parameter which resets all *Main Refinement Control* and *Saving Options* parameters to their default, un-altered values.

Reload File: Should be left as “True”. Each time the program is run, it will re-load the input file. If set to “False”, the program will use the final values set in the *Input S(q)* graph at the end of the previous run. This has not been thoroughly tested and has known termination issues.

Set Intercept to 0: Should be left as “True”. This specifies whether or not the slope of small-r $G(r)$ should be forced to be constrained by $G(r=0) = 0$.

Use 1.5pi/q1: Forces *Start rmin* to be equal to $1.5\pi/q_1$, where q_1 is taken as the position of the first absolute maximum in the input $S(q)$. As previously noted, if this is fixed too far below the minimum before the main peak in $G(r)$ it can result in incomplete removal of ripples, introducing an unphysical bump.

C.3 *BT_Deconstruction.vi*

This program’s primary purpose is to separate out the Bhatia-Thornton (BT) partial structure factors and partial pair-distribution functions for a binary alloy (used in Chapter 5) [5] using two experimental inputs. If the partial weighting of one of the three BT partials is very small for both X-ray and neutron weighting (less than 1%), its contribution can be ignored and the other two partials can be solve numerically. Because both input files are expected to be binned differently as a function of q, this program performs Hermite interpolations to re-bin the data.

There are a many possible user input parameters (Figure C.3), but the majority are consistent with other LabVIEW programs currently in use and will not be described in this section. Instead, only unique parameters will be described here.

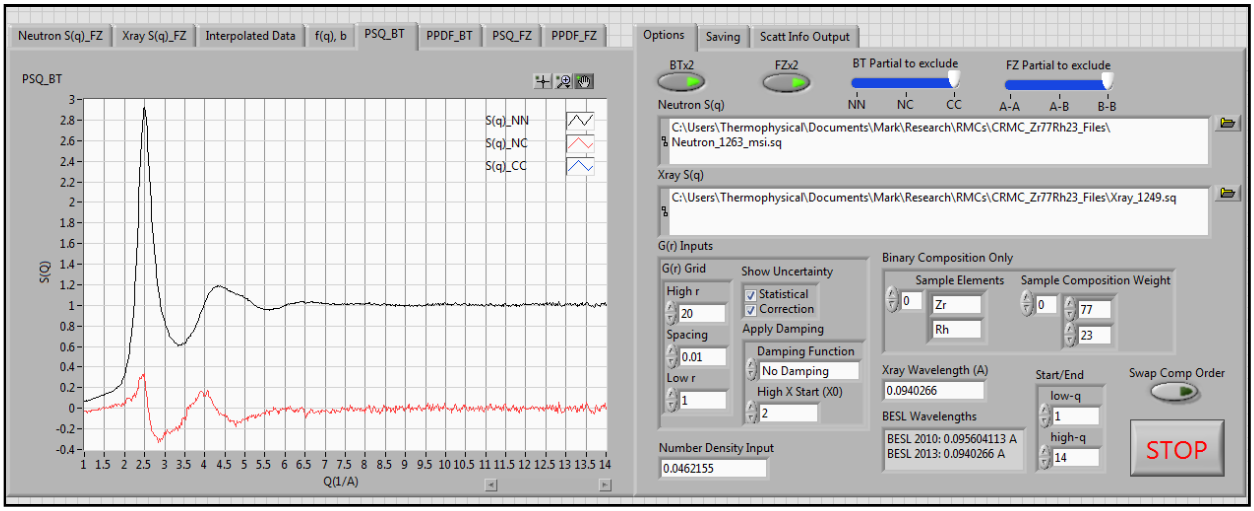

Neutron S(q): C:\Users\Thermophysical\Documents\Mark\Research\RMCs\CRMC_Zr77Rh23_Files\Neutron_1263_msi.sq

Xray S(q): C:\Users\Thermophysical\Documents\Mark\Research\RMCs\CRMC_Zr77Rh23_Files\Xray_1249.sq

G(r) Inputs
G(r) Grid
High r: 20
Spacing: 0.01
Low r: 1
Show Uncertainty
☑ Statistical
☑ Correction
Apply Damping
Damping Function: No Damping
High X Start (X0): 2
Number Density Input: 0.0462155

Binary Composition Only
Sample Elements: 0; Zr; Rh
Sample Composition Weight: 0; 77; 23
Xray Wavelength (A): 0.0940266
BESL Wavelengths
BESL 2010: 0.095604113 A
BESL 2013: 0.0940266 A
Start/End
low-q: 1
high-q: 14
Swap Comp Order

Figure C.3 Front panel of *BT_Deconstruction.vi* displaying the S_{NN} and S_{NC} BT partials.

C.3.1 Options Tab

The most important parameters for calculation of BT partials are the composition and atomic ratios (necessary for calculating the neutron weighting factors) and X-ray wavelength (necessary for calculating the X-ray weighting factors). The order of elements is important in the interpretation of the output curves for the Number-Chemical (S_{NC} or g_{NC}) partials. These weighting factors contain either $\Delta b = b_a - b_b$ or $\Delta f(q) = f_a - f_b$, representing the difference in neutron scattering lengths or X-ray form factors, respectively. As such, the first element listed under *Sample Elements* corresponds to b_a and f_a and will change the direction and interpretation of oscillations in S_{NC} and g_{NC}. A button labeled *Swap Comp Order* will perform a one-time reversal of the order of input elements. The only effect of swapping the order of elements is to change the sign of the cross-correlation term.

Attempts were made to perform a pseudo-inverse of the 3x2 matrix containing the 6 BT partial weighting factors for two input structure factors; this can be accessed by setting *BTx2* to “False”. All attempts were unsuccessful, but the user is welcome to attempt similar tests with their own data. If one partial weighting factor is negligible in both X-ray and neutron scattering calculations, setting this button to “True” will reveal a slide bar named *BT Partial to exclude* to select which partial to exclude. In this dissertation, the only partial that had negligible weighting was the Chemical-Chemical contribution. The labels NN, NC, and CC represent the exclusion of the Number-Number, Number-Chemical, and Chemical-Chemical contributions, respectively.

This program will also calculate the Faber Ziman (FZ) [6] partial structure factors and partial pair-correlation functions. Similar attempts were made to use a pseudo-inverse of the 3x2 matrix containing the 6 FZ partial weighting factors. These were also unsuccessful. If *FZx2* is set to “True”, a slide bar is revealed to select a specific partial structure factor to exclude if the weighting functions are appropriately negligible. As the FZ labels are element specific, the labels use generic names that represent a binary system of composition A_XB_{100-X}.

C.3.2 Saving Tab

Options on this tab are relatively self explanatory. *Add To Filename* differs in this program from others as an underscore is automatically added if this parameter is not empty, but it does nothing if no additional text is specified. The button *Save Files?* will enable saving of all potential outputs. *Saving Options* generates a list of possible types of curves to be saved, along with a button selecting whether the individual curve will be saved.

C.3.3 Scatt Info Output Tab

This tab contains calculated values relevant to the operation of the program for the user to visually check the accuracy of the look-up tables used. The matrices are formatted with the first row representing the neutron weighting factors and the second row representing the X-ray weighting factors. The tabulated values of the elemental neutron scattering lengths (*bi*), weighted averages, Δb (*Neutron scattering info*), and the q=0 value of the X-ray atomic form factors (*f_i(0)*) are displayed.

C.3.4 Graph Tabs

There are several tabs on the left side of the program (Figure C.3) that display various input and output curves. The first two tabs represent the input neutron and X-ray $S(q)$s, respectively, normalized within the Faber-Ziman scheme. The *Interpolated data* tab contains the input graphs from the previous two tabs as well as the same two curves after they have been re-binned to a common q-spacing to convince the user that the interpolations are correct. The *f(q), b* tab plots the X-ray atomic form factors in several formats, including both elemental and individually weighted elemental (*f_a(q), c_a*f_a(q)* respectively), the total summed form factor $<f(q)>$, and the average of the square, $<f^2(q)>$.

The final four tabs contain the BT partial structure factors, the BT partial pair-distribution functions, the FZ partial structure factors, and the FZ partial pair-distribution functions. The FZ partials rarely have negligible weighting in both X-ray and neutron scattering, and the calculated curves are not useful without that condition being met.

C.4 *BT_From_3xPPDF.vi*

If more complete information is available, such as a full set of partial pair-distribution functions or partial structure factors generated either from Molecular Dynamics (MD) or Reverse Monte Carlo (RMC) simulations, the BT partials can be directly calculated based on their relative compositional weighting (Figure C.4).

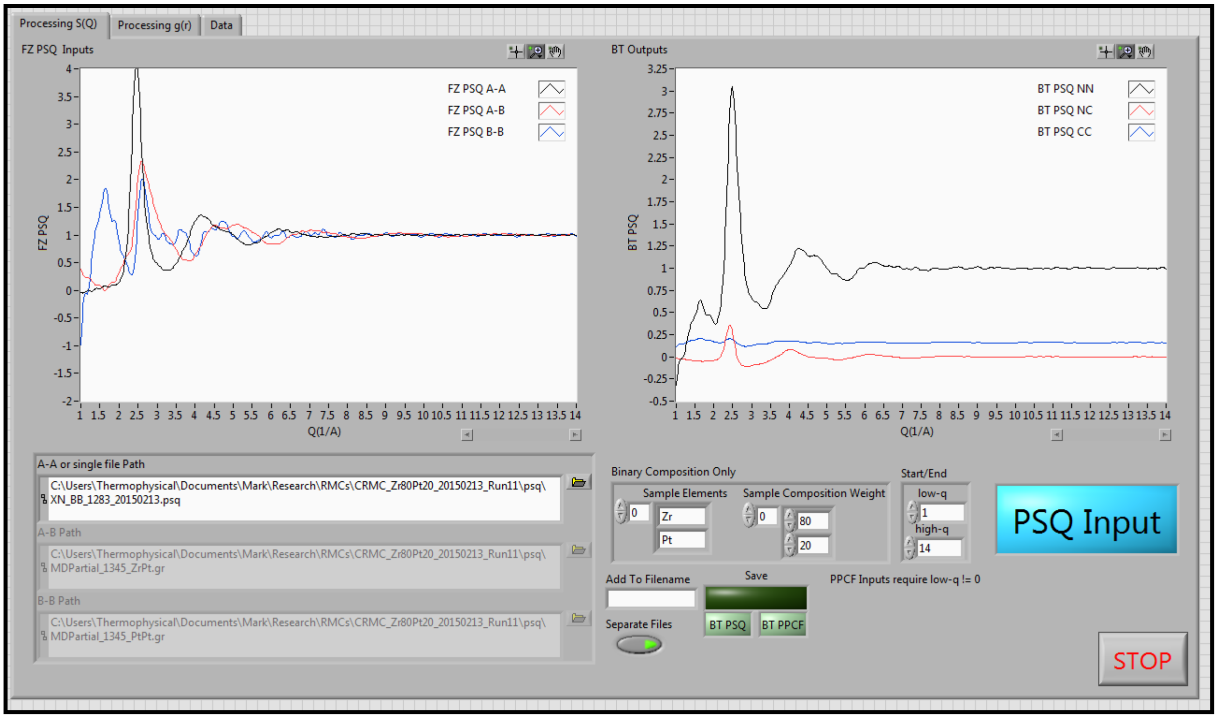

A-A or single file Path: C:\Users\Thermophysical\Documents\Mark\Research\RMCs\CRMC_Zr80Pt20_20150213_Run11\psq\XN_BB_1283_20150213.psq

A-B Path: C:\Users\Thermophysical\Documents\Mark\Research\RMCs\CRMC_Zr80Pt20_20150213_Run11\psq\MDPartial_1345_ZrPt.gr

B-B Path: C:\Users\Thermophysical\Documents\Mark\Research\RMCs\CRMC_Zr80Pt20_20150213_Run11\psq\MDPartial_1345_PtPt.gr

Binary Composition Only

Sample Elements: 0, Zr, Pt

Sample Composition Weight: 0, 80, 20

Start/End

low-q: 1

high-q: 14

Add To Filename:

Separate Files

Figure C.4 Front panel of *BT_From_3xPPDF.vi*.

There are two primary methods of importing three separate partials into this program; it must be specified using *Single File* or *Separate Files* button. The current label is the expected import format. If *Single File* is selected, the program expects the file format to be consistent with either **.psq*, **.pfq*, or **.ppcf* outputs from the RMC program, RMC_POT++. Traditional PPCF constraints used in RMC_POT++ analysis uses files saved as **.gr*, and these individual files are also compatible.

If the input file is **.psq* or **.pfq*, the program expects a 5-line header with either four columns of data containing q, S_{AA}, S_{AB}, and S_{BB} or two columns containing q and a single partial. If multiple files are used, only the first two columns are selected in each file.

If the input file is **.ppcf*, the program expects an 8-line header; if the input file is **.gr*, the program expects a 2-line header with four columns of data containing r, g_{AA}, g_{AB}, and g_{BB} or two columns of data containing *r* and a single partial. If multiple files are used, only the first two columns are used. In all cases, the imported data are Fourier transformed into *q*-space using the input number density on the *processing g(r)* tab.

If the input file contains an unrecognized extension, the program uses the parameters for **.psq*, although this is relatively untested. If any of the four named file extensions are detected, the large button labeled as *PSQ Input* in Figure C.4 will automatically update: Blue with a label of *PSQ Input* if **.psq* or **.pfq* are detected, and Orange with a label of *PPCF Input* if **.ppcf* or **.gr* are detected.

The calculated BT partial structure factors and/or partial pair-correlation functions can be saved using the *Save* button, with the smaller buttons (labeled *BT PSQ* and *BT PPCF*) selecting types of files to save. Similar to *BT_Deconstruction.vi*, *Add To Filename* will automatically add an underscore if the string is not empty, but will otherwise leave the filename un-altered with the exception of the final output extension.

The tabs on the left in Figure C.4 contain plots of the input FZ partials and calculated BT partials for $S(q)$ and $g(r)$ respectively. Input parameters controlling the *r*-spacing (ONLY if the input files are in *q*-space) are contained on the *Processing g(r)* tab, as well as the number density input. It should be noted that *lowr* cannot be smaller than $r = 1$ without causing issues with the calculations. If the user is interested in the exact matrix used to determine the PSQs and PPCFs, these are contained on the *data* tab in the order of AA, AB, and BB.

C.5 *pdf_to_Sq.vi*

The primary purpose of this VI was to test the effect of an overall multiplicative scaling factor, α, while developing the data reduction techniques used for putting X-ray and neutron scattering on the same absolute scale (Section A.7). This VI can also be used to quickly calculate $S(q)$ from $g(r)$. The output cannot be programmatically saved, but it can be exported by right-clicking on the output graph, *S(q)*, and selecting *Export* → *Export Data To Clipboard* or → *Export Data To Excel*.

The expected input file formatting is consistent with the **.PDF.csv* output from *X-ray Batch.vi* [2, 7] and consists of three header lines. A number density input is required to properly Fourier transform to $S(q)$. The start/end points in $g(r)$ can be set using *Start/End*. This VI uses controls similar to *X-ray Batch.vi*, which was designed with the intention of converting from $S(q)$ → $g(r)$. Therefore, the labeling *low-q* and *high-q* actually refer to the parameters for the input $g(r)$ rather than the output calculations. $S(q)$ can be calculated in a specified q-range and spacing using the *Grid* input where, again, this control was designed with the reverse process in mind. The user can alter *g(r) Scaling Factor* to test the effect of a multiplicative constant on $g(r)$ on the final $S(q)$.

There are two additional calculated parameters, *Low-q Mean* and *Rough S(q1)* which were initially used for testing purposes in order to determine how well $S(q)$ tailed towards $q = 0$ Å^{-1} and what the effect was on the peak height, $S(q_1)$. These are very rough calculations and are not intended to be used in quantitative analysis.

C.6 *ppcf_to_Sq.vi*

This VI was designed to quickly build a total $g(r)$ from PPCFs output from RMC_POT using either X-ray or neutron scattering weighting and transform them into $S(q)$.

This VI will take inputs of either a single file containing r and three partial $g(r)$s, or it will load three individual files each containing r and a single partial $g(r)$. If loading a single file, the expected formatting will be consistent with the **.ppcf* file output from RMC_POT, containing 8 lines of header. The file must end in **.ppcf*. If loading individual files, they must all end with **.gr* and contain exactly two lines of header. In this case, the *r*-binning is not expected to be constant and the data will be interpolated.

The experimental or otherwise known number density is required for accurate conversion to $S(q)$. In all cases, the composition must also be known. It should be pointed out that this VI is only designed for BINARY compositions and would require modifications if more complex systems are studied.

Similar to other VIs described in this appendix, several controls are used in other VIs such as *Grid Output*. The labels are still formatted for $S(q)$ → $g(r)$. Like in the VI *pdf_to_Sq.vi* (Section C.5), the *High r* and *Low r* in this control refer to the max and minimum values in the final $S(q)$.

The Boolean *Extend to 0* should always be set to *True*; it is a residual function that should no longer be necessary to change.

The Boolean *Rebin?* was included in case future modifications of this VI were necessary that potentially altered the internal analysis steps. If a single file is loaded that contains all partial $g(r)$s, there is no effect. This must be *True* if three individual partials are loaded in that contain separate *r*-binnings, such as digitization from literature.

The file saving options are similar to other VIs in this appendix. An underscore does not need to be included in *Add To Filename*; the program will automatically add one in if it is needed. If left blank, no alteration is done to the output filename.

C.7 *Batch_VI_Parsing.vi*

This VI was designed for use with the modified Voro++ used for analysis of Voronoi tessellations in this dissertation (Chapter 5). This VI converts the file formatting output from Voro++ into a format useable by a Python selection script written by Z. Markow [8]. This VI can also be used to analyze Voronoi polyhedra as a function of small-face area removed (Figure C.5).

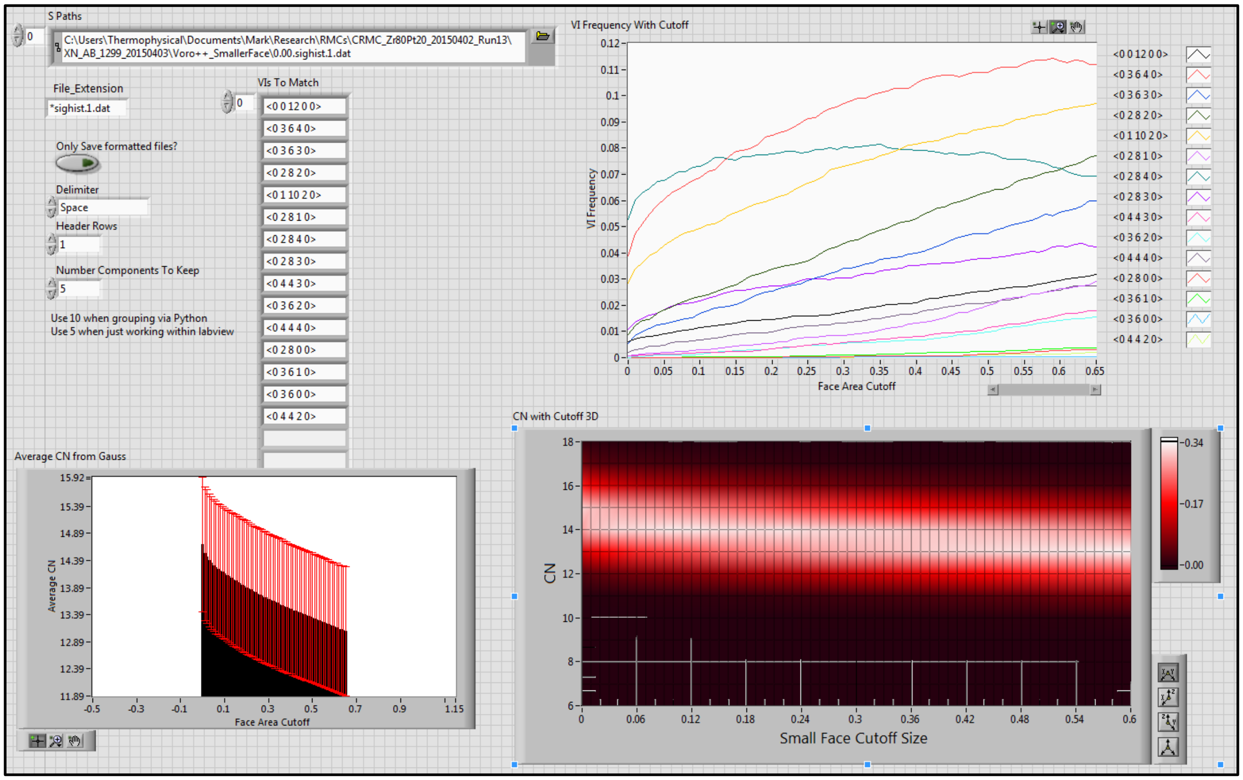

S Paths
0
C:\Users\Thermophysical\Documents\Mark\Research\RMCs\CRMC_Zr80Pt20_20150402_Run13\XN_AB_1299_20150403\Voro++_SmallerFace\0.00.sighist.1.dat

File_Extension: *sighist.1.dat

Only Save formatted files?

Delimiter: Space

Header Rows: 1

Number Components To Keep: 5

Use 10 when grouping via Python
Use 5 when just working within labview

VIs To Match
0
<0 0 12 0 0>
<0 3 6 4 0>
<0 3 6 3 0>
<0 2 8 2 0>
<0 1 10 2 0>
<0 2 8 1 0>
<0 2 8 4 0>
<0 2 8 3 0>
<0 4 4 3 0>
<0 3 6 2 0>
<0 4 4 4 0>
<0 2 8 0 0>
<0 3 6 1 0>
<0 3 6 0 0>
<0 4 4 2 0>

Figure C.5 Front panel of *Batch_VI_Parsing.vi*.

This VI can import one or more files; they can be filtered for partial string matches using *File_Extension*. The input filename is expected to comply with the following format:

#.##.sighist.&.dat

where "#.##" is a three digit value representing the absolute size of the faces that were removed and is used as the "additional specifier" that can be defined within Voro++, *sighist* is part of the default Voro++ output naming scheme, and "&" represents either the atom type or "all" atom types. For the binary systems A-B considered in this dissertation, there were three output files where &=1,2,all. "1" represents A-centered polyhedra, "2" represents B-centered polyhedra, and "all" represents the combined total. Each of these files consists of a single header line containing column labels. The rest of the file is formatted as a histogram of the total counts (first column) found for a given Voronoi index (the remaining columns containing the number of *n*-sided faces, starting with n=3). The histogram is pre-sorted by decreasing frequency.

There are several inputs on the front panel (Figure C.5) which are set by default to the parameters used for the Voro++ **.sighist.** output files, but have the capability of being modified if future users use differently formatted files. These features have not been tested for options other than the default setting. The type of delimiter between numbers can be changed using *Delimiter*. Common delimiters are already included, such as *Space* (default), *Comma*, *Tab*, and *End of Line*. The parameter *Header Rows* can be changed to an arbitrary number of lines. The parameter *Number Components To Keep* is used to select the largest *n*-sided face allowed in the final output. Increasing this value past the number of *n*-sided faces contained in the input file does not add additional 0's, but instead will output the entire Voronoi string. Once unnecessary *n*-sized faces are removed from consideration, the remaining *n*-sized faces are separated by spaces then enclosed in angled brackets ("<" and ">"). If the initial Voronoi index was "0 0 12 0 0 0 0 0 0 0" and only four components were kept, the final output would be the string "<0 0 12 0>". Two common configurations were identified: When performing Voronoi index matching within this program, the default settings contain only 5 components (*VIs To Match*). When sorting the output histogram using the Python script *DataRowSelectorVI.py*, the VIs are formatted with 10 components.

Within this VI, the histogram counts per Voronoi index are summed and converted into "fraction of total". If the user wishes to know the fraction of the total polyhedra that is not type-centered specific, it must be calculated by hand. The coordination number of each polyhedron is also calculated during the conversion.

If the user selects the Boolean *Only Save formatted files?*, no analysis is performed on the selected files and instead each file is quickly converted into a comma-delimited **.csv* file. The output file name is the same as the input, but replaces the file extension "*dat*" with "*formatted.csv*". Within this file is a single header containing column labels: VI, Raw Count, Frequency, and CN.

If further analysis is of interest to the user, the Boolean *Only Save formatted files?* must be set to *False*. The program will compile Voronoi indices into an array of strings defined by *VIs To Match*. The number of elements within the matching strings must be the same as the number of components kept or else the program will find zero matches. The plot *VI Frequency With Cutoff* will scan the *Face Area Cutoff* from the first four characters (assumed to be digits) of the filename, and the frequency will be found from the appropriate column in the row matching the appropriate Voronoi index. A three dimensional histogram, *CN with Cutoff 3D*, will plot the relative frequency of each coordination number between 0 and 25 against the small-face cutoff size. While a 3D plot is available, it has been found to be more useful to view the X-Y projection with the frequency scaled by color. The plot *Average CN from Gauss* outputs the average coordination number at each face cutoff as determined from the peak position of a

Gaussian fit to the histogram. The error bars represent the standard deviation, or width, of the CN distribution.

C.8 References

[1] J. Neuefeind, M. Feygenson, J. Carruth, R. Hoffmann, K.K. Chipley, *Nuclear Instruments and Methods in Physics Research Section B: Beam Interactions with Materials and Atoms* **287**, 68 (2012).

[2] J.C. Bendert, N.A. Mauro, K.F. Kelton, *Journal of Applied Crystallography* **46**, 999 (2013).

[3] J. Kiefer, *Proceedings of the American Mathematical Society* **4**, 502 (1953).

[4] P.F. Peterson, E.S. Božin, T. Proffen, S.J.L. Billinge, *Journal of Applied Crystallography* **36**, 53 (2003).

[5] A.B. Bhatia, D.E. Thornton, *Physical Review B* **2**, 3004 (1970).

[6] T.E. Faber, J.M. Ziman, *Philosophical Magazine* **11**, 153 (1965).

[7] J.C. Bendert, *Thermophysical and Structural Measurements of Liquid Metallic Alloys Using Electrostatic Levitation*, Ph.D. Thesis, Washington University in Saint Louis (2013).

[8] Z. Markow, *Structural Characterization of Amorphous* $Cu_{46}Zr_{54}$ *Using Molecular Dynamics Simulations, Reverse-Monte Carlo Simulations, and Weighted Voronoi Diagrams*, B.S. Thesis, Washington University in St. Louis (2014).